Destabilisation of liquid sheets of dilute emulsions

Clara Vernay

Collège Doctoral du Languedoc-Roussillon

THÈSE

Pour obtenir le grade de

Docteur

Délivré par l'**Université de Montpellier**

Préparée au sein de l'école doctorale **Information Structure et Système**
Et de l'unité de recherche **Laboratoire Charles Coulomb**

Spécialité: **Physique**

Présentée par **Clara VERNAY**

Déstabilisation de nappes liquides d'émulsions diluées

Soutenue le 16 octobre 2015 devant le jury composé de

M. Christian LIGOURE	Professeur, Université de Montpellier	Directeur de thèse
Mme Laurence RAMOS	Directrice de recherche, CNRS	Co-directeur de thèse
M. Arnaud SAINT-JALMES	Directeur de recherche, CNRS	Rapporteur
M. Emmanuel VILLERMAUX	Professeur, Aix-Marseille Université	Rapporteur
M. Jérôme BIBETTE	Professeur ESPCI ParisTech	Président
M. Christophe YBERT	Directeur de recherche, CNRS	Examinateur
M. Jean-Christophe CASTAING	Solvay Novecare	Examinateur

UNIVERSITÉ MONTPELLIER

Remerciements

Ce manuscrit de thèse représente l'aboutissement d'un long cheminement aussi bien professionnel que personnel et ne saurait donc commencer sans des remerciements pour les personnes ayant contribué à ce travail de près ou de loin...

Mes remerciements s'adressent en priorité à mes deux directeurs de thèse, Laurence Ramos et Christian Ligoure. Merci pour vos explications toujours justes, votre patience, votre disponibilité (malgré vos emplois du temps chargés!) et votre confiance. J'ai énormément appris sur le plan scientifique ces trois dernières années. Mais ce que je retiendrai surtout, ce sont ces heures de réunions toujours dans la bonne humeur pendant lesquelles nous riions souvent. Tout en étant exigeants vous avez su créer une atmosphère de travail détendue et très motivante. Je pense que notre petite équipe fonctionnait très bien, je suis heureuse d'avoir passé ces trois dernières années à vos cotés. J'espère que nos chemins se recroiseront.

Je tiens ensuite à remercier l'entreprise Solvay pour m'avoir offert la possibilité de réaliser cette thèse CIFRE, un bel équilibre entre préoccupations industrielles et fondamentales. Merci à Jean-Christophe Castaing pour avoir retenu ma candidature pour cette thèse il y a trois ans, merci de m'avoir fait confiance. Je suis aujourd'hui très heureuse de continuer l'aventure chez Solvay de "l'autre coté"! Jean-Christophe a non seulement été à l'initiative de cette thèse mais il a aussi suivi tout son déroulement au travers de nos nombreuses discussions scientifiques avec Rajesh Goyal. Merci à tous les deux pour ces discussions très enrichissantes qui ont jalonné ma thèse.

Merci aux rapporteurs de ma thèse, Emmanuel Villermaux et Arnaud Saint-Jalmes, et aux membres du jury, Christophe Ybert, Jean-Christophe Castaing et Jérôme Bibette, pour leur lecture détaillée de mon manuscrit et leur remarques pertinentes, c'était un plaisir et un honneur de vous présenter mes travaux. Merci en particulier à Emmanuel Villermaux pour avoir suivi ma thèse tout au long de ces trois ans en participant chaque année à mon comité de suivi de thèse. Nos longues discussions avec Laurence et Christian ont certainement influencé mes travaux.

Merci à toute l'équipe ITAP de l'IRSTEA (Bernadette Ruelle, Ariane Vallet, Jean-Paul Douzals et Cyril Tinet) avec qui j'ai réalisé les expériences de spray. En particulier merci à Jean-Paul Douzals avec qui j'ai passé quelques semaines au cours de ces trois dernières années à mesurer des tailles de gouttes dans un hangar toujours trop froid ou trop chaud! Merci à Jean-Paul pour avoir toujours répondu avec patience à mes nombreuses questions sur les buses, spray et tout l'univers de la pulvérisation que j'ai découvert au cours de cette thèse.

Mes remerciements se dirigent ensuite vers tout le personnel du laboratoire Charles Coulomb, en particulier ceux qui n'ont pas forcément contribué directement à ces travaux mais qui m'ont rendu la vie plus facile et agréable ces trois dernières années. Merci en particulier à Tina, Ado et Jean-Christophe. Merci à tous mes compagnons du second étage, Ty, Jean-Marc, Raymond et Philippe, pour votre bonne humeur permanente et vos sourires. Merci aux mécaniciens de l'atelier pour la conception des pièces de mon montage expérimental. Merci en particulier à Pascal Martinez pour ne pas avoir rechigné quand je demandais des pièces de plus en plus petites!

Merci à tous les permanents de l'équipe Matière Molle: Amélie, Antonio, Christophe, Daniel, Gladys, Julian, Luca, Manouk, Martin, Maurizio, Michel et Serge. Même si j'étais terrorisée à chaque fois que je devais présenter mes travaux devant vous en séminaire interne, j'ai eu la chance de côtoyer ces trois dernières années des personnes réellement passionnées et passionnantes toujours prêtes à discuter science et manip au détour d'un couloir ou autour d'un café.

Je remercie tout chaleureusement les non permanents de l'équipe Matière Molle avec qui j'ai passé quelques semaines ou quelques années au laboratoire : Adrian, Cyrille, Dafne, Dario, Delphine, Domenico, Giuseppe, Laure, Luca, Rym, Sristhi, Stefano, Valentin et Yassine. Je suis arrivée à Montpellier il y a trois ans sans connaître personne, je peux dire maintenant que je laisse des amis derrière moi. Merci pour tous ces moments partagés au laboratoire autour d'un café et en dehors autour d'une bière ou d'une pizza! Je ne pensais pas apprendre l'italien en arrivant à Montpellier... mais c'était sans compter sur la colonie napolitaine / calabraise / milanaise! Une pensée particulière pour le concentré de bonne humeur qui est rentré dans mon bureau il y a un peu plus d'un an, merci Dafne pour ton sourire à toute épreuve et pour avoir amené du soleil dans mon bureau. Merci à Rym pour ta joie de vivre communicative qui a éclairé le labo pendant un an et demi, j'espère que notre amitié se prolongera au-delà de cette thèse. Et enfin un merci tout particulier à Adri pour avoir été un soutien moral sans faille ces deux dernières années.

Pour finir je tiens à remercier ma famille et en particulier mes parents et mes deux frères, Thibaud et Romain. Même si les discussions autour de ma thèse se sont souvent limitées à "comment vont les gouttes?", vous m'avez toujours encouragée et vous avez toujours été très fiers de mon parcours, je vous en remercie.

Merci à Farès pour tout le reste.

Contents

Introduction

One of the major environmental issues during applications of pesticides by spray on cultivated crops is the drift process. Because of the wind, droplets may drift away from the targeted crop and cause contamination for the surrounding areas and populations. As smaller spray drops have a higher potential of off-target movement, the amount of spray drift is often correlated to the spray volume contained in drops with diameter lower than 150 μm. Hence, a straightforward way to reduce the drift process is to control the spray drop size distribution by reducing the proportion of smallest drops in the spray (typically drops with a diameter smaller than 150 μm). Two different approaches have been developed to achieve this goal. One strategy relies on the modification of the operating parameters, such as the applied pressure and the nozzle height, and the modification of the spray-nozzle design with the development of air-induction nozzle [Dorr 2013, Butler Ellis 1999a]. The other strategy relies on the addition of adjuvants in the carrier fluid to modify the physical-chemical parameters of the fluid to be sprayed [Butler Ellis 1997, Miller 2000].

Different anti-drift additives have been developed to produce sprays with relatively large drops ($> 150\mu$m) and with a narrow drop size distribution. High-molecular-weight polymer solutions, such as guar gum, have been used as anti-drift adjuvant for several decades and it has been demonstrated that it significantly increases the volume median diameter of the spray drop size distribution [Mun 1999]. However, one of the major drawback of the utilization of a high-molecular-weight polymer solution as an anti-drift adjuvant is the drastic reduction of the angle of the spray [Dexter 2001]. Dilute oil-in-water emulsions have been developed as an alternative class of anti-drift adjuvants. When sprayed through the nozzle, dilute emulsions increase the volume median diameter of the drop issued from the spray and decrease the volume fraction of small drops [Butler Ellis 1999b, Bergeron 2003, Qin 2010]. Dilute emulsions also slightly increase the spray angle, which is a noticeable advantage compared to dilute polymer solutions [Hilz 2013b].

Although rather well documented [Butler Ellis 1999b, Qin 2010, Hilz 2013a, Altieri 2014], the physical mechanisms at the origin of the size increase of spray drops of emulsions remain unclear. Agricultural spraying involves atomizing a liquid stream through a hydraulic nozzle. At the exit of the nozzle, a free liquid sheet is formed, which is subsequently destabilized into droplets. Hence, an understanding of the origin of the changes of the spray drop size distribution can certainly be gained by investigating the destabilization mechanisms of such liquid sheets. The objective of my PhD thesis is to investigate the destabilization mechanisms of liquid sheets of dilute emulsions in order to characterize the influence of dilute emulsions on spray drop size distributions and so elucidate the origin of their anti-drift properties. The manuscript is divided in 8 chapters.

Chapter 1 is a bibliographic chapter that presents the state of the art on the topics. We define the drift process and present the methods to mitigate the drift exposure, in particular the utilization of anti-drift adjuvants that are our main concern. A specific section is dedicated to the description of the formation of a spray issuing from agricultural nozzles with the different mechanisms involved. We show that, in any case, the atomization process can be seen as three successive steps: (i) the formation of a thin sheet of liquid at the nozzle exit, (ii) the breakup of the sheet in ligaments and (iii) the destabilization of the ligaments into drops. In the last part of this chapter we report the utilization of dilute oil-in-water emulsions as anti-drift adjuvants.

Chapter 2 is dedicated to the description of the anti-drift adjuvants studied in the thesis. For the purpose of our study, model systems, which have the same anti-drift properties as commercial anti-drift adjuvants but will a simple composition, have been used. In this chapter, we present in details the chemical compositions of the studied dilute oil-in-water emulsions, the preparation and characterization methods of the emulsions. In the whole thesis, we will compare the behavior of dilute oil-in-water emulsions to the behavior of reference systems: pure water on the one hand and dilute high-molecular-weight polymer solutions on the other hand, which constitutes the second category of anti-drift adjuvants.

In Chapter 3, we focus on the last step of the atomization process, which is the destabilization of liquid ligaments into drops. We first rapidly introduce some theoretical background concerning the capillary destabilization of liquid columns and the formation of satellite drops. Then, with two model experiments, we investigate the destabilization of liquid ligaments of pure water, dilute oil-in-water emulsion and dilute solution of high-molecular-weight polymer. We show that a dilute emulsion does not have any effect on the destabilization of liquid ligaments, which is in all aspects similar to the one of water. By contrast, the high-molecular-weight polymer solution exhibits a specific destabilization mechanism, which is at the origin of their anti-drift properties.

Chapter 4 is dedicated to the study of the first step of the atomization process, i.e. the destabilization of liquid sheets, in order to understand the mechanism of action of emulsions as anti-drift adjuvants. We first describe the single-tear experimental set-up used to produce controlled liquid sheets and the original method developed to measure the thickness field of liquid sheets. We characterize in details the expansion dynamics of a pure water sheet, its destabilization mechanism and determine its thickness field. We finally use the single-tear experiment to produce liquid sheets of complex fluids and show that emulsion-based liquid sheets are destabilized through a perforation mechanism with the nucleation of holes in the liquid film.

In Chapter 5, we focus on the destabilization mechanism of liquid sheets of dilute oil-in-water emulsions. The objective of this chapter is to understand if the specific perforation mechanism observed for dilute emulsions can explain the role of emulsions as

anti-drift adjuvants for agrochemicals. To answer this question, we compare the results obtained with the single-tear experimental set-up to those collected using a conventional spray technique. Some of the physical-chemical parameters of the emulsion, such as the emulsion concentration and the emulsion droplet size distribution, are modified to rationalize their influence on the perforation mechanism and on the spray drop size distribution. We finally show that the relevant mechanism causing the increase of drops size in the emulsion-based spray is a perforation mechanism.

In Chapter 6, we aim to understand the physical mechanism at the origin of the nucleation of holes in the liquid film. We use the experimental technique developed in Chapter 4 to visualize the thickness modulations during the perforation process of emulsion-based liquid sheet issued from the single-tear experiment. We highlight the existence of a localized thinning of the sheet leading to the hole formation. After characterizing in details the thinning process, we propose a mechanism at the origin of the nucleation of holes in the liquid film.

In Chapter 7, we modify the physical-chemical parameters of the emulsions to play on the perforation mechanism proposed in Chapter 6. Up to now, the studied emulsions were stabilized by non-ionic surfactants, soluble in oil (dispersed phase of the emulsion). In this chapter, we study emulsions stabilized by water-soluble ionic surfactants. We investigate the influence of the addition of salts and amphiphilic copolymers in the emulsion aqueous phase on the perforation mechanism.

In Chapter 8, we propose a summary of the influence of the physico-chemical parameters of the emulsion on the perforation mechanism that we have proposed to explain the nucleation of holes in emulsion-based liquid sheets. Finally, in a conclusive part we discuss the perspectives open by our work for the development of new formulations of anti-drift adjuvants.

Chapter 1

Anti-drift adjuvants for agrochemical sprays: Motivation and state of the art

Contents

The use of pesticides is an integral part of the modern agriculture and plays a key role in safeguarding the productivity and quality of cultivated crop against animal pests, pathogens and weeds. Depending on crops, the worldwide crop lost due to pests varies from 50 % to more than 80 %. The utilization of agrochemicals has been estimated to prevent a loss of up to 45 % of the world food supply [Oerke 2004]. However, in the last decades the intensive utilization of pesticides have raised the issue of its harmful

impact on the environment. Pesticide exposure due to spray drift is one of the major concern regarding the pulverization of agrochemicals. The first section of this chapter is dedicated to the definition of the drift process and the different factors influencing spray drift. In the second section of this chapter, we present the different drift mitigation methods, in particular the utilization of anti-drift adjuvants that are our main concern. The formation of a spray issuing from agricultural nozzles is explained in the third section with the different mechanisms involved. In the fourth section of this chapter, we report the utilization of dilute oil-in-water emulsions as anti-drift adjuvants.

1.1 Pulverization of agrochemicals: the drift process

1.1.1 Definition and evaluation of the spray drift

Pesticides are usually sprayed over crops by the mean of hydraulic nozzle forming a dispersion of drops in air. One of the major environmental issues during applications of pesticides on cultivated crops is the drift process. The spray drift is defined as "the downwind movement of airborne spray droplets beyond the intended area of application originating from aerial or ground-based spraying operations" [Stephenson 2006]. Hence, the drift process is the off-target movement of spray drops principally due to the wind that entails a fraction of the pesticide solution to not reach the target area. Spray drift losses can be either as droplets or as vapor due to volatile substances. The picture shown is Figure 1.1 highlights the spray drift process with the formation of a cloud of pesticide solution around the tractor.

Figure 1.1: Pesticide treatment on orchards highlighting the drift process [TOPPS].

The drift of pesticide solutions is a major source of environmental contamination

[FOCUS 2007a]. For example, spray drift can contaminate surface water, but it can also be harmful for the surrounding population. Butler Ellis et al. [Butler Ellis 2010] have estimated the dermal exposition of bystander to pesticide spray drift. For example, almost 2 mL of pesticide solution is deposited on bystander at a distance of 2.0 m from the sprayed area for a wind of 5 m/s. Their objective was to define a relationship between the measurement of airborne spray and the measurement of bystander dermal exposure in order to develop a predictive model that can evaluate the dermal exposure from the airborne spray measurement.

The evaluation of spray drift can be performed with field trials with full spraying equipment as defined by ISO 22866 standard. Collectors are placed at several distances from the spraying equipment to collect drift deposits. A tracer dye is usually added to the solution to be sprayed to quantify by spectrofluorimetric techniques the drift deposits [Miller 2003]. It is primordial to monitor the conditions at the time of application, in particular those relating to the weather and the operating parameters (nozzle type, pressure applied...) as they have a significant impact on the drift process. This constitutes the best advantage of field trials as the drift evaluations are performed at weather and operating conditions similar to the ones involved during crop protection treatment.

The evaluation of spray drift can also be performed by laboratory measurements, principally with wind tunnel (ISO 22856 standard). The principle of the measurement is the same as for field trial measurements. Collectors are positioned at different distances from the nozzles to collect drift deposits, which are quantified thanks to a tracer dye. But it is not possible to reproduce wind velocity and turbulence profiles in a wind tunnel that match those observed in field conditions. However, the main advantage of wind tunnel measurements is that the operating conditions and the wind applied are perfectly controlled, hence allowing different experiments to be performed with the exact same experimental conditions, which is never the case for field trials [Miller 2003].

1.1.2 Factors influencing spray drift

Spray drift is strongly influenced by many factors. This section is dedicated to the description of some of these factors in particular those relating to the meteorological conditions, the spray drop size distribution and the operating parameters.

1.1.2.1 Meteorological conditions

A clear correlation has been established by several studies between wind speed and spray drift deposition [FOCUS 2007b, Murphy 2000, Permin 1992]. Arvidsson et al. [Arvidsson 2011] extensively studied the influence of meteorological factors on the spray drift with field trials. The authors investigated in particular the influence of the wind speed, the temperature and the air humidity. They quantified the spray drift as a percentage of the total applied volume. They observed that, over the range of wind investigated (1.3 - 5.0 m/s), an increase of wind speed of 1 m/s entails an increase of the spray drift

by about 0.94 %. The influence of wind speed was confirmed by experiments performed in a wind tunnel [Combellack 1996]. Humidity and temperature also have an influence on the drift process as they can lead to the evaporation of the carrier liquid, which entails a decrease of the drop size facilitating the drift (see section 1.1.2.2) [Holterman 2003]. Arvidsson et al. [Arvidsson 2011] experimentally measured the influence of the air temperature on the drift process. They observed that, over the range of air temperatures (3.7-15.7)°C, an increase of the air temperature of 1°C entails an increase of the drift by 0.2 %.

1.1.2.2 Spray drop size distribution

There is an obvious relationship between the spray drop size distribution and the drift process. The smallest is the spray drop, the highest is its potential of off-target movement. Small drops have low inertia making them highly susceptible to be drifted away from the intended area. Bergeron [Bergeron 2003] has estimated the distance that a drop can travel exposed to a crosswind of 5 km/h depending on its size. These estimations are summarized in Table 1.1. From these estimations, it is clear that a spray drop with a diameter lower than 240 μm can significantly drift off target.

Droplet diameter (μm)	Time required to fall 2 meters	Lateral distance travelled in falling 2 m with a 5 km/h wind
5	66 min	5 km
20	4.2 min	1 km
100	10 s	13 m
240	6 s	8.5 m
400	2 s	2.6 m
1000	1 s	1.4 m

Table 1.1: Typical drift values for a range of droplet sizes [Bergeron 2003].

In a recent review, Al Heidary et al. [Al Heidary 2014] have summarized the relationship between the spray drift and the spray drop size distribution. The spray drop size distribution is characterized by the volume median diameter, $DV50$, which corresponds to the spray drop diameter such as 50 % of the volume is contained in drops of smaller diameter and 50 % in drops of bigger diameter. In the review, the authors compared the data obtained by several groups for wind tunnel experiments relating the spray drift to the parameter $DV50$ of the spray drop size distribution [Taylor 2004, Stainier 2006, Miller 2011]. The drift losses are expressed as percentage of the applied volume. These results are presented in Figure 1.2. A decrease of the spray drop size promotes a significant increase of the drift percentage. For $DV50$ around 400 μm the drift losses represent around 3 % of the applied volume whereas for spray drops such as $DV50$ is equal to 150 μm the drift losses represent almost 14 % of the applied volume.

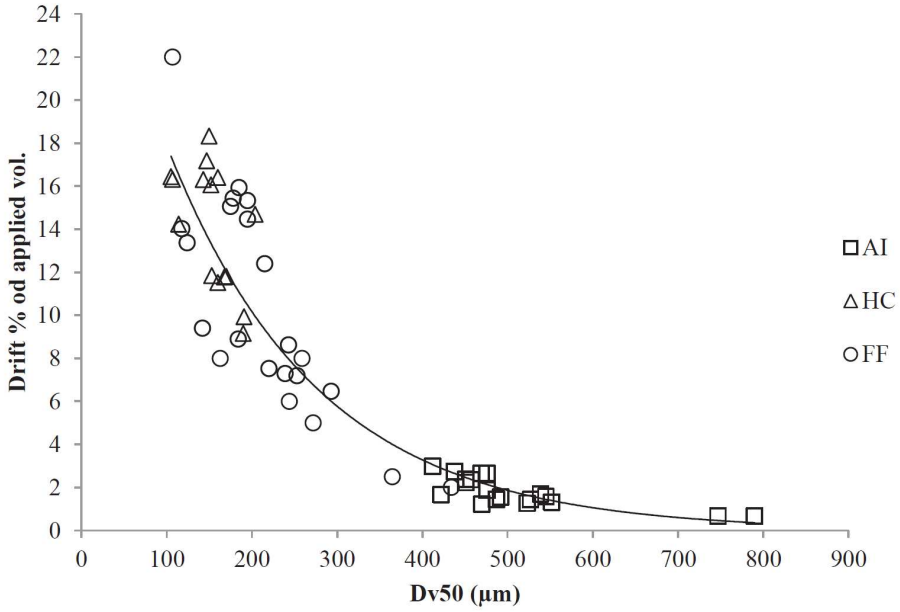

Figure 1.2: Drift losses expressed as percentage of applied volume collected in wind tunnel as a function of the spray drop size distribution parameter $DV50$ for various nozzles. AI: air injection nozzle: FF: flat-fan nozzle and HC: hollow cone nozzle [Al Heidary 2014].

From these data, it is clearly that the drift is primally affected by the spray drop size and that bigger spray drops permit to consequently reduce the drift losses. Therefore, a straightforward solution to reduce the drift process is to control the spray drop size distribution by reducing the formation of small drops.

Several parameters are used to characterize the spray drop size distribution. The parameter $V150$ (resp. $V100$) represents the volume fraction of spray drops with a diameter lower than 150 μm (resp. 100 μm). The amount of spray drift is often correlated with the proportion of driftable drops in the spray, i.e. the spray volume contained in small drops characterized (depending on the studies) by $V150$ or $V100$. The risk of off-target exposure decreases when $V150$ or $V100$ is reduced.

The spray drop size distribution is strongly affected by the operating parameters such as the nozzle type and the pressure applied. The influence of these parameters on the spray drop size distribution and so on the spray drift are presented in the next subsection.

1.1.2.3 Operating parameters

Operating parameters have a crucial importance on the spray drift. First, the boom height can strongly modify the spray drift. Wind velocity generally increases with height from the ground. Therefore, the closer to the ground the boom is kept, the smaller is the risk of drift. Arvidsson et al. [Arvidsson 2011] observed that an increase of the boom height of 0.1 m (over the range 0.3-1.7 m) entails an increase of the drift losses of 0.94 %

of applied volume. The drift losses are reduced by 40 % when the boom height decreases from 1.7 m to 0.9 m and by 75 % when the spray boom is further decreased to 0.3 m.

The drift process is also affected by the pressure applied to produce the spray. Nuyttens et al. [Nuyttens 2007] reported that higher spray pressure results in smaller spray drops for a large variety of nozzles. For example, the spray volume median diameter, $DV50$, is reduced by 10 % (from 274 μm to 247 μm) when the pressure applied is increased from 3.0 to 4.0 bar (for a Hardi ISO F110 03 flat-fan nozzle).

The design of the nozzle has also a significant impact on the drift process. The most commonly used for agricultural applications are flat-fan nozzles and hollow-cone nozzles (Figure 1.3). Flat-fan nozzles produce a spray with an ellipsoidal cross section whereas for hollow-cone nozzles the spray pattern is a circular ring as illustrated in Figure 1.3. For the same nozzle size and pressure, hollow-cone nozzles produce spray with smaller drops and so with the highest proportion of drops prone to drift [Nuyttens 2007]. In the last decades, nozzles have been designed to specifically reduce the spray drift. These nozzles will be presented in section 1.2.2.

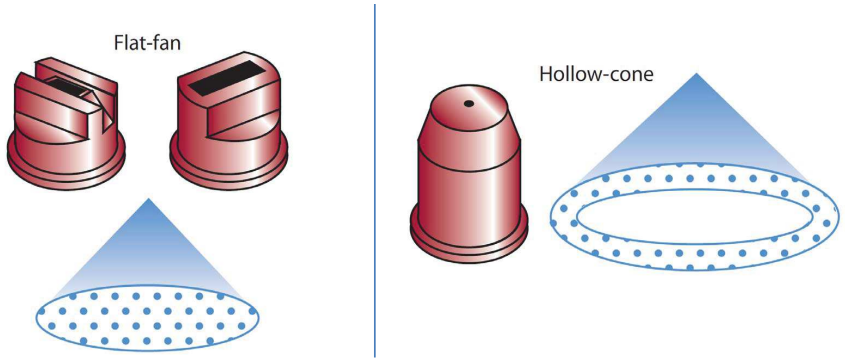

Figure 1.3: Flat-fan and hollow-cone nozzles with the resulting spray pattern [Grisso 2013].

Different parameters are used to characterize a nozzle: the nozzle type (flat-fan, hollow-cone...), the spray top angle and the nozzle flow rate measured at 2.8 bar expressed in Gallon per minute (GPM, 1 GPM=3.8 L/min). A nozzle "F 110 03" corresponds to a flat-fan nozzle (F) with a top spray angle equal to 110° and a flow rate of 0.3 GPM at 2.8 bar. At a given pressure, the flow rate of the nozzle is directly related to the size of the hole in the nozzle. Therefore, the two last digits of the nozzle names are usually referred as the size of the nozzle. For agricultural spray application it typically varies between 02 and 08. Nuyttens et al. [Nuyttens 2007] measured the drop size distribution of spray produced by a same type of nozzle (flat-fan nozzles with a top angle of 110°) but of different sizes (Hardi ISO F 110 03, Hardi ISO F 110 04 and Hardi ISO F 110 06). They reported a relative increase by 21 % of $DV50$ with the size of the nozzle from 274 μm for the nozzle Hardi ISO F 110 03 to 345 μm for the nozzle Hardi ISO F 110 06 operating at 3 bar.

1.2 Drift mitigation methods

Spray drift is considered as a main source of contamination of surface water and in general of environmental contamination. With the increasing concern about the potential risk of pesticides for environmental and human safety, different mitigation measures to reduce pesticide exposure via spray drift have been developed. The EU reports "Landscape and mitigation factors in aquatic risk assessment" [FOCUS 2007a, FOCUS 2007b] present an overview of the existing procedures in spray drift mitigations. They mainly recommend the utilization of three types of mitigation measures: the utilization of no-spray buffer zones, the use of windbreaks and the application of drift-reducing technology [FOCUS 2007a]. These different spray drift mitigation measures are briefly presented in this section. Another drift mitigation strategy relies on the addition of adjuvants in the pesticide carrier fluid to modify the physical-chemical parameters of the fluid to be sprayed. The different types of anti-drift adjuvants will be presented in the last part of this section. Note that the utilization of anti-drift adjuvants is not yet well evaluated and not implemented in the drift mitigation scenarios proposed by the EU report [FOCUS 2007a], which highlights that more work should be done to "assess the influence of formulation type of spray solution on spray drift (e.g. the addition of extra adjuvants)".

1.2.1 No-spray buffer zones and windbreaks

A no-spray buffer zone is an area in which direct application of pesticides is prohibited. These zones are defined between a sensitive area (pond, wetland...) and a crop being treated in order to protect the sensitive area from spray drift (see Figure 1.4). No-spray buffer zones are mandatory for pesticide pulverization in many European countries including France. The regulations concerning the no-spray buffer zones differ from country to country. The zones width depends on the toxicity of the pesticide to be sprayed. In France, four classes are defined that involve no-spray buffer zones of 5 m, 20 m, 50 m and 100 m width ("Arrêté du 12 septembre 2006 relatif à la mise sur le marché et à l'utilisation des produits visés à l'article L. 253-1 du code rural et de la pêche maritime"). Following the EU report "Landscape and mitigation factors in aquatic risk assessment" [FOCUS 2007a] the implementation of no-spray buffer zone provides more than 95 % reduction of drift exposure. Brown et al. [Brown 2004] highlighted the influence of no-spray buffer zone on the reduction of the spray deposit in field trials.

Windbreaks comprising trees or vegetation can act as vegetation barriers and be efficient to mitigate spray drift. The EU report "Landscape and mitigation factors in aquatic risk assessment" [FOCUS 2007a] highlights that the relative reduction in drift deposition due to windbreak can be up to 90 % depending on the vegetation barrier. However, with field trials Brown et al. showed that no-spray buffer zones are more efficient to reduce drift deposits than natural windbreaks in high wind conditions (>4 m/s), i.e. conditions favorable to spray drift [Brown 2004].

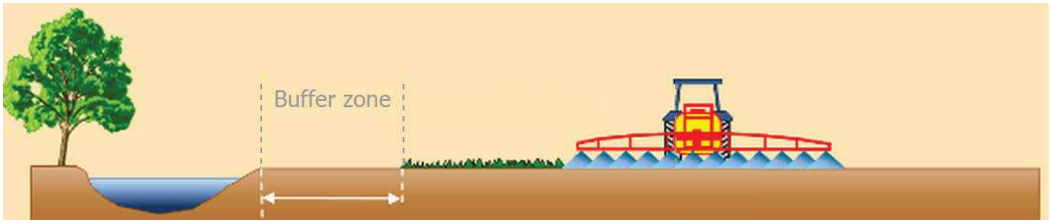

Figure 1.4: Illustration of the no-spray buffer zones implemented to reduce the risk of drift process [TOPPS].

The implementation of large no-spray buffer zones removes a significant area from the cultivated and treated crops and so constitutes a loss in the production. The width of no-spray buffer zones can be reduced when anti-drift technology are used. For example, in France, the no-spray buffer zone width can be reduced from 20 m to 5 m or 50 m to 5 m if two conditions are respected ("Arrêté du 12 septembre 2006 relatif à la mise sur le marché et à l'utilisation des produits visés à l'article L. 253-1 du code rural et de la pêche maritime"):

- the presence of natural vegetation barrier (windbreak) adjacent to ecologically sensitive wetlands environments,
- the utilization of anti-drift nozzles.

In the following section, we will describe the drift-reducing technology developed and their efficiency to mitigate spray drift.

1.2.2 Drift reducing equipment

Drift reducing equipment is a more straightforward way to reduce the spray drift by modifying the spray drop size distribution. The nozzle design considerably influences the size of the spray drops. In the last decades, efforts have been made to design new nozzles to minimize drift potential by increasing the spray drop size, as we have seen that smaller drops are more prone to be drifted off-target (section 1.1.2.2). The principally used drift reducing equipments are low-drift and air-induction nozzles. Low-drift nozzles are nozzles with a pre-orifice that reduces the internal effective pressure in the nozzle and so produce spray drops larger than those produced with a standard flat-fan nozzle operating at the same pressure. The air-induction nozzle mechanism relies on Venturi principle and is illustrated Figure 1.5. Air is drawn into the nozzle due to Venturi effect. Thus air bubbles are incorporated into the liquid producing coarser spray drops as compared to those obtained with a conventional flat-fan nozzle operating at the same pressure (see sketch Figure 1.5).

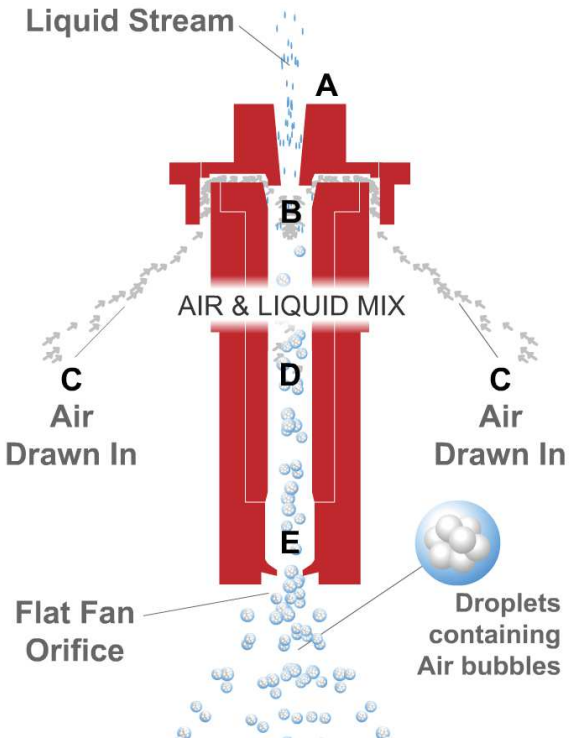

Figure 1.5: Sketch of an air-induction nozzle [BFS].

Nuyttens et al. [Nuyttens 2007] measured the spray drop size distribution for a wide variety of nozzles. In particular, they compared a conventional flat-fan nozzle (Hardi ISO F 110 02), a low-drift nozzle (Hardi ISO LD 110 02) and an air-induction nozzle (Hardi ISO Injet 110 02) operating at the same flow rate. They observed that bigger spray drops are obtained for the air-induction nozzle ($DV50$=507 μm), intermediate drops are obtained with the low drift nozzle ($DV50$=295 μm) and smaller spray drops with the conventional flat-fan nozzle ($DV50$=214 μm). Clearly, the air-induction nozzles are the more efficient to increase the size of the spray drops, with an increase by 137 % compared to conventional flat-fan nozzles. Similar conclusions are obtained in the study conducted by Dorr et al. [Dorr 2013]. Air-induction nozzles are very efficient to reduce the proportion of driftable spray drops. However the formation of very large drops (>400 μm) raises a concern about an increase of runoff and a decrease of the pesticide solution efficiency due to a bad homogeneity of leaf coverage [Nuyttens 2007].

1.2.3 Anti-drift adjuvants

An alternative strategy to mitigate the spray drift is to use anti-drift adjuvants. These adjuvants are added to the pesticide solution and permit to control the spray drop size distribution and so to reduce the drift process. Different anti-drift additives have been developed to produce sprays with relatively large drops and with a narrow drop size distri-

bution. These additives can be classified into two categories: dilute high-molecular-weight polymer solutions and dilute oil-in-water emulsions, which will be presented separately in this section.

1.2.3.1 Dilute solutions of high-molecular-weight polymer

The first category of anti-drift adjuvants is based on the utilization of high-molecular-weight polymer, principally polyacrylamides (PA), polyethylene oxide (PEO) and polysaccharides such as guar gum and xanthan gums [Young 2004]. Polyacrylamides were the first drift control adjuvants to be widely adopted for crop treatment. The use of guar gum is a more recent technology but guar gum is nowadays widely used as anti-drift adjuvant. Dilute solutions of high-molecular-weight polymer significantly increase the spay drop size and reduce the proportion of small drops in the spray. Mun et al. [Mun 1999] have investigated the effect of PEO solutions of high molecular weight on the drop size distribution of sprays produced with agricultural nozzles. They measured the volume median diameter, $DV50$, of spray produced with a conventional flat-fan nozzle for polymer solutions and pure water. $DV50$ is equal to 700 μm for a solution of PEO of molecular weight 600,000 g/mol at a concentration of 0.095 % w/w in water and to 150 μm for pure water. The utilization of high-molecular weight polymer solution involves an increase by 365 % of the spray volume median diameter and a decrease by 86 % of the proportion of spray drops with a diameter lower than 105 μm [Mun 1999]. High-molecular-weight polymer solutions are efficient to reduce the proportion of small drops in the spray and so to reduce the drift risk. The mechanisms at the origin of the increase of the spray drop size for high-molecular-weight polymer solutions will be described in section 3.1.3. The utilization of large polymers have benefits other than reducing drift to enhance the agricultural solution efficiency. Indeed, polymer solutions increase the retention of the formulation by the plants by reducing the rebound of the formulation on the leaves [Green 2007, Bergeron 2003].

However, the utilization of high-molecular-weight polymers as anti-drift adjuvants have some drawbacks. First, the polymers notably reduce the top angle of the spray [Mun 1999, Dexter 2001]. By decreasing the spray angle, the overlap between spray is decreased leading to an inferior spray distribution homogeneity. What is more, the polymer macromolecules are susceptible to be broken as they repeatedly pass through the pump of an agricultural sprayer, which reduces their efficiency with time [Young 2004]. Finally, solution of high-molecular-weight polymer entails a global shift of the spray drop size distribution towards larger sizes. Therefore, polymers increase the population of bigger spray drops (typically drops with a diameter larger than 500 μm), which leads to a bad homogeneity of leaf coverage.

An ideal anti-drift adjuvant would be one that reduces the proportion of small drops in the spray but without increasing the proportion of bigger drops.

1.2.3.2 Dilute oil-in-water emulsions

Dilute oil-in-water emulsions have been developed more recently as an alternative class of anti-drift adjuvants. When sprayed through the nozzle, dilute emulsions increase the volume median diameter of the drop issued from the spray and decrease the volume fraction of small drops. Miller et al. [Miller 2000] studied the atomization of vegetable oil based oil-in-water emulsions with conventional flat-fan nozzles. They showed that emulsions are able to increase the volume median diameter of the spray, $DV50$, by about 22 % and to reduce the proportion of drops with a diameter lower than 100 μm by about 73 %. Similar conclusions were obtained later by Qin et al. [Qin 2010] for the atomization of soybean oil based dilute oil-in-water emulsions with conventional flat-fan nozzles. More recently, Hilz et al. [Hilz 2013a] showed that a large variety of emulsified oils (mineral, vegetable, polydimethylsiloxane...) are able to reduce the proportion of small drops in the spray as shown in Table 1.2 summarizing some of their experimental data. Their results clearly show that emulsified oils permit to reduce the proportion of small drops in the spray (<100 μm, V100) without increasing the proportion of big drops in the spray (>400 μm, V400). What is more, they reported that emulsions involve an increase of the spray angle, which is a noticeable advantage over dilute polymer solutions [Hilz 2013a].

	water	sunflower oil	methyl ester oil	mineral oil	white oil
$DV50$ (μm)	194.6	256.9	246.1	237.5	231.2
$V100$ (% v/v)	11.0	3.3	3.8	5.8	6.1
$V400$ (% v/v)	92.9	82.7	84.9	85.2	85.8

Table 1.2: Volume median diameter of the spray drops, $DV50$, proportion of spray small drops, $V100$, and proportion of spray big drops, $V400$ [Hilz 2013a], for the atomization with conventional flat-fan nozzles of different emulsified oils as indicated in the Table.

Finally, dilute oil-in-water emulsions are efficient anti-drift adjuvants that present some advantages compared to adjuvants based on high-molecular-weight polymers. The dilute oil-in-water emulsions do not involve a global shift of the spray drop size distribution towards bigger sizes but only reduce the proportion of small drops in the spray. This point and the increase of the spray angle constitute precious advantages of dilute oil-in-water emulsions as anti-drift adjuvants compared to polymer-based adjuvants. The physical mechanisms at the origin of the increase of the spray drop size for dilute oil-in-water emulsions will be discussed in section 1.4 and experimentally investigated in Chapter 6.

1.3 Spray formation

1.3.1 Formation of a liquid sheet

Conventional flat-fan nozzles are the most widely used nozzles for agricultural applications. Flat-fan nozzles used to spray pesticide solutions on crop fields produce a two dimensional sheet of fluid, as shown in Figure 1.6. The liquid sheet is then destabilized into drops forming the spray. The velocity of the sheet at the output of the flat-fan nozzle ranges from 2 to 7 m/s [Nuyttens 2007] depending on the nozzle size, the nozzle design and the pressure applied. As visible in Figure 1.6, liquid sheets produced by nozzles are bounded by a thicker rim. In 1960, Dombrowski et al. showed that the thickness of the liquid sheet is inversely proportional to the distance from the nozzle [Dombrowski 1960].

The first investigations of the destabilization of liquid sheets produced by agricultural nozzles were reported by Dombrowski et al. in 1954 [Dombrowski 1954]. These authors studied with a stroboscopic photographic technique the breakup mechanisms of liquid sheets of different complex fluids produced by a variety of agricultural nozzles. They distinguished three destabilization mechanisms of liquid sheets: (i) the destabilization of the rim, (ii) the destabilization of the sheet by oscillations and (iii) the destabilization of the sheet by perforations. These three breakup mechanisms will be described in details in the following sections.

1.3.2 Rim destabilization

The edges of the sheet are destabilized by a specific mechanism different from the breakup mechanisms of the liquid film. Rapidly after the nozzle orifice, disturbances appear in the thicker rim bounding the liquid film, which result in the formation of short ligaments [Clark 1971, Clark 1972], as shown in Figure 1.7. These short ligaments are then destabilized into drops through a Rayleigh-Plateau instability (this instability will be described in details in section 3.1.1). The diameter of the drops scales with the thickness of the short ligaments and so with the thickness of the rim. Hence, the drops issued from the destabilization of the edges of the sheet are coarser than the ones issued from the destabilization of the liquid film as the rim is thicker.

1.3.3 Sheet destabilization by oscillations

The liquid sheet can be destabilized by an oscillations mechanism due to the interactions with the ambient air. The sheet follows a flapping motion due to a Kelvin-Helmholtz instability, described in details in [Villermaux 2002]. The Kelvin-Helmhotz instability results from the velocity difference between the moving liquid sheet and quiescent air. The flag-like motion of the liquid is visible in Figure 1.8(a) for a liquid sheet formed with an agricultural nozzle [Clark 1972] and also in Figure 1.8(b) for a model liquid sheet formed

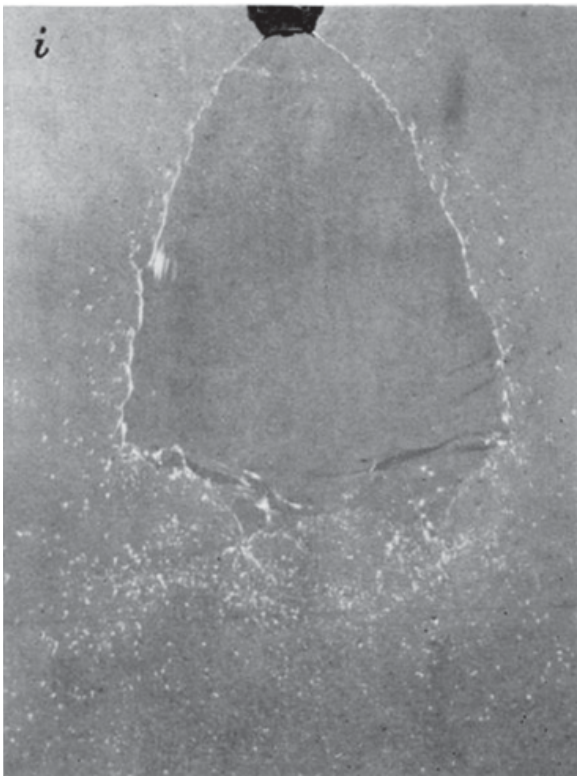

Figure 1.6: Pure water liquid sheet that emerges from a conventional flat-fan nozzle [Dombrowski 1954].

Figure 1.7: Formation of ligaments at the edges of a sheet produced by a flat-fan nozzle [Dombrowski 1954].

by the impact of two jets [Bremond 2007]. The undulations of the sheet are clearly visible in these two pictures. The flapping motion is also illustrated in Figure 1.9(a) with a sketch of the breakup mechanism by oscillations. These oscillations imply a modulation of the sheet thickness forming indentations at the sheet free edge due to a Rayleigh-Taylor instability as shown in Figure 1.9(b), which represents a transverse cross-section of the liquid sheet (shown with a frame in Figure 1.9 (a)). Liquid ligaments emerge from these indentations perpendicularly to the sheet leading edge. The formation of these perpendicular ligaments are highlighted in Figure 1.8(b). The ligaments are then destabilized into drops following a Rayleigh-Plateau instability.

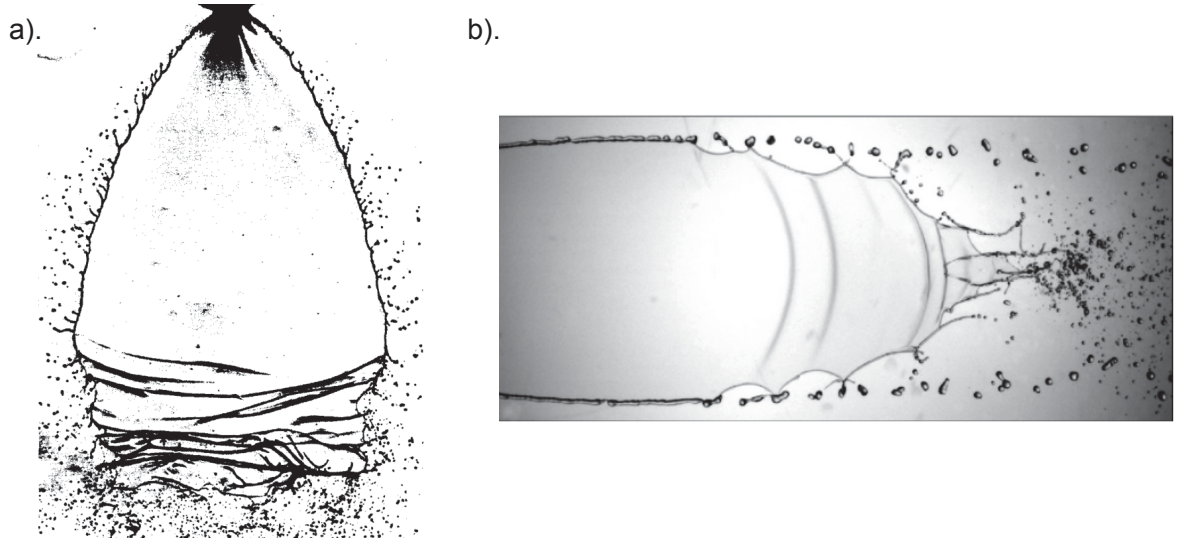

Figure 1.8: a). Destabilization by an oscillation mechanism of a liquid sheet formed by a flat-fan nozzle [Clark 1972]. b). Wave propagation along the sheet and ligament formation; the sheet is produced by the impact of two oblique liquid jets [Bremond 2007].

1.3.4 Sheet destabilization by perforations

The third sheet breakup mechanism is perforation. Dombrowski et al. [Dombrowski 1954] were the first to report the existence of this destabilization mechanism. Holes are found to nucleate in the liquid sheet, growing until they merge together and form a web of ligaments. These ligaments are then destabilized into drops following a Rayleigh-Plateau instability. This destabilization mechanism is illustrated in Figure 1.10 with the perforation breakup of an oil-in-water emulsion-based liquid sheet formed with a conventional flat-fan nozzle [Dombrowski 1954]. The destabilization by perforation has been reported for solution of solid suspensions [Dombrowski 1954, Addo-Yobo 2011], dilute oil-in-water emulsions [Dombrowski 1954, Butler Ellis 1999b, Dexter 2001, Hilz 2013a, Altieri 2014], and air bubbles stabilized by

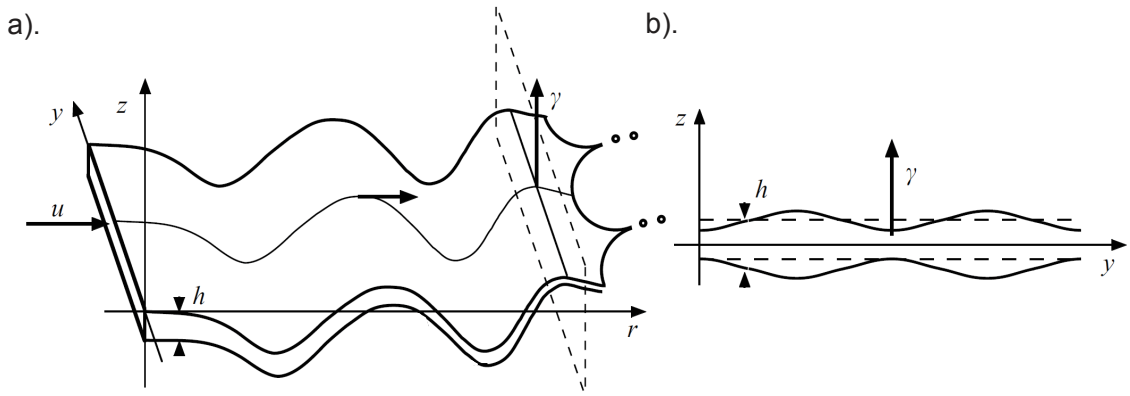

Figure 1.9: Sketch of the oscillations breakup mechanism of a liquid sheet [Bremond 2007] (a). Undulations of the liquid sheet due to Kelvin-Helmholtz instability. b). Transverse cross-section of the liquid sheet showing the thickness modulations.

surfactants in water [Lhuissier 2013]. Spielbauer et al. [Spielbauer 1994] also observed the perforation of liquid sheets produced by the impact of a jet on a solid surface for solutions with inhomogeneities not clearly identified (presumably dust particles and air bubbles).

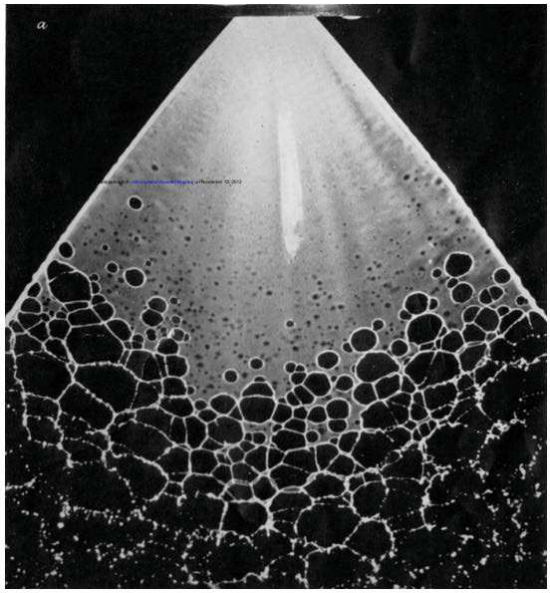

Figure 1.10: Growth of holes in the liquid sheet [Dombrowski 1954]; the sheet is produced by a flat-fan nozzle and the liquid investigated is an oil-in-water emulsion.

1.3.5 Conclusion

In conclusion, a spray produced with a conventional agricultural nozzle results from the destabilization of a liquid sheet formed at the exit of the nozzle. The liquid sheet is destabilized by a combination of three breakup mechanisms. The edges of the sheet can be destabilized into ligaments by air friction, waves can propagate along the sheet causing the formation of ligaments in the direction of the flow and holes may also appear in the sheet and grow leading to the formation of a web of ligaments. For all these destabilization mechanisms, the liquid sheet is first destabilized into ligaments. Hence, the spraying process can be seen as three successive steps: first the formation of a thin sheet of liquid, then the breakup of the sheet in ligaments and finally the destabilization of the ligaments into drops.

1.4 Dilute oil-in-water emulsions as anti-drift adjuvants

The development of efficient anti-drift adjuvants is a subject of great concern for the agrochemical industry. The mode of action of anti-drift adjuvants based on polymers of high molecular weight have been the subject of many studies and is today well understood [Mun 1999, Bergeron 2003, Dexter 1996]. The mechanism by which dilute solutions of high-molecular-weight polymer control the spray drop size will be presented in section 3.1.3 of this thesis. The utilization of dilute oil-in-water emulsions as anti-drift adjuvants is more recent. Although being documented, the physical mechanisms at the origin of the size increase of spray drops of emulsions remains unclear. In the last decade, several research groups have focused on the understanding of the mode of breakup of liquid sheet made of oil-in-water emulsions to understand their anti-drift properties. This sections is dedicated to a brief description of these studies. We will focus on few studies that investigated in details the influence of physico-chemical parameters of emulsions on the destabilization of liquid sheet and proposed a rational mechanism to explain the anti-drift properties of oil-in-water emulsions.

1.4.1 "Bridging-dewetting" mechanism

In 1954, Dombrowski et al. [Dombrowski 1954] studied the destabilization mechanism of liquid sheets formed with conventional flat-fan nozzle thanks to a stroboscopic photographic technique. They studied in particular the destabilization of liquid sheets made of liquid (oil droplets) or solid (glass or clay particles) suspensions in water. The stability of the sheet has been found to strongly depend on the type of suspended particles. Wetted particles are found to have no effect on the sheet disintegration: the authors observed the same breakup mechanism as for pure water liquid sheet. By contrary, unwettable particles, such as oil droplets, are found to puncture the liquid film and so to entail the

breakup of the sheet by a perforation mechanism (section 1.3.4). The size of the emulsion oil droplets was increased by adding an electrolyte, which causes the sheet to be destabilized by perforation closer to the nozzles therefore where the sheet is thicker.

Dombrowski et al. [Dombrowski 1954] claimed that the perforation of liquid sheets is due to the presence of unwettable particles that puncture the liquid sheet when their thickness is of order of the thickness of the film. If the particle is sufficiently hydrophobic, the particle surface is dewetted by the liquid and so connects the two interfaces. Note that a similar mechanism has been proposed for oil-based antifoams, see Figure 1.11 for a sketch of the "bridging" mechanism [Denkov 2004]. The two configurations are represented. If the particle is hydrophobic (left part of Figure 1.11) the formation of an oil bridge between the two interfaces leads to the rupture of the film by the particle dewetting. On the contrary, if the particle is hydrophilic (right part of Figure 1.11), the connection of the two interfaces leads to the formation of a stable bridge. Hence, the unwettable characteristic of the particle is crucial for this mechanism. The study conducted by Dombrowski et al. [Dombrowski 1954] was purely qualitative. For example they did not perform any measurement of the emulsion droplet size to validate their hypothesis.

1.4.2 Correlation between sheet perforations and anti-drift properties

In a series of studies [Butler Ellis 1997, Butler Ellis 1999a, Miller 2000, Butler Ellis 1999b], Butler Ellis et al. have investigated the destabilization mechanism of liquid sheets made of dilute oil-in-water emulsions formed with conventional flat-fan nozzles. They measured spray drop size distributions and took picture of the sheet during the destabilization process. Their objective was to correlate the destabilization mechanism of the liquid sheet to the resulting spray drop size distribution. They showed that liquid sheets made of pure water or surfactant aqueous solutions are destabilized through an oscillation mechanism (section 1.3.3), whereas dilute emulsion-based sheets are systematically destabilized through perforations (section 1.3.4). In the same time, they observed that dilute oil-in-water emulsions systematically increase the size of the spray drops. They thus showed a clear correlation between the sheet length at breakup and the diameter of the spray drops. The perforations cause the sheet to be destabilized closer to the nozzle, where the sheet is thicker, and so entail the formation of bigger spray drops compared to a pure water sheet that is destabilized through oscillations.

Butler Ellis et al. [Butler Ellis 1999b] investigated the effect of the emulsion concentration on the perforation mechanism. They observed that a higher emulsion concentration entails the sheet to be destabilized closer to the nozzle (a shorter breakup length) and so the formation of larger spray drops.

In conclusion, in their numerous studies, Butler Ellis et al. have clearly highlighted the relation between the perforation process and the anti-drift properties of dilute-oil-

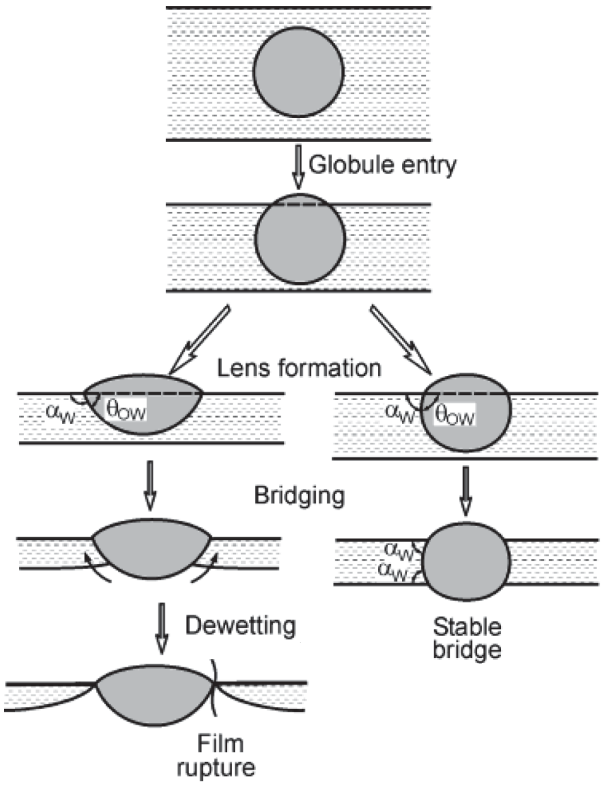

Figure 1.11: Schematic representation of the "bridging" mechanism. An oil droplet enters both interfaces of the liquid film when its diameter is equal to the thickness of the liquid film. If the particle is hydrophobic (left part), the formation of an oil bridge between the two film surfaces leads to a dewetting of the hydrophobic oil droplet and so the rupture of the liquid film. If the particle is hydrophilic (right part), a stable oil bridge is formed [Denkov 2004].

in-water emulsions. However, they did not propose any clear mechanism to explain how emulsion oil droplets provoke the nucleation of holes within the liquid film.

1.4.3 Particle deformability: a crucial parameter

Dexter [Dexter 2001] and Qin et al. [Qin 2010] investigated in two distinct studies the destabilization of sheets produced with conventional flat-fan nozzles and made of liquid or solid particle suspensions. They measured the spray drop size distribution and observed the sheet destabilization process.

In both studies, the authors showed that sheet made of suspension of solid particles is destabilized through the same breakup process as pure water sheet, i.e. through oscillations. What is more, the resulting spray drop size distribution is comparable to the one of pure water spray. In the same time, Dexter [Dexter 2001] showed that sheets made

of oil-in-water emulsions, with oil droplet of comparable diameter to the one of the solid particles, are destabilized through perforations and significantly increase the spray drop size distribution. They also showed that emulsion oil droplets entail the nucleation of holes within the sheet at thicknesses of the liquid film larger than the oil diameter. Their observations are in contradictions with the mechanism proposed by Dombrowski et al. [Dombrowski 1954].

Qin et al. [Qin 2010] argued that the destabilization through perforations is not specific to dilute oil-in-water emulsions as they observed it for sheet made of pure water. They argued that these perforations are due to turbulent flow in the nozzle and that the perforations are not at the origin of the change of the spray drop size distribution observed for dilute emulsions.

In conclusion, the studies conducted on one hand by Dexter [Dexter 2001] and on another hand by Qin et al. [Qin 2010] highlighted that the deformation or rearrangement of the particles in suspension is a crucial parameter to significantly increase the spray drop size distribution.

1.4.4 "Spreading - fluid entrainment" mechanism

Hilz et al. [Hilz 2013a] investigated the influence of different parameters of dilute oil-in-water emulsions on the spray drop size distribution, for sprays formed with conventional flat-fan nozzles. They studied different oils (mineral oil, vegetable oil, white oil and methyl ester) and showed that all emulsions increase the spray drop size distribution compared to water, but the extent depends on the type of oil used to formulate the emulsions. They found a correlation between the volume median diameter of the spray drop size distribution, $DV50$, and the ability of the oil to spread at the air/water interface. An oil droplet will spread at the air/water interface if its spreading coefficient S is positive. S is defined as $S = \gamma_{\text{air/aq}} - \gamma_{\text{air/oil}} - \gamma_{\text{aq/oil}}$, where $\gamma_{\text{a/b}}$ stands for the interfacial tension between phases "a" and "b", and "aq" stands for the aqueous phase (see Figure 1.12).

Following their experimental observations, they suggested a mechanism to explain the nucleation of holes in emulsion-based sheet. This mechanism has already been proposed by several research groups [Bergeron 1997, Denkov 2004] for the mode of action of oil-based antifoams. They argued that oil droplets enter the air/water interface. Once at the interface, emulsion droplets with a positive spreading coefficient ($S > 0$) will inevitably spread, inducing a bulk flow. This flow thins out the sheet below the spreading droplet and may become a starting point for the hole formation. This "spreading-fluid entrainment" mechanism is schematically represented in Figure 1.12(a,b).

The authors also observed that the addition of water soluble nonionic and anionic surfactants entails a decrease of the volume median diameter of the spray, $DV50$, and a destabilization of the sheet further down from the nozzle. They argued that the accumulation of surfactants at the air/water interface would decrease the air/water surface tension and so decrease the spreading coefficient S leading to a slower spreading process

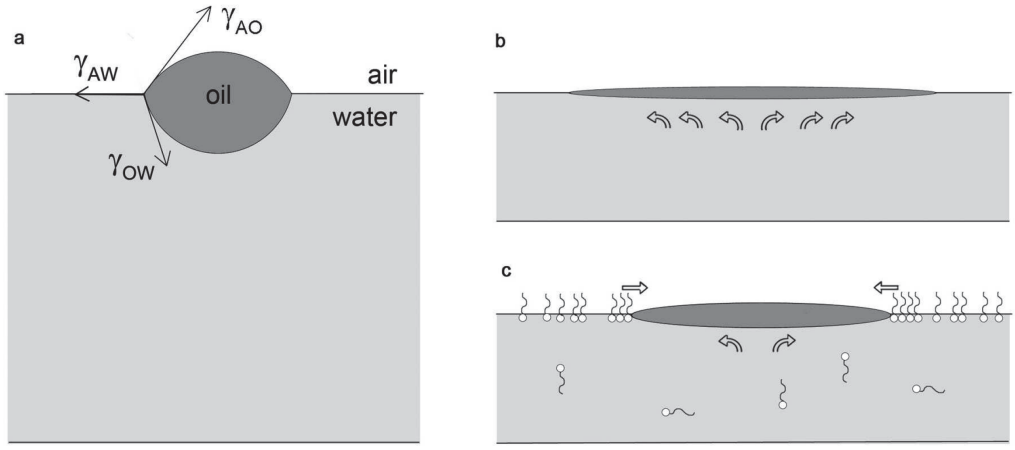

Figure 1.12: Schematic representation of the "spreading - fluid entrainment" mechanism. a). An oil droplet enter the air/water interface. b). The oil droplet spreads at the air/water interface due to its positive spreading coefficient, $S > 0$. The spreading of the oil droplet induces a subphase flow leading to a thinning of the liquid film. c). Surfactants at the air/water interface counteract the spreading of the oil droplet. The arrows indicate the direction of the subphase flow and the counteracting forces caused by the interfacial surfactant layer [Hilz 2013a].

(see Figure 1.12). As a consequence, the subphase flow is weaker and so would inhibit or retard the perforation of the liquid film. Hence, spray formation will occur further down from the nozzles and so smaller droplets are formed.

In conclusion, Hilz et al. [Hilz 2013a] suggested an interesting mechanism, already proposed for oil-based antifoams [Bergeron 1997, Denkov 2004], to explain the nucleation of holes within the liquid film. However, their experimental evidences are not completely convincing as their are only based on the measurement of the spray drop size distribution. In particular the authors did not observe directly the perforation mechanism. What is more, only four oils were studied to obtain a correlation between the spray drop size distribution and the spreading of oil drop at the air/water interface.

1.5 Objectives of the thesis

We have seen that different mitigation measures to reduce pesticide exposure via spray drift have been developed . The EU reports "Landscape and mitigation factors in aquatic risk assessment" [FOCUS 2007a, FOCUS 2007b] present an overview of the existing procedures in spray drift mitigations (no-spray buffer zones, windbreaks and drift-reducing equipment) and highlight that "more work is needed to assess the influence of formulation type of the spray solution on spray drift", i.e. the addition of adjuvants.

In the last decades, the agrochemical industry has developed efficient anti-drift adjuvants that enable a control of the spray drop size distribution by reducing the proportion of small drops in the spray. Whereas the mode of action of polymer-based adjuvants is today well understood [Mun 1999, Bergeron 2003, Dexter 1996], the mechanism by which emulsion-based adjuvants control the spray drop size distribution is still a subject of active discussion. Although being documented, the physical mechanisms at the origin of the size increase of spray drops of emulsions remain unclear even if possible mechanisms have been presented in the literature [Dombrowski 1954, Hilz 2013a].

The objective of my PhD project is to understand the physical mechanism at the origin of the control of the drop size distribution of emulsion-based spray and so at the origin of the anti-drift properties of emulsion-based anti-drift adjuvants. To rationalize the change of spray drop size distribution, we will study the destabilization mechanism of liquid sheets. We have seen that, whatever the global breakup mechanism of the sheet (oscillations or perforations), the sheet destabilization mechanism can be divided in two successively steps. First, the destabilization of the liquid sheet into ligaments and then the destabilization of these ligaments into drops. We will study these two destabilization mechanisms separately by using, in both cases, model experiments to produce well controlled ligaments and sheets to study their breakup mechanism. Indeed, as we have seen with the literature review, the experiments with liquid sheets formed by conventional flat-fan nozzles do not permit to establish without ambiguity the mechanism of action of oil-in-water emulsions as anti-drift adjuvants.

Chapter 2

Experimental systems

Contents

This chapter is dedicated to the description of the anti-drift adjuvants studied in this thesis. For the purpose of our study, model systems, which have the same anti-drift properties as commercial anti-drift adjuvants but with a simple composition, have been used. In the first two parts of the chapter, we introduce the chemical systems used: first, the different dilute oil-in-water emulsions with their composition and the emulsification techniques and then the high-molecular-weight polymer solution. The last section of this chapter is an overview of the methods used to characterize the physical properties of our chemical systems, especially the surface tension properties.

2.1 Dilute oil-in-water emulsions

The emulsions studied are dilute oil-in-water emulsions, i.e. dilute dispersions of surfactant-stabilized oil droplets in water. In this section, we present the emulsions composition, the methods used to characterize their drop size distribution and the different emulsification techniques. The common point of the different emulsions studied is that the same oil, methyllaurate, is used to formulate the emulsions. Methyllaurate is a methyl ester with a alkyl chain composed of 12 carbon atoms, see formula Figure 2.1. It is liquid at room temperature and its molecular weight is equal to 214.34 g/mol. The main difference between the different emulsions studied is the nature of the surfactant used to stabilize the oil droplets. Three different surfactants are used: a mixture of non-ionic surfactants (poly(ethylene oxide) alkyl ethers, see below), an anionic surfactant (sodium dodecyl sulfate) and a cationic surfactant (cetylpyridinium chloride). The non-ionic surfactants are initially dissolved in the emulsion oil phase whereas the ionic surfactants in the aqueous phase.

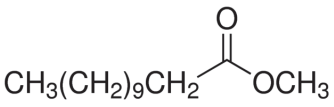

Figure 2.1: Chemical structure of methyllaurate.

2.1.1 Composition of the emulsions

2.1.1.1 Industrial emulsion

The first emulsion studied is designated as industrial emulsion as it is the formulation that is the closest to the commercial product among all the emulsions studied in this thesis. The oil phase of the industrial emulsion is composed of a mixture of methyllaurate and non-ionic surfactants of the form C_nEO_3, with C_n a hydrocarbon chain with n carbon atoms and EO_3 a short polyethylene oxide chains of three ethylene oxide units (CH_2CH_2O). The exact composition of the mixture of surfactants is the following: 1.5% w/w of $C_{10}EO_3$, 53% w/w of $C_{12}EO_3$, 44% w/w of $C_{14}EO_3$ and 1.5% w/w of $C_{16}EO_3$. The ratio between methyllaurate and the mixture of surfactants is set at 97:3 % w/w. The oil phase is provided as one product by Solvay and diluted at 0.3% v/v in milliQ water to obtain the emulsion.

2.1.1.2 Model emulsion

The composition of the model emulsion is very close to the industrial one. The oil phase of the emulsion is composed of methyllaurate (purchased from Sigma-Aldrich) and a mixture of non-ionic surfactants (provided by Solvay) of the form C_nEO_3, with C_n a hydrocarbon chain with n carbon atoms and EO_3 a short polyethylene oxide chains of three ethylene oxide units (CH_2CH_2O). The exact composition of the surfactants mixture is the same as for the industrial emulsion. The ratio between methyllaurate and the mixture of surfactants is set at 97:3 % w/w. The viscosity of the aqueous phase of the emulsion is modified thanks to glycerol/milliQ water mixtures. The different mixtures used as emulsion aqueous phase are: milliQ water (viscosity 1.0 mPa.s), glycerol/water 62/38% w/w (viscosity=12.5 mPa.s, tabulated value at 20°C [Sheely 1932]) and glycerol/water 75/25% w/w (viscosity=36.5 mPa.s, tabulated value at 20°C [Sheely 1932]). The oil phase is diluted at different concentrations in milliQ water. The emulsion concentration C is defined in the following as the ratio between the volume of oil phase and the total volume. In our study, C is varied between 0.0015 and 2.4 % v/v. In the following if it is not specified, the aqueous phase of the model emulsion is pure water.

2.1.1.3 Emulsion stabilized by sodium dodecyl sulfate

Sodium dodecyl sulfate (SDS) is a very common anionic surfactant, which is present in the formulation of many domestic cleaning products. It is composed of an alkyl chain

of 12 carbon atoms and a sulfate group (see the chemical structure in Figure 2.2), its molecular weight is equal to 288.4 g/mol. The emulsion aqueous phase is a solution of sodium dodecyl sulfate (purchased from Sigma-Aldrich) at different concentrations in milliQ water. The range of concentration investigated is: $(0.1 - 2.5)$ g/L, i.e. molar concentrations in the range: $(0.35 - 8.67)$ mM. The critical micelle concentration (CMC) of SDS in pure water is equal to 2.4 g/L. Thus, the higher concentration investigated is slightly larger than the CMC whereas all the other concentrations are below the CMC. For some experiments, sodium chloride salt is added to the aqueous phase at a weight concentration ranging from 5 to 40 g/L, i.e. molar concentration ranging from 0.09 to 0.68 M. The oil phase of the emulsion is composed of methyllaurate purchased from Sigma-Aldrich. The emulsion concentration, C, is set at 0.3 % v/v.

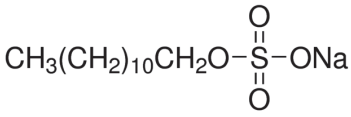

Figure 2.2: Chemical structure of sodium dodecyl sulfate.

2.1.1.4 Emulsion stabilized by cetylpyridinium chloride

Cetylpyridinium chloride (CpCl) is a cationic quaternary ammonium molecule used in some types of toothpaste and throat spray. Due to its long alkyl chain and the quartenary ammonium group, CpCl is an amphiphilic molecule that we use as surfactant to stabilize oil-in-water emulsions, see its chemical structure in Figure 2.3. The cetylpyridinium chloride is purchased from Sigma-Aldrich and purified by three successive recrystallizations in the laboratory. The oil phase of the emulsion is composed of methyllaurate purchased from Sigma-Aldrich. The emulsion concentration, C, is set at 0.3 % v/v. The aqueous phase of the emulsion is a solution of CpCl at a concentration of 0.9 mM in milliQ water, this concentration corresponds to the critical micelle concentration of CPCl. For some experiments, a monovalent or a divalent salt is added to the aqueous phase. The monovalent salt used is sodium chloride (purchased from Sigma-Aldrich), it is added to the surfactant solution at a molar concentration ranges from 0.02 to 0.34 M. The divalent salt used is sodium sulfate (purchased from Merck Millipore), it is added to the aqueous phase at a concentration in the range: $(0.5 - 20)$ mM.

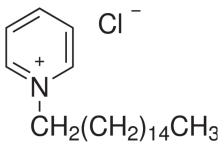

Figure 2.3: Chemical structure of cetylpyridinium chloride.

In another set of experiments, a water-soluble polymer, Pluronic F108, is added to the aqueous phase of the emulsion. The objective is to decorate the emulsion oil droplets with polymer chains that adsorb at the interfaces to create steric repulsion. We choose a cationic surfactant (CpCl) to perform these experiments because the Pluronic F108 interacts with anionic surfactant such as SDS and not with cationic surfactant [Hayakawa 1991]. The Pluronic F108 is a commercial PEO.PPO.PEO triblock copolymer composed of a central chain of polypropylene oxide (PPO) with two lateral chains of polyethylene oxide (PEO), see the chemical structure in Figure 2.4. The Pluronic F108 is purchased from Serva Electrophoresis GmbH and its physical form at room temperature is in flakes. The Pluronic F108 molecular weight is approximately 14,000 g/mol. On average, the PPO block is made of 56 monomers and each PEO block of 132 monomers. At room temperature, the PPO central block of the polymer is hydrophobic and the two PEO lateral blocks hydrophilic. Therefore, Pluronic F108 macromolecules can adsorb at the hydrophobic/aqueous interface due to its amphiphilic nature. The polymer flakes are dissolved in the emulsion aqueous phase which is, in this case, a solution of CpCl at 0.9 mM and NaCl at different concentrations (C_{NaCl}=0, 0.09, 0.17 and 0.34 M) in milliQ water. The Pluronic F108 concentration ranges from 0.1 to 1 % w/w. These concentrations are below the critical micelle concentration (CMC) which is equal to 3 % w/w at 20°C [Molino 1998]. At concentration higher than the CMC, the Pluronic F108 molecules form spherical micelles with a hydrophobic core (PPO block) and a hydrophilic corona (PEO blocks). In our study, the polymer concentration is always below the CMC, which means that the polymer is fully dissolved and present in the solution as unimers and not micelles. The radius of gyration of PEO blocks of the copolymer is equal to 2.6 nm [Cabane 1982].

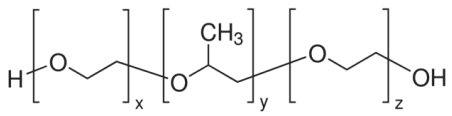

Figure 2.4: Chemical structure of Pluronic F108 triblock copolymer, x=132, y=56 and z=132.

2.1.2 Characterization of the emulsion drop size distribution

One of the important characteristics of the emulsion is the size distribution of the oil droplets. To measure the size distribution we use a set-up of laser granulometry and light microscopy.

2.1.2.1 Laser granulometry

The measurement of the drop size distribution of the emulsions is performed using a Malvern instrument, the Mastersizer 2000. It is a static light scattering-instrument which allows resolution of drop diameter between 0.02 μm to 2000 μm. Light scattering methods are a powerful tool to investigate the structure of systems such as colloidal dispersions like emulsions or solid suspensions. In light scattering measurements, the sample is illuminated by a incident beam which, passing through the sample, induces oscillations in electrons that become sources of secondary radiation. This scattered intensity is then collected as a function of the scattered angle and analyzed to get information on the sample structure. As the measurements are performed on dilute samples, the scattered intensity as a function of the angle is converted into the size distribution of the drops.

The Mastersizer 2000 is composed of:

- two light sources (red laser He-Ne, $\lambda = 632.8$ nm and blue light source $\lambda = 466$ nm),
- a measurement cell where the emulsion to analyze is introduced under agitation,
- a series of detectors that collect the scattered intensity at different angles.

To perform the measurement, it is necessary to indicate the refractive indexes of the two phases of the emulsion which are measured independently with a refractometer. For all the emulsions, the refractive index of the aqueous phase is equal to 1.33 and the one of the oil phase to 1.43. For all measurement in laser granulometry, the dispersion to analyze should be a dilute dispersion with no aggregates. In practical, about 3 mL of the emulsion to analyze are diluted in about 700 mL of distilled water in the dispersion unit of the Mastersizer 2000 where it is vigorously agitated to ensure a good dispersion of the oil droplets in the measurement cell.

As a result of the measurement, we obtain the volume distribution of the oil droplet diameter. From this distribution, different parameters are calculated: $d_{0.1}$, resp. $d_{0.9}$, corresponds to the drop diameter such as the cumulative undersized volume fraction is equal to 10%, resp. 90%, see Figure 2.5. The median volume diameter, $d_{0.5}$, is defined as the diameter for which 50% of the oil volume is contained in droplet of smaller diameter, as schematically shown in Figure 2.5. From these different parameters, one can estimate the width of the distribution by calculating the span which is equal to: $(d_{0.9} - d_{0.1})/d_{0.5}$. In the following, we characterize the obtained emulsions through the span value, $\mathcal{S}$, and the $d_{0.5}$ value, that we rename as d_{oil} for clarity in the remaining of the manuscript.

2.1.2.2 Optical microscopy

To complete the measurement with the Mastersizer 2000, the prepared emulsions are also observed with an optical microscope. Most of the observations are performed thanks to an optical microscope (Leica DMRX) connected to a camera (ImagingSource)

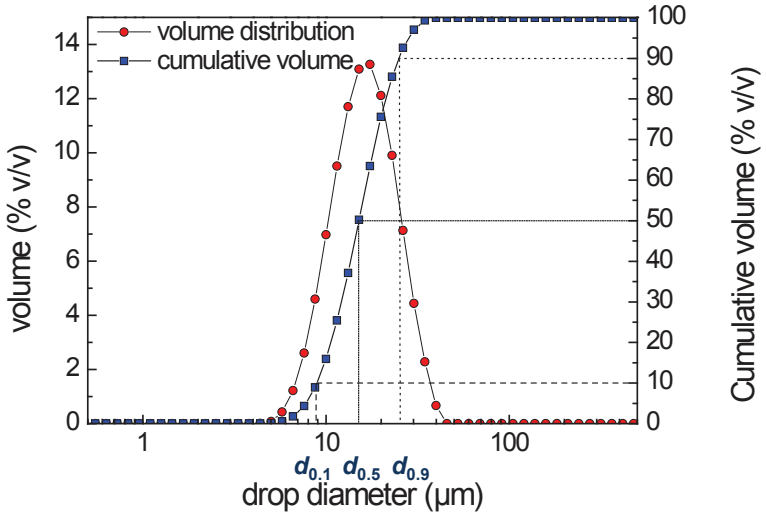

Figure 2.5: Volume distribution of emulsion drop diameter with the definition of the parameters $d_{0.1}$, $d_{0.5}$ and $d_{0.9}$.

allowing the capture of images. We use objectives with a magnification ×10 and ×32. The emulsions are injected into glass cells for observation. The glass cell is made by a glass lamella and a cover slip separated by a 250 μm thick 16×16 mm^2 double-adhesive gene frame (Thermo Scientific). On contrary to the granulometry measurement, the microscope observation permits a direct visualization of the sample and gives information not available with the granulometry such as the shape of the drop. The microscope observation may also highlight some instabilities of the emulsion like the flocculation of the emulsion droplets and the existence of multiple drops, i.e. the presence of water droplets in oil drops.

2.1.3 Formulation of the emulsions

In this section, we present the different methods used to prepare the emulsions and then how we formulate the emulsions depending on their composition.

2.1.3.1 Emulsification techniques

Three different methods have been used to prepare the emulsions depending on their composition and the targeted drop size distribution.

- The first and simplest emulsification method used is a gentle manual shaking. For some of the systems studied (industrial and model emulsions), the interfacial tension between the aqueous and oil phases is extremely low. Thus, a manual agitation is sufficient to ensure a good emulsification. In practice, the oil phase is poured in

the aqueous phase and the container is gently agitated for 10 seconds (typically ten inversions of the emulsion bottle).

- An alternative method used in this study to prepare calibrated emulsions is a mechanical stirring with a T18 digital Ultra-Turrax provided by IKA. It consists of a rotor with a stationary stator system. The rotor and the stator are two concentric cylinders of internal diameters of 12.7 mm respectively 19 mm (model S18N 19G). The gap between the two cylinders is equal to 0.4 mm. The extremities of the rotor and the stator are serrated to permit the fluid circulation. The motor controls the circumferential speed of the rotor from 500 to 25,000 rotations per minute. Due to the high circumferential speed, the liquid is forced radially through the slots in the rotor-stator arrangement. The strong shear forces produced by the rotor-stator system due to the high rotation speed results in a good dispersion. The Ultra-Turrax T18 allows the preparation of emulsion over a large range of volume, from 1 to 1,500 mL. In our case, we vary the rotation speed from 3,000 to 15,000 rpm and usually prepare emulsion volumes of 30, 50 or 100 mL. By varying the stirring time and the rotation velocity, we can modify the emulsion drop size distribution. The minimal oil droplet size obtain with the Ultra-Turrax is around 4 μm. In practice, the aqueous phase is poured in a beaker of suitable volume. The Ultra-Turrax is plunged in the solution and the rotation velocity is progressively increased up to the selected speed. Once the selected speed is reached, the oil phase of the emulsion is added by the mean of a micropipette. The stirring time is measured from the moment of addition of the oil phase.

- The last emulsification method used in our work is ultrasounds with a Vibracell provided by Bioblock Scientific. Ultrasounds are used to prepare emulsion with oil droplet smaller than 1 μm. Those sizes are not reachable by mechanical stirring. In practice, the ultrasounds probe is placed in a beaker containing the aqueous phase. Once the ultrasounds are activated, we add the oil phase by the mean of a micropipette. The ultrasounds power is set a 40 W and the duration time at 10 minutes.

2.1.3.2 Formulation of the industrial emulsion

Industrial emulsions are prepared by manual agitation at a concentration of the oil phase of 0.3 % v/v. In Figure 2.6(a) we plot the emulsion drop size distribution as measured with a granulometer. We observe a large polydispersity of the oil droplet diameters with a broad main peak around 40 μm and two smaller peaks around 0.1 and 1 μm. The median volume diameter, d_{oil}, is equal to 26.0 μm and $\mathcal{S}$ is large, equals to 1.9 which confirms the large width of the drop size distribution. Corresponding microscopy images are represented in Figure 2.6(b). These images highlight the presence of multiple drops, i.e. oil droplets containing smaller water droplets and the large polydispersity of the oil droplet diameters.

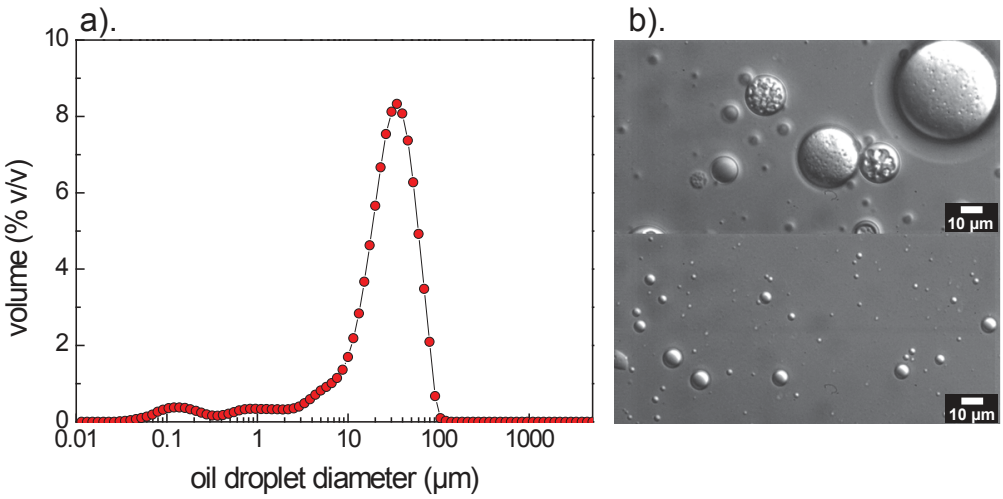

Figure 2.6: a). Oil droplet size distribution measured with a Mastersizer Malvern device for an industrial emulsion at a concentration of 0.3 % v/v prepared by manual shaking. b). Light microscopy images of the industrial emulsion.

2.1.3.3 Formulation of the model emulsion

Model emulsions are prepared by the three different emulsification methods, detailed in 2.1.3.1, yielding different size distribution of the oil droplets.

The interfacial tension between water and the oil phase is equal to 1.1 mN/m (see Appendix A.2 for the measurement method). Due to this low interfacial tension a manual agitation ensures a good emulsification as shown in Figure 2.7, where the oil droplet size distribution for two emulsions at different concentrations, 0.3 % v/v and 2.4 % v/v are presented (Figure 2.7(a)). We observe that the emulsion concentration has no influence on the oil droplet size distribution. For both concentrations, we obtain a non-symmetric size distribution with a shoulder around 6 μm and a broad peak centered around 46 μm, the volume median diameter is around 39 μm for the two emulsions. The light microscopy images of the two formulations (Figure 2.7(b,c)) confirm the broad drop size distribution of the emulsions.

To investigate the stability of the model emulsions towards coalescence and Ostwald ripening processes, we measure the drop size distribution of the emulsions one day after its preparation. Ostwald ripening corresponds to the diffusion of the oil through the aqueous phase from the smaller droplets to the bigger ones, it results in an increase of the oil droplet size. Few hours after the emulsion preparation, we observe the formation of a cream at the top of model emulsion samples due to the density difference between the oil phase ($\rho = 871$ kg/m^3) and the water phase ($\rho = 998$ kg/m^3), see microscopy image of the cream in Figure 2.8(b). Before to measure the emulsion drop size distribution, we manually and gently agitate the sample to homogenize it and redisperse the oil droplets. We show in Figure 2.8 the oil droplet size distribution of an emulsion at a concentration of 0.3 % v/v prepared by manual shaking just after its preparation (red squares) and one

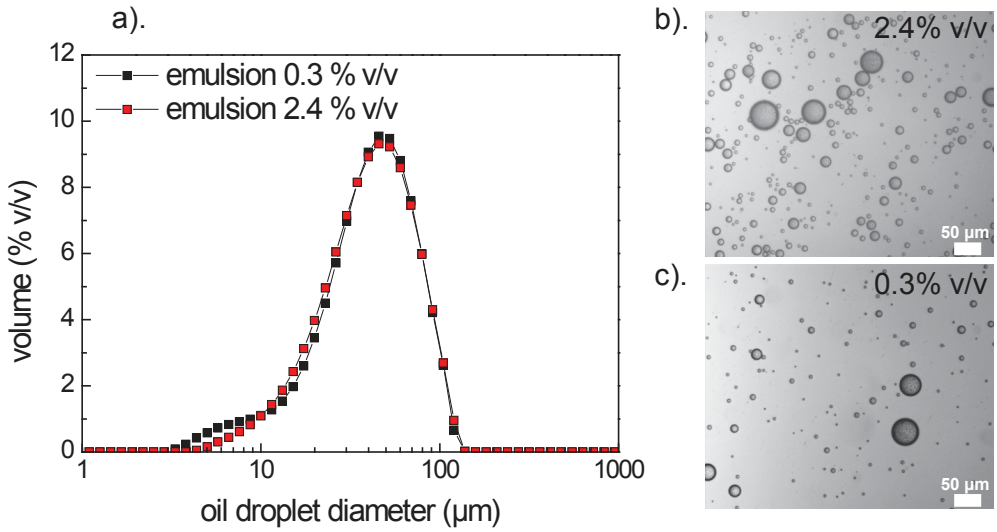

Figure 2.7: a). Oil droplet size distribution measured with a Mastersizer Malvern device for two emulsions at different concentration: $C = 0.3$ % v/v and 2.4 % v/v, prepared by manual agitation. The volume median diameter of the emulsion droplets is d_{oil}=39.2 μm for $C = 0.3$ % v/v, and d_{oil}=38.9 μm for $C = 2.4$ % v/v. b). and c). Light microscopy images of two emulsions with concentration $C = 2.4$ % v/v b). and $C = 0.3$ % v/v c).

day later (blue circles). We observe that the form of the two drop size distributions are very close. There is a slight shift of the main peak; just after the preparation, d_{oil} is equal to 39.2 μm and to 47.6 μm one day later. After one day, there is a slight increase of the emulsion droplet size but the phenomenon is limited. In conclusion, even if the emulsion is subject to creaming there is no major destabilization due to coalescence and Ostwald ripening process, at least for a duration of one day.

The different emulsification methods allow the preparation of emulsions with different oil droplet size distributions as shown in Figure 2.9. The emulsions are prepared by manual agitation (d_{oil}=39.1 μm), mechanical stirring, (d_{oil}=20.0, 11.7 and 3.8 μm) and ultrasounds (d_{oil}=0.5 μm). For the emulsions prepared by mechanical stirring, the stirring time is set at 30 seconds and we only vary the rotation speed, which is fixed at 3,000 rpm (d_{oil}=20.0 μm), 5,000 rpm (d_{oil}=11.7 μm) and 15,000 rpm (d_{oil}=3.8 μm).

To evaluate the reproducibility in the preparation of the model emulsion, we prepare three times an emulsion with the same protocol. For this experiment, we set the emulsion concentration at 0.3 % v/v and the emulsions are prepared by mechanical stirring with a stirring time set at 30 seconds and a rotation speed of 3,000 rpm. The drop size distribution obtained are plotted in Figure 2.10 and the values of d_{oil} and $\mathcal{S}$ are indicated in the legend. The three drop size distributions obtained are very close and consist of a broad main peak centered around 20 μm and a smaller peak around 1 μm. The third distribution (green triangles) is slightly shifted towards bigger droplets as highlighted by

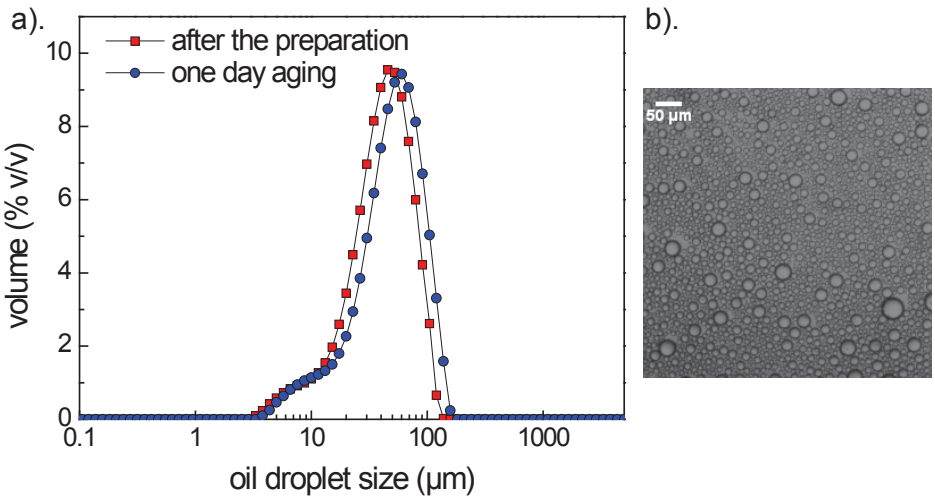

Figure 2.8: a). Oil droplet size distribution measured with a Mastersizer Malvern device for a model emulsion at $C = 0.3$ % v/v prepared by manual shaking and measured just after its preparation and one day later. b). Light microscopy image of the cream of the emulsion obtained after one day at rest.

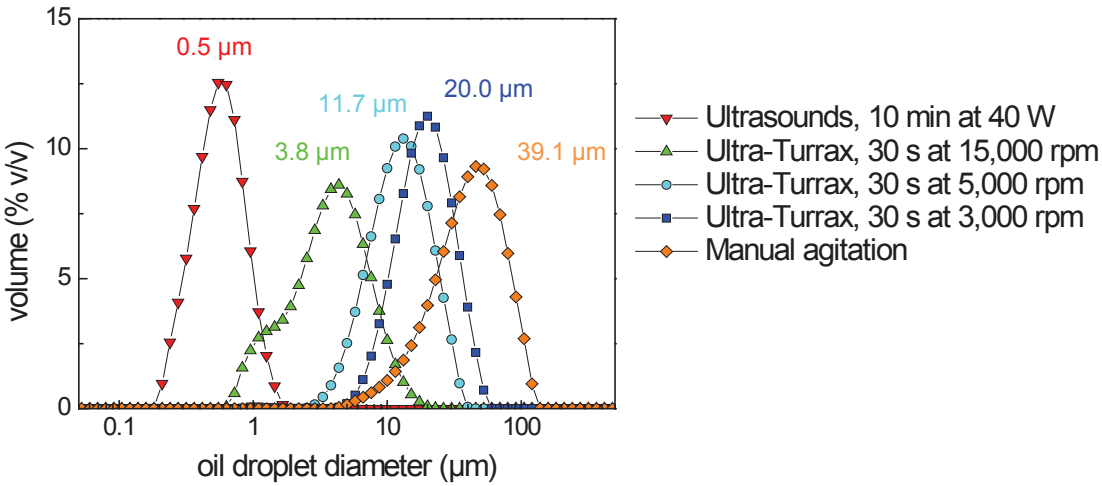

Figure 2.9: Oil droplet size distribution measured with a Mastersizer Malvern device for model emulsions at $C = 0.3$ % v/v prepared by different emulsification methods.

larger values of d_{oil} and $\mathcal{S}$. In conclusion, the reproducibility in the preparation of the model emulsion is quite satisfactory even if some slight shifts are observed.

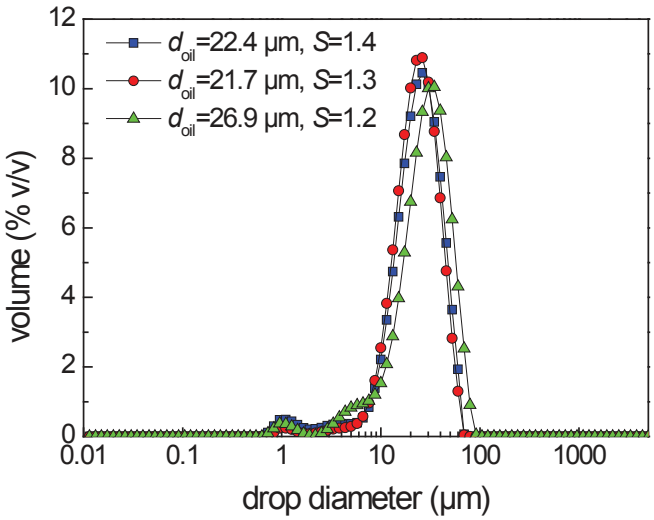

Figure 2.10: Oil droplet size distribution measured with a Mastersizer Malvern device for three model emulsions at $C = 0.3$ % v/v prepared by mechanical stirring (30 seconds at 3,000 rpm) to evaluate the reproducibility of the preparation.

The viscosity of the model emulsion aqueous phase is modified thanks to water/glycerol mixture as explained in section 2.1.1.2. For the three viscosities investigated, we obtain similar oil droplet size distribution for the emulsion as shown in Figure 2.11. Here, the emulsions are prepared by mechanical stirring (Ultra-Turrax, 30 seconds at 3,000 rpm) and the emulsion concentration, C, is set at 0.3 % v/v.

2.1.3.4 Formulation of the emulsion stabilized by sodium dodecyl sulfate

The emulsions stabilized by sodium dodecyl sulfate are prepared by mechanical stirring with a stirring time of 1 minute and a rotational velocity of 6,000 rpm. All these emulsions are prepared with a concentration of the oil phase of 0.3 % v/v. We show in Figure 2.12(a) the drop size distribution of emulsions with a concentration of SDS equals to 2.5 g/L and different salt concentrations. The values of d_{oil} are indicated in the graph legend. The addition of salt does not notably modify the drop size distribution, the main peak remains at the same size, around 10 μm, however we observe the formation of a small peak around 1 μm. The mean value of d_{oil} averaged over the different salt concentrations is equal to 9.4 ± 1.9 μm. In Figure 2.12(b) we report the drop size distribution of emulsion prepared with different SDS concentrations without salt. The increase of the SDS concentration entails a shift of the main peak toward smaller drop size as indicated by the values of d_{oil} in the graph legend. For a concentration of SDS equals to 0.1 g/L, d_{oil}=20.3 μm whereas d_{oil}=9.6 μm for a concentration of SDS equals to 2.5 g/L.

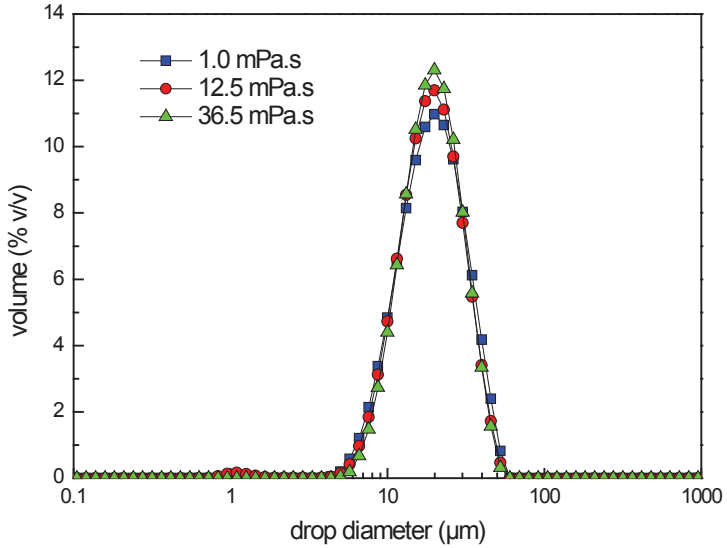

Figure 2.11: Oil droplet size distribution measured with a Mastersizer Malvern device for three model emulsions with different viscosities of the aqueous phase as indicated in the legend. The emulsion concentration is set at $C = 0.3$ % v/v and the emulsions are prepared by mechanical stirring (30 seconds at 3,000 rpm).

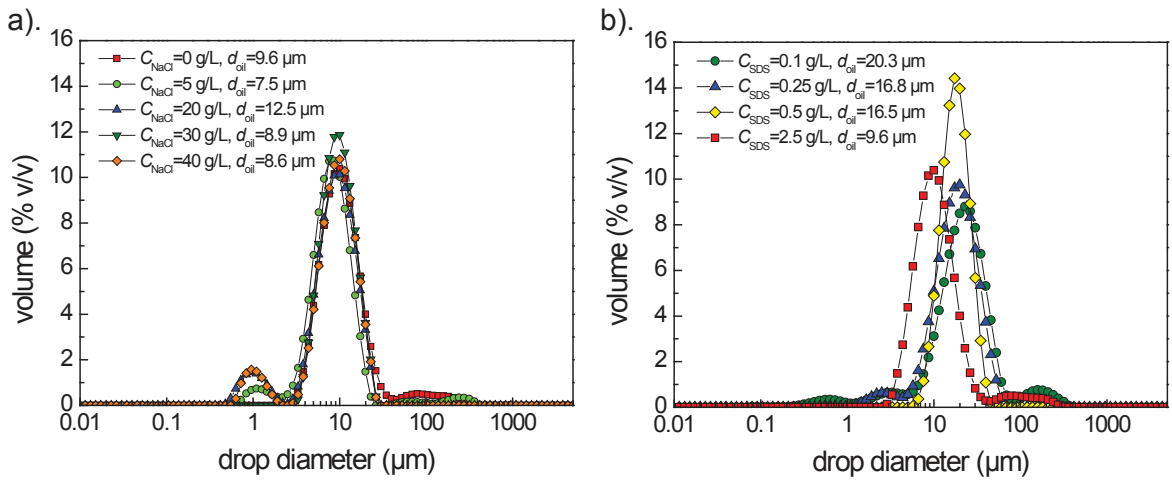

Figure 2.12: Oil droplet size distribution measured with a Mastersizer Malvern device for emulsion stabilized by sodium dodecyl sulfate at $C = 0.3$ % v/v. a). C_{SDS}=2.5 g/L and NaCl concentration ranging from 0 to 40 g/L. b). SDS concentration ranging from 0.1 to 2.5 g/L without salt.

2.1.3.5 Formulation of the emulsion stabilized by cetylpyridinium chloride

The emulsions stabilized by cetylpyridinium chloride are prepared by mechanical stirring with a stirring time of 1 minute and a rotational velocity of 6,000 rpm. All these emulsions are prepared with a concentration of the oil phase of 0.3 % v/v. We show in Figure 2.13(a) the drop size distribution of emulsions with different concentrations of NaCl. Without salt, the size distribution consists of one broad peak centered around 11 μm. The addition of NaCl does not notably modify the position of the main peak but it entails the formation of smaller droplets around 0.1 μm and bigger droplets around 80 μm. We report in Figure 2.13(b) the drop size distribution for emulsions prepared at different sodium sulfate concentrations. As for NaCl, the addition of divalent salt does not modify the position of the main peak but entails the formation of bigger drops around 100 μm. In Figure 2.13(c), we report the effect of the addition of Pluronic F108 polymer on the drop size distribution of emulsion stabilized by cetylpyridinium chloride and sodium chloride (C_{NaCl}=20 g/L). The drop size distributions are very similar for the different polymer concentrations. As remarkable with the values of d_{oil} (in the legend of the graph), the addition of polymer very slightly shifts the main peak of the distribution towards bigger droplets. In conclusion, the addition of monovalent or divalent salt and the addition of Pluronic F108 copolymer do not drastically modify the drop size distribution of the emulsion. For all the configurations, the drop size distribution are comparable.

2.2 High-molecular-weight polymer solutions

Dilute solutions of polymers of high molecular weight constitute the second category of anti-drift adjuvants. The polymer the most used as anti-drift additive is the guar gum. We use, as a model system, polyethylene oxide (PEO) which has a similar behavior as guar gum regarding the anti-drift application. Polyethylene oxide with a molar mass equals to 1,000,000 g/mol is purchased from Sigma-Aldrich and used as received. The radius of gyration of the polymer chain is equal to 69.6 nm [Cabane 1982]. Solutions are prepared in milliQ water at a weight concentration of 0.05 % w/w. Since the boundary concentration between the dilute and the semi dilute regimes, C^*, is equal to 0.12 % w/w (calculated from the gyration radius and the molar mass), the solution is in the dilute regime. The viscosity of the solution is equal to 1.31 mPa.s.

2.3 Equilibrium surface tensions

In this section, we present the different methods used to measured the surface tensions of our systems. The equilibrium surface tensions of the solutions are measured by two techniques available in the laboratory: a pendant drop tensiometer and a Wilhelmy plate tensiometer. The pendant drop tensiometer (SINTERFACE PAT-1M) enables measure-

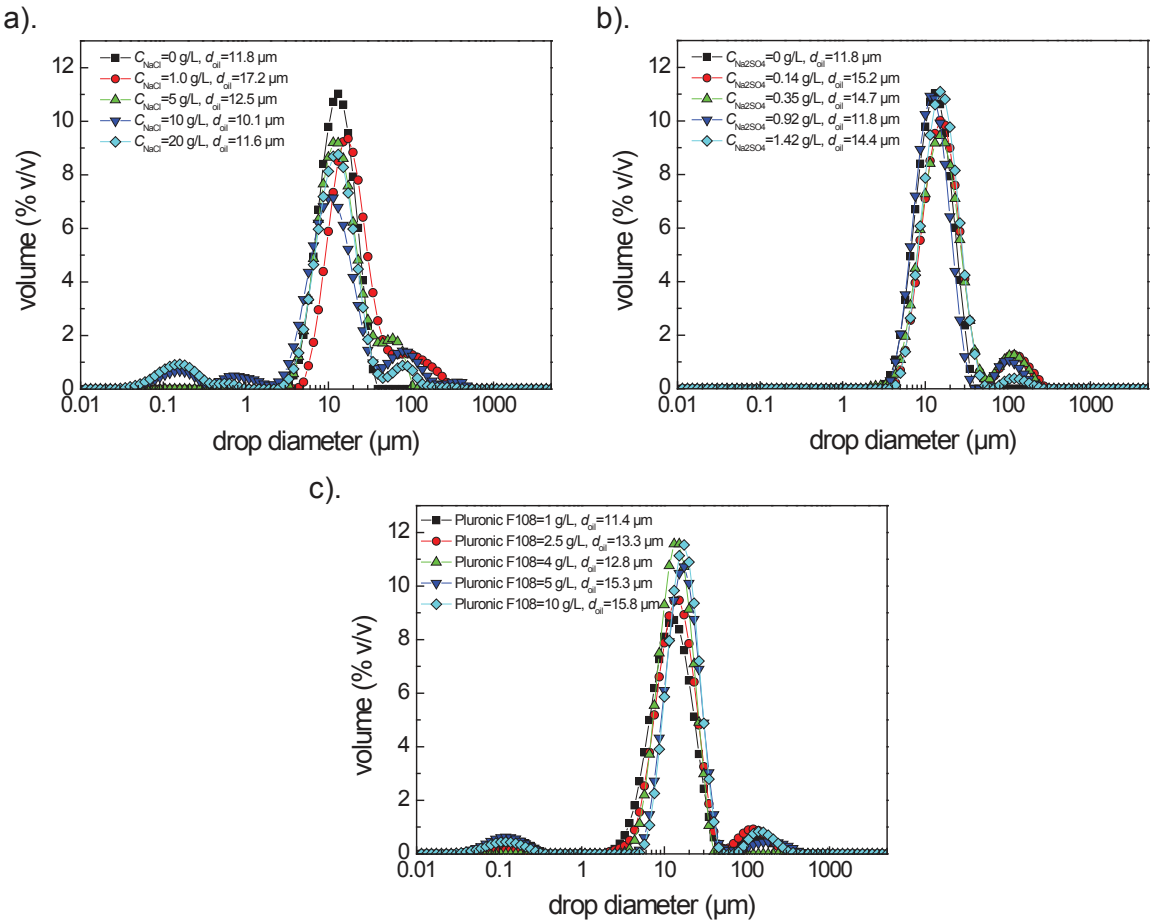

Figure 2.13: Oil droplet size distribution measured with a Mastersizer Malvern device for emulsion stabilized by cetylpyridinium chloride at C = 0.3 % v/v. a). C_{CpCl}=0.9 mM and NaCl concentration ranging from 0 to 40 g/L. b). C_{CpCl}=0.9 mM and Na_2SO_4 concentration ranging from 0 to 1.42 g/L. c). C_{CpCl}=0.9 mM, C_{NaCl}=20 g/L and Pluronic F108 concentration ranging from 1 to 10 g/L.

ment of the surface tension over a large range: $(1 - 1000)$ mN/m with a resolution of 0.1 mN/m. It can perform dynamic measurement over a long period, up to 100,000 seconds, with a minimum frame rate of 1 second. The other method available in the laboratory is a Wilhelmy plate tensiometer (KSV NIMA). This tensiometer enables measurement of the equilibrium surface tension over the range: $(1 - 150)$ mN/m with a resolution of 0.1 mN/m.

In the Table 2.1 are summarized some equilibrium surface tension of the investigated systems with their densities and zero shear viscosities. Data are reported here for milliQ water, the oil used for all the emulsions (methyllaurate) and the PEO solution. We also report the physico-chemical parameters of two emulsions (industrial and model emulsions at a concentration of 0.3 % v/v). The densities are measured with an Anton Paar density meter DMA 4500M; the measurement is based on the oscillating U-tube method. The viscosities are measured thanks to an Anton Paar microviscometer Lovis 2000 ME. We note that the density and the viscosity of the PEO solution and the two emulsions are really close to the water values.

	ρ (kg/m^3)	γ (mN/m)	η (mPa.s)
milliQ water	998	72.3	1.00
methyllaurate	870	29.6	3.18
PEO solution 0.05%w	993	61.8	1.31
Industrial emulsion at 0.3 % v/v	998	36.7	1.05
Model emulsion at 0.3 % v/v	998	33.4	1.04

Table 2.1: Physico-chemical characteristics of the studied systems. ρ is the density (measured at 20°C) , γ the equilibrium surface tension (measured at room temperature) and η the zero shear viscosity (measured at 20°C).

Chapter 3

Destabilization of liquid ligaments into drops

Contents

The formation of spray drops results from the destabilization of the liquid sheet formed at the exit of the nozzle. This destabilization can be divided in two successively steps: first the liquid sheet is destabilized into liquid ligaments and then these ligaments are destabilized into drops forming the spray. In this chapter, we focus on the destabilization of liquid ligaments into drops as it is, in any case, the last step of the atomization process. In the first section of this chapter, we rapidly introduce some theoretical background about the capillary destabilization of a liquid column, the non-linear analysis explaining the formation of satellite drop and the main results reported in the literature concerning dilute polymer solution of high-molecular weight. With a first experimental set-up, we study the simplest configuration to observe the formation of a drop: the detachment of a pendant drop from a reservoir. Then, with a second experimental set-up, we investigate the destabilization of stretched ligaments. Our objective is to determine if the industrial emulsion modifies the destabilization mechanism of liquid ligaments by comparing its behavior to that of two test fluids: pure water and dilute solution of water-soluble polymers.

3.1 Destabilization of liquid ligaments - Theoretical aspects

3.1.1 Destabilization of a liquid column: Rayleigh-Plateau instability

The destabilization of a liquid column corresponds to the Rayleigh-Plateau instability [Eggers 2008]. If we consider a liquid cylinder, any perturbation of sufficiently long wavelength decreases the surface energy. Therefore the perturbation grows until the cylinder is destabilized into drops. Using linear stability analysis, Rayleigh found that a cylinder with a radius R is unstable to any disturbance greater than the cylinder perimeter. Among all these unstable wavelengths the dynamics select the dominant wavelength (the one with the fastest growing disturbance) which is: $\lambda_m = 9.01R$ for an inviscid liquid. Assuming that one drop is formed per wavelength, Rayleigh predicted the drop radius to be: $r = 1.89R$. The characteristic time associated to this instability is: $t_R = 2.91t_\gamma$ with t_γ the capillary time equal to $\sqrt{\frac{\rho R^3}{\gamma}}$ where ρ is the density of the liquid and γ its surface tension. For example, a water cylinder with a radius $R = 1$ mm will be destabilized into a series of drops of radius $r = 1.89$ mm with a characteristic time $t_R = 10.8$ ms.

This linear stability analysis can predict the size of the main drops of a jet but it fails to predict non-linear phenomena, as for instance the appearance of smaller drops between two main drops (Figure 3.1). These smaller drops, called satellite drops, are of great interest for this study as the aim is to reduce the proportion of driftable drops, i.e. the proportion of small drops in the spray. For a water jet, the satellite drops are about three times smaller than the main drops [Christanti 2001].

Below, we describe the thinning dynamics of a liquid cylinder and its subsequent destabilization into drops.

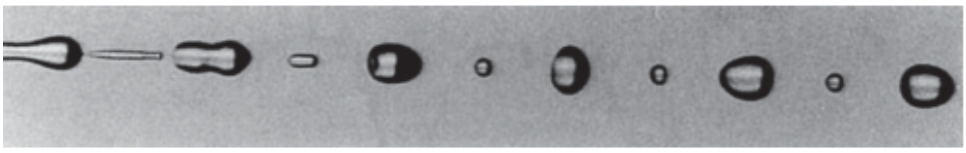

Figure 3.1: Instability of a water jet with diameter of 0.27 mm and velocity of 3.3 m/s; appearance of satellite drops [Vassallo 1991].

3.1.2 Non-linear analysis: Thinning dynamics

We consider the simplest case of the formation of a drop through the detachment of a pendant drop from a reservoir. First a cylinder forms between the drop and the reservoir.

This cylinder thins out forming a fluid neck that pinches near the drop and near the reservoir, leading to the detachment of the main drop and the formation of a satellite drop. The satellite drop results from to the detachment of the fluid neck. This process is shown is Figure 3.2. We can follow the time evolution of the minimum diameter of the cylinder, $H_{\min}$, normalized by the cylinder diameter at the exit of the syringe, D (see Figure 3.2). The linear stability analysis of Rayleigh predicts that the thinning dynamics of the fluid neck follows an exponential decrease [Clanet 1999]:

$$\frac{H_{\min}}{D} = 1 - e^{\frac{t-t_c-t_0}{t_R}} \tag{3.1}$$

with t_c the breakup time and t_0 the breakup time if the exponential dynamics would be verified until the rupture. This exponential regime is only expected at the onset of the thinning dynamics. When the singularity, i.e. the drop detachment is approached, the thinning dynamics follows an universal non-linear behavior, which is independent of the boundary and initial conditions [Eggers 2008].

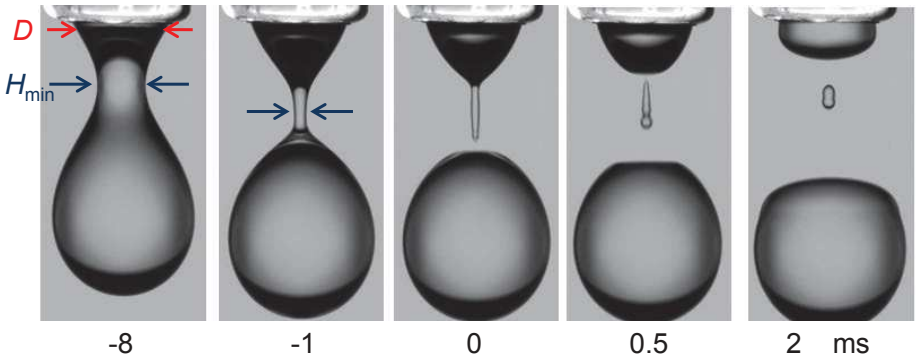

Figure 3.2: Sequence of images of the detachment of a pendant drop with the definition of $H_{\min}$, the fluid neck minimum diameter, and D, the fluid neck diameter at the exit of the syringe. The origin of time is taken at the moment of the drop detachment. The fourth picture highlights the formation of a satellite droplet.

The universal final pinch-off process is determined by three parameters: the capillary time (t_γ), the viscous time (t_η) and the viscous length (L_η).

$$t_\gamma = \sqrt{\frac{\rho R^3}{\gamma}} \quad ; \quad t_\eta = \frac{\eta R}{\gamma} \quad ; \quad L_\eta = \frac{\eta^2}{\gamma\rho}$$

Where ρ is the fluid density, γ the fluid surface tension, η the fluid viscosity and R the radius of the cylinder.

A dimensionless number, the Ohnesorge number (Oh), which balances the viscous force to the inertial and surface tension forces can be built from t_γ and t_η.

$$Oh = \frac{t_\eta}{t_\gamma} = \frac{\eta}{\sqrt{\rho\gamma R}} \tag{3.2}$$

The thinning regimes have been the subject of many theoretical studies [Keller 1983, Papageorgiou 1995, Eggers 1993]. The different thinning regimes expected depending on the value of the Ohnesorge number are summarized in Figure 3.3 [Basaran 2004]. The initial stage of the thinning depends on the value of the Ohnesorge number. When $Oh << 1$, the viscous effects are negligible compared to the inertial effects; the inertio-capillary regime is dominant and $H_{\min}$ decreases with time as a power law with an exponent 2/3:

$$H_{\min}/D = 0.7 \left(\frac{t_c - t}{t_\gamma} \right)^{\frac{2}{3}} \tag{3.3}$$

On the contrary, if the inertial effects are negligible compared to the viscous effects ($Oh >> 1$), the visco-capillary regime is dominant and the minimum diameter decreases linearly with time:

$$H_{\min}/D = 0.0709 \left(\frac{t_c - t}{t_\eta} \right) \tag{3.4}$$

These two regimes are transitory: when the singularity approaches, the previously neglected term, the viscosity for the inertio-capillary regime or the inertia for the visco-capillary regime, becomes of the same order of magnitude as the two others. The final regime is the visco-capillary-inertial regime that also predicts a linear decreasing of the minimum diameter with time:

$$H_{\min}/D = 0.0304 \left(\frac{t_c - t}{t_\eta} \right) \tag{3.5}$$

This regime is observed when the minimum diameter becomes smaller than the viscous length. During the inertio-capillary regime the neck profile is asymmetric around its minimum radius whereas during the visco-capillary regime it is symmetric, as can be seen on Figure 3.3.

3.1.3 Influence of the presence of high-molecular-weight polymer in solution

The detachment of a drop and the destabilization of liquid jets into drops have been extensively investigated for dilute solutions of high-molecular-weight polymers [Amarouchene 2001, Wagner 2005, Tirtaatmadja 2006, Christanti 2001, Mun 1998].

Different studies have investigated the effect of the addition of a very small amount of long polymeric chains on the breakup dynamics [Amarouchene 2001, Wagner 2005, Tirtaatmadja 2006]. In these studies, the polymer used is a polyethylene oxide (PEO) of high-molecular weight (typically ranging from 10^5 to 5×10^6 g/mol), in the dilute regime. The polymer solutions are prepared in a mixture of glycerol and water to keep constant the shear viscosity (typically equal to 6 mPa.s) when varying the polymer concentration. For these low viscosity polymer solutions, the viscous force is negligible and therefore the

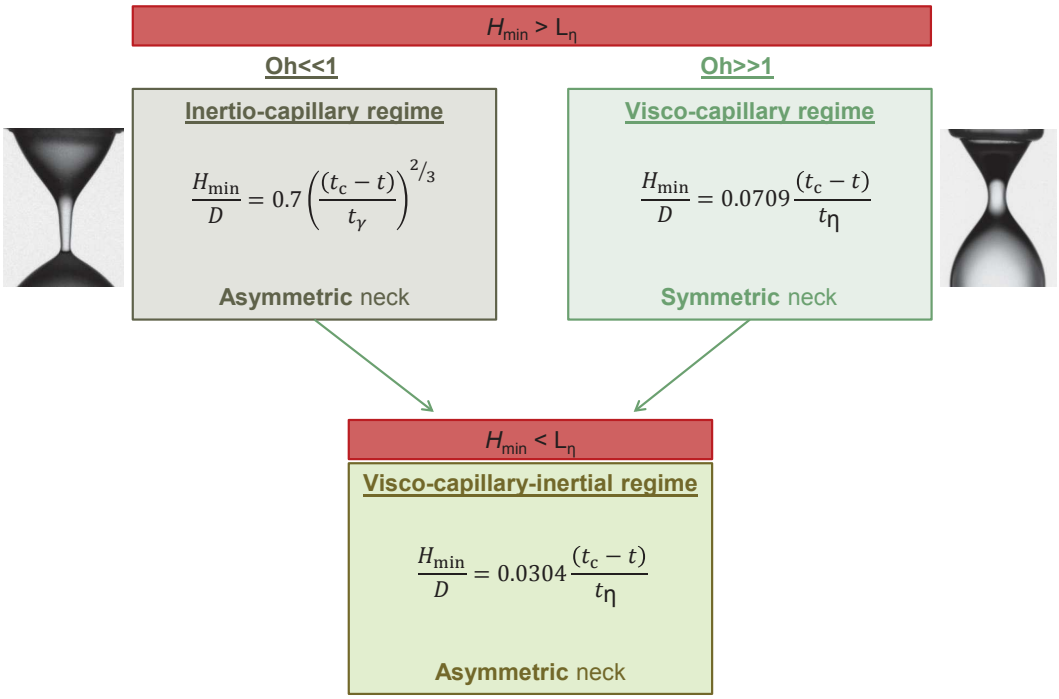

Figure 3.3: The different thinning regimes observed depending on the value of the Ohnesorge number. The visco-capillary-inertial regime is observed when the minimum diameter $H_{\min}$ becomes smaller than the viscous length L_η [Basaran 2004].

balance of inertia and capillary forces leads to a 2/3 power law scaling of the minimum diameter with time as for pure water (Equation 3.3). However, at the approach of the breakup point, the polymer molecules are highly extended due to the high extension rate at the neck location. The molecules extension gives rise to an elastic stress which balances the capillary stress and so stabilizes the pinch region and retards the breakup. This results in the formation of two thin cylindrical filaments connecting the satellite drop to the main drop and to the upper fluid reservoir forming a "bead-on-string" structure. The radius of the thin cylindrical filaments decreases exponentially with time following:

$$\frac{H_{\min}}{D} \propto e^{-\frac{t-t_c}{3\tau}} \tag{3.6}$$

with τ the characteristic relaxation time of the polymer chains calculated from the Zimm model [Christanti 2002, Tirtaatmadja 2006]. The formation of these filaments prevents the neck from breaking off as expected for Newtonian fluids.

The same "bead-on-string" structure is observed for the destabilization of a liquid jet of dilute solution of high-molecular-weight polymer. The study conducted by Y. Christanti and L. M. Walker [Christanti 2001] shows that the jet destabilization is strongly affected by the presence of long polymer chains in solution. They compare the capillary breakup of a jet of a Newtonian fluid (50-50 % w/w water/glycerol) with that of dilute solutions of polyethylene oxide (PEO) at different molecular weights (10^5, 3×10^5, and 10^6 g/mol).

They show that the presence of high-molecular-weight polymer chains retards the breakup process, i.e. the jet is destabilized further from the nozzle, and also modifies the breakup mechanism. They highlight the formation of very thin ligaments between the main drops and the satellite drops, Figure 3.4.

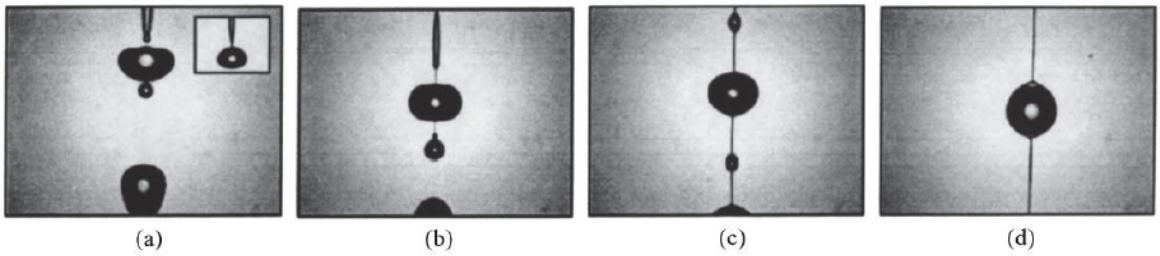

Figure 3.4: Capillary jet breakup a). 50% w/w glycerol b). 0.3% w/w 100,000 g/mol PEO, c). 0.1% w/w 300,000 g/mol PEO, and d). 0.05% w/w 1,000,000 g/mol PEO. Each image is 5.12 mm x 3.84 mm [Christanti 2001].

The drop size distributions of the jet obtained with the Newtonian fluid and with the dilute polymer solutions are measured (Figure 3.5). The drop size distribution of the 50 % w/w glycerol solution consists of two peaks, one corresponding to the main drops and the other to the satellite drops. The 10^6 g/mol PEO solution at 0.05 % w/w exhibits the same peak corresponding to the main drops. However the peak corresponding to the satellite drops is suppressed (Figure 3.4(d)). The authors also observe the formation of smaller drops, "sub-satellite drops", which are drops resulting from the destabilization of the thin ligaments connecting the main and satellite drops. In conclusion, the authors show that dilute solutions of high-molecular-weight polymer inhibit the formation of satellite drops thanks to the formation of a thin filament connecting the drops. This filament allows the satellite drops to migrate and coalesce with the upper or lower main drop. The suppression of the satellite drops is however accompanied with the formation of sub-satellite drops.

In the study conducted by Mun et al., [Mun 1999], the atomization of dilute solutions of polyethylene oxide with agricultural spray nozzle is investigated. They show that, for four different types of nozzles, a dilute solution of PEO of high-molecular weight (6×10^5 g/mol at a concentration of 0.095 % w/w) increases the mean spray drop size and eliminates the presence of fine droplets thanks to the mechanism described above [Christanti 2001]. The property of the high-molecular-weight polymer solutions to suppress the formation of satellite drops has been used to formulate agricultural anti-drift adjuvant whose objective is to inhibit the formation of small drops. For this application, the polymer principally used in the industry is the guar gum but the mechanism involved is the same as that for PEO solution. The formation of the sub-satellite drops, highlighted by [Christanti 2001], could be a priori considered as an important drawback for agricultural spray application. However the volume of solution into these drops is

so small that it is not relevant. From [Christanti 2001] data, we estimate the volume of solution contained in the main drops (580 μL) and the volume in the sub-satellite drops (0.03 μL). Hence the volume of sub-satellite drops (about 0.005% v/v of the volume of the main drops) is negligible. The formation of the sub-satellite drops is therefore not an issue for agricultural spray application.

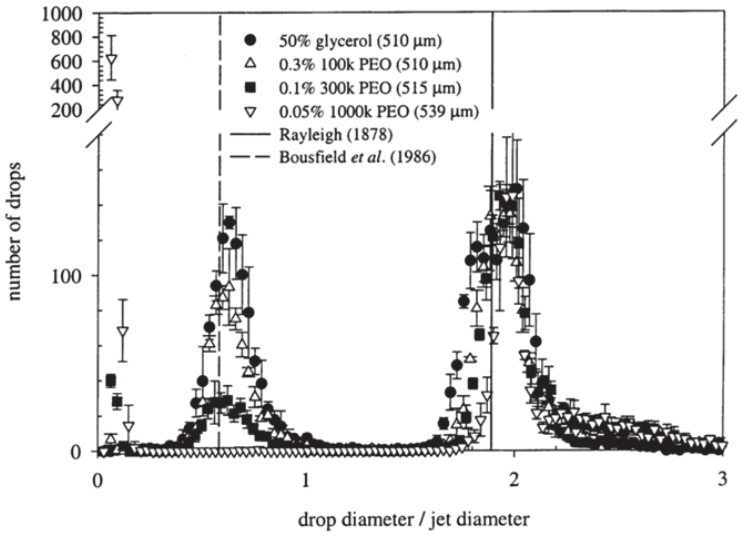

Figure 3.5: Drop size distributions resulting from the breakup of a jet of a Newtonian solution and dilute PEO solutions of different molecular weights [Christanti 2001].

3.2 Detachment of a pendant drop - Experimental results

We have seen that the detachment of a pendant drop, the destabilization of a liquid jet, and the atomization of a solution are completely modified by the addition of a minute quantity of high-molecular-weight polymers. The formation of long-living ligaments due to the large extensional viscosity of the polymer solutions is at the origin of their effect on the spray drop size distribution and their utilization as anti-drift adjuvants. Dilute emulsions have also been shown to reduce the amount of small drops in agricultural spray [Qin 2010, Hilz 2013a]. Hence, our objective is to investigate if dilute emulsion displays a similar behavior as dilute high-molecular-weight polymer solution concerning the destabilization of ligaments. In the following, we investigate the detachment of a pendant drop from a reservoir as it is the simplest configuration to observe the formation of a drop. We study the detachment of a pendant drop of milliQ water, dilute high-molecular-weight PEO solution, as two reference systems, and dilute emulsion (the industrial emulsion has been studied here).

3.2.1 Samples, experimental set-up and image analysis

3.2.1.1 Experimental set-up

The experimental setup is presented on Figure 3.2: a drop is detached from a syringe thanks to a syringe pump which injects fluid at a low flow rate (Q = 2 mL/min). The dynamics of the falling drop is recorded with a high-speed-motion camera, Phantom V7.3, operating at 2,000 frames per second. The minimum diameter of the liquid neck, $H_{\min}$, normalized by the neck diameter at the exit of the syringe, D, is measured until the detachment of the drop. The Reynolds number can be calculated : $Re = \frac{\rho v D_0}{\eta}$ with η the fluid viscosity, ρ the fluid density, D_0 the internal syringe diameter (D_0=2 mm), v the fluid velocity which is deduced from the flow rate, Q, as $Q = vs$ with s the section of the syringe (Q=2 mL/min, s=3.3 mm^2). In these experiments, the Reynolds numbers are low, around 20, which means that experiments are run in a laminar regime with no turbulence.

3.2.1.2 Image analysis

The images are analyzed using ImageJ. The image analysis procedure is illustrated in Figure 3.6. Figure 3.6(a) shows a typical image of a pendant drop with the definition of the x (horizontal) and z (vertical) axes. First, for each pixel of the image, we measured the normalized intensity, I_{norm}, as the ratio between the measured intensity and the measured intensity for an image of the background (the syringe without liquid) taken in the same experimental conditions. In Figure 3.6(b) is plotted the normalized intensity profile along the horizontal line shown in Figure 3.6(a). For small and high values of x, I_{norm} is constant and equal to 1, which corresponds to the exterior of the pendant drop, i.e. the background. We note the presence of two sharp peaks corresponding to the interfaces of the pendant drop. We calculate the average of I_{norm} over the x axis and we define a threshold value equal to 90 % of the mean value (blue dotted line in Figure 3.6(b)). The locations of the interfaces (X_1 and X_2) are determined by taking the first value lower than the threshold value from the two extremities of the line. From the positions of the interface, we deduce the value of the liquid neck diameter, H, which is equal to the distance between X_1 and X_2. By performing the same analysis for the different values of z, we obtain the profile of the neck diameter along the vertical axis, Figure 3.6(c). From these data, we can determine the minimum value of the diameter of the fluid neck (indicated in Figure 3.6(c)) at a given time. By performing the same analysis on the different images, i.e. at different times, one is able to obtain the evolution of the fluid neck minimum diameter as a function of time, Figure 3.6(d). The spatial resolution is equal to 0.01 mm (1 pixel).

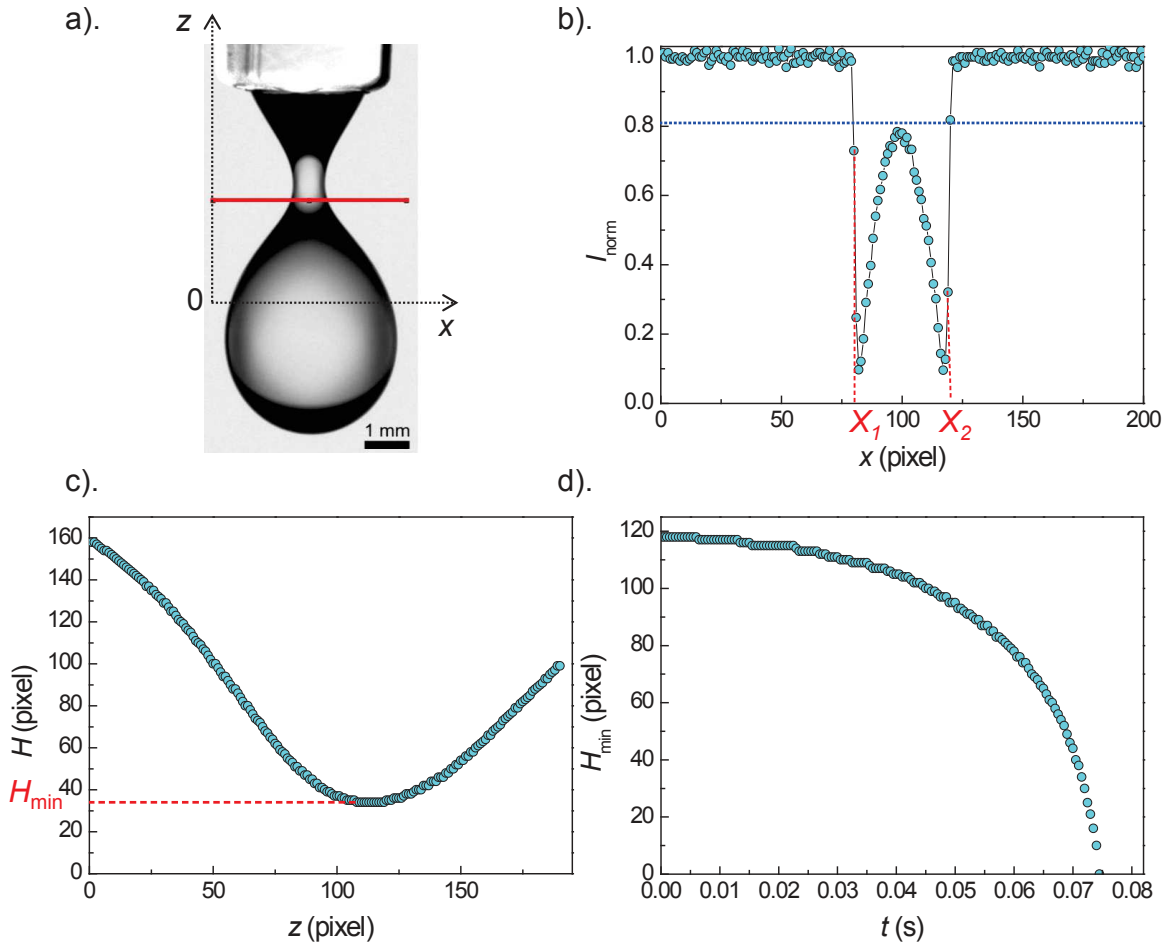

Figure 3.6: Procedure for the image analysis. a). Image of a pure water pendant drop detaching from a syringe with the definition of the x and z axes. b). Normalized intensity profile as a function of the distance on the x axis as measured along the horizontal line shown in (a). The blue dotted line corresponds to the threshold value used to determine the locations on the x axis of the fluid neck interfaces, X_1 and X_2. c). Fluid neck diameter profile along the vertical axis; the minimum diameter, $H_{\min}$, is indicated. d). Time evolution of $H_{\min}$.

3.2.1.3 Samples

The investigated solutions are: milliQ water, high-molecular-weight PEO solutions ($1,000,000$ g/mol, $C = 0.05$ % v/v) and the industrial emulsion (see Chapter 2 for details about the composition). In the Table 3.1 are summarized the values of the capillary and viscous times, the viscous length and the Ohnesorge number for the three systems.

For the three systems, the Ohnesorge number is lower than 1 which indicates that the viscous effects are negligible compared to the inertia and the expected thinning regime is the inertio-capillary regime. The very low viscous lengths prevent any observation

	t_γ (ms)	t_η (ms)	L_η (nm)	Oh
milliQ water	3.8	0.01	14	3.7 x 10^{-3}
Industrial emulsion	5.2	0.03	30	5.5 x 10^{-3}
PEO solution	4.0	0.02	28	5.3 x 10^{-3}

Table 3.1: Physico-chemical characteristics of the studied systems. t_γ and t_η are calculated for $R = 1$ mm.

of the visco-capillary-inertial regime as we cannot observe the thinning at such small length scale due to the experimental resolution. Hence, for the thinning dynamics of the three systems, we first expect an exponential thinning as predicted by the linear stability analysis of Rayleigh, $\frac{H_{\min}}{D} = 1 - e^{\frac{t-t_c-t_0}{t_R}}$ (Equation 3.1). Then, when we approach the drop detachment the thinning should speed up and follow a power law scaling corresponding to the inertio-capillary regime, $\frac{H_{\min}}{D} = 0.7\left(\frac{(t_c-t)}{t_\gamma}\right)^{2/3}$ with t_c the breakup time (Equation 3.3).

3.2.2 Detachment mechanism and thinning dynamics

3.2.2.1 MilliQ water

In Figure 3.7 is represented the detachment of a milliQ water drop. We observe the formation of a neck between the reservoir and the drop. The neck gets thinner and longer until the detachment of the drop at Figure 3.7(f). The neck is detached from the reservoir and forms a satellite drop in Figure 3.7(g). The thinning dynamics is shown in Figure 3.8. We observe the two expected regimes: first an exponential thinning (blue dashes), the experimental curve is well fitted by the expression $H_{\min}/D = B - e^{\frac{t-t_c-t_0}{t_R}}$ with B, t_R and t_0 as fitting parameters. We obtain $B = 0.98$, $t_R = 19.46$ ms and $t_0 = 6.05$ ms. t_0 corresponds to the breakup time if the exponential thinning was valid until the drop detachment, see Figure 3.8. In the last milliseconds, the thinning speeds up with a power law in 2/3 (red dots) corresponding to the inertio-capillary regime. The experimental data are well fitted by the expression: $H_{\min}/D = 0.7\left(\frac{t_c-t}{t_\gamma}\right)^{\frac{2}{3}}$ with t_γ as unique fitting. We find t_γ=12.86 ms. In conclusion, the thinning dynamics of a water drop detaching from a reservoir is correctly predicted by the exponential thinning announced by the linear analysis and, in the last milliseconds, by the inertio-capillary regime predicted by the non-linear analysis.

3.2.2.2 High-molecular-weight polymer solution

In Figure 3.9 is represented the detachment of a drop of the PEO solution. Until 9 ms before the breakup, the destabilization is precisely similar to the one of a water

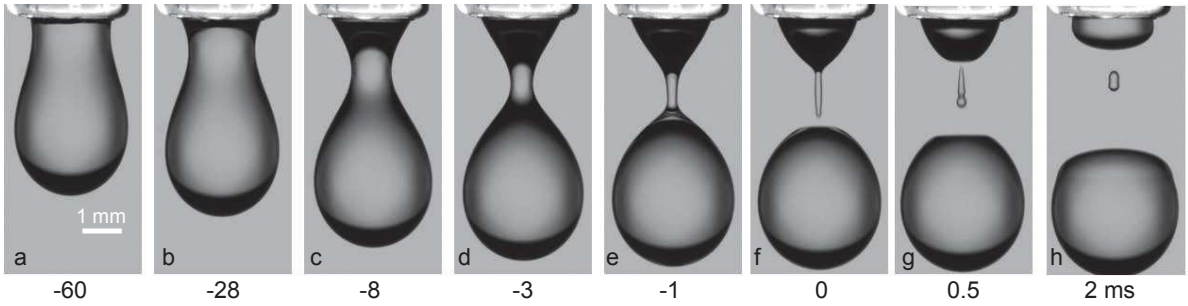

Figure 3.7: Detachment of a milliQ water drop. $Q = 2$ mL/min, $D_0 = 2$ mm and $Re = 20$. The origin of time is taken at the moment of the drop detachment.

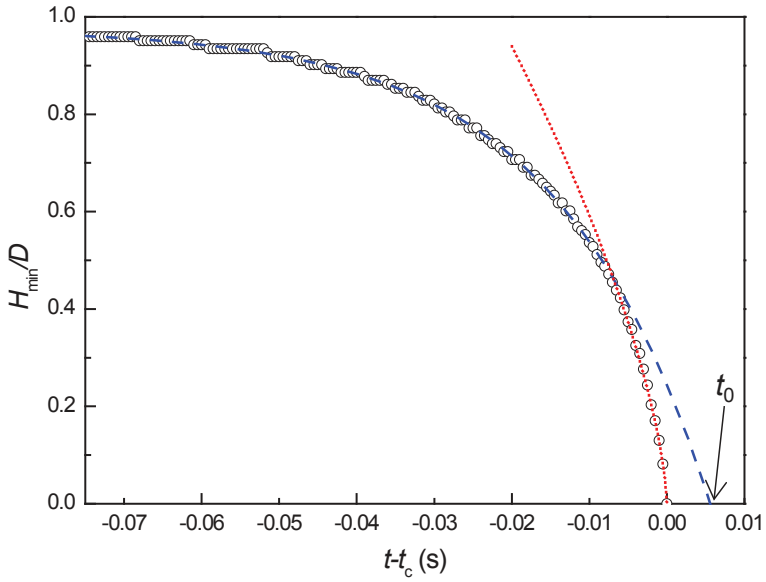

Figure 3.8: Thinning dynamics of a milliQ water drop. $Q = 2$ mL/min, $D_0 = 2$ mm and $Re = 20$. The blue dashes correspond to the exponential fit of the experimental data of the form $H_{\min}/D = B - e^{\frac{t-t_c-t_0}{t_R}}$ with fitting parameters $B = 0.98$, $t_R = 19.46$ ms and $t_0 = 6.05$ ms. The red dots correspond to the power law fit of the experimental data of the form $H_{\min}/D = 0.7\left(\frac{t_c-t}{t_\gamma}\right)^{\frac{2}{3}}$ with fitting parameter $t_\gamma = 12.86$ ms.

drop, Figure 3.7. However, on Figure 3.9(e), at -8.5 ms, a very thin filament is formed connecting the upper reservoir to the main drop. A satellite drop is suspended on this filament that gets longer and thinner. Eventually, the filament breaks up liberating the satellite drop. This destabilization mechanism is similar to the "bead-on-string" structure described by [Amarouchene 2001, Wagner 2005, Christanti 2001].

The thinning dynamics plotted in the Figure 3.10 exhibits the same first two regimes as those observed for water drops. First an exponentially thinning well fitted by an ex-

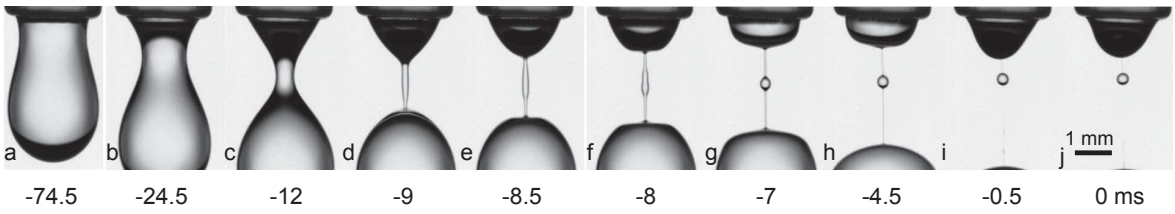

Figure 3.9: Detachment of a drop of PEO solution 10^6 g/mol 0.05%w. $Q = 2$ mL/min, $D_0 = 2$ mm and $Re = 16$. The origin of time is taken at the moment of the drop detachment.

pression of the form $H_{\min}/D = B - e^{\frac{t-t_c-t_0}{t_R}}$ with fitting parameters $B = 0.95$, $t_R = 19.83$ ms and $t_0 = -1.53$ ms. t_0 corresponds to the breakup time is the exponential thinning was valid until the drop detachment. Here $t_0 < 0$ as the breakup occurs later than predicted by the linear analysis. The exponential thinning is followed by the inertio-capillary regime with a power law in 2/3 well fitted by the expression $H_{\min}/D = 0.7\left(\frac{t_c-t}{t_\gamma}\right)^{\frac{2}{3}}$ with fitting parameter $t_\gamma = 14.97$ ms. The breakup time is however delayed with the appearance of a new regime. In order to investigate this new regime, which lasts about 8 ms, we have performed experiments with a higher acquisition rate (up to 20,000 frame/s). These data are represented in the inset of Figure 3.10 in a semi-log graph. This representation highlights the existence of the new regime. We observe a very good reproducibility of our data: the data recorded at higher frame rate are also very well fitted by the fits previously determined. The new regime observed corresponds to the thinning of the filament formed between the main drop and the reservoir and it follows an exponential thinning indicated by the green dashes, as experimentally measured by [Amarouchene 2001, Tirtaatmadja 2006]. The thickness of the filament is closed to the spatial resolution of the set-up, this is why the data are less well-defined in this regime but we can still note an exponential evolution well fitted by the expression $H_{\min}/D = Ce^{\frac{-(t-t_c)}{3\tau}}$ with fitting parameters C=0.005 and τ =1.28 ms. Following Equation 3.6, τ should be equal to the relaxation time of the polymer chains calculated from the Zimm model. Our experimental value is really closed to the one obtained by [Christanti 2002] for PEO solution of same molecular weight and concentration. They experimentally found $\tau = 2.4$ ms and they compared this value to the longest relaxation times of the polymer chain according to the Zimm model: $\tau_{\text{Zimm}} = 0.92$ ms. Our experimental value is in good agreement with these two values. A consequence of the formation of this filament is to retard the breakup. In the case of a Newtonian fluid, the drop would have been detached at the intersection of the red dotted line with the abscissa axis (Figure 3.10) but for the PEO drop the formation of the filament prolongs the process and therefore retards the breakup.

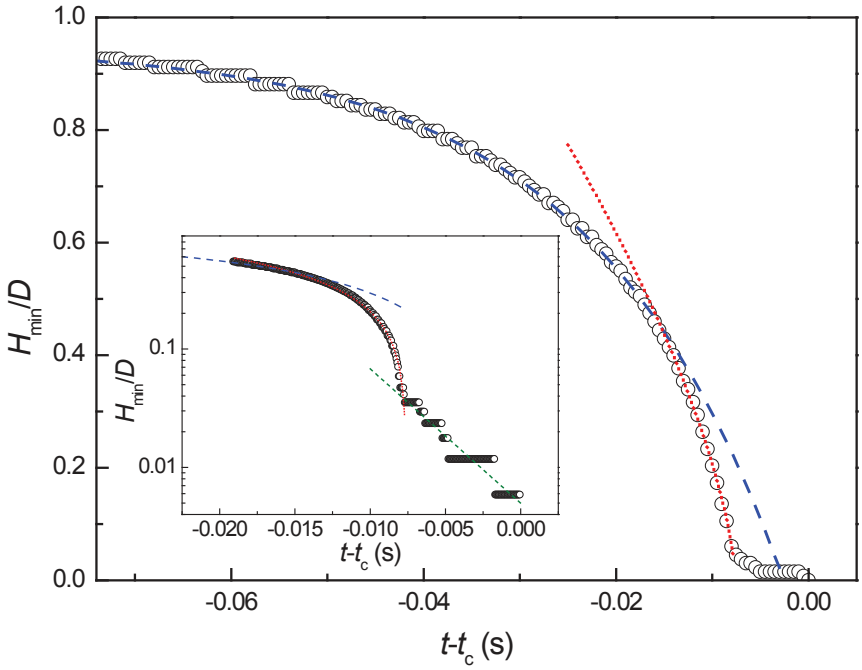

Figure 3.10: Thinning dynamics of a drop of 10^6 g/mol PEO solution at a concentration of 0.05 % w/w, $Q = 2$ mL/min, $D_0 = 2$ mm and $Re = 16$. The blue dashes correspond to the exponential fit of the experimental data of the form $H_{\min}/D = B - e^{\frac{t-t_c-t_0}{t_R}}$ with fitting parameters $B = 0.95$, $t_R = 19.83$ ms and $t_0 = -1.53$ ms. The red dots correspond to the power law fit of the experimental data of the form $H_{\min}/D = 0.7\left(\frac{t_c-t}{t_\gamma}\right)^{\frac{2}{3}}$ with fitting parameter $t_\gamma = 14.97$ ms. (Inset) Thinning dynamics recorded at 20,000 frame/s in a log/lin graph to highlight the exponential thinning of the long-living filament formed. The short green dashes correspond to the exponential fit of the experimental data of the form: $H_{\min}/D = Ce^{\frac{-(t-t_c)}{3\tau}}$ with fitting parameters C=0.005 and τ =1.28 ms.

3.2.2.3 Industrial emulsion

We show in Figure 3.11 the detachment of a pendant drop of the industrial emulsion. The destabilization process is in all aspects similar to the one of a water drop (Figure 3.7). In the same way, the thinning dynamics of the industrial emulsion drop (presented in Figure 3.12) is identical to the water drop dynamics (see inset Figure 3.12 for the superimposition of the two thinning dynamics). First, the fluid neck exponentially thins: the experimental data are well fitted by the expression $H_{\min}/D = B - e^{\frac{t-t_c-t_0}{t_R}}$ with fitting parameters $B = 0.99$, $t_R = 19.46$ ms and $t_0 = 6.00$ ms. Second, the thinning speeds up with the inertio-capillary regime and the data are well fitted by the expression $H_{\min}/D = 0.7\left(\frac{t_c-t}{t_\gamma}\right)^{\frac{2}{3}}$ with fitting parameter $t_\gamma = 13.32$ ms.

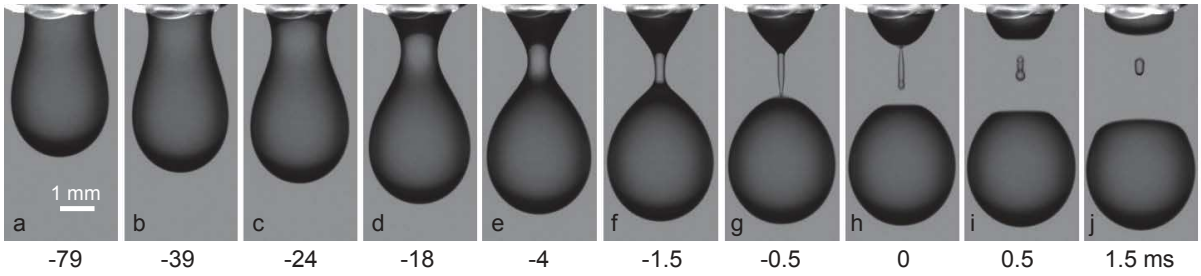

Figure 3.11: Detachment of an industrial emulsion drop. $Q = 2$ mL/min, $D_0 = 2$ mm and $Re = 20$. The origin of time is taken at the moment of the drop detachment.

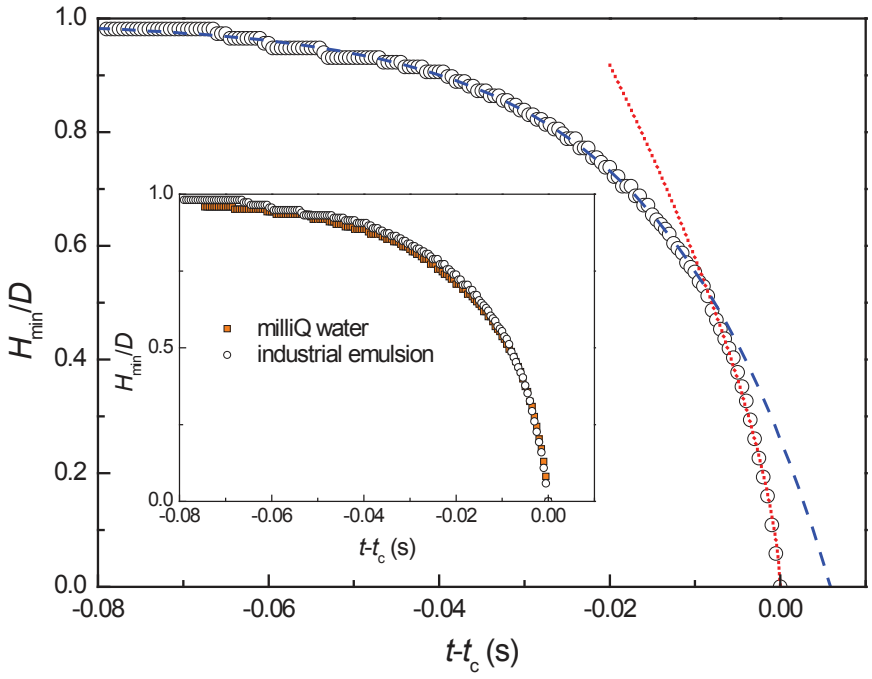

Figure 3.12: Thinning dynamics of an industrial emulsion drop. $Q = 2$ mL/min, $D_0 = 2$ mm and $Re = 20$. The blue dashes correspond to the exponential fit of the experimental data of the form $H_{\min}/D = B - e^{\frac{t-t_c-t_0}{t_R}}$ with fitting parameters $B = 0.99$, $t_R = 19.46$ ms and $t_0 = 6.00$ ms. The red dots correspond to the power law fit of the experimental data of the form $H_{\min}/D = 0.7\left(\frac{t_c-t}{t_\gamma}\right)^{\frac{2}{3}}$ with fitting parameter $t_\gamma = 13.32$ ms. (Inset) Superimposition of the dynamics of a milliQ water drop (orange squares) and of an industrial emulsion drop (white circles).

3.2.3 Conclusion

We have seen that a water and an industrial emulsion pendant drops present the same breakup mechanism and follow the same thinning dynamics. The first stages of the

detachment of a drop of dilute solution of high-molecular-weight polymer are similar to those of a water drop. However, at the approach of the drop detachment, the PEO solution drop exhibits a specific breakup mechanism with the formation of a thin cylindrical filament which retards the detachment of the drop in agreement with previous studies [Amarouchene 2001, Wagner 2005, Christanti 2001].

In Table 3.2 are summarized the fitting parameters of the two thinning regimes compared to their theoretical values for the three systems investigated. We report in particular the experimental characteristic times of the two thinning regimes, t_R for the exponential regime (Equation 3.1) and t_γ for the inertio-capillary regime (Equation 3.3). These experimental values obtained from the fits of the data are compared to the theoretical values calculated from the physico-chemical properties of the solutions (Table 3.1). The theoretical values of t_R and t_γ are calculated by taking $R = D/2$ with D the neck diameter at the exit of the syringe. We observe that the experimental characteristic times of the exponential regime, t_R (fit), are in excellent agreement with the theoretical values, t_R (th). The experimental values obtained for t_γ are twice larger than the theoretical values expected, we are not able to explain this discrepancy.

	t_R (fit) (ms)	t_R (th) (ms)	t_γ (fit) (ms)	t_γ (th) (ms)	B (fit)	B (th)	t_0 (fit) (ms)
milliQ water	19.5	17.1	12.9	5.9	0.98	1.00	6.05
emulsion	19.5	21.8	13.3	7.5	0.95	1.00	-1.53
PEO solution	19.8	21.4	15.0	7.4	0.99	1.00	6.00

Table 3.2: Fitting parameters of the two thinning regimes compared to their theoretical values. Experimental characteristic times deduced from the fit for the exponential regime (t_R (fit)), resp. inertio-capillary regime (t_γ (fit)), compared to their theoretical values t_R (th), resp. t_γ (th).

3.3 Destabilization of stretched ligaments - Experimental results

In the previous section, we have seen that the industrial emulsion does not modify the breakup mechanism and the thinning dynamics of a pendant drop detaching from a reservoir comparing to a water drop. In this section, we investigate the destabilization of stretched ligaments. Once again, we will compare the destabilization mechanism of the industrial emulsion with two test fluids: milliQ water and the dilute solution of high-molecular weight PEO.

The destabilization of liquid ligaments into drops is the last step of the destabilization process of a liquid sheet. During spray formation, liquid ligaments are formed at the sheet boundaries or holes and stretched by the ambient air. Therefore the liquid ligaments are destabilized under stretching while they are still alimented in liquid by the sheet. In order to mimic this situation, we use an original experimental set-up to visualize the destabilization of stretched ligaments fed by a reservoir. The experimental set-up is described in the first part of this section. We then present the different destabilization mechanisms observed and the resulting drop size distribution for the three solutions investigated.

3.3.1 Experimental set-up

The principle of the experimental set-up is to form liquid ligaments that will be stretched by the ambient air due to centrifugal forces. We use a spin coater to rotate a petri dish that acts as the liquid reservoir. Some pictures and scheme of the experimental set-up are presented in Figure 3.13. The petri dish is fixed on the spin coater plate by vacuum. The petri dish is drilled at two diametrically opposed positions to insert glass capillary, Figure 3.13(b) and (c). Once the petri dish is in rotation, the liquid is ejected from the reservoir through the glass capillaries forming liquid ligaments that are stretched by the ambient air and destabilized into droplets. We use a SPIN150 spin coater provided by SPS-Europe, the accessible velocity range is $0-10,000$ rpm and the acceleration range $1-7,000$ rpm/s. For our experiments, we set the rotation velocity to 700 rpm (i.e. 73.3 rad/s) and the acceleration to its maximum value, i.e. 7,000 rpm/s (733 rad/s^2). The length of the glass capillaries is equal to 0.4 cm, their internal, resp. external, diameter is 0.75 mm, resp. 1.0 mm. The tangential velocity at the extremity of the glass capillaries, v, is equal to 1.76 m/s. We can estimate the Reynolds number: $Re = \frac{\rho v D_c}{\eta}$ with D_c the external diameter of the capillaries, which leads to Reynolds numbers in the range: (1,300-1,800) for the three systems. The liquid reservoir, i.e. the petri dish, is filled before each experiment. A white cartoon is placed inside the spin coater, below the petri dish to obtain a white homogeneous background. The destabilization of the liquid ligaments is recorded from the top with a high-speed motion camera, Phantom V7.3. The frame rate is set at 6,700 frame/s.

In Figure 3.14 is represented a typical image of the destabilization of a stretched ligament obtained with our experimental set-up. At the bottom right corner of the image, we see the glass capillary from which a liquid jet is formed and rapidly destabilized into drops. We see that the contrast of the liquid itself on the white background is not really good and it will be difficult to perform an automated analysis as it is based on grey level contrast. However the black shadow of the ligament and drops on the white background is very well defined. For practice purpose, we decide to used the shadow of the drops to perform the analysis.

In Figure 3.15 is detailed the image analysis used to determine the size distribution

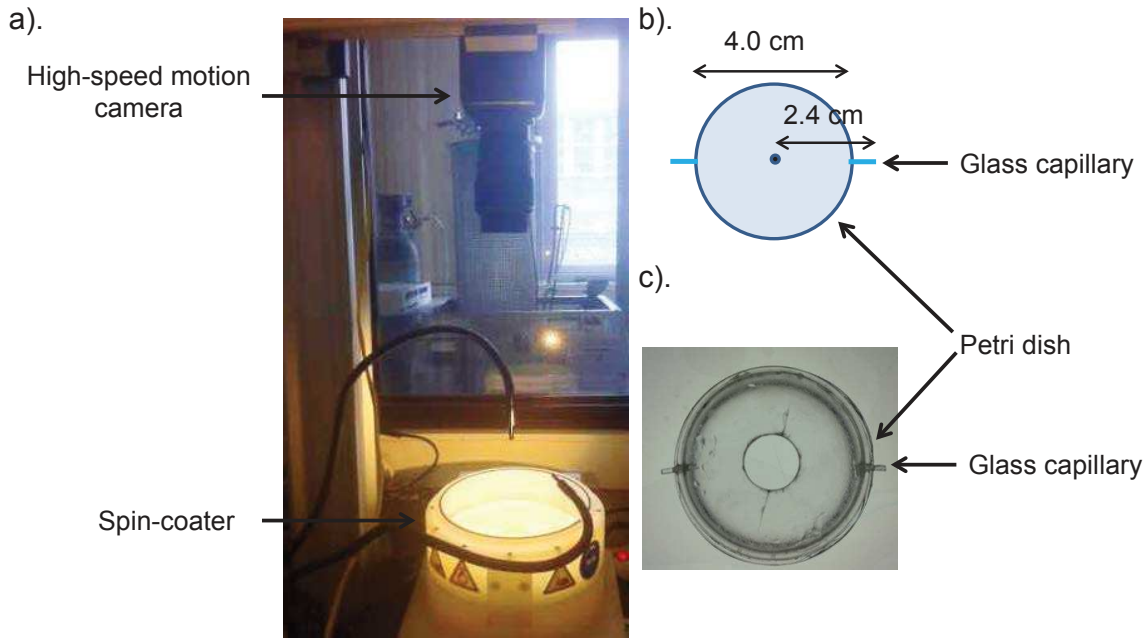

Figure 3.13: Pictures and scheme of the experimental setup. a). Global view of the experimental setup with the high-speed motion camera and the spin coater used to rotate the liquid reservoir b). Scheme of the petri dish and the two glass capillaries used to form liquid ligament. Relevant length scales are indicated on the scheme. c). Zoom on the liquid reservoir.

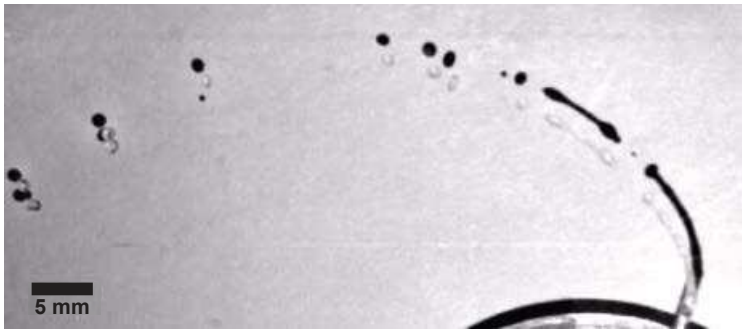

Figure 3.14: Image of the destabilization of a stretched ligament obtained with our experimental set-up. The liquid and its shadow are visible.

of the drops issued from the ligament destabilization. In Figure 3.15(a) is represented a typical image obtained with our experimental set-up with the shadow of the drop well-defined on the background. The software ImageJ is used for the image analysis. We apply a binary threshold on the images, Figure 3.15(b), allowing one to count and measure the drop area (A), Figure 3.15(c). An apparent drop diameter is simply deduced from the area of the drop according to $d = \sqrt{4A/\pi}$. For each solution investigated, 23 ligaments are analyzed. For each ligament, one image is analyzed. The resolution of the experimental setup is equal to 0.1 mm which means that drops smaller than this limit could not be measured. From the measurement of the drop diameter, we determine the drop size distribution by plotting the relative and cumulative frequencies as a function of the drop diameter normalized by the external capillary diameter.

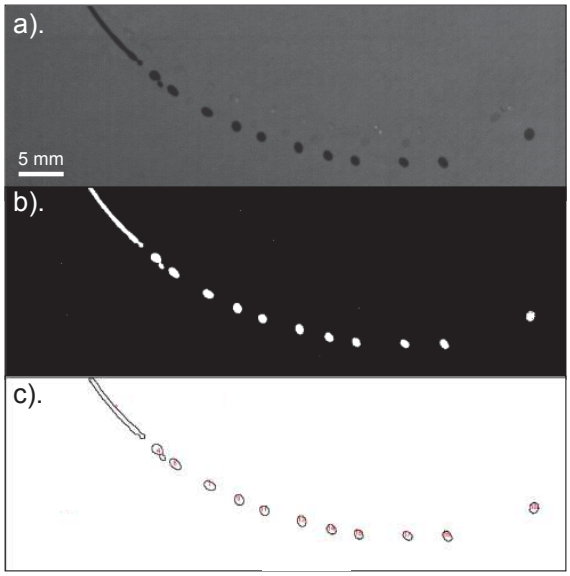

Figure 3.15: Image analysis to determine the size distribution of drops issued from ligament destabilization. a). Typical image of the destabilization of a liquid ligament obtained with our experimental set-up. b). Binary thresholded image obtained by considering the shadow of the liquid on the white background. c). Determination of the number and area of the drops.

3.3.2 Mechanism of ligament destabilization

In Figure 3.16 is represented the destabilization of liquid ligaments of water (Figure 3.16(a)), high-molecular-weight PEO solution (Figure 3.16(b)), and industrial emulsion (Figure 3.16(c)). At the top right corner of each image, there is a zoom on the ligament destabilization region. For the water and industrial emulsion, we observe that the destabilization is regular with the formation of main drops and between them small

satellite drops. For the PEO solution ligament, we observe the formation of long-living filaments between the main drops close to the ligament (zoom Figure 3.16 (b)). The satellite drops are suspended on these filaments, we observed the same "beads-on-string" structure described previously (section 3.2.2.2). The satellite drops are able to merge with the main drops along the thin filament. This phenomenon results in fewer and bigger drops formed by the destabilization of one ligament, as it is visible by comparing Figure 3.16(b) to Figures 3.16(a) and (c). The size distributions of the drops issued from the ligament destabilization are measured in order to quantify the role of the different adjuvants in the fragmentation processes.

3.3.3 Drop size distribution

In Figure 3.17 is represented the drop size distribution in number for the three solutions investigated. As explained above, we have analyzed the same number of ligaments, 23, for the different systems. The number of drops analyzed from the destabilization of these ligaments is equal to 364 for water, 376 for industrial emulsion and 262 for the PEO solution. The number of emulsion and water drops produced are comparable. Our first impression regarding the destabilization of PEO ligament is confirmed: the number of drops produced per one ligament is reduced by 28 % compared to that for water and emulsion due to the coalescence of the satellite drops along the thin filament formed. Concerning the drop size, for the three systems we observe a large main peak around 1.0 times the capillary diameter and a smaller peak around 0.5 times the capillary diameter. We notice a large distribution of sizes for the three systems ranging from approximately 0.1 to 1.5 times the capillary diameter for water and industrial emulsion and 0.4 to 1.4 times the capillary diameter for the PEO solution. For the PEO solution, the mean value is equal to 0.91 and the standard deviation 0.25. Whereas for the water, resp. industrial emulsion, the mean value is equal to 0.90, resp. 0.86, and the standard deviation to 0.32, resp. 0.33. For the three systems the mean values are really close but the standard deviation is noticeably lower for the PEO solutions reflecting the narrower width of the distribution.

We now consider the proportion of drops with a diameter lower than 0.25 times the capillary diameter. The proportion of such small drops is equal to 3.8 % for water, 5.3 % for industrial emulsion and 0.8 % for the PEO solution. As previously observed on the ligament images, the PEO solution permits to reduce considerably (a decrease of 79 % compared to water) the proportion of small drops issued from the destabilization of liquid ligaments. The industrial emulsion slightly increases the proportion of small drops even if the destabilization mechanism is similar to the one of water ligament.

We remark that the size of the main drops is around 1.0 times the capillary diameter, which is different of the value predicted by Rayleigh (1.89 times the ligament radius). We are not able to explain this difference, however we did not further investigate this aspect, as it was clear that the emulsion has not effect on the destabilization mechanism

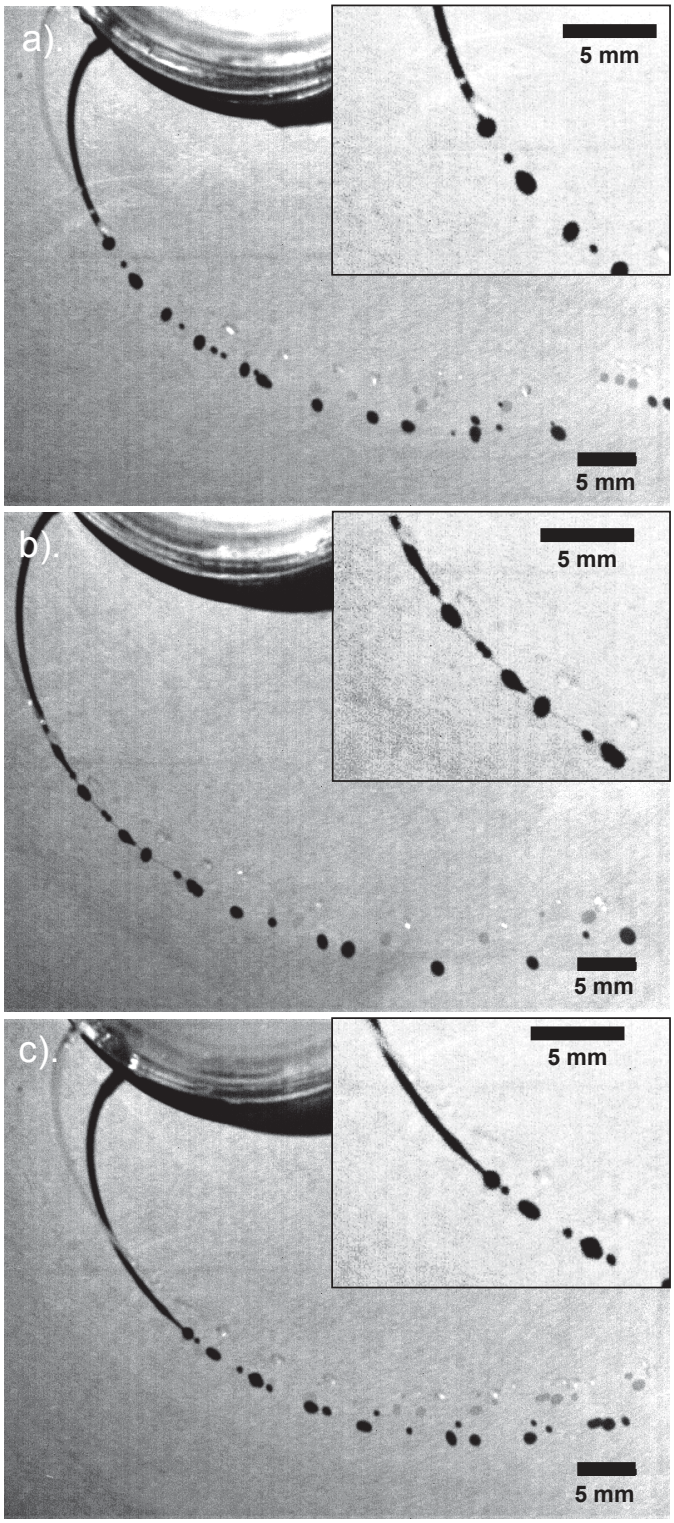

Figure 3.16: Destabilization of liquid ligaments of a). milliQ water, b). PEO solution 1,000,000 g/mol at 0.05 % w/w and c). industrial emulsion.

of liquid ligament.

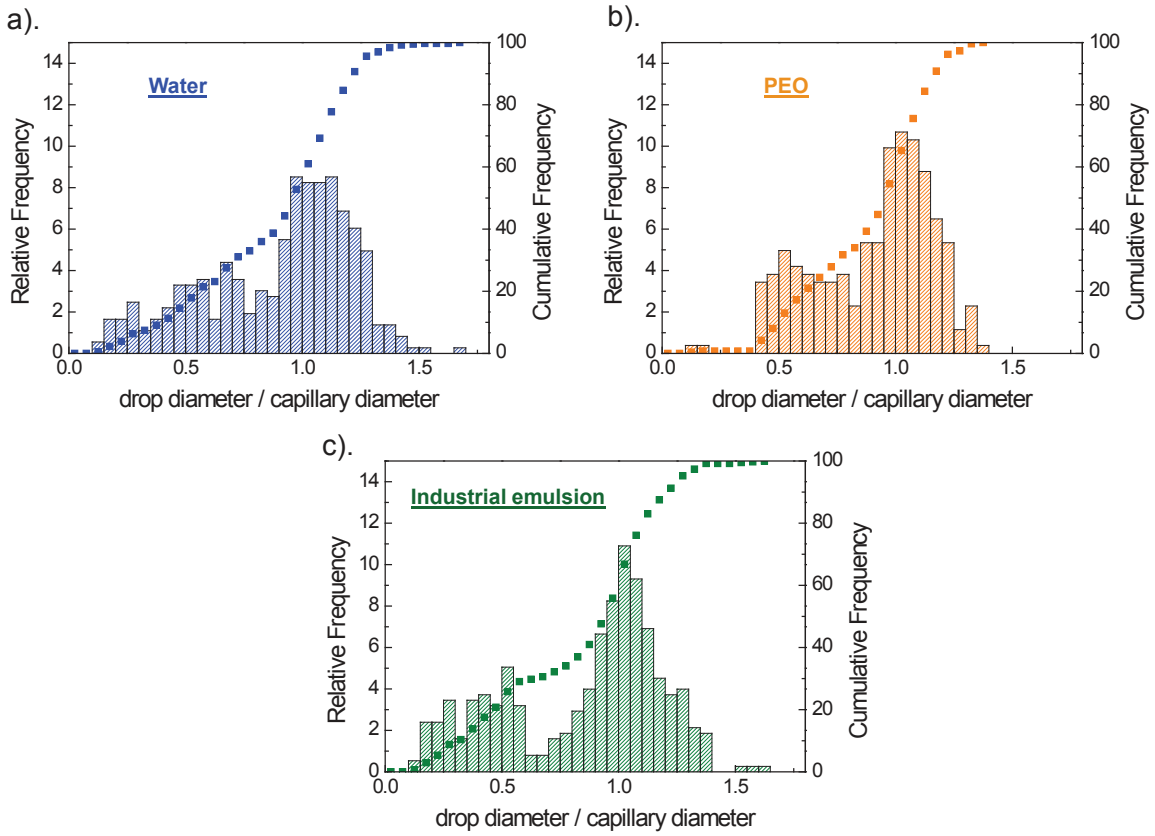

Figure 3.17: Size distribution of the drop issued from the destabilization of liquid ligaments for a). water b). PEO solution 1,000,000 g/mol 0.05 % w/w and c). industrial emulsion. The drop diameter is normalized by the capillary diameter.

3.4 Conclusion

The formation of spray drops results from the destabilization of the liquid sheet formed at the exit of the nozzle. This destabilization can be divided in two successively steps: first the liquid sheet is destabilized into liquid ligaments and then these ligaments are destabilized into drops forming the spray. In this chapter, we have focused on the last step of the destabilization process: the destabilization of liquid ligaments into drops. We have studied the simplest configuration of destabilization of liquid ligament that is the detachment of a pendant drop from a reservoir. Then, we have investigated the destabilization of stretched ligaments fed by a reservoir to mimic the destabilization taking place during the spray formation. We have compared the behavior of the industrial emulsion with two references systems: milliQ water and high-molecular-weight polymer solution.

We have shown that the industrial emulsion has not effect on the dynamics of detachment of a pendant drop and on the destabilization of stretched ligament. The destabilization mechanisms are in all aspects similar to those of water. By contrast, the high-molecular-weight polymer solution exhibits a specific behavior with the formation of thin cylindrical filaments which retards the breakup and suppresses the formation of satellite drops, in agreement with previous results.

Thanks to this experimental study, we understand the action of high-molecular-weight polymer solution as anti-drift adjuvant for agricultural spray. The polymer solution strongly affects the last step of the destabilization process: the destabilization of liquid ligament into drops. The formation of the long-living filament suppresses the formation of satellite drops and so reduces the proportion of small drops in the spray. On contrary, we have shown that the mechanism of action of the industrial emulsion as anti-drift adjuvant for agricultural solutions does not arise from the destabilization of liquid ligaments. Therefore in the next chapters, we will investigate the first step of the atomization process, which is the destabilization of liquid sheet.

Chapter 4

Free radially expanding liquid sheet

Contents

We have seen in the previous chapter that the emulsion has no effect on the destabilization of liquid ligaments. From these results, one can conclude that the anti-drift properties of the emulsions are not related to the ligament fragmentation. The next chapters of the thesis are dedicated to the study of the first step of the atomization process, i.e. the destabilization of liquid sheets, in order to understand the mechanism of action of emulsions as anti-drift adjuvant. Our first objective is to develop an experimental

set-up to produce liquid sheets in a controlled way in order to study their destabilization mechanisms. This is the purpose of this chapter. In the first section of this chapter, we present a short literature review about free radially expanding liquid sheets. We first present the different experimental set-ups used in the literature to form liquid sheets. Then, we present the theoretical models developed and the numerical simulations performed to predict the kinematic fields of liquid sheets produced by the impact of a tear on a small target. The second section of this chapter is dedicated to the presentation of the single-tear experiment used to produce controlled liquid sheets and the experimental method developed to measure the thickness field of the sheet. The third section of this chapter is dedicated to the description of water-based liquid sheets. We describe the formation and destabilization of a pure water liquid sheet and measure the thickness field of the sheets. In the last section of the chapter, we finally use the single-tear experiment to produce liquid sheets of complex fluids. A part of the results presented in this chapter has been published in *Free radially expanding liquid sheet in air: time- and space-resolved measurement of the thickness field*, C. Vernay, L. Ramos and C. Ligoure, Journal of Fluid Mechanics, 764(428-444), January 2015 [Vernay 2015c].

4.1 Literature review

4.1.1 Experimental set-up

Many studies have focused on the formation and destabilization of liquid sheets using different experimental set-ups. In the context of agricultural application, most studies simply used agricultural flat fan nozzle to produce a liquid sheet and visualize it with a high-speed motion camera [Butler Ellis 1999b, Dexter 2001, Qin 2010, Hilz 2013a]. The pioneers in this domain are Dombrowski et al. [Dombrowski 1954]. In 1954, they studied the breakup mechanism of liquid sheets of different complex fluids (solutions of different viscosities, solid suspensions, dilute emulsions...) with an agricultural nozzle and a stroboscopic photographic technique (Figure 4.1). The main disadvantages of this set-up are that a large quantity of solution (about 3 liters) is needed to perform one experiment and the liquid sheets thus formed are not well-controlled as some turbulent events can take place in the nozzle. We have chosen a different experimental strategy in order to produce well controlled liquid sheets that require small amounts of solution.

In 1833, Savart studied by simple eye observation the liquid sheets formed by the impact of a jet on a solid target and the impact of two liquid jets [Savart 1833]. Most of the studies of the last decades about the destabilization of controlled liquid sheets are inspired by the early work of Savart with modern visualization technique, principally high-speed motion camera. Several groups used the original set-up designed by Savart [Savart 1833]: the oblique collisions of two identical liquid jets to form stationary liquid sheet [Bush 2004, Miller 2005, Bremond 2006]. Upon impact, the liquid expands radially from the impacting point forming a liquid sheet (Figure 4.2). The extent of the liquid

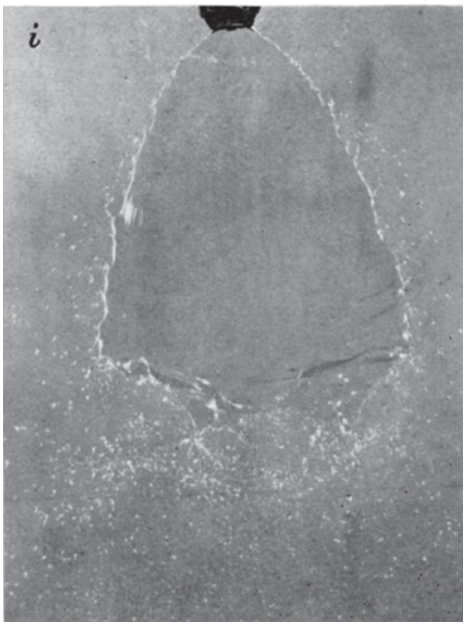

Figure 4.1: Pure water liquid sheet formed with a nozzle [Dombrowski 1954].

sheet is controlled by the velocity of the impinging jets. A variation of this experimental set-up is the impact of one liquid jet on a cylindrical solid target [Clanet 2002]. As for the impact of two jets, upon impact on the target the jet forms a stationary liquid sheet (Figure 4.3).

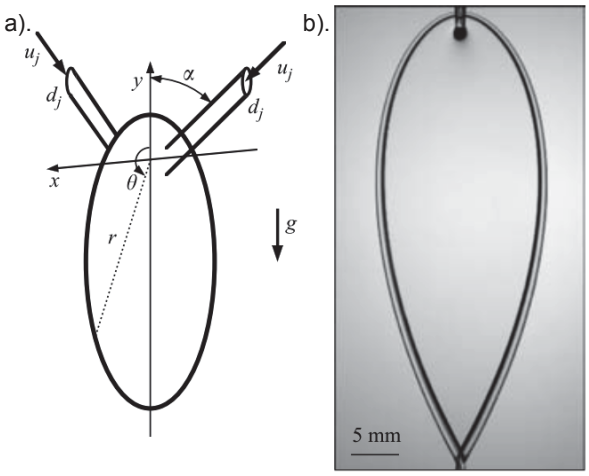

Figure 4.2: Formation of a liquid sheet by the collision of two jets. a). Sketch of the experimental set-up. b). Ethanol liquid sheet formed with the set-up shown in (a) [Bremond 2006].

More recently, Gart et al. [Gart 2013] developed an interesting experimental set-up to form transient liquid sheets with a limited volume of solution. Their original set-up was designed to mimic "the motion of clapping hands": a small volume of fluid is quickly

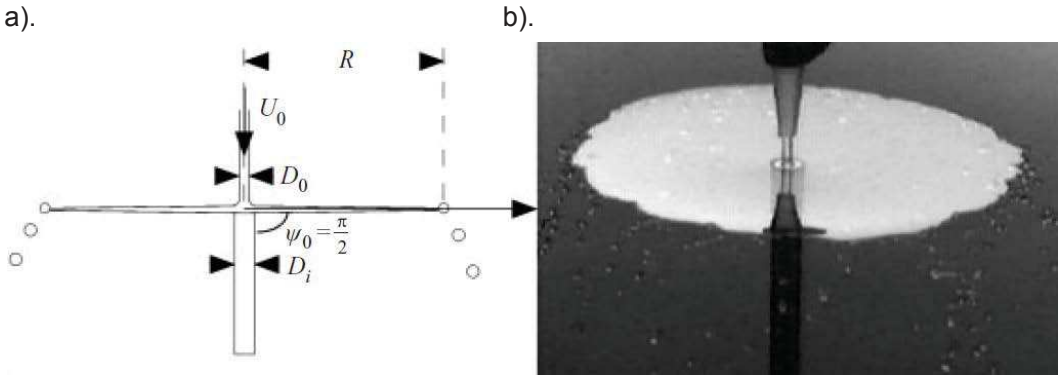

Figure 4.3: Formation of a liquid sheet by the impact of a jet on a small target. a). Sketch of the experimental set-up. b). Side view of a water sheet formed with the set-up shown in (a) [Clanet 2002].

compressed between two small solid surfaces. In practice, the set-up is composed of two aligned plates, the upper one being movable. A small quantity of liquid is deposited on the lower plate and the upper plate is then let fall on the lower one. Upon impact, the fluid is ejected, through the small gap between the two plates, in a radial direction forming a liquid sheet (Figure 4.4).

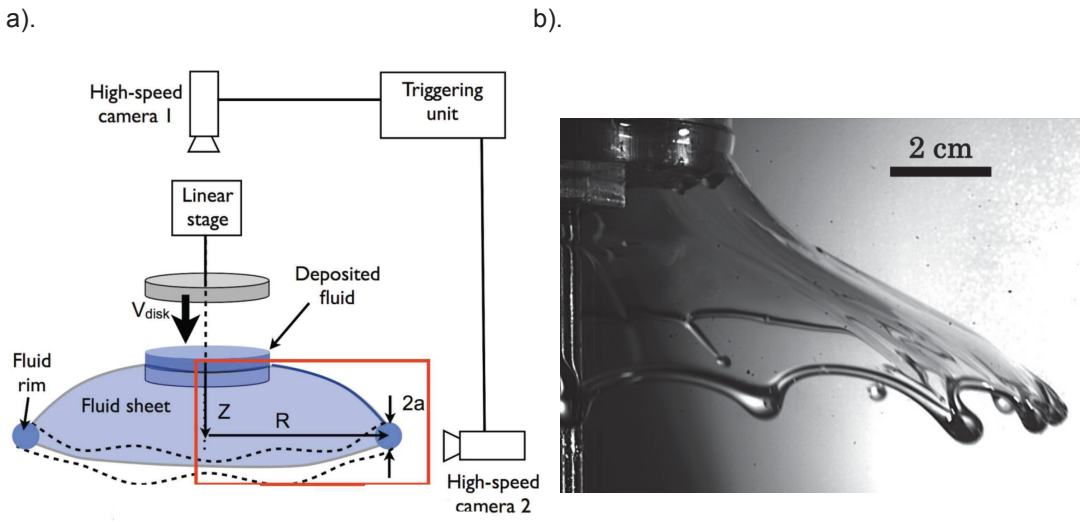

Figure 4.4: Formation of a liquid sheet by the impact of two plates. a). Sketch of the experimental set-up. b). Image of a liquid sheet (silicone oil of 100 cSt) formed with the set-up shown in (a) [Gart 2013].

Another interesting set-up to form transient liquid sheets is the one designed by Rozhkov et al. [Rozhkov 2002], which is a discrete adaptation of the jet impact set-up initially developed by [Savart 1833]. Transient liquid sheets are here formed by the impact

of a single tear on a small solid circular target. Upon impact the tear flattens into a free radially expanding liquid sheet (Figure 4.5). The great advantage of this set-up is that it requires only a tear of liquid, i.e. around 30 μL, to perform the experiment. What is more, this experiment is easier to set up than the experiments involving liquid jets. For these reasons, we have decided to use this type of set-up to study liquid sheet.

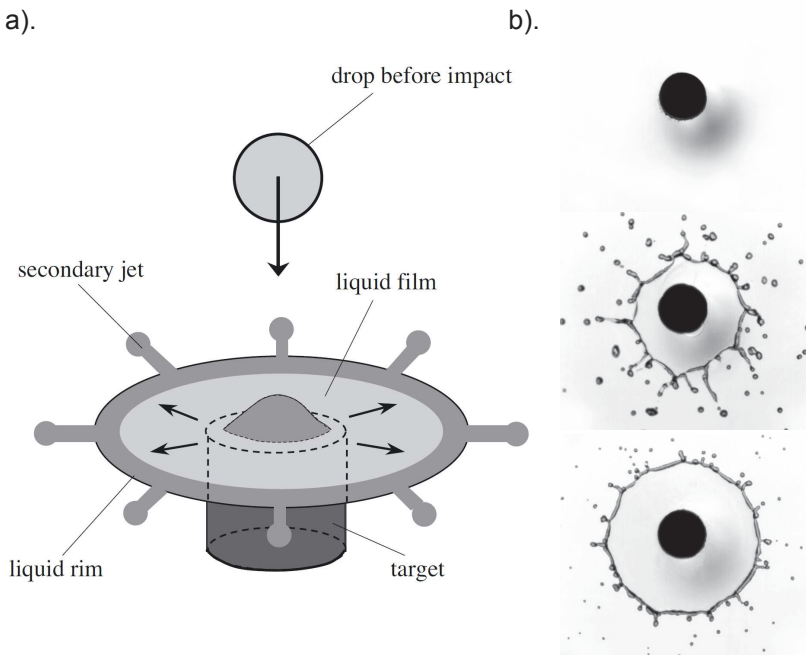

Figure 4.5: Formation of a liquid sheet by the impact of one tear on a small target. a). Sketch of the experimental set-up. b). Images of a water liquid sheet formed with the set-up shown in (a), the time interval between images is 1 ms [Rozhkov 2004].

Different models have been developed to predict the evolution of the sheet maximum diameter and the sheet thickness field for liquid sheet formed by the impact of a single tear on a small target. These models are presented in the next section.

4.1.2 Impact of a tear on a small target: theoretical predictions

Rozhkov et al. [Rozhkov 2002, Rozhkov 2004] on the one hand and Villermaux et al. [Villermaux 2011] on the other hand have proposed two distinct theoretical models to describe the hydrodynamics of a free radially expanding liquid sheet. The studied liquid sheets are made of inviscid fluid and formed by the impact of a tear on a small target. These two models lead to the same radial velocity field, $u(r,t)$, but to different predictions for the radial sheet thickness field, $h(r,t)$ and the sheet diameter, $d(t)$. The two models intend to describe two different limits of the phenomenon: the first one addresses time scales that are short compared to the collision time ($\tau_{\text{coll}} = d_0/u_0$) [Rozhkov 2002] and

the second one is explicitly concerned with larger time scales [Villermaux 2011]. Both theoretical approaches are based on the resolution of Euler equations in the slender-slope approximation with axisymmetry associated with the resolution of linear momentum balance equation for the variable-mass sheet rim.

Rozhkov et al. [Rozhkov 2004] have developed a simple model to describe the dynamics of the liquid in the sheet based on experimental observations. The authors consider that the tear impact is equivalent to a cylindrical point source that will feed the expanding sheet at short times. They define the ejection functions (velocity and flow rate of ejection) of the equivalent source based on experimental observations. Following their observations, during the tear collision, for $t < 3\tau_{\text{coll}}$, the liquid is ejected at an approximately constant flow rate with a ejection velocity that significantly decreases with time. For $t > \tau_{\text{coll}}$, the ejection ceases. The resulting distribution velocities, local flow rates and film thickness in the liquid sheet are calculated. This leads to a velocity field $u(r,t)$ that decreases with t and increases with r, whereas the thickness field, $h(r,t)$, increases with t and decreases with r. The asymptotic behavior, valid for short times $t < 3\tau_{\text{coll}}$, gives

$$h(r,t) = \alpha {d_0}^3 u_0 \frac{t}{r^3} \tag{4.1}$$

$$u(r,t) = \frac{r}{t} \tag{4.2}$$

with α an experimental constant, Rozhkov et al. have measured $\alpha = 0.038$ in their experiments. The time evolution of the sheet diameter is obtained by numerical integration of the model. The authors predict the maximum sheet diameter normalized by the tear diameter, $d_{\max}/d_0$, to be equal to $\sqrt{We/K}$ with K=20.

By contrast, Villermaux et al. [Villermaux 2011] consider the implicit opposite limit $t >> \tau_{\text{coll}}$. The authors propose an elegant solution for $u(r,t)$ and $h(r,t)$ that is a time-dependent adaptation of a steady-state axisymmetric solution of Euler equations for a continuous jet impacting a solid target [Clanet 2002]:

$$h(r) = {d_0}^2/8r \tag{4.3}$$

$$u(r) = u_0 \tag{4.4}$$

Arguing that an impacting tear will produce a similar expanding sheet but with an unknown time-dependent injection rate, they propose a solution for the thickness field of the form: $h(r,t) = f(t)/r$. Considering $u(r_0,t) = 0$, the volume conservation leads to a velocity field of the form: $u(r,t) = -\frac{f'(t)}{f(t)}(r - r_0)$, with r_0 the radius of the tear and of the target. They consider the pressure in the liquid to be constant over r. The zero pressure gradient in the liquid film implies a constant velocity of fluid particles while traveling along the sheet. Resolving the momentum balance equation for the variable-mass sheet rim leads to the expression of the injection function $f(t)$, which enables one to write the kinematic fields of the transient liquid sheet:

$$h(r,t) = \beta \frac{\pi d_0^3}{6u_0} \frac{1}{rt} \tag{4.5}$$

$$u(r,t) = \frac{r}{t} \tag{4.6}$$

with $\beta = 1/2\pi$. The theoretical model developed by Villermaux et al. predicts the radius of the expanding tear to follow an asymmetric one-period oscillatory motion

$$\frac{d(t) - d_0}{d_0} = \sqrt{\frac{2}{3}} \sqrt{We} \frac{t}{\tau} \left(1 - \frac{t}{\tau}\right)^2 \tag{4.7}$$

with $\tau = \sqrt{\frac{\rho {d_0}^3}{6\gamma}}$ proportional to the capillary time. The maximal amplitude of the motion is reached for t/τ=1/3 and reads

$$\frac{d_{\max} - d_0}{d_0} \approx 0.12\sqrt{We} \tag{4.8}$$

In conclusion, the two models [Rozhkov 2004, Villermaux 2011] provide the same theoretical prediction for the motion within the sheet, $u(r,t) \propto r/t$, but the sheet thickness field predicted by [Villermaux 2011], $h(r,t) \propto 1/rt$, differs strongly from Rozhkov predictions, $h(r,t) \propto t/r^3$.

Up to now, the confrontations of the theoretical models developed by [Rozhkov 2004] and [Villermaux 2011] have been mainly restricted to the indirect comparison of the measurement of the sheet diameter $d(t)$. In both experimental reports [Rozhkov 2004, Villermaux 2011], the sheet diameter time evolution exhibits a maximum in semiquantitative agreement with theoretical models. However, this indirect comparison is clearly not sufficient to discriminate between the different theoretical models. To reach this goal, direct measurements of the hydrodynamic fields are clearly desired. In this optics, Bakshi et al. [Bakshi 2007] measured the profile of a tear impacting onto a small sphere from the direct capture of sequences of side view images of the impact. However, the spatial resolution was too low to quantitatively compare experimental results with theoretical predictions except close to top of the sphere where the tear has impacted its target. To overcome those limitations we have used a robust and sensitive experimental method presented in section 4.2.2 to measure the sheet thickness field $h(r,t)$. Thanks to our measurements, a comparison of the experimental evolution of $h(r,t)$ for various tear volumes and impact velocities with the theoretical models developed by [Rozhkov 2004] and [Villermaux 2011] is possible.

4.1.3 Impact of a tear on a small target: simulations

Eggers et al. investigated by numerical simulations the impact of a tear onto a planar solid surface. They consider the case of a fluid perfectly repelled by the surface. They

predict a velocity field, $u(r,t)$

$$u(r,t) = \frac{r}{t + \frac{\tau_{\text{coll}}}{2}} \tag{4.9}$$

This velocity field includes a delay time equal to $\tau_{\text{coll}}/2$, which corresponds to the time for the pressure gradients to vanish. For $t >> \tau_{\text{coll}}/2$ this velocity field is equivalent to the one predicted by Villermaux et al., which describes the dynamics of liquid sheets at time scales that are long compared to the collision time, τ_{coll} [Villermaux 2011].

Concerning the thickness of the liquid sheet, Eggers et al. propose a similarity solution of the thickness field, $h(r,t)$ valid for any function F.

$$h(r,t) = \left(\frac{\tau_{\text{coll}}}{2}\right)^2 \frac{r_0}{(t + \frac{\tau_{\text{coll}}}{2})^2} F\left(\frac{r}{t + \frac{\tau_{\text{coll}}}{2}}\right) \tag{4.10}$$

with r_0 the radius of the tear ($r_0 = d_0/2$). The function F is deduced from the fit of their numerical simulations.

$$F(x) = \frac{D}{\left(1 + C\left(\frac{\tau_{\text{coll}}}{2r_0}\right)^2 x^2\right)^6} \tag{4.11}$$

with C and D numerical constants respectively equal to 0.625 and 1.0.

4.2 Experimental set-up

This section is dedicated to the description of the experimental set-up and to the image analysis performed. The single-tear experimental set-up is described in the first part of this section. We then detail the method developed to measure the thickness of the liquid sheet and then briefly the image analysis.

4.2.1 Single-tear experimental set-up

Our experimental set-up is adapted from the original set-up designed by [Rozhkov 2002]. A scheme of the set-up is shown in Figure 4.6(a). In brief, we let a liquid tear fall on a solid cylindrical target of diameter slightly larger than that of the tear. The liquid tear is injected with a syringe pump and a needle positioned vertically with respect to the target. The impact velocity of the tear, u_0, is set by the height of fall of the tear. The impact velocities are experimentally measured thanks to side view imaging of the experimental set-up. The experimental values are in very good agreement with the theoretical values calculated assuming a free fall of the tear, with a zero initial velocity (air friction is negligible over small height of fall): $u_0 = \sqrt{2gL}$ with L the height of fall. The tear diameter, d_0, is set by the needle diameter. Three different tear diameters ($d_0 = 3.0, 3.7$ and 4.8 mm) and two impact velocities ($u_0 = 2.8$ and 4.0 m/s) are studied. In all experiments the ratio between the tear diameter and the target diameter is kept

constant at 0.6. The Weber number, $We = \frac{\rho u_0^2 d_0}{\gamma}$, respectively the Reynolds number, $Re = \frac{\rho u_0 d_0}{\eta}$, where γ is the fluid surface tension, ρ its density and η its viscosity, varies from 320 to 810, respectively from 8,400 to 19,000.

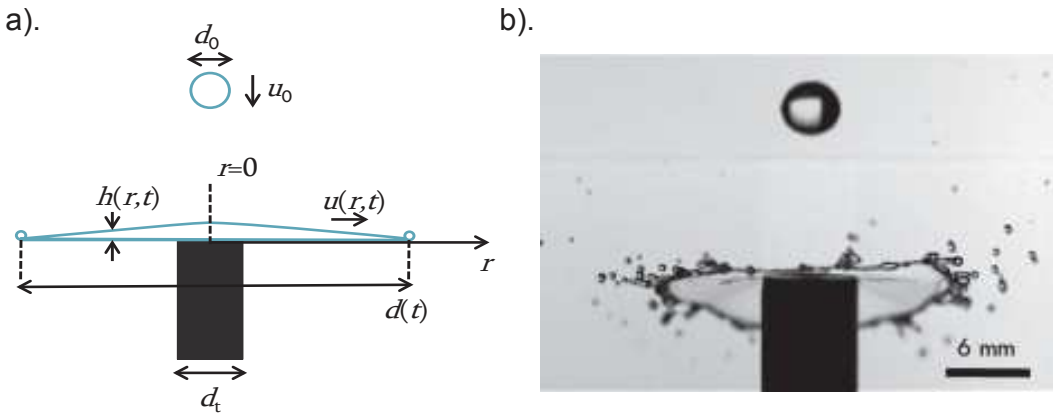

Figure 4.6: a). Sketch of the tear impact experimental set-up. The experimental parameters are defined on the sketch. b). Side view of the experimental set-up, showing a tear falling on the target and the resulting liquid sheet.

The target is an aluminum cylinder coated on the top with a glass lamella. The glass is rendered hydrophilic thanks to a plasma treatment with a plasma gun (Corona Surface Treater, Electro-Technic products), which suppresses the dewetting on the surface [Marengo 2011, Dhiman 2010]. The plasma gun is used to clean the glass surface. The principle is the following: an electrode with a high potential is used to ionize surrounding air and create a plasma region. Ultraviolet light and oxygen species created by the plasma are very effective to remove organic components at the glass surface. In Figure 4.7 is illustrated the effect of the hydrophilic treatment. In Figure 4.7(a) is presented a liquid sheet formed on a un-treated target. In that case, we observe dewetting on the surface of the target, in contrast to the case where the target surface is treated (Figure 4.7(b)).

A thin aluminum coaxial cylinder is added around the target as suggested in the literature by [Villermaux 2011] in order to keep the sheet ejection angle to 90° (with respect to the target axis) and thus obtain a horizontal and flat sheet (see Figure 4.8 for the effect of the coaxial cylinder on the flatness of the sheet). A vertical tube which runs from the needle to slightly above the target is mounted to avoid the effect of draughts and ensure a centered impact on the target. The target is mounted on a transparent plexiglass floor lighted from below by a high-luminosity backlight (Phlox High Bright LED Backlights). The tear impact is recorded from the top with a weak angle using a Phantom V7.3 camera operating at 9,708 pictures per second and with a resolution of 576 pixels × 552 pixels. Side views are also recorded to check the flatness of the liquid sheet (Figure 4.8(b)) and to measure the impact velocity.

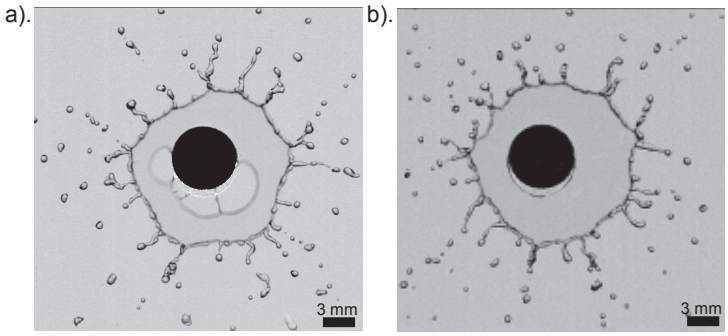

Figure 4.7: Effect of the hydrophilic treatment of the glass target surface on the formation of liquid sheet. a). The glass surface of the target is not treated, dewetting is observed on the surface. b). The glass surface of the target is treated with a plasma gun to render it hydrophilic; this treatment suppresses the dewetting on the target.

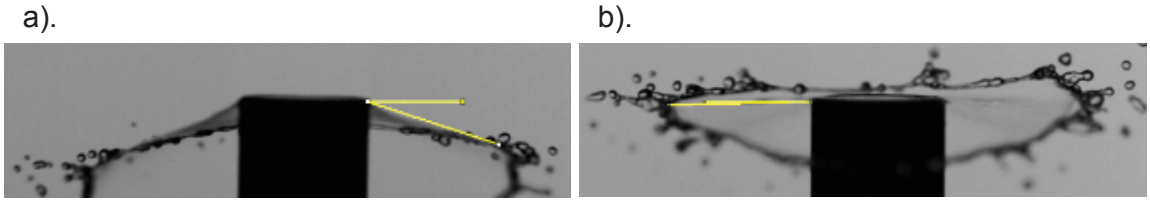

Figure 4.8: Effect of the coaxial cylinder on the flatness of the sheet. a). Without the coaxial cylinder, the sheet formed an angle with the horizontal axis as highlighted by the yellow lines. b). With the coaxial cylinder, the sheet is flat and parallel to the horizontal axis. The target diameter is equal to 6 mm.

4.2.2 Sheet thickness measurement method

Measuring liquid film thicknesses at the micrometer scale range is a problem of great interest for various industrial and academic applications. Different thickness measurement techniques have been developed over the last century. Tibirica et al. [Tibiriçá 2010] presented a comprehensive literature review of the experimental techniques developed to measure liquid film thicknesses ranging from micrometres to centimetres. Available methods can be classified based on the physical principles, acoustic, electrical or optical, involved in the measurements. In particular, numerous optical methods have been developed, including interferometry methods [Ohyama 1988], fluorescence intensity methods [Makarytchev 2001], methods based on imaging a diffusive liquid [Berhanu 2013] or light absorption methods [Lilleleht 1961, Kim 2005]. Mouza et al.[Mouza 2000] compared two methods to measure liquid film thickness, a photometric technique based on the absorption of light passing through a layer of dyed liquid and a conductance measurement and found a very good agreement between these two methods. The authors also pointed out the advantages of optical methods based on light absorption over conductance method.

Optical methods are non-intrusive, suitable for non-conducting fluids and can display sensitivity to thin films and high spatial resolution.

Here, we present a method to determine the thickness of liquid sheets, which is based on the light absorption by a dyed liquid. The method that we have developed relies on the utilization of a dye solution to visualize the variation of the thickness field $h(r,t)$, with t the time elapsed since the impact and r the radial position. Note that a similar method was recently used by Lastakowski et al. [Lastakowski 2014] to investigate the thickness field of a tear impacting onto solid substrates. We have chosen a dye (erioglaucine disodium salt, purchased from Sigma-Aldrich) that exhibits a very high molar extinction coefficient ($\varepsilon > 80,000$ $\mathrm{M^{-1}cm^{-1}}$ for wavelength in the range $(627-637)$ nm). The erioglaucine salt is here dissolved in milliQ water at a concentration of 2.5 g/L and the solution filtered using membrane with pore size 5 μm. This concentration corresponds to the minimum dye concentration required to obtain a sufficient contrast between the air and the liquid sheet and hence to accurately quantify thickness variations. We have checked that the dye does not influence the viscosity and the surface tension of the solution. For erioglaucine solution at 2.5 g/L in water, we measure a viscosity of 1.0 mPa.s and a surface tension of 71 mN/m at 20°C, i.e. values comparable to the ones obtained for pure water. We have also checked that the addition of dye at this concentration has no effect on the maximal extension of the sheet (see Figure 4.9 for the time evolution of the sheet maximum diameter for pure water and dye solution).

The principle of the measurement is to correlate the grey level of each pixel of the image of a dyed liquid sheet to the local thickness of the liquid sheet. The key point for the success of this method is a very meticulous calibration performed using liquid films of precise known thicknesses. Liquid films of controlled thickness from 6 to 450 μm are obtained by introducing various controlled volumes of liquid between two microscope coverslips ($22 \times 22\,\mathrm{mm^2}$) with a micropipette as shown in Figure 4.10(a,b). The uniform thickness of the liquid films (h_0) is determined from the volume of liquid (V_{liq}) and the microscope coverslip area (A_{cov}): $h_0 = \frac{V_{\mathrm{liq}}}{A_{\mathrm{cov}}}$. Images of the liquid between the two coverslips are recorded in experimental configurations comparable with that used for the liquid sheet imaging. The contribution of the empty cell (the two microscope coverslips) is taken into account by dividing the grey level of the image of a dyed liquid film in the cell by the grey level of the image of the empty cell. Hence, one defines a normalized intensity, $I_{\mathrm{norm}} = I/I_0$, where I is the intensity measured for the cell filled with liquid and I_0 is the intensity measured for an empty cell. I and I_0 are intensities spatially averaged over all pixels of the cell made with the two coverslips. By construction I_{norm} is equal to one for a film thickness equal to zero. Moreover, $I_{\mathrm{norm}} = I/I_0$ tends to zero for large thicknesses. The calibration curve, where the film thickness, h, is plotted as a function of the normalized intensity, I_{norm}, is shown in Figure 4.11(a), and shows an exponential decrease of h with I_{norm}, over the whole range of thicknesses investigated $(6-450)\,\mu$m. The calibration curve has been obtained by at least three repetitive measurements for each film thickness. The envelope curves represented in Figure 4.11(a) corresponds to

the standard deviation of the measurements. The different measurements for a given thickness were obtained by slightly modifying the incident light intensity to ensure that a slight change in the illumination conditions does not notably modify the numerical values for the computed normalized intensity. We note that the calibration curve differs from the exponential decrease of the intensity with the thickness predicted by the Beer-Lambert law presumably because of the non-monochromatic light source [Wentworfh 1966]. Sequences of images of the tear impacting the target are recorded in the same conditions (illumination, camera settings) as those used for the calibration.

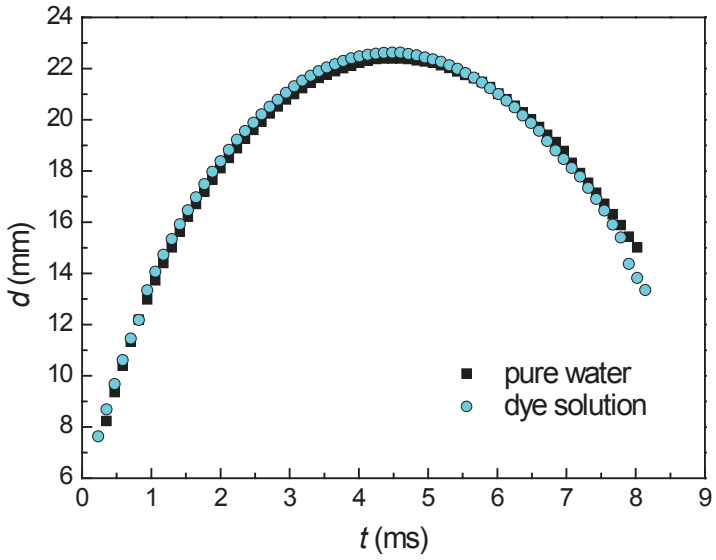

Figure 4.9: Time evolution of the sheet diameter for pure water and solution of erioglaucine salt at 2.5 g/L in water.

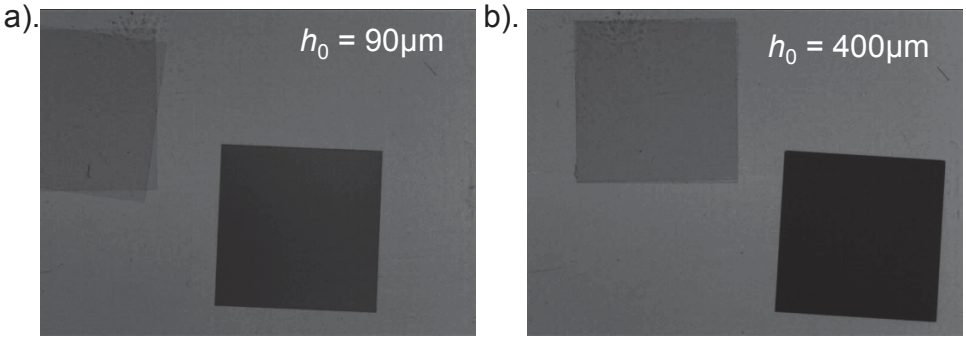

Figure 4.10: Liquid films of controlled thickness a). h_0=90 μm and b). h_0=400 μm obtained by introducing various controlled volumes of liquid between two microscope coverslips ($22 \times 22\,\mathrm{mm}^2$). On the left top angle the empty cell is visible.

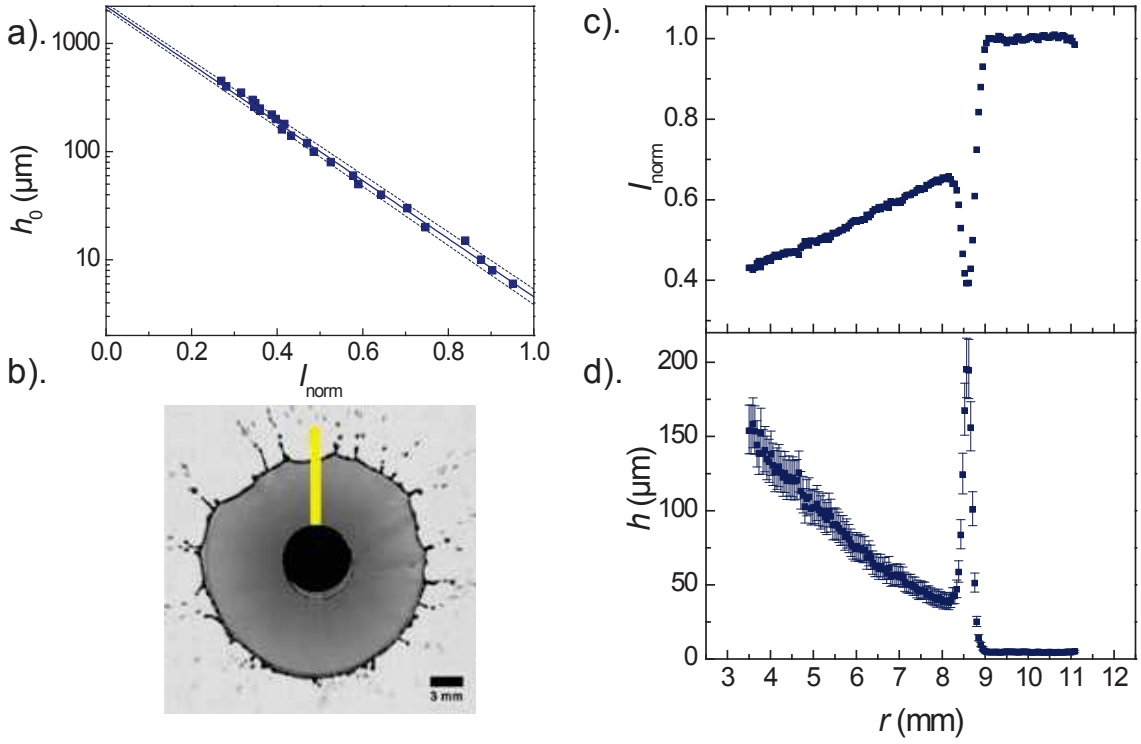

Figure 4.11: Calibration process a). Calibration curve, film thickness, h_0, as a function of the normalized intensity. The full line is the best fit of the experimental data with the functional form $h_0 = L\exp(-BI)$, where $L = 2,207\mu$m and $B = 6.184$ are fitting parameters, and the dashed lines are the two envelope curves deduced from the standard deviation of the fit parameters. b). Image of an expanding dyed liquid sheet, at time $t = 2.70$ ms. The tear diameter is $d_0 = 3.7$ mm and the impact velocity is $u_0 = 4.0$ m/s. c). Normalized intensity profile as a function of the radial distance from the target center as measured along the line shown in (b). d). Thickness profile as deduced from the calibration curve shown in (a) along the line shown in (b). Error bars are deduced from the ones of the calibration curve a).

4.2.3 Image analysis

The software ImageJ is used for the image analysis. First to determine the thickness, we measure for each pixel of polar coordinates (r, θ) the normalized intensity $I_{\text{norm}}(r, \theta)$ as the ratio between the measured intensity for a given image of the liquid sheet $I(r, \theta)$ and the measured intensity for an image taken just before the tear impact. The liquid sheet thickness $h(r, \theta)$ is then evaluated thanks to the calibration curve (Figure 4.11(a)). The procedure is illustrated in Figure 4.11. Figure 4.11(b) shows a typical image of a dyed liquid sheet. The normalized intensity profile along the radial line shown in Figure 4.11(b) (the origin of the radial distance is taken at the centre of the target) is plotted in Figure 4.11(c). The profile displays a non-monotonic evolution, with a

continuous increase with r, which is followed by a sharp drop related to the thicker rim, before reaching a constant intensity equal to 1 corresponding to the exterior of the liquid sheet. The related thickness profile has been calculated using the calibration curve (Figure 4.11(a)) and is shown in Figure 4.11(d). Here the error bars are deduced from those of the calibration curve. The peak in the thickness visible in Figure 4.11(d) corresponds to the thicker rim.

In the following, unless noted, the thickness profiles are averaged over all azimuthal angles, θ, to obtain a thickness that only depends on the radial distance, r, and on time, t: $h(r,t) =< h(r,\theta,t) >_\theta$. However, a careful observation of Figure 4.11(b) reveals the presence of small fluctuations of the thickness of the liquid sheet. These azimuthal thickness modulations will be discussed in section 4.3.7. Moreover, we systematically exclude the rim from our data analysis because of the irregularities of the contour of the sheet.

Second, to quantify the time evolution of the size of the sheet, we locate the rim by binary thresholding the images using ImageJ. This allows one to determine the sheet contours and measure the area of the sheet (A). An apparent diameter for the sheet, d, is simply deduced from the area of the sheet according to $d = \sqrt{\frac{4A}{\pi}}$.

Third, in order to determine the ejection volume rate at the target periphery, the time evolution of volume of liquid remaining on the target after the impact of the tear is measured thanks to side-view images of the tear. As illustrated in Figure 4.12(a,b), for each image we measure the apparent radius $R(z)$ of the liquid tear as a function of the z-axis from $z = 0$ corresponding to the target and $z_{\max}$ corresponding to the top of the tear. Thanks to the axisymmetry of the tear crushing on the target, the liquid volume V remaining on the target at each time t is computed using $V = \int_0^{z_{\max}} \pi R(z)^2 \, \mathrm{d}z$.

Finally, azimuthal profile along a circle centered on the centre of the target are derived using a MATLAB program (courtesy of Adrian-Marie Philippe).

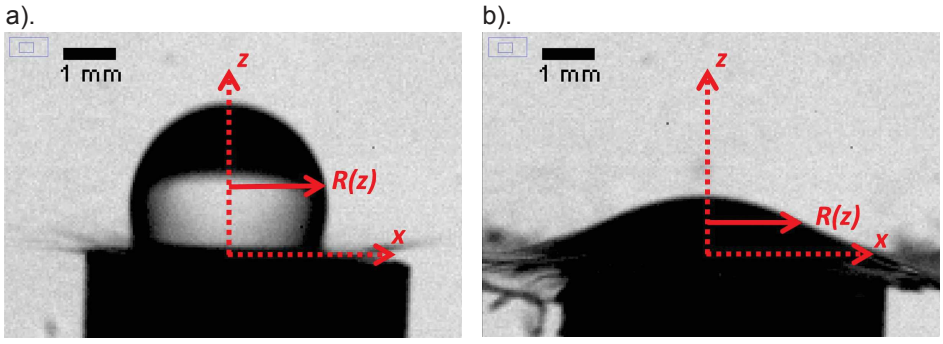

Figure 4.12: Side views of a liquid tear impacting a target, at time $t = 0.10$ ms (a) and $t = 0.79$ ms (b).

4.3 Water-based liquid sheet

In this section, we describe the formation and destabilization of a pure water liquid sheet. We first illustrate the sheet destabilization mechanism, then we study the time evolution of the sheet maximum diameter and finally we describe the sheet thickness field by comparing our experimental results to theoretical predictions and simulations.

4.3.1 Formation and destabilization of the sheet

In Figure 4.13 is shown the formation and destabilization of a pure water liquid sheet. The origin of time is taken at the moment of the tear impact. Upon impact, the tear flattens into a liquid sheet radially expanding in air (Figure 4.13(a)). The sheet consists of a free liquid film surrounded by a thicker rim. The sheet expands with time (Figure 4.13(b)) until it reaches a maximum diameter (Figure 4.13(c)) and then recedes due to the effect of the surface tension (Figures 4.13(d) to (f)). The maximum diameter of the sheet, $d_{\max}$, depends on u_0, the impact velocity, and on d_0, the falling tear diameter [Rozhkov 2002, Villermaux 2011]. Simultaneously to the sheet expansion and retraction, the rim corrugates forming radial ligaments, which are subsequently destabilized into drops as visible in Figure 4.13(a) to (f).

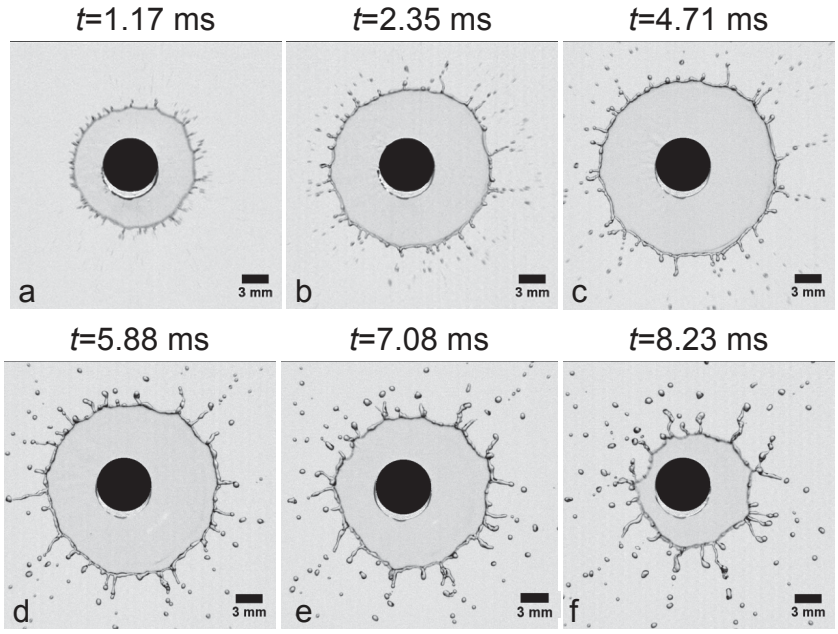

Figure 4.13: Sequence of events of the formation and destabilization of a milliQ water sheet. The tear diameter is $d_0 = 3.7$ mm, the impact velocity is $u_0 = 4.0$ m/s, and the target diameter is 6 mm.

4.3.2 Maximal extension of the sheet

4.3.2.1 Results for a given set of experimental parameters

In a first set of experiments, we fix the size of the tear and the impact velocity. We measure a tear diameter $d_0 = 3.7$ mm and an impact velocity $u_0 = 4.0$ m/s, yielding a Weber number $We = 810$. Representative pictures of the dyed liquid sheet upon its expansion and retraction are shown in Figure 4.14. Note that, from the very beginning of the sheet expansion, small droplets are expelled, recalling the microsplash studied by [Thoroddsen 2012] upon tear impacts. The time evolution of the normalized sheet diameter, d/d_0 (right axis), shows a non-monotonic evolution, reflecting the expansion and retraction regimes. In the following, we take as the origin of time the moment at which the tear impacts the target. In practice, the time t=0 is defined as the time when small droplets are expelled from the target, as determined from a top view of the experiment, as shown in Figure 4.14(a). On the left axis of Figure 4.14(b) the sheet diameter, d, is normalized by the target diameter, d_t. We find that at $t = 0$ the sheet diameter is closed to the target diameter, ensuring that our determination of the origin of time is reasonable. On the right axis, d is normalized by the tear diameter, d_0. In Figure 4.14(b), we show data both as a function of the natural time, t, and as a function of a normalized time $T = t/\tau$, where $\tau = \sqrt{\frac{\rho d_0^3}{6\gamma}}$ is proportional to the capillary time. Here ρ =1,000 kg/m^3 the density of the dyed water, and $\gamma = 71$ mN/m is the air-liquid surface tension. The maximal expansion occurs at a time $t = 4.57$ ms ($T = 0.42$) and is equal to 22.62 mm ($d/d_0 = 6.11$). These numbers are consistent with the literature, although the exact shape cannot be fitted satisfyingly with the analytical model developed by [Villermaux 2011].

In Figure 4.15 is shown the best fit of the time evolution of the sheet diameter with the analytical expression predicted by Villermaux et al. : $\frac{d(t)}{d_0} = 1 + BT(1-T)^2$ with B a free fitting parameter that should be equal to $\sqrt{\frac{2}{3}}\sqrt{We}$ following the theoretical model (Equation 4.7). We note that the theoretical model does not fit quantitatively our experimental data. It underestimates the time to reach the sheet maximum extension and overestimates the sheet maximal extension. The time at which the sheet reaches its maximum expansion is not the one predicted by the model ($T = 1/3$) [Villermaux 2011], nor is this time in agreement with the one ($\frac{4d_0}{u_0} = 3.7$ ms in our case) found by [Rozhkov 2004]. However, it should be highlighted here that we are not quite in the same experimental conditions as those considered by the model of Villermaux et al. [Villermaux 2011] and Rozhkov et al. [Rozhkov 2002]. In these models, the ratios between the tear diameter and the target diameter were closer to 1 ([Villermaux 2011] $d_0 = d_t$; [Rozhkov 2002] $d_0/d_t = 1$ and $d_0/d_t = 0.72$). What is more, in these studies the surface of the targets were not rendered hydrophilic. These different parameters could explain the discrepancies with the theoretical predictions observed for the evolution of the sheet maximum diameter. We will investigate these possibilities by modifying the surface treatment of the target and the ratio between the tear diameter and the target diameter in the last parts of this

section.

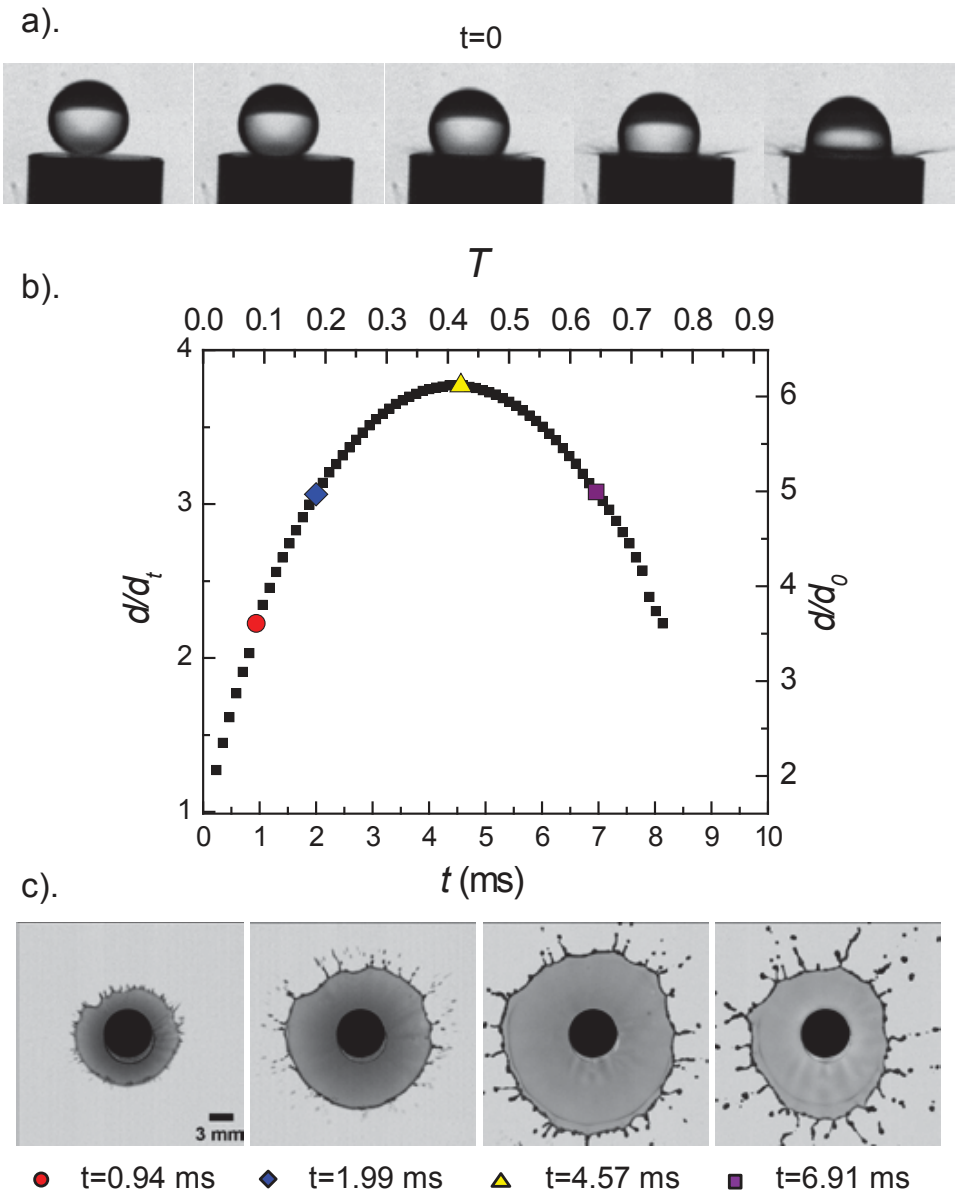

Figure 4.14: a). Sequence of events of the tear just before and after the impact. The time delay between consecutive images is 0.1 ms. The time $t = 0$ corresponds to the impact time of the tear on the target, i.e. the third image in the row. b). Time evolution of the normalized sheet diameter. The instants corresponding to the four images shown in (c) are highlighted. c). Sequence of events of the liquid sheet after tear impact. The tear diameter is $d_0 = 3.7$ mm, the impact velocity is $u_0 = 4.0$ m/s, and the target diameter is 6 mm.

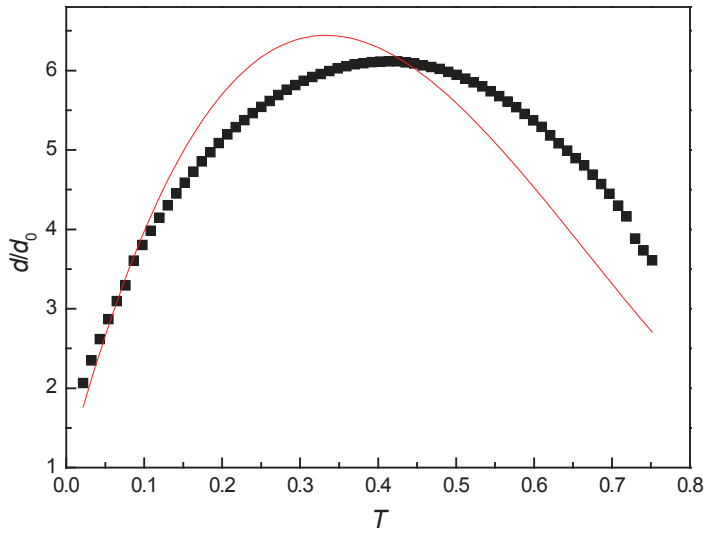

Figure 4.15: Time evolution of the normalized sheet diameter with the best fit of the form: $\frac{d}{d_0} = 1 + BT(1-T)^2$ with B a fitting parameter equals to 36.73, R^2=0.66.

4.3.2.2 Results at different Weber numbers

We perform the same type of measurements and analysis as detailed above, for different Weber numbers where the impact velocity and the volume of the tear are varied. Five different experimental conditions, for which the Weber numbers varies between 320 and 810, are performed (Table 4.1).

d_0 (mm)	u_0 (m/s)	We
3.0	2.8	320
3.7	2.8	410
4.8	2.8	540
3.0	4.0	620
3.7	4.0	810

Table 4.1: Impact parameters of the performed experiments. The values of the tear diameter, d_0, the impact velocity, u_0, and the Weber number are reported.

In all experiments, we vary the diameter of the target to keep constant (0.6) the ratio between the diameter of the tear and that of the target. Figure 4.16 shows the time evolution of the maximal extension of the liquid sheet for the different experiments. The maximum extension of the sheet occurs at a time that depends on the tear diameter and not on the impact velocity. In Figure 4.17 are represented the same data but as a function of the normalized time, T. We find that the maximum extension occurs roughly at the same normalized time $T_{\max} = 0.40 \pm 0.01$. Here the standard deviation results from the statistics over the five experimental configurations. We measure that the sheet

expands more as We increases, from $d_{\max}/d_0 = 4.1$ to $d_{\max}/d_0 = 6.1$. Although on a very restricted range, we find that our data are compatible with a maximum expansion scaling with $(We)^{0.5}$, as observed and predicted theoretically for liquid sheets expanding in air [Rozhkov 2004, Villermaux 2011] but also on solid surfaces [Eggers 2010, Bennett 1993, Marengo 2011]. A fit of the data using the functional form $d_{\max}/d_0 = \sqrt{We/K}$ gives $K = 19$, in excellent agreement with the values ($K = 20$) given in [Rozhkov 2004] for similar experimental conditions.

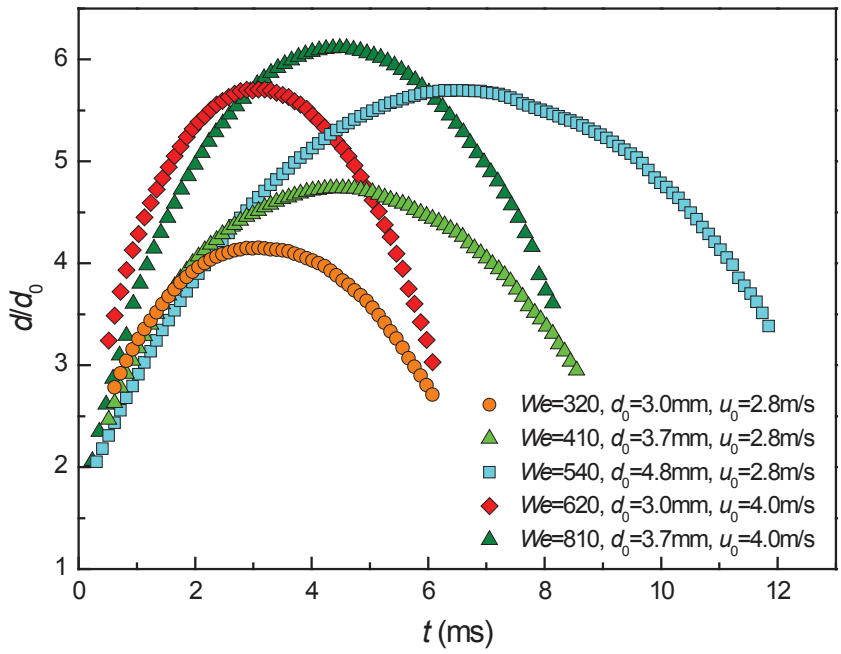

Figure 4.16: Time evolution of the sheet diameter for several experiments at different We numbers as indicated in the legend.

4.3.2.3 Influence of the ratio between the tear diameter and the target diameter

We modify the ratio between the tear diameter and the target diameter to investigate its influence on the dynamics of the liquid sheet and to determine if this parameter can be at the origin of the discrepancies observed between our experimental measurements and the theoretical predictions [Villermaux 2011]. This ratio was set to 0.6 in the experiments shown previously in sections 4.3.2.1 and 4.3.2.2. It is varied between 0.5 and 1 here (Table 4.2). For this set of experiments, the glass surface of the target was not treated.

For these different experiments we measure the maximum diameter, $d_{\max}$, of the sheet and the normalized time to reach this maximum diameter, $T_{\max}$. In Figure 4.18 are plotted the evolutions of $d_{\max}/d_0$ and $T_{\max}$ as a function of the ratio d_0/d_t. We observe that the normalized sheet maximum diameter, $d_{\max}/d_0$, does not depend (for a given set of impact

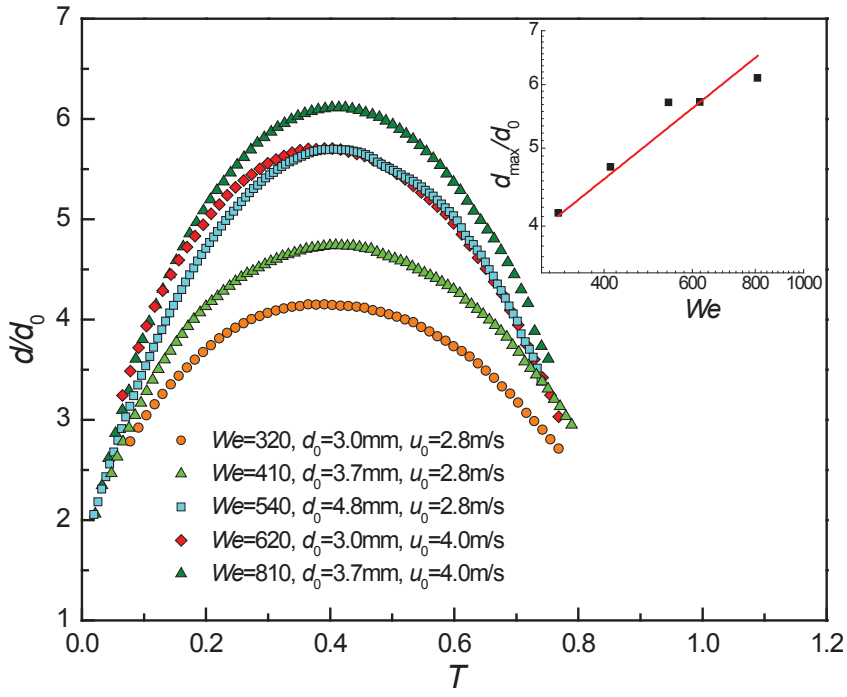

Figure 4.17: Normalized sheet diameter as a function of the normalized time, T, for several experiments at different We numbers as indicated in the legend. (Inset) Normalized maximal expansion plotted as a function of We. Symbols are experimental data and the line is a power law fit with an exponent of 0.5: $d_{\max}/d_0 = \sqrt{We/19}$.

parameters) on the ratio between the tear diameter and the target diameter for $d_0/d_t<1$. The values of $d_{\max}/d_0$ for the two different set of impact parameters are really closed due to very similar values of the Weber number (810 and 540). On the contrary, $T_{\max}$ depends strongly on the ratio d_0/d_t : when d_0/d_t increases the time to reach the maximum sheet diameter is longer. When d_0/d_t is closed to 1, i. e. in the condition of the model developed by Villermaux et al. and Rozhkov et al. [Villermaux 2011, Rozhkov 2004], $T_{\max}$ is equal to 0.53 different from the value of 0.33 predicted by the model. The discrepancy observed between our experimental data and the model developed by Villermaux et al. [Villermaux 2011] does not seem to arise from the difference of diameter between the tear and the target. In conclusion, the dissipation on the target surface (that presumably changes when the tear diameter over target diameter varies) is also a crucial parameter for the dynamics of the expansion of the liquid sheet.

4.3.2.4 Influence of the surface target treatment

To investigate the influence of the glass surface treatment of the target on the dynamics of the liquid sheet, we perform tear impact experiments in different surface treatment conditions, for a given set of impact parameters (u_0=4 m/s, d_0=3.7 mm and d_t=6 mm).

d_0 (mm)	d_t (mm)	d_0/d_t	u_0 (m/s)	We
3.7	5	0.7	4.0	810
3.7	8	0.5	4.0	810
4.8	5	1	2.8	540
4.8	6	0.8	2.8	540
4.8	8	0.6	2.8	540

Table 4.2: Impact parameters of the performed experiments. The values of the tear diameter, d_0, the target diameter, d_t, the ratio between these two diameters, d_0/d_t, the impact velocity, u_0, and the Weber number are reported.

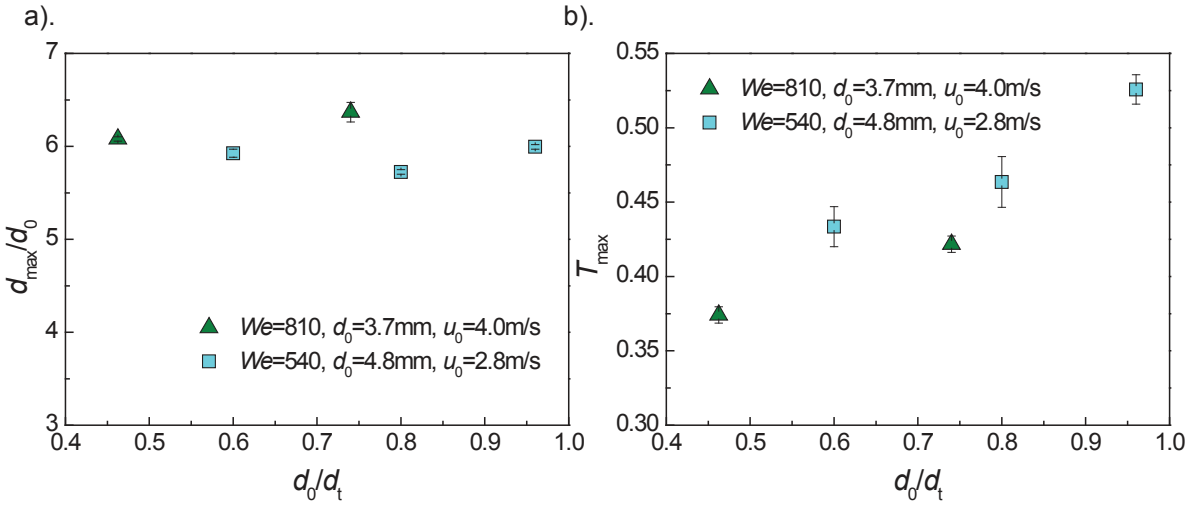

Figure 4.18: a). Evolution of the normalized maximum diameter of the sheet, $d_{\max}/d_0$, as a function of the ratio between the tear diameter and the target diameter, d_0/d_t, for different impact parameters as indicated in the legend. b). Evolution of the normalized time to reach the maximum diameter of the sheet, $T_{\max}$, as a function of the ratio between the tear diameter and the target diameter, d_0/d_t, for different impact parameters as indicated in the legend.

For the first set of experiments, the glass surface was rendered hydrophilic thanks to a plasma treatment (experiments shown in section 4.3.2.1). As shown in Figure 4.19(a), a water drop on the hydrophilic glass surface of the target forms a contact angle equal to 41.9°. In a second set of experiments, the glass surface was rendered hydrophobic by a silane treatment. Figure 4.19(b) we observe that a water drop on the hydrophobic treated surface of the target forms a contact angle close to 90° (measured value: 89.4°).

In Figure 4.19 we compare the evolution of the sheet maximum diameters normalized by the tear diameter as a function of the normalized time T for the two surface treatment conditions. We find that the hydrophobicity of the glass surface entails a decrease of the sheet maximum diameter (relative change is 12%). The time to reach this maximum is

shorter than in the case of a hydrophilic surface treatment (relative change 23%). For the hydrophobic treated surface target, the maximum diameter is obtained for T =0.35, i.e. a value really close to the one expected from the theoretical model developed by Villermaux et al. [Villermaux 2011] T=1/3. Hence, the discrepancy observed between our experimental results with hydrophilic treated glass surface target and the model developed by Villermaux et al. [Villermaux 2011] could be explained by the surface treatment of the surface of the target. In the hydrophobic case, the contribution of the target/tear contact area to the surface energy of the sheet is larger than in the hydrophilic case.

From these experimental data, it is clear that the surface treatment of the glass lamella at the top of the target has a significant influence on the expansion dynamics of the liquid sheet. In the following, we decide to systematically render hydrophilic the glass surface of the target to suppress the dewetting (see Figure 4.7).

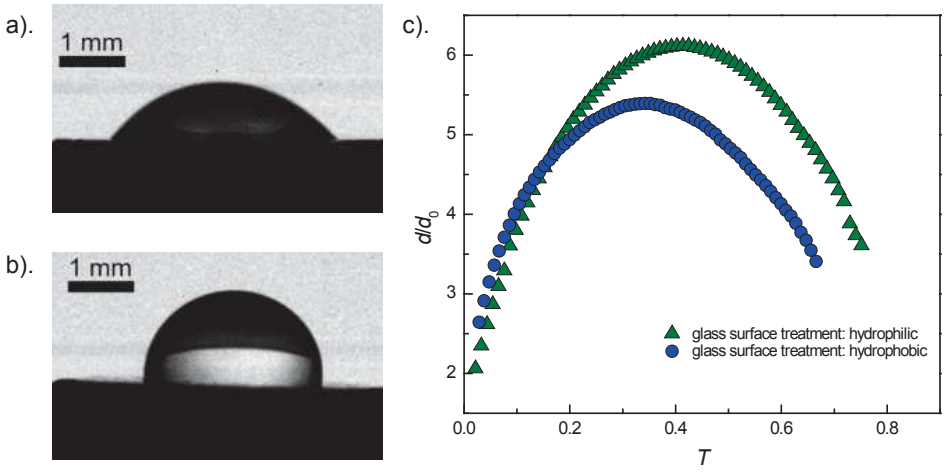

Figure 4.19: a) and b). A water drop on the glass surface of the target rendered hydrophilic (a) and hydrophobic (b). Time evolution of the normalized sheet diameter impacting on a target surface with a hydrophilic treatment and a hydrophobic treatment as indicated in the legend.

4.3.3 Time- and space-resolved measurements of the sheet thickness

In a first set of experiments, we fix the size of the tear and the impact velocity. We measure a tear diameter $d_0 = 3.7$ mm and an impact velocity $u_0 = 4.0$ m/s, yielding a Weber number $We = 810$. We measure the radial evolution of the sheet thickness, h, at different times, t, as a function of the radial distance, r, with the origin taken at the centre of the target. Both actual values and normalized data, $H = h/d_0$ and $R = r/d_0$, are shown in Figure 4.20. At short times, the liquid sheet is rather thick and its thickness

decays very rapidly with the radial distance. The radial evolution becomes smoother as time evolves. At the maximum expansion ($t = 4.57$ ms, $T = 0.42$), the thickness is almost uniform: it increases from 35 μm to 39 μm for short distances and then decreases down to 26 μm. In the retraction regime, the thickness is measured to vary non-monotonically with the radial distance, but is always small. We will not consider the retraction regime in the following due to the absence of theoretical models and to the very restricted range of variation of the thickness in this regime. We will therefore only consider in the following data taken for $t < 4.57$ ms ($T < 0.42$). In the inset of Figure 4.20, representative values plotted on a log/log scale indicate two scaling regimes at short and long times and a cross-over between these two regimes at intermediate time.

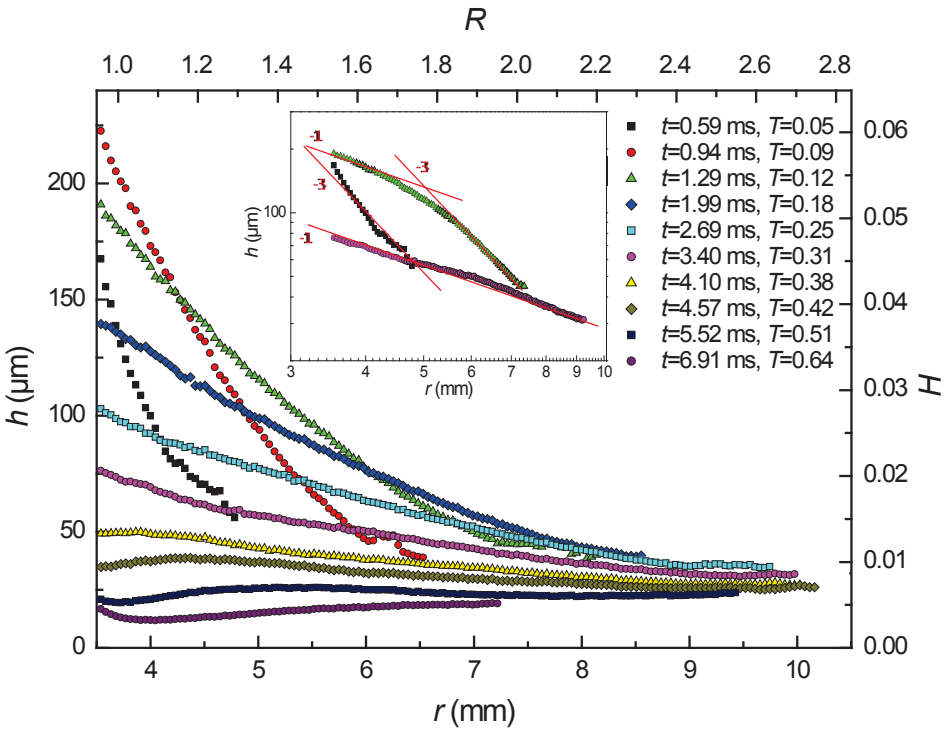

Figure 4.20: Thickness of the liquid sheet as a function of radial positions. Actual and normalized data are plotted at different times as indicated in the legend. The tear diameter is $d_0 = 3.7$ mm and the impact velocity is $u_0 = 4.0$ m/s. (Inset) Representative data in a log/log scale to highlight the two asymptotic scaling regimes.

It is more instructive to plot the time- and space-resolved data of the thickness as a function of time for different radial distances. This is shown in Figure 4.21(a) for both natural and normalized data. For all radial positions, the thickness of the sheet exhibits a non-monotonic evolution with time with the presence of a maximum. We find that the maximum thickness occurs at longer times for larger radial positions. Representative data in a log/log scale are shown in the inset of Figure 4.21(a) and indicate two asymptotic regimes. The inset of Figure 4.21(b) shows $r_{\mathrm{h_{max}}}$ versus $t_{\mathrm{h_{max}}}$, where $t_{\mathrm{h_{max}}}$ is the time at

which the thickness is maximum at the radial position $r_{h_{max}}$. We find a linear variation, demonstrating a constant velocity. Best fit of the data yields a speed $v_{h_{max}} = 3.2$ m/s for the displacement of the maximum thickness. Interestingly, all of the data acquired at different radial positions collapse on a single master curve once the thickness and the time are normalized by their values at the maximum thickness (Figure 4.21(b)), which highlights a universal shape for the evolution of the thickness with time and radial distance. In the following, we evaluate how the thickness scales with time and radial distances, both for the short-time regime, where the thickness increases with time, and for the long-time regime, where h decreases with t.

4.3.4 Scaling and comparison with theoretical predictions

We first consider the short-time regime where $t < t_{h_{max}}$. In this regime, the thickness varies over almost one order of magnitude, ranging from 36 μm to 217 μm. We find that all data acquired at different radial positions and different times can be collapsed onto a single mastercurve if the thickness is plotted as a function of t/r^3 (Figure 4.22(a)). Moreover, a fit of the master curve (dashed line) shows that $h \propto t/r^3$ in this regime as predicted by Rozhkov et al. [Rozhkov 2004]: $h(r,t) = \alpha {d_0}^3 u_0 \frac{t}{r^3}$ (Equation 4.1). A fit of the experimental data yields $\alpha = 0.061$. This value is twice as large as the value ($\alpha \approx 0.038$) derived by Rozhkov et al. [Rozhkov 2004] for roughly equivalent experimental conditions. Note that in [Rozhkov 2004] α could be evaluated based on the observation of Mach-Taylor rupture waves generated by cutting radially the liquid sheet with a very thin obstacle, but not from thickness measurements. Hence, at short times, experimental data seem well accounted for by the model developed by Rozhkov et al. [Rozhkov 2004]. This model is predicted to be valid at short times, up to three times the typical collision time $\tau_{coll} = d_0/u_0 = 0.93$ ms. Our data fall safely within this limit as, independently of the radial position, the maximum thickness occurs at times no longer than 2.2 ms (inset of Figure 4.21 (b)).

One key hypothesis of this model is that a point source, i.e. the impacting tear, feeds the sheet at a constant volume rate. We directly check this assumption thanks to side-view images of the tear impacting the target and feeding the liquid sheet (Figure 4.12 (a,b)). We evaluate the time evolution of the volume of the liquid tear still available on the target, assuming that the tear remains axisymmetric at all times. The volume V of the liquid is measured to decrease linearly with time yielding a constant volume rate (Figure 4.23). Hence, the assumption of a constant volume rate is checked. We measure $Q = -\mathrm{d}V/\mathrm{d}t = 12.1$ mL/s, which is in relatively good agreement with the value ($Q \simeq 6$ mL/s) found indirectly by [Rozhkov 2004].

On the other hand, in the late stage of the expansion regime, $t > t_{h_{max}}$, the thickness varies between 26 μm and 191 μm. We find that all data acquired at different radial positions can be collapsed onto a single master curve if the thickness is plotted as a function of $1/rt$ (Figure 4.22(b)). We find that $h \propto 1/rt$, as predicted in [Villermaux 2011]:

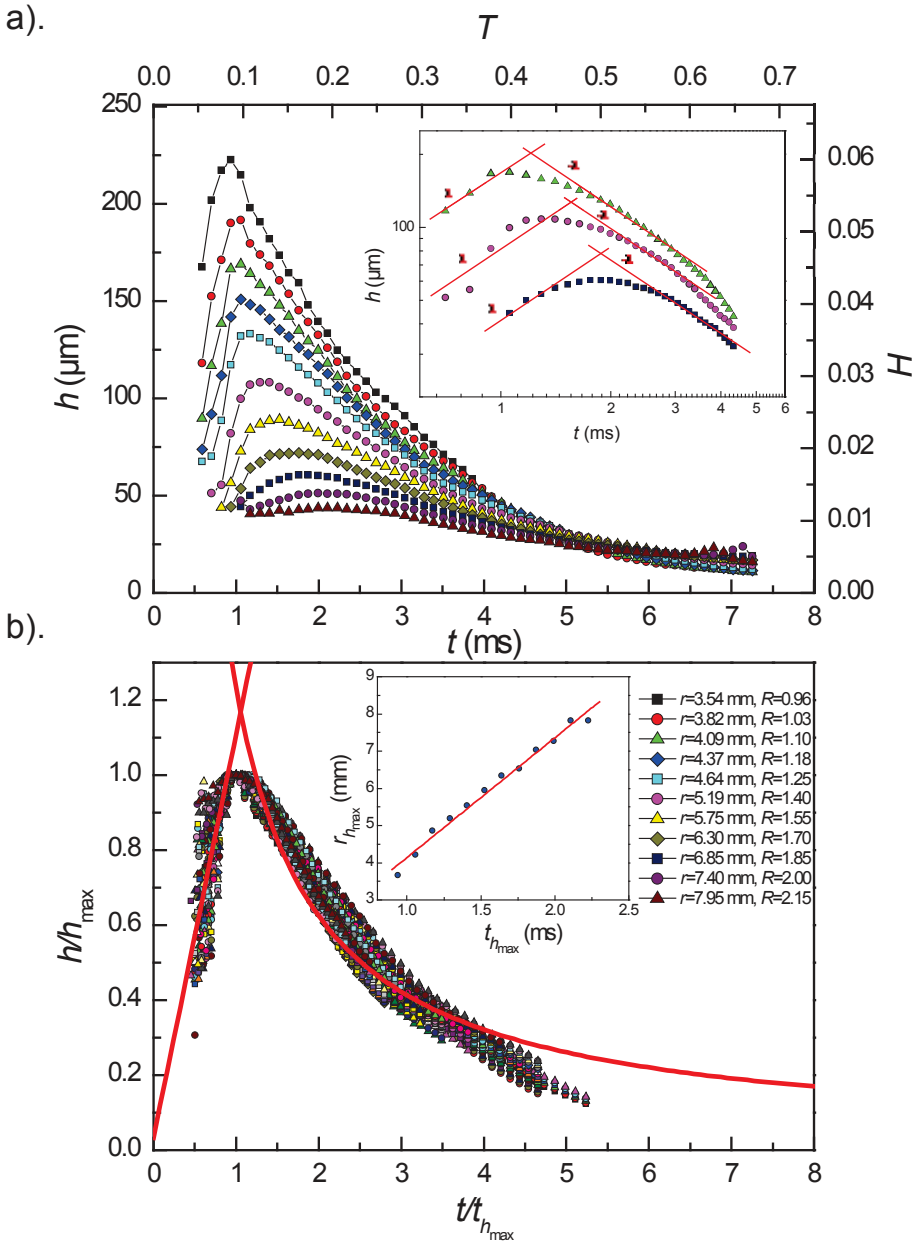

Figure 4.21: a). Time evolution of the thickness of a liquid sheet. Actual and normalized data are plotted for different radial positions, as indicated in the legend of (b). (Inset) Representative data in a log/log scale to highlight the two asymptotic scaling regimes. b). Same data as those shown in (a), but normalized in the x axis by the time at which the thickness is maximum, $t_{\mathrm{h_{max}}}$, and in the y axis by the maximum thickness, h_{max}. The lines correspond to the two asymptotic scaling regimes (as deduced from Figure 4.22). Only data corresponding to the expansion regime are shown in (b). The tear diameter is $d_0 = 3.7$ mm and the impact velocity is $u_0 = 4.0$ m/s. (Inset) Variation of the radial position of the maximum thickness of the sheet as a function of time. The symbols are the experimental data and the line is the best linear fit of the data, yielding a velocity $r_{\mathrm{h_{max}}}/t_{\mathrm{h_{max}}} = 3.2$ m/s.

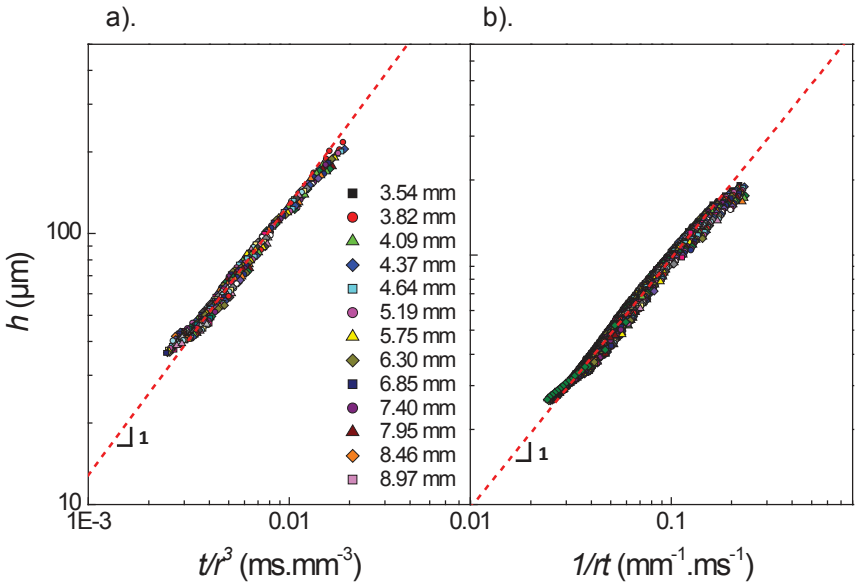

Figure 4.22: Same data as in Figure 4.21 but plotted as a function of t/r^3 (a) and $1/rt$ (b) where r is the radial distance and t is the time elapsed from the impact of the tear. The data corresponding to $t < t_{\mathrm{h_{max}}}$ are shown in (a), and those corresponding to $t > t_{\mathrm{h_{max}}}$ are shown in (b). Same symbols as in Figure 4.21. The dashed lines are power law fits of the experimental data with a slope of 1.

$h(r,t) = \beta \frac{\pi d_0^3}{6u_0} \frac{1}{rt}$ (Equation 4.5). A fit of the experimental data provides an estimate of the prefactor $\beta = 0.142$. Note that this value is in very good agreement with the predicted value ($\beta = \frac{1}{2\pi} = 0.159$).

Combining our findings for the scaling with time and position of the sheet thickness for the two stages of the expansion regime, one can provide a prediction for the maximum thickness position. By equalling the two functional forms found for the thickness, Equation 4.1 and Equation 4.5, one finds

$$v_{\mathrm{h_{max}}} = r_{\mathrm{h_{max}}}/t_{\mathrm{h_{max}}} = \sqrt{\frac{6\alpha}{\pi\beta}}\, u_0 \tag{4.12}$$

First, Equation 4.12 shows that the position of the maximum thickness moves at a constant velocity with time, as found experimentally. Moreover, it predicts that the velocity is controlled by the impact velocity u_0. The proportionality constant between $v_{\mathrm{h_{max}}}$ and u_0 is $\sqrt{\frac{6\alpha}{\pi\beta}} = 0.906$. Hence, one predicts $v_{\mathrm{h_{max}}} = 3.6$ m/s (for $u_0 = 4.0$ m/s), in good quantitative agreement with the direct measurements ($v_{\mathrm{h_{max}}} = 3.2$ m/s). The good agreement can also be inferred from the normalized experimental data shown in Figure 4.21(b), where the lines corresponding to fits of the data in the two regimes are found to cross very close to the point corresponding to $h = h_{\mathrm{max}}$ and $t = t_{\mathrm{h_{max}}}$.

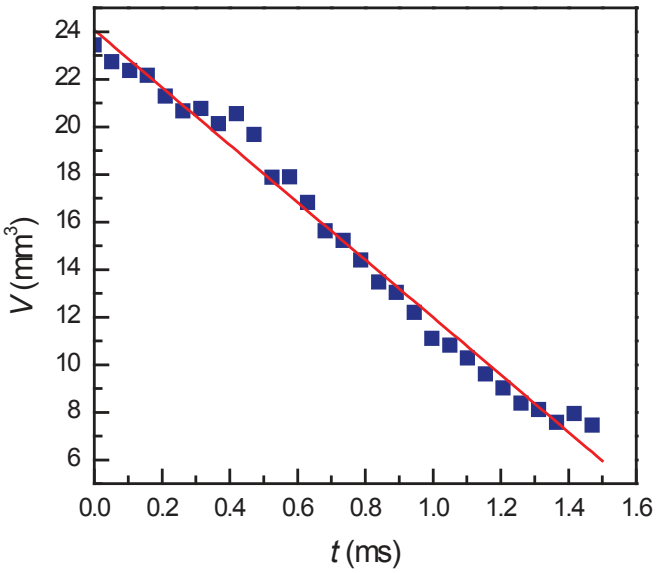

Figure 4.23: Time evolution of the volume of liquid on the target. Symbols are experimental data and the continuous line is a linear fit yielding a constant liquid ejection rate. Here, the tear diameter is $d_0 = 3.7$ mm and the impact velocity is $u_0 = 4.0$ m/s.

4.3.5 Sheet thickness at different Weber numbers

To check the generality of our measurements, we perform the same type of measurements and analysis as detailed above, for different Weber numbers where the impact tear velocity and the volume of the tear are varied. Five different experimental conditions, for which the Weber numbers varies between 320 and 810, are performed (see Table 4.1). In all experiments, we vary the diameter of the target to keep constant (0.6) the ratio between the diameter of the tear and that of the target. The raw data of the sheet thickness in the short-time regime and long-time regime of the expansion stage are shown in Figure 4.24(a) as a function of t/r^3 and in Figure 4.24(c) as a function of $1/rt$. Overall the thickness varies between 12 μm and 272 μm, and the maximal thicknesses are measured for the experiments performed with $d_0 = 4.8$ mm and $u_0 = 2.8$ m/s ($We = 538$). In all cases a good scaling of the data acquired at different radial positions is obtained, showing the robustness of our findings. Using as normalized data, $H = h/d_0$, $R = r/d_0$, $T = t/\tau$ and $U = \frac{u_0\tau}{d_0}$, Equation 4.1 for the short-time expansion regime ($t < t_{\mathrm{h_{max}}}$) can be rewritten as

$$H = \alpha \frac{UT}{R^3} \tag{4.13}$$

Equation 4.5 for the late-time expansion regime ($t > t_{\mathrm{h_{max}}}$) can be rewritten as

$$H = \beta \frac{\pi}{6} \frac{1}{URT} \tag{4.14}$$

Remarkably, Figures 4.24(b) and (d) show a nice collapse of the data acquired for different Weber numbers once plotted in a normalized fashion. A fit with a power law with an exponent 1 of the data in the early expansion regime (Figure 4.24(b)) gives $\alpha = 0.062$, and a fit with a power law with an exponent 1 of the data in the late stage of the expansion regime (Figure 4.24(d)) gives $\beta = 0.144$. By equating Equations 4.13 and 4.14, one predicts a constant normalized velocity for the maximum thickness:

$$V_{h_{max}} = (R/T)_{h_{max}} = \sqrt{\frac{6\alpha}{\pi\beta}}U = 0.91U \tag{4.15}$$

By directly measuring the normalized velocity of the thickness maximum for the different experiments, we find $V_{h_{max}} = (0.70 \pm 0.18)U$, in good agreement with the previous determination.

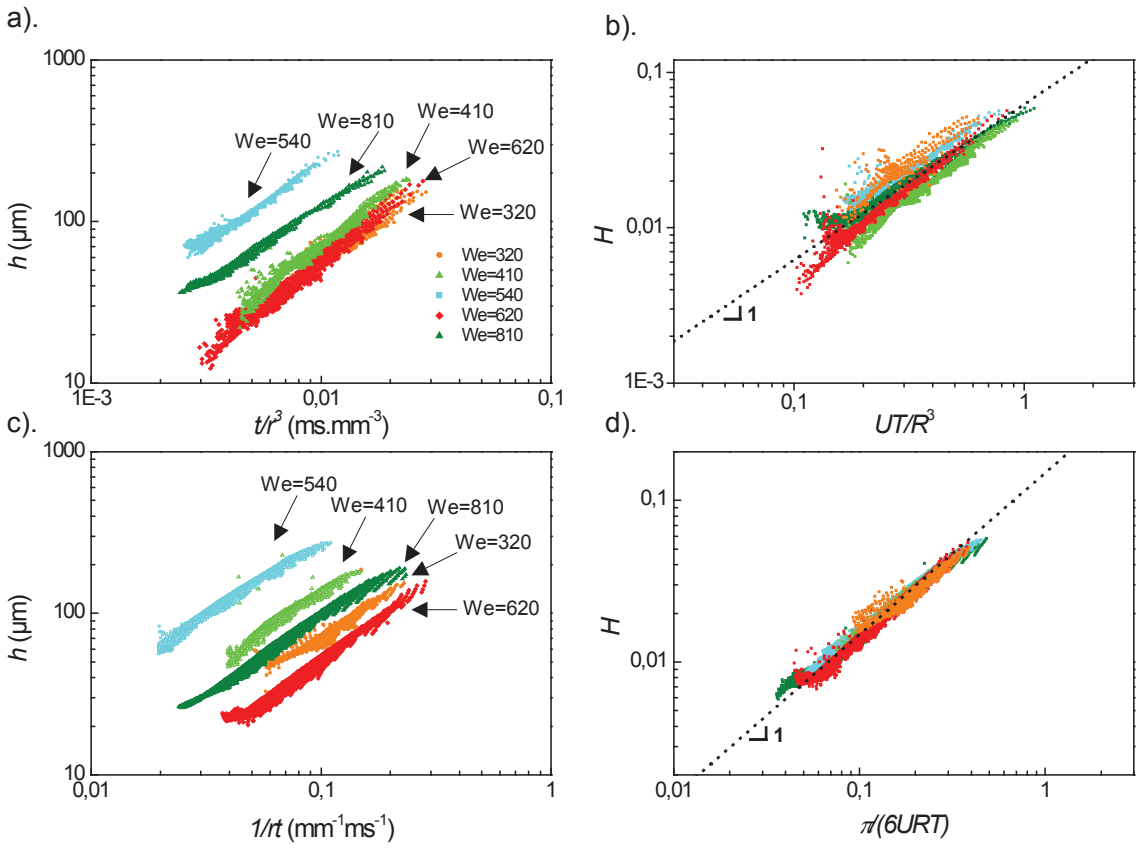

Figure 4.24: Evolution with time, t, and radial distance, r, of the thickness of a liquid sheet for five different experimental configurations as indicated in the legend. (a, b) correspond to data in the early stage expansion regime ($t < t_{h_{max}}$), and (c, d) correspond to data in the late stage expansion regime ($t > t_{h_{max}}$). (a, c) Actual thickness plotted as a function of (a) t/r^3 and (c) $1/rt$. (b, d) Normalized thickness, H, plotted as a function of (b) UT/R^3, and (d) $1/URT$. In (b, d), the dashed lines are power law fits of the experimental data with a slope of 1.

4.3.6 Comparison with simulations and experiments

In this section, we compare our experimental data concerning the sheet thickness field to the numerical simulations performed by Eggers et al. [Eggers 2010] presented in section 4.1.3. They propose a thickness field of the form

$$h(r,t) = \left(\frac{\tau_{\text{coll}}}{2}\right)^2 \frac{r_0}{(t+\frac{\tau_{\text{coll}}}{2})^2} \frac{D}{\left(1+C\left(\frac{\tau_{\text{coll}}}{2r_0}\right)^2\left(\frac{r}{t+\frac{\tau_{\text{coll}}}{2}}\right)^2\right)^6} \tag{4.16}$$

from Equation 4.10 and 4.11 with C and D numerical constants. Lastakowski et al. [Lastakowski 2014] measured a thickness field in agreement with the one deduced by Eggers et al. They perform tear impact experiments onto superheated surfaces (Leidenfrost impact situation), see Figure 4.25. In this configuration, the interactions with the substrate are minimized and so it is comparable with the impact of tear onto a small target. The authors have investigated the velocity field of liquid sheets by adding small particles to the solution to perform particle image velocimetry analysis. The thickness field of liquid sheets is measured using light absorption with a dye being added to the liquid, a technique similar to the one that we have developed. They measured a velocity field and a thickness field in agreement with the ones obtained by Eggers et al. [Eggers 2010].

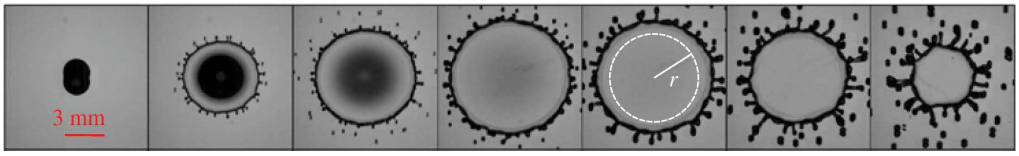

Figure 4.25: Image sequence of the Leidenfrost impact of an ethanol drop on a heated plate [Lastakowski 2014] .

In Figure 4.26 is shown our experimental data for the time evolution of the sheet thickness for different radial positions (same data as presented in Figure 4.21(a)) fitted by the expression proposed by Eggers et al. (Equation 4.16) with C and D two fitting parameters [Eggers 2010].

Our experimental data for the sheet thickness are satisfactorily fitted by the expression proposed by Eggers et al. [Eggers 2010] and experimentally confirmed by Lastakowski et al. [Lastakowski 2014] even if we observe some deviations at short times (t<2 ms) for large radial distances (r>4.37 mm) and at long times (t>3 ms) for short radial distances (r<4.37 mm). From their numerical simulations, Eggers et al. obtained for the fitting parameters: C=0.625 and D=1. Lastakowski et al. deduced the values of C and D from the fits of their experimental data obtained with experiments in Leidenfrost configuration, which lead to C=0.604 and D=3.19. The fits of our experimental data (Figure 4.26) yield C=0.48 and D=3.09. These values are of the same order of magnitude as the ones obtained by Eggers et al. [Eggers 2010] and Lastakowski et al. [Lastakowski 2014].

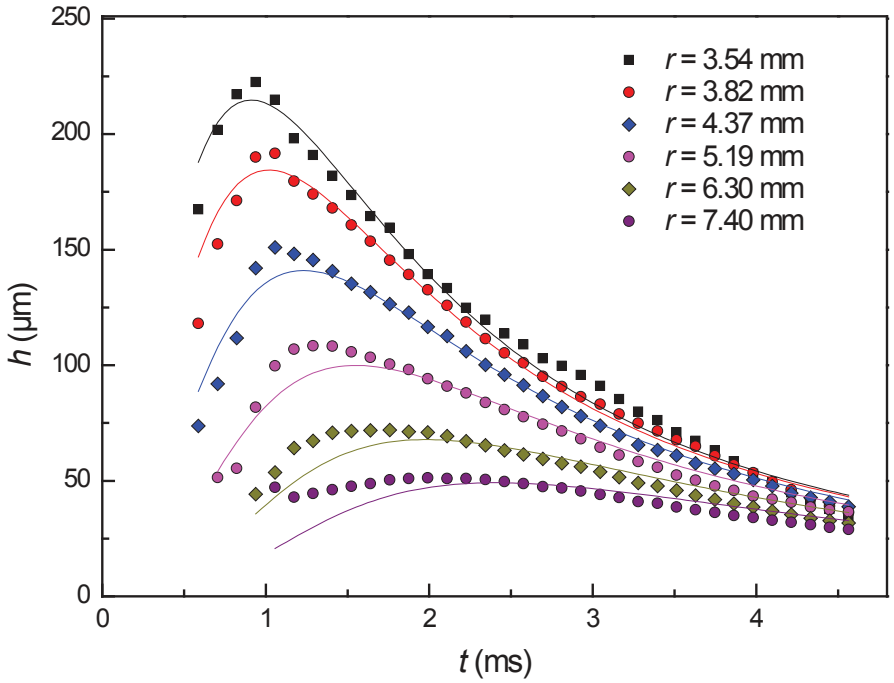

Figure 4.26: Time evolution of the thickness of a liquid sheet for different radial positions. Solid lines correspond to the best fits of the experimental data with Equation 4.16. Only data corresponding to the expansion regime of the sheet are represented, i.e. t<4.57 ms.

In Figure 4.27 is shown the evolution of the sheet thickness with the radial position for different times (same data as presented in Figure 4.20(inset)). On the graph are superimposed the fits proposed by Eggers et al. [Eggers 2010] (blue solid lines) and the ones deduced from Rozhkov et al. model ($h \propto t/r^3$, red dotted lines) [Rozhkov 2004] and Villermaux et al. model ($h \propto 1/rt$, black dashed lines) [Villermaux 2011].

In Figure 4.27 it is clear that the thickness field proposed by Eggers et al. (solid lines) fits less accurately our experimental data than the thickness field deduced from the combination of Rozhkov et al. and Villermaux et al. models (dotted and dashed lines). It should be highlighted that the thickness field proposed by Eggers et al. [Eggers 2010] intends to describe the two regimes of evolution of the sheet thickness. By contrary the models developed by Rozhkov et al. [Rozhkov 2010] on the one hand and Villermaux et al. [Villermaux 2011] on the other hand, respectively describe the two different limits. Indeed, Rozhkov et al. model is valid for times short compared to the collision time, τ_{coll}, whereas Villermaux et al. model describes the other limit.

In conclusion, the thickness field proposed by Eggers et al. [Eggers 2010] fit satisfactorily our experimental data but not as well as the thickness field obtained by combining Rozhkov et al. model [Rozhkov 2010] at short time and Villermaux et al. model [Villermaux 2011] at long time. The approaches of Eggers al. on the one hand and Rozhkov et al. and Villermaux et al. on the other hand are very different. The thickness

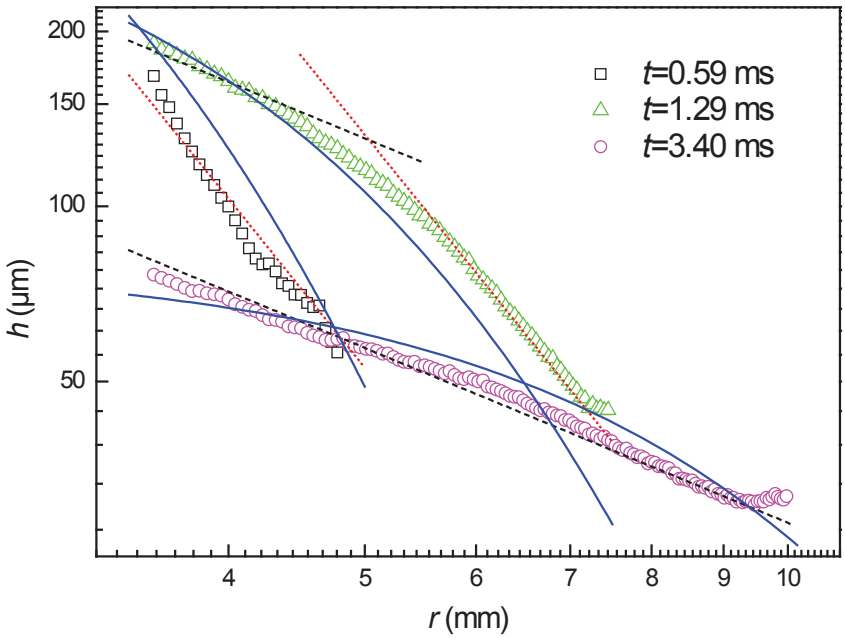

Figure 4.27: Thickness of the liquid sheet as a function of radial distance for different times. Blue solid lines correspond to the best fits of the experimental data of the form given by Equation 4.16 [Eggers 2010]. Dashed and dotted lines correspond to the best fits deduced from the models proposed by Rozhkov et al. (red dotted lines) [Rozhkov 2004] and Villermaux et al. (black dashed lines) [Villermaux 2011] (see section 4.3.4).

field proposed by Eggers et al. is deduced from a fit of their numerical simulations, it is therefore an empirical model, whereas the two other models are theoretical models based on the resolution of Euler equations and the momentum balance equation for the variable-mass sheet rim.

4.3.7 Azimuthal thickness modulations

Thanks to the presence of a dye in the sheet, we are able to directly visualize small fluctuations of the thickness of the liquid sheet. We have previously integrated the values of the thickness measured at different azimuthal angles to obtain averaged data that just depend on the radial distance. A careful examination of the liquid sheet shows however a clear azimuthal modulation of the thickness. Thicker than the average, channels are observed to run over the whole extension of the sheet (Figure 4.28(a)). The profile of the thickness along a circle centered at the centre of the target clearly shows fluctuations of the thickness of typical amplitude 15 μm (hence about 30% of the average thickness (52 μm)) (Figure 4.28(c)). Moreover the channels are rather regularly arranged as evidenced by a peak in the Fourier transform of the profile (Figure 4.28(d)), indicating a characteristic spacing of 15 degree between adjacent channels. We are not aware of any experimental or

theoretical studies of such thickness modulations. We were not able, however, to see any clear correlation between the thickness modulation and the rim corrugation. Note that the thickness modulation can also be inferred from the side view of a sheet, as shown in Figure 4.28(b). We believe that these phenomena would deserve further investigations.

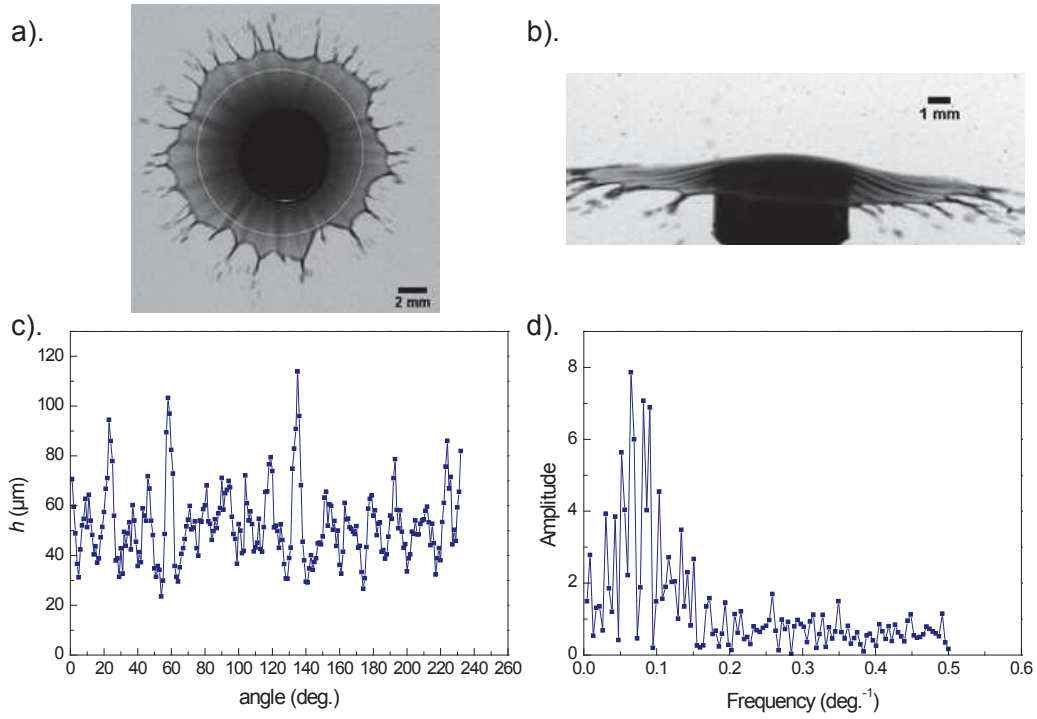

Figure 4.28: Front a). and side b). views of liquid sheets showing a modulation of the thickness. In a). (resp. b).) $t = 1.03$ ms, $T = 0.064$ (resp. $t = 1.44$ ms, $T = 0.09$). c). Azimuthal profile of the thickness along the circle shown in (a). d). Fourier transform of the profile shown in (c). Here, the tear diameter is $d_0 = 3.7$ mm and the impact velocity is $u_0 = 4.0$ m/s

4.3.8 Conclusion

We have used an experimental set-up adapted from the original one designed by Rozhkov et al. to form liquid sheet [Rozhkov 2004]. The collision of a liquid tear against a small target results in the formation of a thin liquid sheet that extends radially until it reaches a maximum diameter. Water-based liquid sheet are destabilized by the formation of liquid ligaments at the rim, these ligaments are destabilized into drops during the whole lifetime of the sheet.

We have described a quantitative yet simple method to measure the thickness field $h(r, t)$ of this class of liquid sheet, based on the grey-level measurement of the image of a dyed liquid sheet. Measurable thicknesses lie in the range $(6 - 450)$ μm. This method

allowed one to determine the thickness field of expanding liquid sheet and provide evidence of new features.

(i) Two asymptotic hydrodynamic regimes characterize the expansion of the liquid sheet. In the first regime observed at short time, $h(r,t) \propto t/r^3$ corresponding to the feeding of the sheet by a central point source reminiscent of the impacting tear in agreement with [Rozhkov 2004]. The later regime of expansion corresponds to a pseudo-stationary regime deduced from the stationary regime of a Savart's sheet where $h(r,t) \propto 1/(rt)$ as theoretically predicted [Villermaux 2011].

(ii) Experimentally, we observe for each radial position a maximum of the thickness $h_{\max}$ with time, which propagates at a constant celerity, close to the impact velocity of the tear. This maximum as well as its constant propagation celerity can be theoretically inferred from the cross-over between the two asymptotic regimes.

(iii) An azimuthal modulation of the thickness is observed during the expansion of the sheet, but it seems not directly at the origin of the radially expelled ligaments, which are localized at the rim and result from a Rayleigh-Taylor-like instability.

4.4 Liquid sheet of complex fluids

In the first section of this chapter, we have described an experimental set-up to form controlled liquid sheet and visualize their destabilization mechanism. We have investigated the formation and destabilization of pure water liquid sheet and characterized their thickness field. The next objective is to use this experimental set-up to study the destabilization mechanism of liquid sheet of complex fluids. In this section, we present the destabilization of liquid sheet of dilute solution of high-molecular-weight polymer and dilute oil-in-water emulsion.

4.4.1 High-molecular-weight polymer solution

In Figure 4.29 is presented the formation and destabilization of a liquid sheet made of a dilute solution of high-molecular-weight PEO. The origin of time is taken at the moment of the tear impact. As for a pure water tear, upon impact, the tear flattens into a liquid sheet radially expanding in the air surrounded by a thicker rim (Figure 4.29(a)). This rim is corrugated with the formation of small ligaments, as observed for pure water sheet (Figure 4.13(a)). For a pure water sheet, drops are continuously detached from these ligaments. The same mechanism is observed for PEO solution, however we remark the formation of thin long-living filaments connecting the ligaments to the drop formed (Figure 4.29(b) and (c)). Drops are suspended on the thin filaments, recalling the "beads-on-string" structure observed for the destabilization of ligament of dilute solution of high-molecular-weight polymer (Chapter 3). On the same time the liquid sheet retracts due to the effect of surface tension (Figure 4.29(d)). The thin filaments persists after the

complete retraction of the sheet (Figure 4.29(e)). The filaments are then destabilized into drops liberating the main drops and forming smaller drops (Figure 4.29(f)). The specific destabilization mechanism of liquid sheet made of dilute solution of high-molecular-weight polymer has been described in details by [Rozhkov 2006].

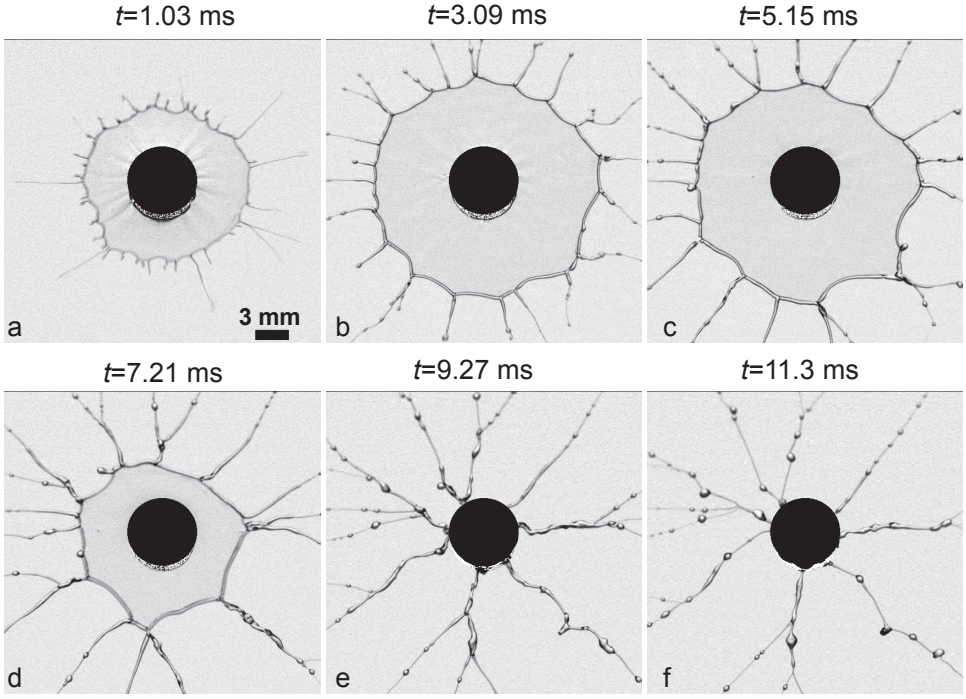

Figure 4.29: Sequence of events of the formation and destabilization of a liquid sheet of dilute PEO solution (1,000,000 g/mol at 0.05 % w/w). The tear diameter is $d_0 = 3.7$ mm, the impact velocity is $u_0 = 4.0$ m/s, and the target diameter is 6 mm.

4.4.2 Dilute oil-in-water emulsion

In Figure 4.29 is presented the formation and destabilization of a liquid sheet made of a dilute model emulsion (C=0.3 % v/v). The origin of time is taken at the moment of the tear impact. As observed for a pure water tear, upon impact the liquid sheet spreads out radially surrounded by a thicker rim (Figure 4.30(a)). But in addition, holes are observed to nucleate, perforating the sheet before its retraction (Figure 4.30(b) and (c)). The holes grow until they merge together and form a web of ligaments (Figure 4.30(d) and (e)). These ligaments are then destabilized into drops (Figure 4.30(e)). Note that such perforation mechanism has already been observed for solution of solid suspensions [Dombrowski 1954, Addo-Yobo 2011], dilute oil-in-water emulsions [Dombrowski 1954, Butler Ellis 1999b, Dexter 2001, Hilz 2013a, Altieri 2014], and air bubbles stabilized by surfactants in water [Lhuissier 2013], as described in section 1.3.4.

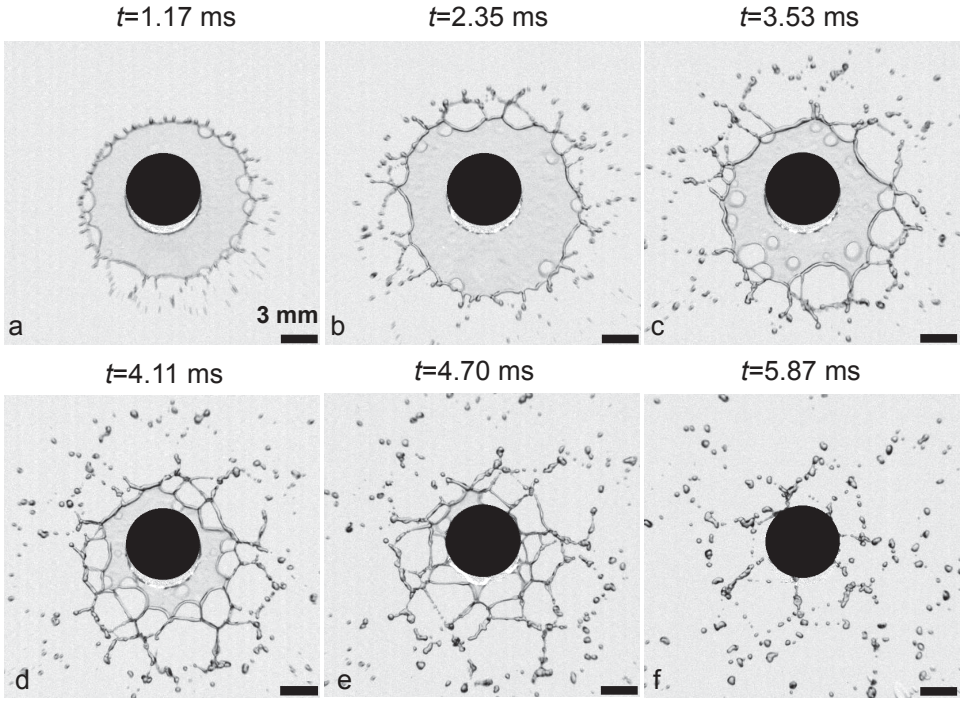

Figure 4.30: Sequence of events of the formation and destabilization of a liquid sheet of dilute model emulsion (C=0.3 % v/v). The tear diameter is $d_0 = 3.7$ mm, the impact velocity is $u_0 = 4.0$ m/s, and the target diameter is 6 mm.

4.5 Conclusion

We have used an experimental set-up originally designed by Rozhkov et al. [Rozhkov 2002] to form controlled liquid sheet based on the impact of a single tear on a solid target. The main advantage of this experimental set-up is the very small volume of solution needed, around 30 μL. With this set-up, we have studied the destabilization mechanism of a pure water sheet. Water-based liquid sheet are destabilized by the ejection of drops from the ligaments formed at the corrugated rim of the sheet. We have measured the thickness field of the liquid sheet thanks to an original method that we have developed based on the utilization of a dye. We have highlighted the existence of two thickness regimes that were predicted theoretically but never observed experimentally. Once pure water liquid sheet fully described, we have used the single-tear experimental set-up to study the destabilization mechanisms of liquid sheet of complex fluids. The destabilization mechanism of a dilute oil-in-water emulsion is drastically modified compared to a pure water sheet. The emulsion-based liquid sheet is destabilized by nucleation of holes within the sheet. Our objective for the next chapter is to investigate if the particular destabilization mechanism of emulsion-based liquid sheets explains the anti-drift properties of emulsions as adjuvant for agricultural solution.

Chapter 5

Destabilization of emulsion-based liquid sheet: single-tear and standard spray experiments

Contents

In the previous chapter we have seen that the destabilization mechanism of a liquid sheet made of the model emulsion is drastically modified compared to that of a pure water liquid sheet. The emulsion-based sheet is destabilized by the nucleation and growth of holes that perforate the sheet. In the following we refer to this mechanism as a "perforation mechanism". The objective of this chapter is to understand if this specific perforation mechanism can explain the role of emulsions as anti-drift adjuvants for agricultural spray solutions. In other words, we are asking the following question: is there some correlation between the perforation process and the reduction of the proportion of small drops in an emulsion-based spray? To answer this question, we compare the results obtained with the single-tear experimental set-up to those collected using a conventional spray technique. We modify the physicochemical parameters of the model emulsion, the emulsion concentration and the emulsion droplet size, to rationalize their influence on the perforation

mechanism and the spray drop size distribution. The first section of this chapter is dedicated to the description of the experimental set-ups, the samples and the image analysis. In the second and third sections we present the results concerning the variation of the emulsion concentration and the emulsion drop size distribution. A part of the results presented in this chapter has been reported in the publication *Drop impact experiment as a model experiment to investigate the role of oil-in-water emulsions in controlling the drop size distribution of an agricultural spray*, C. Vernay, L. Ramos, J. P. Douzals, R. Goyal, J. C. Castaing, and C. Ligoure that has been accepted for publication in Atomization and Sprays [Vernay 2015a].

5.1 Experimental set-up, samples and image analysis

5.1.1 Conventional spray experiments

In this section, we present the conventional spray technique used to form spray and to measure the spray drop size distribution. These measurements enable one to characterize the anti-drift properties of solutions by quantifying the proportion of small drops in the spray. The conventional spray experiments were performed at the laboratory ITAP (Information, Technologies, Analyse environnemental, Procédés agricoles), IRSTEA, in Montpellier with Jean-Paul Douzals and Cyril Tinet.

5.1.1.1 Formation of the spray

A picture and a sketch of the experimental set-up are represented in Figure 5.1. We use a Teejet flat fan nozzle (XR 110 03), a cat's-eye-shaped nozzle. The nozzle yields, for pure water, flat sheet with a spray angle of 110 degrees. The flow rate at the nozzle exit is 1.2 L/min for a pressure of 3 bar. The liquid is injected at high pressure through the nozzle, producing a thin liquid sheet, which is destabilized into drops, as schematically represented in Figure 5.1(b). The nozzle is mounted on a 3D Charly Robot frame allowing the displacement of the nozzle at a velocity of 20 mm/s along the main axis of the spray (x axis on the sketch of Figure 5.1(b)).

5.1.1.2 Measurement of the spray drop size distribution

The drop size distribution is measured with a Malvern Spraytec device (Malvern Instrument Ltd, UK), see Figure 5.1(a) for a picture of the set-up. Briefly, a laser beam of 5 mW HeNe (Helium Neon source, 632.8 nm) passes through the spray. Light diffraction is analyzed by the reception optics that includes 33 photoreceptors. Basic settings are an acquisition time of 100 ms every second and a focal of 750 mm that allow measurement of drop diameters in the range (1-2,500) μm, assuming spherical drops. The adjustment of the background light and the alignment of the emission and reception optics are performed

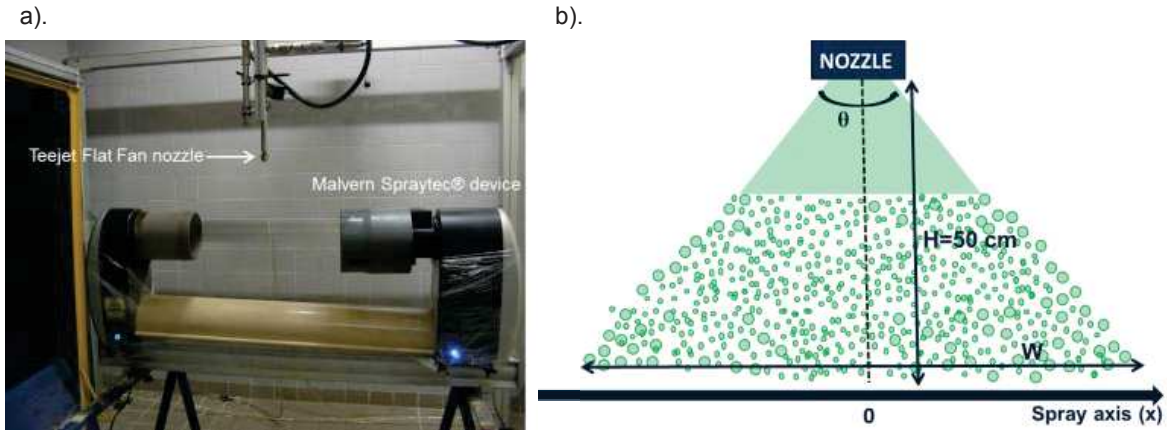

Figure 5.1: (a) Experimental set-up to measure the spray drop size distribution. The Teejet flat fan nozzle is mounted on a movable frame to scan the spray drop size distribution, measured by the Malvern Spraytec device, along the main axis (x) of the spray at a distance H=50 cm to the nozzle. (b) Sketch of the experimental set-up; the zero position corresponds to the center of the spray.

before each measurement. The Spraytec software provides drop distribution values every second. As the nozzle is displaced during the measurement (at a velocity of 20 mm/s), the Spraytec scans the drop size distribution along the spray axis with a resolution of 20 mm. At each position, the spray drop size distribution is averaged over 10 mm due to the width of the laser beam. The distance between the nozzle outlet and the laser beam is set at $H = 50$ cm. The average time to scan the whole spray is about 70 s (i.e. a spray width of about 150 cm with a nozzle height of 50 cm). Each experiment is repeated 3 times to ensure the reproducibility of the measurement.

The direct information given by the Spraytec measurement is the volume size distribution of the spray drops at different positions on the spray axis. Some of these distributions are represented in Figure 5.2(a) for a pure water spray. The drop size distribution at the center of the spray (x=0 cm) and at different positions towards the edge of the spray are shown (x =+20, +40, +60 and +74 cm). In Figure 5.2(b) are presented the drop size distribution and the cumulative distribution at the center of the spray (x=0 cm). From the cumulative distribution, one can define different parameters to characterize the spray drop size distribution. $DV50$ (resp. $DV10$, resp. $DV90$) is the drop diameter such as the cumulative undersized volume fraction of drops is equal to 50 % (resp. 10 %, resp. 90%) (Figure 5.2(b)) [Lefebvre 1989]. To estimate the width of the distribution one can define the span value, $\mathcal{S}= \frac{DV90-DV10}{DV50}$. To characterize the proportion of small drops in the spray, we define the parameter $V150$ as the volume fraction of drops that have a diameter lower than 150 μm (Figure 5.2(b)). This parameter is particularly interesting for our study as driftable drops are generally defined as those with a diameter below 150 μm [van de Zande 2004].

In Figure 5.2(a), we observe that in the center of the spray, x =0 and +20 cm, the drop size distributions are very broad centered around 170 μm. For x=+40 cm, the drop size distribution is very slightly shifted towards bigger drops and is narrower. On the edges of the spray, x =+60 and +74 cm, the drop size distributions are even narrower and shifted towards bigger drops. The positions of the peak of the spray drop size distribution, d_{peak}, and the span values, $\mathcal{S}$, for the different positions on the spray axis are given in Table 5.1. The size distributions of the spray drops are correctly fitted by log-normal distributions:

$$P(x) = \frac{1}{\sqrt{2\pi}xS} \exp\left(-\frac{(\ln x - M)^2}{2S^2}\right) \tag{5.1}$$

with S and M two fitting parameters that are, respectively, the mean and the standard deviation of the variable's logarithm. The mean of the distribution, μ, is equal to $e^{M+S^2/2}$ and the variance, σ^2, to $e^{S^2+2M}(e^{S^2} - 1)$. In Table 5.1 are summarized the standard deviation, σ, and the mean values, μ, calculated from the parameters S and M of the log-normal fits of the distributions for the different x positions along the spray axis. Here, the spray drop size distribution are fitted by log-normal distributions to briefly characterize the shift and narrowing of the curves. However, it has been reported in the literature [Villermaux 2011, Lhuissier 2013], that spray drop size distributions are physically better described by gamma distributions.

position along the spray axis	d_{peak} (μm)	$\mathcal{S}$	μ (μm)	σ (μm)
0 cm	173	1.5	250.1	144.0
+20 cm	173	1.5	259.8	152.8
+40 cm	173	1.2	245.2	119.8
+60 cm	256	0.6	278.6	71.8
+74 cm	332	0.5	343.8	72.3

Table 5.1: Positions of the center of the peak, d_{peak} and the span values, $\mathcal{S}$, of the spray drop size distributions for the different x positions along the spray axis. The standard deviation, σ, and the mean values, μ, calculated from the log-normal fits of the distributions are also indicated.

As observed in Figure 5.2(a), flat fan nozzles typically induce the formation of large drops at the periphery of the spray and small drops are more concentrated in the middle of the spray. Comparable spray patterns are obtained with different types of nozzle such as air injection and hollow cone nozzles [Vallet 2011, Vallet 2013]. Free liquid sheets formed at the exit of the nozzle are bounded by a thicker rim due to the effect of the surface tension. The destabilization of this thicker rim is at the origin of the bigger drops observed at the periphery of the spray.

From these drop size distributions, we can calculate the parameter $DV50$ for each position on the spray axis (with a resolution of 20 mm) as shown in Figure 5.2(b) for x=0 cm. We obtain the evolution of $DV50$ along the spray axis represented in Figure 5.2(c).

$DV50$ varies symmetrically around the spray center ($x = 0$ cm): smaller drops are obtained at the spray center and bigger drops at the edges.

From the drop size distributions at each point of the spray axis (Figure 5.2(a)), one can calculate the drop size distribution averaged along the whole spray (x between $-W/2$ and $+W/2$) weighted by a coefficient corresponding to the volumetric density of spray drops along the spray axis. The weighted average distribution is shown in Figure 5.3. From the cumulative volume distribution (red circle data points), we define the parameters $DV50$ and $V150$ averaged values along the whole spray.

In the following, we principally characterize the spray volumetric distributions with the parameters $DV50$ and $V150$ averaged over the spray axis. The evolution of $DV50$ along the spray axis gives also precious and synthetic information about the volumetric distribution along the spray axis.

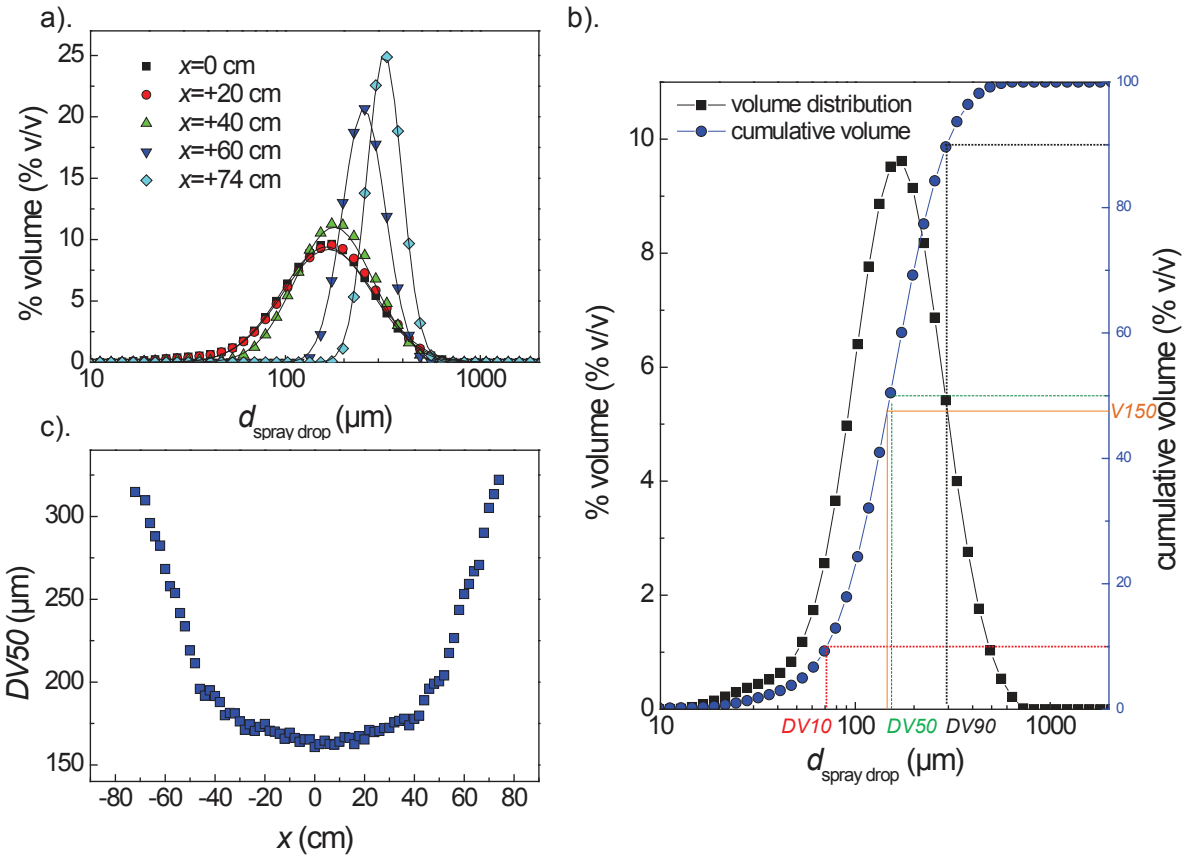

Figure 5.2: a). Volumetric drop size distribution of a pure water spray at different positions on the spray axis. b). Volumetric drop size distribution and cumulative distribution at the center of the spray, x=0 cm, with the definitions of the different volumetric parameters. The lines correspond to the best log-normal fits of the distributions, the fit parameters are indicated in Table 5.1. c). Evolution of the parameter $DV50$ of the spray drop size distribution along the spray axis.

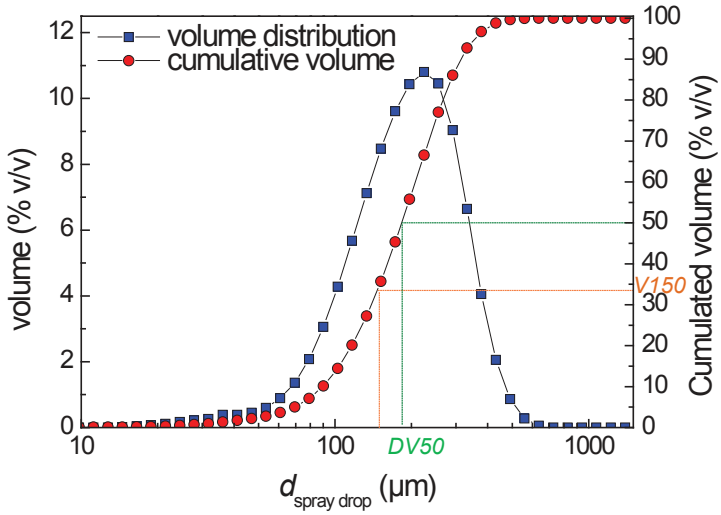

Figure 5.3: Spray drop size distribution averaged along the whole spray with the cumulative distribution for a pure water spray. We define the averaged parameters $DV50$ and $V150$.

5.1.2 Samples and experimental procedures

5.1.2.1 Samples

The emulsion studied in this chapter is the model emulsion. For details about the emulsion composition see section 2.1.1.2. For all the emulsions studied in this chapter, the aqueous phase is pure water.

The study of the role of the emulsion concentration on the destabilization process has been conducted with emulsions prepared by manual shaking. The emulsion concentration, C, is varied between 0.0015 and 2.4 % v/v. We verify that the emulsion concentration has no influence on the oil droplet size distribution. For the different concentrations, the volume median diameter of the oil droplet distribution, d_{oil}, is around 39 μm. More details about the preparation of the emulsions and the emulsion droplet size distribution can be found in section 2.1.3.3.

The study of the influence of the emulsion oil droplet size on the destabilization process has been conducted with emulsions prepared by different methods, yielding different size distributions of the surfactant stabilized oil droplets. Details about the preparation methods and the resulting drop size distributions are given in section 2.1.3.3. The volume median diameter of the oil droplet distribution, d_{oil}, is varied over the range $(0.5 - 39.1)$ μm. The emulsion concentration is also varied over a large range depending on the emulsion oil droplet diameter, to obtain, for the different oil droplet sizes, comparable number of oil droplets per liter. The concentration ranges investigated for the different oil droplet sizes are summarized in the Table 5.2.

d_{oil} (μm)	Concentration range (% v/v)
0.5	0.003 - 0.6
3.8	0.003 - 5
11.7	0.003 - 5
20.0	0.003 - 2.4
39.1	0.0015 - 2.4

Table 5.2: Investigated concentration ranges of the emulsion for the different oil droplet sizes.

For the single-tear experiments, small volume of emulsions are prepared (typically 30 mL) as few tears are necessary for each experiment. For the spray experiment, 3 liters are necessary for each experiment. In that case, we prepare emulsion by batch of 1.5 L (the volume limit of the Ultra-Turrax). To obtain the same drop size distribution for batch of 30 mL and batch of 1.5 L, the rotation velocity of the Ultra-Turrax is adjusted. Indeed, at the same rotation velocity, emulsions prepared in batch of 1.5 L have noticeably larger oil droplets than emulsions prepared in batch of 30 mL. For the spray experiment, distilled water is used to prepare the emulsion instead of milliQ water for the single-tear experimental set-up.

5.1.2.2 Experimental procedures

Controlled liquid sheets are formed with the single-tear experimental set-up presented in the Chapter 4. The impact velocity of the tear, u_0, is set at 4 m/s. The needle diameter, d_n, used to form the tear is adapted for the different emulsions to obtain in all cases a tear of constant diameter, $d_0 = 3.7$ mm, i.e. a volume of the tear $V_0 = 26.5$ μL. Indeed, the surface tension of the emulsion decreases when the concentration increases. Hence, a larger needle diameter is required for high emulsion concentration to obtain a tear of equal diameter to that for dilute emulsions. In Table 5.3 are summarized the surface tensions of the emulsion at different concentrations and the corresponding diameter of the needle used to form the tear.

C (% v/v)	γ (mN/m)	d_n (mm)
0.003	65.5	1.65
0.03	46.5	1.8
0.3	34.1	2.8
0.6	30.6	2.8
2.4	29.6	2.8

Table 5.3: Values of the surface tension of the model emulsion at different concentrations and the corresponding diameter of the needle used to form the tear.

The impact, formation and destabilization of the liquid sheet are visualized from the top with a weak angle using a fast camera (Phantom V7.3) operating at 9,708 pictures per second and with a resolution of 576 pixels × 552 pixels. The software ImageJ is used for image analysis. For each formulation, experiments are triplicated and in the following results are given as an average over the three experiments with error bars corresponding to the standard deviation.

5.1.3 Analysis of the perforation

As shown in Figure 5.4(a), holes are eventually found to occur and grow in liquid sheets made of model emulsion. In the following, we discuss the different methods to characterize the perforation of the liquid sheet.

5.1.3.1 Perforated area of the liquid sheet

The first method consists in quantifying the time evolution of the cumulated area of holes and that of intact (non perforated) sheet. In Figure 5.4(a) is shown a typical image of the destabilization of an emulsion-based liquid sheet 3.40 ms after the tear impact. The liquid sheet is partially perforated. Using ImageJ, we can define a continuous area of the sheet, which corresponds to the blue selection in Figure 5.4(b). The perforated area of the sheet is calculated as the sum of the area of the holes (red selections in Figure 5.4(c)). From Figure 5.4(c), one can determine the number of holes (manually counted) present in the sheet at a given time, $\mathcal{N}$.

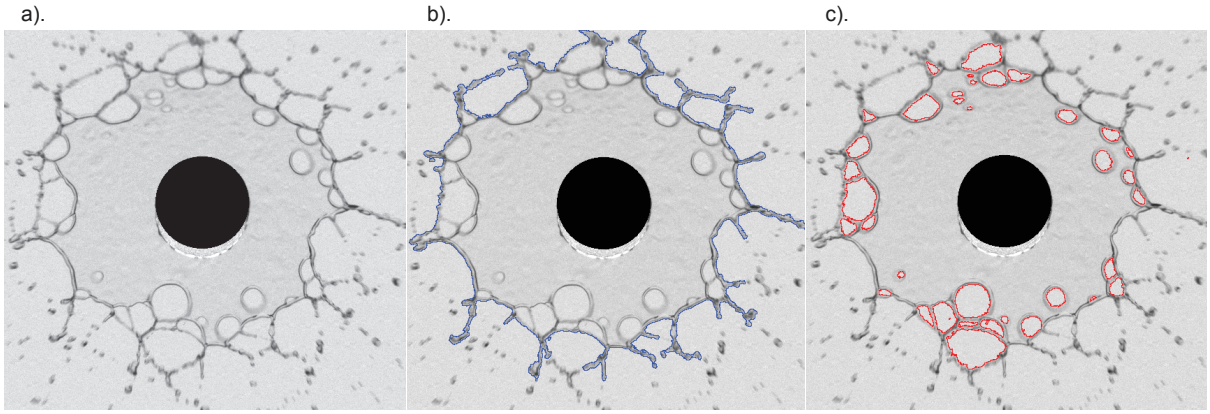

Figure 5.4: a). Image of the destabilization of a model emulsion-based liquid sheet, C=0.3 % v/v, d_{oil}=39.1 μm, 3.40 ms after the tear impact. b). Same image with the blue selection representing the continuous area of the sheet. c). Same image with in red the perforated area.

In Figure 5.5(a) is represented the time evolution of the continuous and the perforated areas. For a typical experiment, $t = 0$ corresponds to the time of impact of the tear on

the target. The continuous area increases with time up to a maximum obtained here at t=3.4 ms and then decreases due to the surface tension-driven retraction of the sheet. The perforated area is equal to 0 at short time as no hole has yet perforated the sheet. From t=1 ms, the perforated area increases with time up to a maximum (t=4.8 ms) and then slightly decreases. From 4.8 ms to the complete destabilization of the liquid sheet (t=5.2 ms), the perforated area decreases because the holes at the sheet periphery disappear. One can define the intact area of the liquid sheet as the difference between the continuous area and the perforated area. The intact area is also shown in Figure 5.5(a), it follows the same trend as the continuous area however the maximum expansion area is shifted towards shorter times (t=3.0 ms).

In Figure 5.5(b) is shown the evolution of the number of holes present in the sheet, $\mathcal{N}$, as a function of time. $\mathcal{N}$ increases with time up to a maximum of 56 holes at 4.2 ms. Then $\mathcal{N}$ decreases down to 20 holes at t =5.2 ms. From 4.4 to 4.8 ms, the perforated area increases whereas the holes number decreases. This means that holes are coalescing, leading to a reduction of the number of holes and concomitantly to an increase of the total holes area.

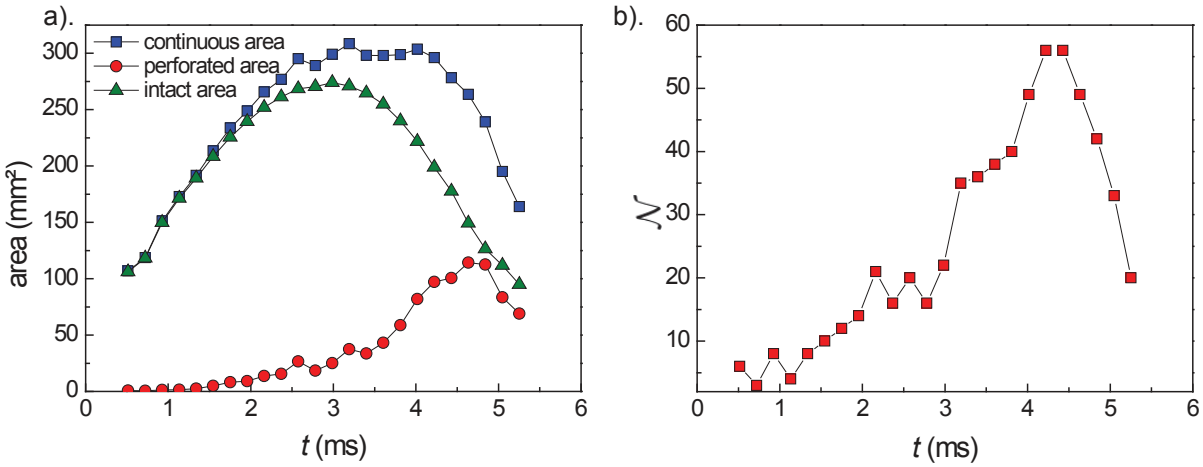

Figure 5.5: a) Time evolution of the continuous, perforated and intact areas of a model emulsion-based liquid sheet (C=0.3 % v/v, d_{oil}=39.1 μm). b). Time evolution of the number of holes present in the sheet, $\mathcal{N}$.

5.1.3.2 Cumulated number of perforation events

In the previous section we have defined the parameter $\mathcal{N}$ as the number of holes present in the sheet at a given time. $\mathcal{N}$ is the result of two contributions. A positive one due to the nucleation of new holes and a negative one due to the merging of growing holes as they come into contact and the disappearance of the border holes. An alternative way to characterize the perforation mechanism is to count the number of nucleation events that perforate the sheet during the whole experiment (from the impact of the tear to

the complete disintegration of the sheet into drops). We define λ as the instantaneous nucleation rate, i.e. the number of holes that have nucleated between t and $t + dt$. N is defined as the cumulated number of perforation events (i.e. the integrated value of λ over time). On contrary to $\mathcal{N}$, λ and N quantify only one process, that is the nucleation of new holes in the sheet, and do not take into account the coalescence of holes that impacts on $\mathcal{N}$.

In practice, the number of nucleation events is counted manually. It is really easy to determine, from an image to the next one, the number of new holes created. In Figure 5.6(a) is shown the time evolution of the instantaneous perforation rate, λ. We observe a delay time before the nucleation of holes (around 0.6 ms), then the instantaneous perforation rate oscillates without a clear trend between 3 to 15 holes per time interval, dt, taken here equal to 0.2 ms. In the same graph (right Y axis) is plotted the evolution of the intact area of the sheet. We observe that there is no correlation between the instantaneous perforation rate and the intact area of the sheet. Hence, the instantaneous perforation rate seems to be independent of the intact surface available. On average from the beginning of the perforation to the whole destabilization, 7.1 ± 2.9 holes nucleate in the sheet every 0.2 ms. We can define a perforation density per unit of intact area, $\mathcal{D}$, by dividing the instantaneous perforation rate, λ, by the intact area of the sheet. The time evolution of the perforation density is plotted in Figure 5.6(b). The perforation density fluctuates around a mean value ($\mathcal{D}$=0.032 $\pm$ 0.016 mm^{-1}) during the whole perforation process without a clear trend. We can estimate the perforation density to be constant over time, which means that the perforation density is independent of the thickness of the sheet. Indeed, as we have seen in Chapter 4 the thickness of the sheet varies with time. At t=1 ms, the sheet thickness is in average equal to (105.3 ± 55.3 μm) (depending on the radial position) and at t=4.5 ms equal to (29.9 ± 5.2 μm). The perforation density is of the same order of magnitude at t=1 ms and 4.5 ms whereas the sheet thickness values are very different, which implies that the perforation density is independent of the thickness of the sheet, a not trivial result.

We show in Figure 5.7(a) the time evolution of the cumulated number of perforation events, N. As already observed, we note that there is a delay time, t_d, before the nucleation of the first hole is detected. For $t > t_\mathrm{d}$, the cumulated number of perforation events increases almost linearly with time up to a maximum value. Note that the linear increase is the direct consequence of a time independent instantaneous perforation rate. We define N_tot as the total number of perforation events that occur in the liquid sheet during the whole experiment.

In the following, we decide to characterize the perforation mechanism of a liquid sheet by the values of N_tot, the total number of perforation events, and t_d the delay time. We prefer this analysis to the one of the perforated area and the number of holes present in the sheet, $\mathcal{N}$, (section 5.1.3.1) as it only considers the nucleation of new holes. As $\mathcal{N}$ results from different contributions (nucleation, coalescence and disappearance of holes) it is more difficult to interpret.

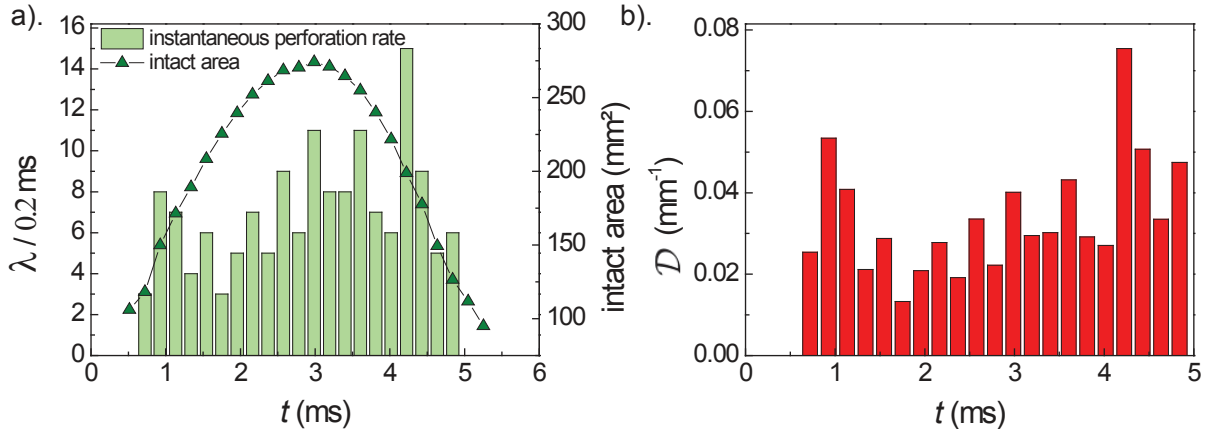

Figure 5.6: a). Left Y axis: Time evolution of the instantaneous perforation rate , λ; Right Y axis: Time evolution of the intact area of the sheet. b). Time evolution of the density of perforation, $\mathcal{D}$.

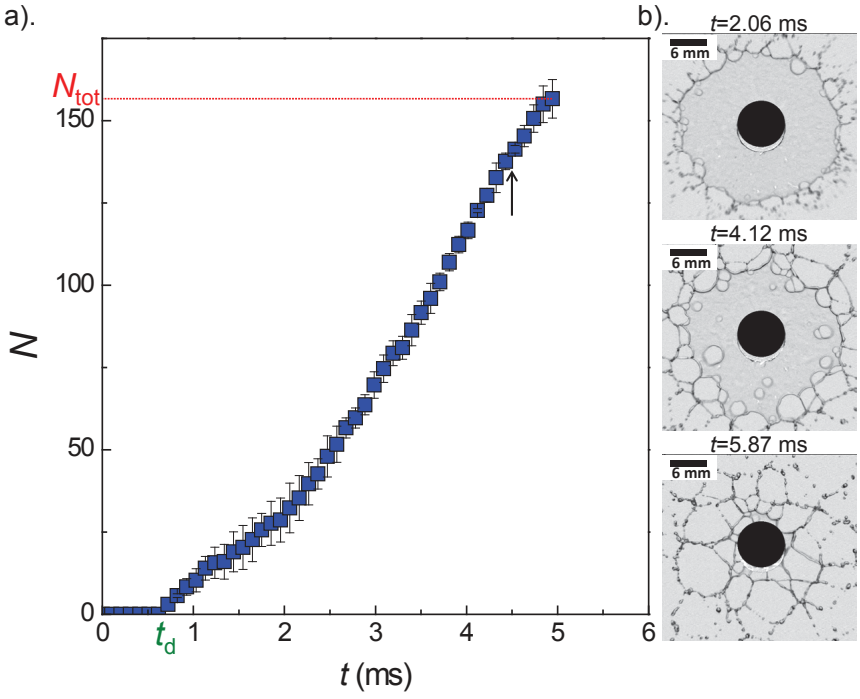

Figure 5.7: a). Time evolution of the cumulated number of perforation events, N, that occur in the liquid sheet during the whole experiment with the definition of N_{tot} the total number of perforation events and t_{d} the delay time. The emulsion is a model emulsion at C=0.3 % v/v with d_{oil}=39.1 μm. An arrow indicates the time of the maximal sheet expansion for an equivalent pure water liquid sheet. b). Destabilization of a model emulsion-based liquid sheet. The origin of time is taken at the impact of the liquid tear on the target.

5.2 Effect of the emulsion concentration

We quantitatively investigate the effect of the emulsion concentration on the perforation mechanism and on the spray drop size distribution. The results for the two experimental set-ups are presented separately in the first two sections. In the third section, we show the correlation between the single-tear model experiment and the standard spray experiment.

5.2.1 Single-tear model experiments

Figure 5.8(a) shows images of the sheets for different emulsion concentrations taken at the same time after the tear impact. Clearly, the amount of perforation events increases with increasing emulsion concentration. The total number of perforation events, N_{tot}, is plotted as a function of the emulsion concentration in Figure 5.8(b) (top axis). We find that the emulsion concentration entails a continuous increase of the total perforation events per liquid sheet up to a concentration C of the order of $(0.3 - 0.6)$ % v/v. For higher concentrations and up to the maximal concentration we have investigated (2.4% v/v), the number of perforation events slightly decreases (Figure 5.8(b)). The optimal concentration to promote perforation events is equal to 0.6 % v/v.

Alternatively, and to get a better physical insight of the effect of the oil droplets, the emulsion concentration C can be easily converted into a mean number of oil droplets contained in the impact tear, n, according to $n = (CV_0)/(\pi/6d_{\text{oil}}^3)$ with V_0 the volume of the impacting tear and d_{oil} the volume median diameter of the oil droplets. n ranges from 12 for $C = 0.0015$ % v/v to $18,980$ for $C = 2.4$ % v/v, as shown on the bottom x axis of Figure 5.8(b). Interestingly, the data measured at low concentration, and equivalently low n, are consistent with a proportionality between the total number of perforation events, N_{tot}, and the number of oil droplets per impacting tear, n. The fact that N_{tot} is directly proportional to n would suggest that the emulsion oil droplets are at the origin of the nucleation process. In addition, the proportionality constant at low concentration N_{tot}/n is of the order of 0.4, suggesting a very efficient process, as about 40 % of the oil droplets would promote a perforation event. A saturation is nevertheless detected rapidly, for n larger than 100. The saturation could be due to interactions between the oil droplets in the liquid sheet and between adjacent holes.

In Figure 5.9 is shown the evolution of the delay time, t_{d}, with the emulsion concentration. Values lower than 0.36 ms are not measurable as the sheet moves too rapidly to accurately identify nucleation event. Therefore, in the following if t_{d}=0.36 ms, we can estimate that the perforation starts as soon as the sheet is formed. We observe that the delay time decreases when the emulsion concentration increases for $C < C_0$ with C_0 =0.018 % v/v. The experimental data of t_{d} are reasonably well fitted by an expression of the form: $t_{\text{d}} = k \ln(C/C_0)$ with fitting parameters k=-0.88 and C_0 =0.018 % v/v. For $C > C_0$, the delay time is constant and approximately equal to 0.36 ms. For the lower

concentration investigated, $C = 0.0015$ % v/v, the perforation starts 3.7 ms after the tear impact whereas for the higher concentration, $C = 2.4$ % v/v, the perforation of the liquid sheet starts as soon as the sheet is formed. In conclusion, the more concentrated is the emulsion, the sooner the sheet is destabilized as there are more oil droplets in solution likely to cause the nucleation of a hole.

5.2.2 Spray drop size distribution

We present in this section, the spray drop size distribution measured with the Spraytec Malvern device for the same emulsions as the ones investigated in section 5.2.1. The evolution of the parameter $DV50$, the threshold diameter for which drops represent 50 % of the total volume of the spray drops, is represented in Figure 5.10(a) as a function of x, the location with respect to the spray (see scheme Figure 5.1(b)). Data for pure water and emulsions at different concentrations are plotted. Reproducibility experiments with water showed that $DV50$ can be determined with an uncertainty of $\pm$ 5 μm.

First, we find that the emulsions influence the spray angle, θ, which is calculated following $\tan(\theta/2) = W/2H$, where $H = 50$ cm is the distance between the nozzle and the measurement device and W is the width of the spray fan, which is the maximal distance from the center at which drops are detected by the Spraytec apparatus. As shown in Figure 5.10(b), θ continuously increases from 112.9°, for pure water, to 120.2° as the emulsion concentration C increases, and saturates for $C > 0.3$ % v/v. Despite being weak, the increase of the spray angle is an interesting advantage of emulsions over other spray additives. Indeed, high-molecular weight polymers have been observed to notably decrease the spray angle [Dexter 2001]. By increasing the spray angle, the overlap between sprays is potentially increased leading to a better spray distribution homogeneity. Note that this increase of the spray angle has already been observed for different types of emulsions in the literature [Dexter 2001, Hilz 2013a].

Second, we find a clear effect of the emulsion on the size distribution at the center of the spray: the emulsions systematically increase the volume median diameter of the spray compared to that for pure water. This effect increases with increasing emulsion concentration until reaching a maximum and eventually slightly decreasing. On the contrary, the emulsion has almost no effect on the drop size distribution at the edges of the spray. These two effects are clearly visible in Figure 5.11. In Figure 5.11(a), the drop size distributions at the center of the spray, x=0 cm, for pure water and model emulsion at different concentrations are presented. We note that the peak of the distribution is shifted toward bigger drops for the emulsions compared to the case for pure water. This phenomenon is enhanced with the increase of the emulsion concentration up to 0.3 % v/v. For pure water the drop size distribution is centered around 173 μm. For emulsion, it is centered around 197 μm (resp. 225 μm and 225 μm) for C=0.03 % v/v (resp. 0.3 % v/v and 0.6 % v/v). In Figure 5.11(b) is shown the drop size distributions at the edge of the spray, x=+70 cm. In contrast to the data obtained at the center of the spray,

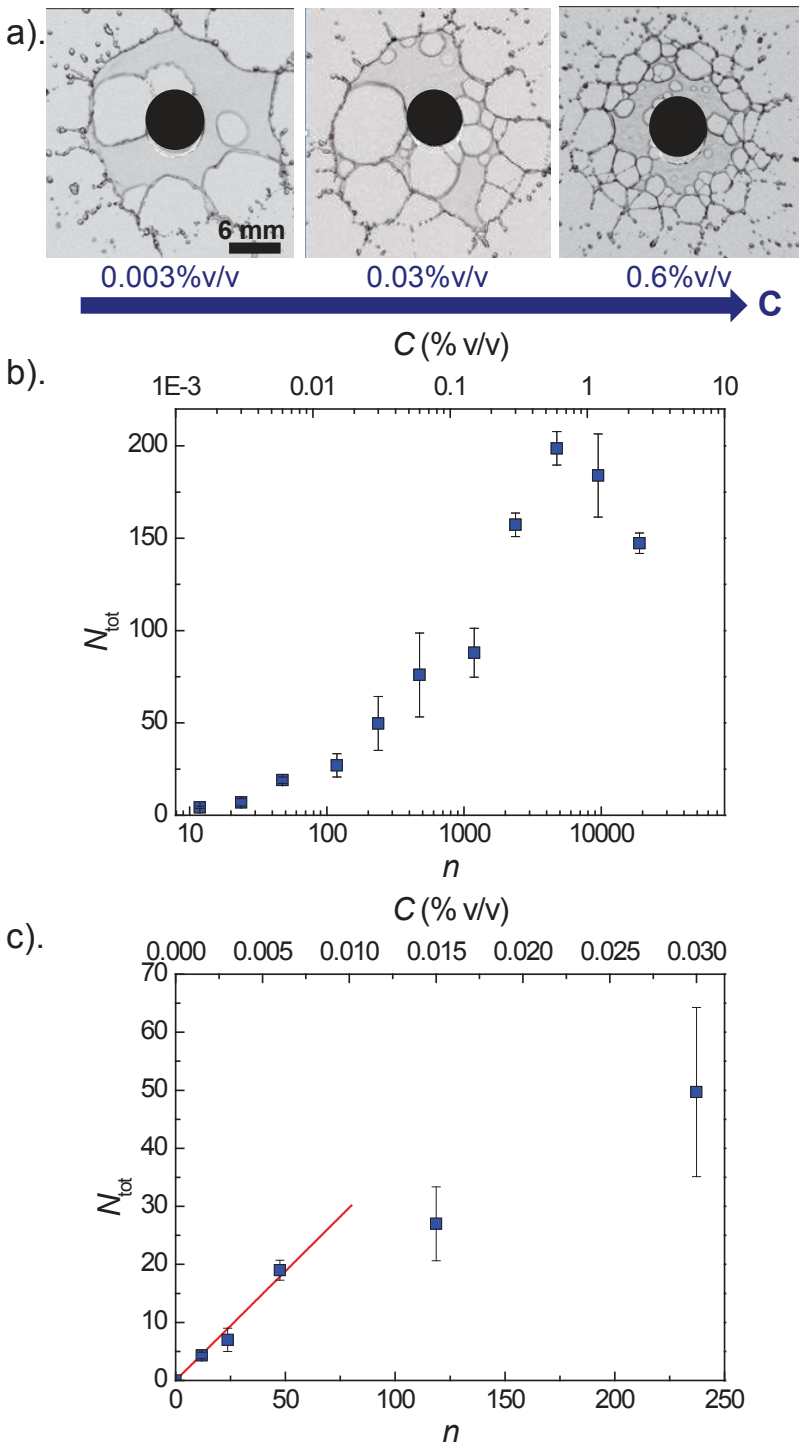

Figure 5.8: a). Images of the emulsion liquid sheet for different emulsion concentrations $C = 0.003$, 0.03 and 0.6% v/v, taken 5.0 ms after the impact of the liquid tear. b). Evolution of the total number of perforation events, N_{tot}, as a function of the emulsion concentration, C, (top x axis) and of the number of oil droplets per impacting tear, n, (bottom x axis). c). Same data as in (b) but plotted on a linear scale and restricted to small n (low emulsion concentration). The red line is a linear fit of the experimental data at small n.

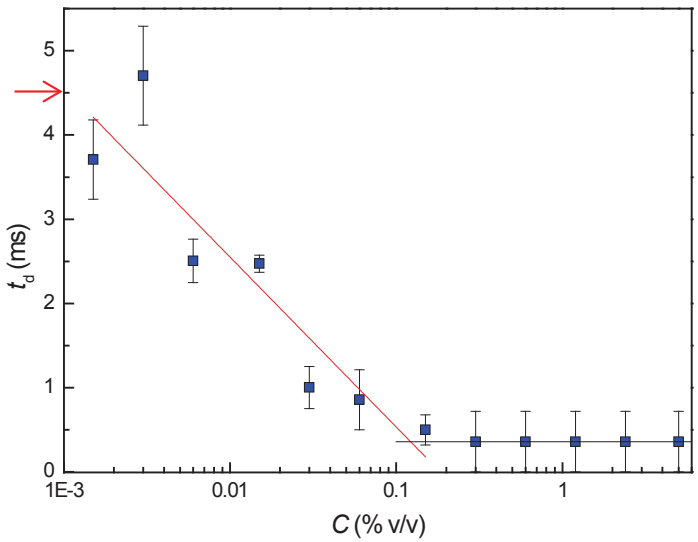

Figure 5.9: Evolution of the delay time, t_d, with the emulsion concentration. t_d characterizes the beginning of the perforation process. An arrow indicates the time corresponding to the maximal expansion of a pure water liquid sheet. The red line is a fit of the experimental data of the form $t_d = k \ln(C/C_0)$ with fitting parameters k=-0.88 and C_0 =0.018 % v/v for $C < C_0$. The black line is a fit of the experimental data for $C > C_0$, $t_d = 0.36$ ms.

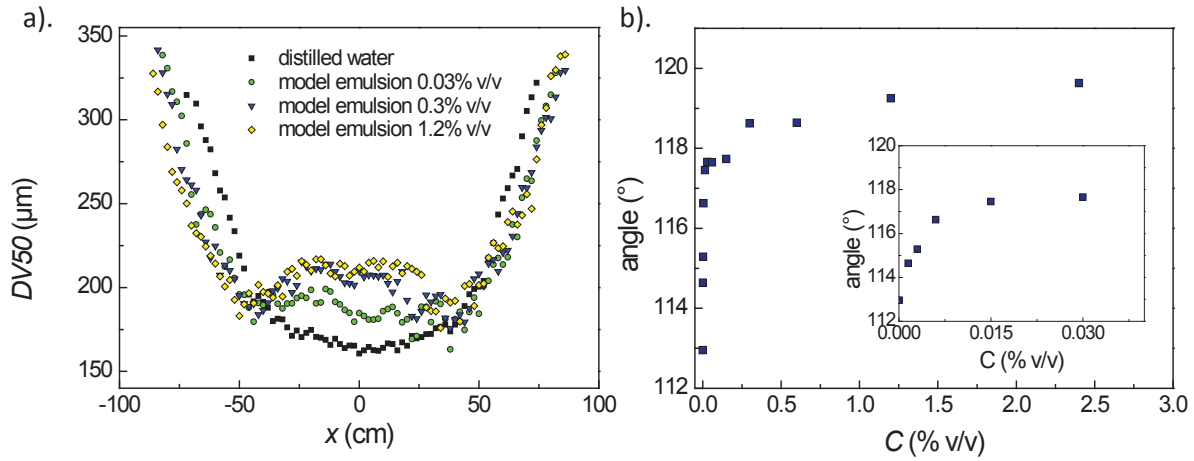

Figure 5.10: a). Evolution of the parameter $DV50$ of the spray drop size distribution as a function of the location along the spray axis for pure water and dilute oil-in-water emulsions at different concentrations, as indicated in the legend. b). Evolution of the spray angle as a function of the emulsion concentration. The inset is a zoom at low concentration.

the drop size distribution at the edge is not impacted by the increase of the emulsion concentration. The drop size distribution for model emulsion is slightly shifted towards smaller drops compared to pure water (size distribution centered around 291 μm for water and around 256 μm for an emulsion with C=0.6 % v/v) but we observe no systematic evolution of the peak position with the emulsion concentration.

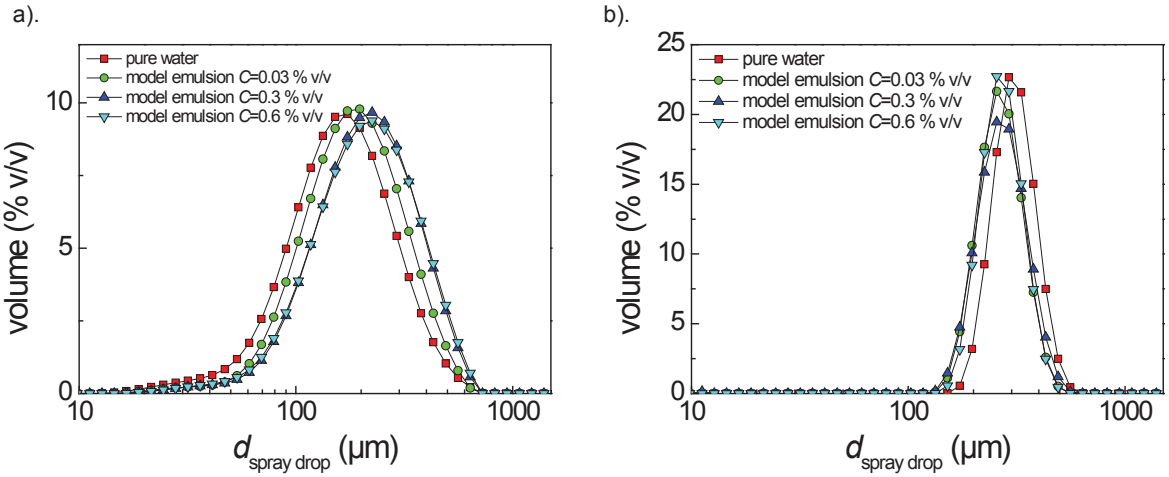

Figure 5.11: a). Volumetric drop size distribution of pure water and model emulsion at different concentrations at a). the center of the spray x=0 cm and b). at the edge of the spray x=+70 cm.

We have quantified this effect by computing the volume median diameter $DV50$ averaged over the whole spray (from $x = -W/2$ to $x = +W/2$), averaged over the center of the spray (from $x = -25$ to $x = +25$ cm) and averaged over the edges of the spray (from $x = -W/2$ to $x = -W/2 + L$ and from $x = W/2 - L$ to $x = W/2$ with L=25 cm). The evolution with emulsion concentration of $DV50$ averaged over the different portions of the spray is plotted in Figure 5.12(a). The values for water are indicated in open symbols and placed arbitrary in the lin/log graph. A first remark is that whatever the emulsion concentration, the spray drops are larger at the edges of the spray than in the center, as already highlighted.

For the data averaged over the edges of the spray (green triangle data points) $DV50$ is equal to 241 μm for pure water. The presence of oil droplets and then the increase of the emulsion concentration have almost no effect on the volume median diameter and the values are found to fluctuate around 250 μm for the model emulsion at different concentrations. For the data averaged over the centre of the spray (red circle data points), we find $DV50 = 158$ μm for pure water and $DV50 = 197$ μm for $C = 1.2$ % v/v. The same behavior is observed if the volume median diameter is averaged over the whole spray (blue square data points), $DV50$ is equal to 181 μm for pure water, and is measured to continuously increase with the emulsion concentration up to a value of 209 μm obtained for $C = (0.6 - 1.2)$ % v/v, and then to very slightly decrease for higher concentrations.

Here the relative increase (16%, as compared to 25% for an average over the centre of the spray) due to emulsions is weaker as the emulsion impacts principally the size distribution in the centre of the spray.

Equivalent conclusions are derived if one computes the evolution of the volume fraction of small drops in the spray, $V150$. Figure 5.12(b) show the evolution of $V150$ in the spray, averaged over the entire spray axis (blue square data points), over the center of the spray (red circle data points) and over the edges of the spray (green triangle data points). At the edges of the spray, the presence of emulsion slightly reduces de proportion of small drops in the spray compared to pure water spray but then the increase of the emulsion concentration has not effect on the proportion of small drops in the spray ($V150$=9.9 % v/v for pure water and $V150 = 5.7 \pm 1.0$ % v/v averaged over the different emulsion concentrations). On the contrary, for the whole spray and at the center of the spray, $V150$ decreases with the concentration down to a plateau value. Hence, an increase of the emulsion concentration entails a continuous diminution of the proportion of small drops in the spray. At the optimal emulsion concentration of 1.2% v/v, the proportion of small drops in the spray is equal to 31.5 % v/v (in the center of the spray), i.e. a diminution of 31 % compared to that for a pure water spray.

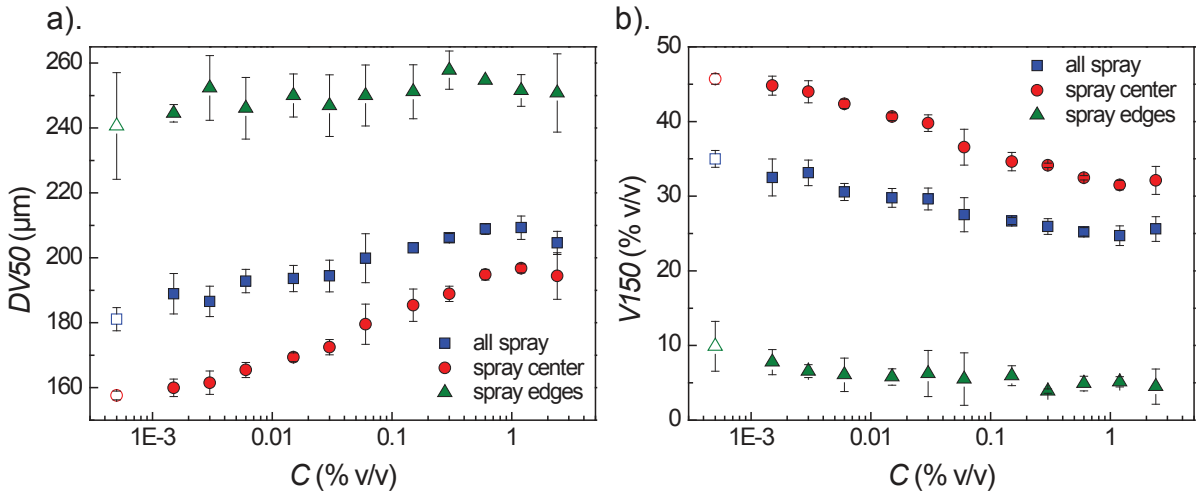

Figure 5.12: a). Evolution of the volume median diameter ($DV50$) of the spray drop size distribution as a function of the emulsion concentration averaged over the entire spray fan, averaged over the center of the spray (-25 cm$< x < 25$ cm) and averaged over the edges of the spray (from $x = -W/2$ to $x = -W/2+L$ and from $x = W/2-L$ to $x = W/2$ with L=25 cm) b). Evolution of the volume fraction of small drops (diameter ≤ 150 μm) in the spray averaged over the entire spray fan, averaged over the center of the spray (-25 cm$< x < 25$ cm) and averaged over the edges of the spray (from $x = -W/2$ to $x = -W/2+L$ and from $x = W/2-L$ to $x = W/2$ with L=25 cm). Symbols are averaged values and error bars correspond to standard deviation. The values for pure water are indicated with open symbols and placed arbitrary in the log/lin graph.

5.2.3 Correlation between model and standard spray experiments

Model single-tear experiments and spray drop size distribution measurements show clearly an impact of the presence of oil droplets in the liquid. Both experiments demonstrate an influence that increases continuously with the emulsion concentration C up to an optimum value of the order of $(0.6-1.2)$ % v/v. The effect of emulsion was quantified by computing the total number of perforation events in a liquid sheet, N_{tot}, from the model single-tear experiment and the parameters from the size distribution of the drops ($DV50$ and $V150$) were obtained from the spray experiment.

To go a step further, we here correlate directly those two sets of parameters. In Figure 5.13, we show the evolution of $DV50$ and $V150$ (averaged over the whole spray or over the center of the spray) as the function of N_{tot}, for the various fluids investigated (pure water and model emulsion at various concentrations). We find a continuous increase (resp. decrease) of $DV50$ (resp. $V150$) with N_{tot} demonstrating clearly a direct correlation between those parameters. More quantitatively we find that functional forms such as $DV50 = DV50_{\text{water}} + kN_{\text{tot}}^{a}$ and $V150 = V150_{\text{water}} - k'N_{\text{tot}}^{a'}$ account well the experimental data. The best fits are shown in Figure 5.13 and the values of the various fitting parameters are listed in the caption of Figure 5.13.

Our data unambiguously show a clear correlation between the total number of perforation events that occur in a liquid sheet formed with the single-tear experiment set-up and the proportion of small drops in the spray measured with the conventional spray experiment. More exactly, the more holes nucleate in the liquid sheet, the smaller is the proportion of small drops in the spray. Our results clearly indicate that the specific perforation mechanism observed for the emulsion is at the origin of the change of the spray drop size distribution. We will discuss the physical origin of the correlation between the total number of perforation events in a liquid sheet and the proportion of small drops in a spray at the end of this chapter (section 5.4).

5.3 Effect of the emulsion droplet size distribution

Another interesting parameter of the emulsion that can be tuned is the size distribution of the oil droplets. In the following, we quantitatively investigate the effect of this parameter on the perforation process and on the spray drop size distribution.

5.3.1 Single-tear model experiments

The droplet size distribution of the model emulsion is modified thanks to the preparation method as described in section 2.1.3.3. In Figure 5.14(a) are represented the droplet size distributions of the different emulsions. The volume median diameters of the drop size distribution, d_{oil}, is varied between 0.5 and 39.1 μm. We show in Figure 5.14(b) the evolution of N_{tot}, the total number of perforation events, as a function of n, the number

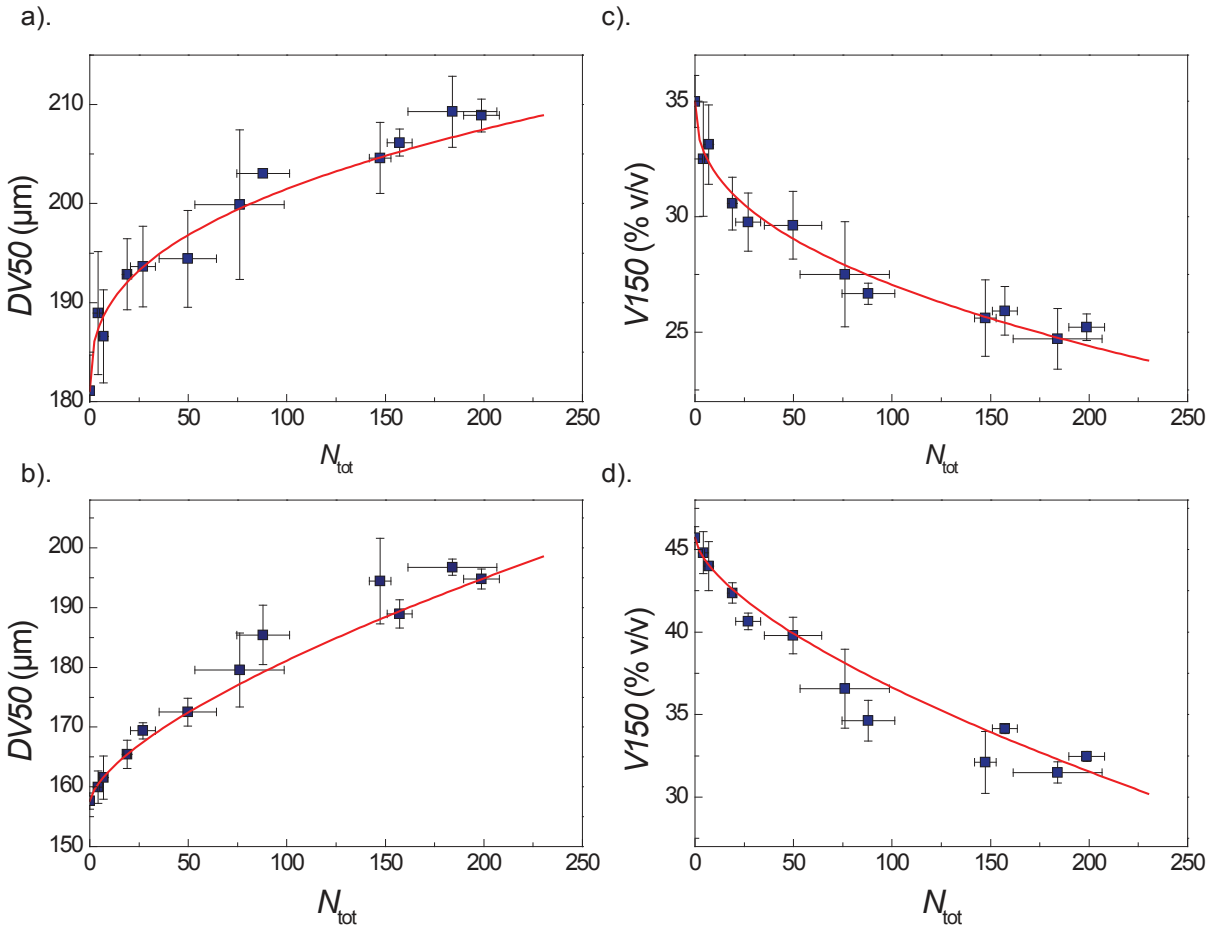

Figure 5.13: (a,b) Correlation between the volume median diameter ($DV50$) of the spray drop size distribution and the total number of perforation events. In a). (resp. b).) $DV50$ is averaged over the entire spray fan (resp. the center of the spray.) (c,d) Correlation between the volume fraction of small drops in the spray ($V150$, $d \leq 150$ μm) and the total number of perforation events. In c). (resp. d).) $V150$ is averaged over the entire spray fan (resp. the center of the spray). Symbols are experimental data and the continuous lines are fits of the form $DV50 = DV50_{\text{water}} + kN_{\text{tot}}^{a}$ (or $V150 = V150_{\text{water}} - k'N_{\text{tot}}^{a'}$) with N_{tot} the number of perforation events, and k (k') and a (a') fitting parameters. The best fits yield a). $k = 3.63$, $a = 0.37$, $R^2 = 0.90$, b). $k = 1.10$, $a = 0.67$, $R^2 = 0.94$; c). $k' = 1.17$, $a' = 0.42$, $R^2 = 0.93$; d). $k' = 0.46$, $a' = 0.65$, $R^2 = 0.93$.

of oil droplets per impacting tear. In all cases, a behavior similar to the one described previously for $d_{\text{oil}} = 39.1$ μm (in section 5.2.1 and Figure 5.8(b)) is measured. We observe that for each emulsion droplet size distribution, the total number of perforation events increases with the number of oil droplets until reaching a maximum and then slightly decreases. However, the curves are found to shift towards smaller n as d_{oil} increases. We note also that the maximum total number of perforation events slightly decreases as d_{oil} decreases. At a given number of oil droplets, bigger droplets are more efficient to

onset the perforation. For example, for $n = 9.5 \times 10^3$, an emulsion with $d_{oil} = 11.7$ μm entails 60 cumulated perforation events whereas an emulsion with $d_{oil} = 39.1$ μm entails 184 cumulated perforation events yielding a more than threefold increase. To obtain the same number of perforation events, say around 45, only 240 droplets of diameter 39.1 μm are required against 2.2×10^9 droplets of diameter 0.5 μm. As observed previously for one oil droplet size distribution (section 5.2.1), for each size distribution, we find at small n values a proportionality between the total number of perforation events, N_{tot}, and the number of oil droplets, n. From the slope of this linear regime, we can determine an effective efficiency of the oil droplets to promote a perforation event. Interestingly, we measure that the effective efficiency continuously and strongly decreases as the oil droplet size decreases (Figure 5.14(c)), from an efficiency of 40 % for $d_{oil} = 39.1$ μm down to an effective efficiency of 8×10^{-6} % for $d_{oil} = 0.5$ μm.

Hence the emulsion droplet size distribution has a dramatic influence on the destabilization mechanism of the liquid sheet and more precisely on the number of holes that perforate the sheet. In the next section, we investigate the effect of the emulsion droplet diameter on the spray drop size distribution.

5.3.2 Spray drop size distribution

Emulsions with different drop size distributions are prepared and sprayed. Before investigating the influence of the oil droplet diameter on the spray drop size distribution, we study the influence of the spraying process on the emulsion. We collect a sample of the sprayed emulsions at the exit of the nozzle, measure its oil droplet size distribution and compare it with the initial one. In Figure 5.15(a) are represented the emulsion oil droplet size distributions before pulverization (filled symbols) and after pulverization (open symbols). We observe in Figure 5.15(a) that the oil droplets with a diameter around 1.3 μm are not broken into the nozzle since the droplet size distributions before and after the pulverization are essentially identical. On the contrary, the emulsions with the bigger oil droplets ($d_{oil} = 28.7$ μm and $d_{oil} = 7.7$ μm) are broken during the pulverization, due to the strong shear and elongation flows the droplets are submitted to [Leal-Calderon 2007], since the oil droplets obtained at the exit of the nozzle have, for both emulsions, a volume median diameter around $(5 - 6)$ μm. This phenomenon is also visible in the microscopic images shown in Figure 5.15(b,c). In Figure 5.15(b) is shown a microscopic image of an emulsion, with d_{oil}=28.7 μm, before pulverization and in Figure 5.15(c) a microscopic image of the same emulsion after pulverization. The breakup of big oil droplets during the pulverization is clearly evidenced. From our experimental results, it is clear that there is a threshold droplet diameter such as droplets with a larger diameter are broken into the nozzle. In our case the threshold diameter is around 5 μm but this threshold diameter may depend on the nozzle used and the operating parameters.

Hence the experimental investigation on the role of the oil droplet mean size is much more restricted here than in the single-tear experiments, since only emulsions with oil

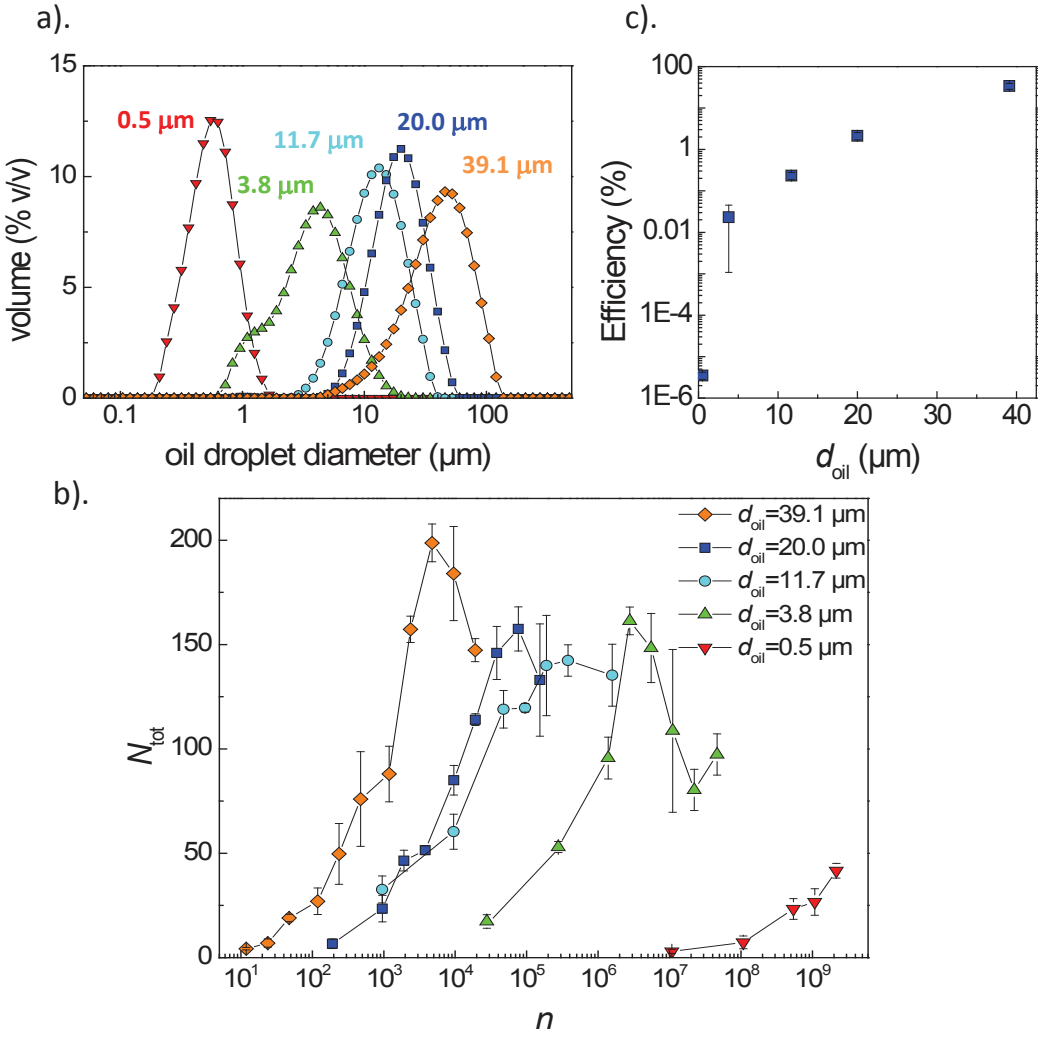

Figure 5.14: a). Emulsion oil droplet size distributions. b). Evolution of the total number of perforation events, N_{tot}, as a function of the number of oil droplets per impacting tear, n, for the emulsions whose droplet size distributions are shown in (a). c). Evolution of the effective efficiency, see definition in the text, of the oil droplets to promote a perforation event as a function of the droplet size d_{oil}. Error bars are indicated in the plot. Most of them are of the size of the symbols or smaller.

droplets below 5 μm can be investigated. Below we compare the drop size distribution of sprays produced with emulsions with median oil droplets of 5 and 0.9 μm

We define $\widetilde{V}150$ as the relative evolution of the volume fraction of small drops in the spray compared to the volume fraction for water, $\widetilde{V}150 = (V150_{water} - V150)/V150_{water}$, where $V150$ is the volume fraction of drops that have a diameter lower than 150 μm and $V150_{water}$ the value of $V150$ obtained with water. We use here this relative parameter (instead of $V150$ as previously) to compare experiments performed at one year interval due to discrepancies observed between these two series of experiments for pure water sprays (5 % of relative difference between the values of $V150$ at the center of the spray

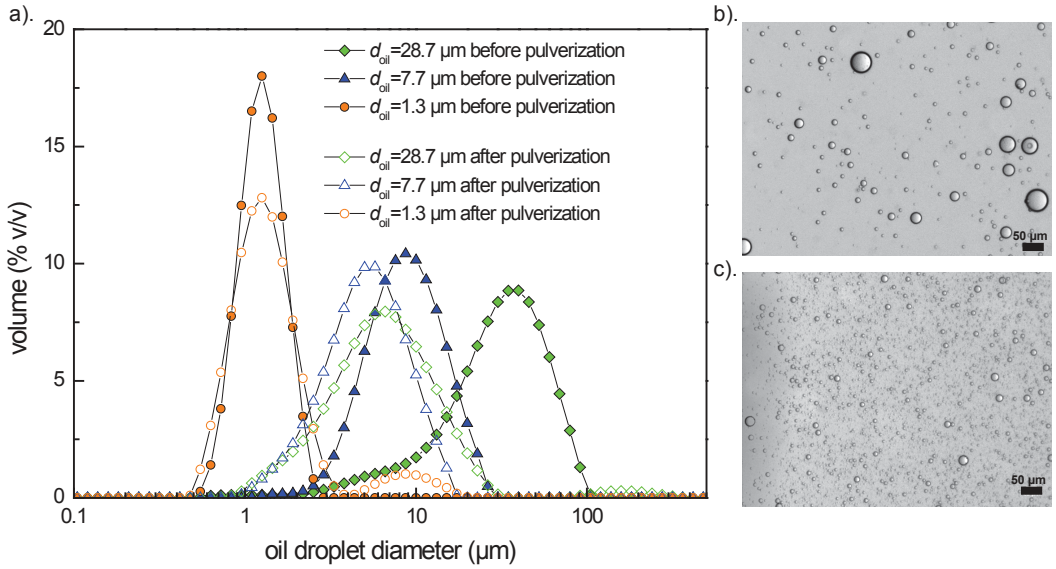

Figure 5.15: a). Oil droplet size distribution of different emulsions measured with a Mastersizer Malvern device. The filled symbols correspond to measurements before the pulverization and the open symbols corresponds to measurements on the samples collected after pulverization. b) Microscopic image of the emulsion with d_{oil}=28.7 μm before pulverization. c). Microscopic image of the same emulsion as in (b) but after pulverization.

for the two sets of experiments for pure water spray). These discrepancies for the water sprays may be due to a modification of the operating parameters that are not controlled such as the precise nozzle used to form the spray and the temperature.

Figure 5.16 shows the evolution of the relative volume fraction of small drops in the spray averaged over the center of the spray, $\widetilde{V}150$, as a function of the number of oil droplets per volume for two emulsions. These two emulsions have different oil droplets size distribution: one emulsion has been prepared by manual agitation yielding $d_{\text{oil}} = 40$ μm but we can estimate that the oil droplet diameter is around 5 μm when they are injected into the liquid sheet as the oil droplets with diameter superior to 5 μm are broken into the nozzle. For the other emulsion, prepared using ultrasound, $d_{\text{oil}} = 0.9$ μm. We observe that for both emulsions the reduction of the volume fraction of small drops in the spray (compared to water) increases with the number of oil droplets, as already observed. For a same number of oil droplets per volume, the bigger oil droplets are more efficient to reduce the proportion of small drops in the spray, in agreement with the observations made by [Qin 2010]. For example, for 10^{10} droplets per liter, the droplets of diameter $d_{\text{oil}} = 5.0$ μm induce a reduction of the volume fraction of small drops in the spray by 20 % compared to water whereas the smaller droplets, $d_{\text{oil}} = 0.9$ μm, induce a reduction by only 5 % compared to water. Our experimental results highlight that emulsions with large oil droplets are more efficient as anti-drift adjuvants than emulsions with smaller oil droplets.

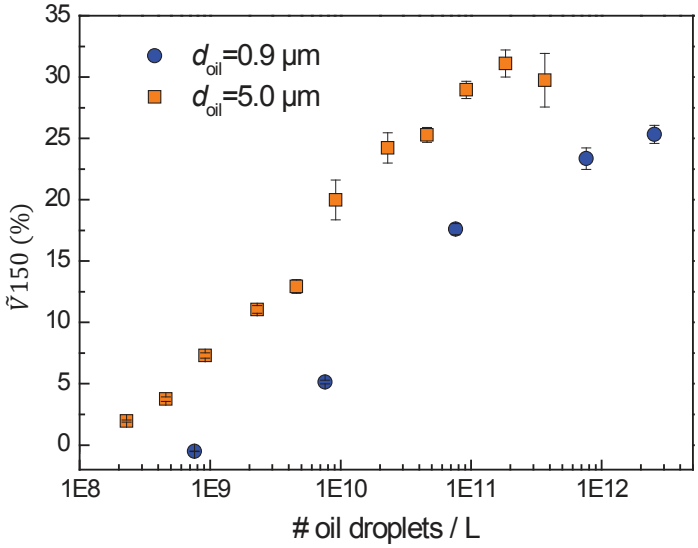

Figure 5.16: Evolution of the relative volume fraction of small drops in the spray averaged over the center of the spray, $\widetilde{V}150$, as a function of the number of oil droplets per volume for two emulsions with different oil droplet size distributions as indicated in the legend.

In both the spray experiment and the single-tear model experiment, we have highlighted a strong influence of the emulsion droplet size. We observe that bigger oil droplets are more efficient to onset the perforation (single-tear model experiment) and more efficient to reduce the volume fraction of small drops in the spray (spray experiment). Once again, we observe a clear correlation between the total number of perforation events and the volume fraction of small drops in the spray. These findings confirm that the perforation mechanism is the mechanism at the origin of the change of the spray drop size distribution. However, due to a breakup process of the oil droplets in the nozzle, the effect of the oil droplet size distribution on the liquid sheet destabilization mechanisms could not be investigated in detail using the spray experiment.

5.4 Discussion

We have seen that the presence of emulsion oil droplets strongly influences the destabilization of liquid sheets and the size distribution of spray drops. We observe a good correlation between the total number of perforation events that occur in the liquid sheet and the proportion of small drops in the spray. The destabilization of the sheet by perforation was also observed with the spray experiment, by taking pictures of the spray as illustrated in Figure 5.17. Perforations cause the sheet to be destabilized closer to the nozzle (compared to a pure water liquid sheet for which there is no perforation). As shown by [Dombrowski 1960] for a liquid sheet issued from a flat-fan nozzle and by us for a model liquid sheet [Vernay 2015c], the thickness of the sheet decreases with the

distance from the nozzle or from the center of the liquid sheet for the model single-tear experiment. The perforation of the liquid sheet leads to the formation of a web of ligaments, these ligaments are then destabilized into drops. The size of drops resulting from the Rayleigh-Plateau destabilization of a ligament scales with the diameter of the ligament, which itself is expected to scale with the thickness of the sheet. Consequently, the drops resulting from the sheet destabilization will be larger as the sheet is thicker, that is closer to the nozzle exit [Dombrowski 1960]. Hence, the more perforation events occur, the closer to the nozzle the sheet will be destabilized and consequently the bigger are the sprays drops, as observed experimentally. This mechanism explains the correlation observed between the number of perforation events occurring in the liquid sheet and the proportion of small drops in the spray.

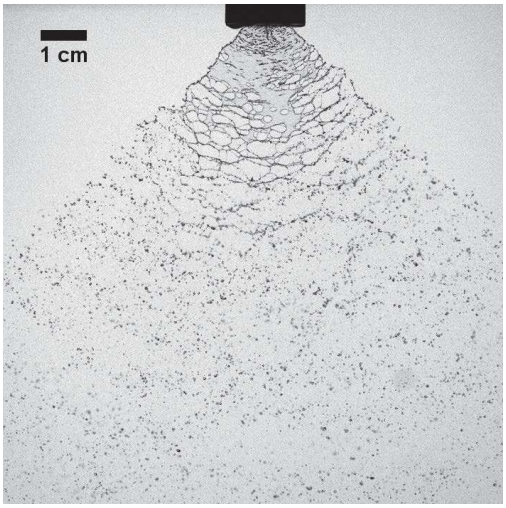

Figure 5.17: Photographic picture of a spray of dilute emulsion at 0.3 % v/v. The spray is generated with a Teejet flat fan XR8002 nozzle at 2.8 bar.

We have seen that the presence of emulsion oil droplets has almost no influence on the drop size distribution at the periphery of the spray. The drop at the periphery of the spray result from the destabilization of the thicker rim bounding the sheet. This rim is destabilized by the formation of short ligaments that are then destabilized into drops [Clark 1972]. We have seen in Chapter 3, that the emulsion does not modify the destabilization of liquid ligaments (compared to water). Hence, the emulsion does not modify the spray drop size distribution at the periphery of the spray (compared to water).

The atomization process of the liquid sheet can be divided into two successive steps: first the destabilization of liquid sheet into ligaments and then the destabilization of these ligaments into drops. From our experimental study, it is now clear that the anti-drift properties of dilute model emulsions arise from the specific destabilization mechanism of liquid sheet into ligaments, i.e. the first step of the atomization process, and not from the destabilization of ligaments into drops.

It is interesting to compare the anti-drift properties of the model emulsion to the ones

of the other category of anti-drift adjuvants, i.e. dilute solution of high-molecular-weight polymer. In Figure 5.18 is shown the evolution of the volume median diameter of spray drop for pure water, different concentrations of the model emulsion and a dilute solution of high-molecular-weight polymer. For this experiment, we used a solution of PEO of molecular weight M=1,000,000 g/mol diluted at 0.05 % w/w in distilled water. For the dilute solution of PEO, we observe a large increase of the drop diameter over the whole width of the spray compared to our findings with water and model emulsion. The PEO solution modifies the drop size at the center of the spray and at the periphery of the spray. On the contrary to model emulsions, the mechanism of action of the dilute solutions of high-molecular-weight polymer as anti-drift adjuvant is related to the destabilization of liquid ligaments, i.e. the last step of the atomization process, as illustrated in Chapter 3. Another major effect of the PEO solution is an important decrease of the spray angle (83° compared to water spray angle 113°). This effect is one the major drawback of solution of high-molecular polymer as anti-drift adjuvants. Indeed, due to the decrease of the spray angle with polymer adjuvants some portions of the crops may be not treated. On the contrary, the dilute emulsions slightly increases the spray angle, which assures a good repartition of the agrochemical solution on the crops.

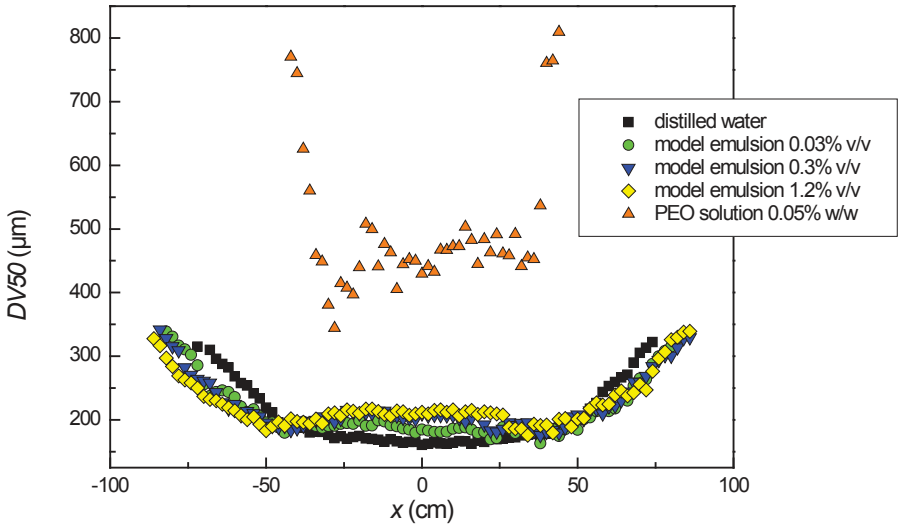

Figure 5.18: Evolution of the parameter $DV50$ of the spray drop size distribution as a function of the location along the spray axis for pure water, dilute oil-in-water emulsion at different concentrations and dilute PEO solution of high molecular weight, as indicated in the legend.

Compared to water, the model emulsion notably reduces the proportion of small drops in the spray and these anti-drift properties are enhanced with the emulsion concentration. The optimal concentration of the model emulsion for anti-drift application is around 0.6 % v/v, by optimal one means smaller quantity of adjuvant that will produce the maximum effect. Our results with the single-tear experiment show that the emulsion

oil droplet diameter is a crucial parameter to control the liquid sheet destabilization by perforation. The physical origin of the influence of the emulsion oil droplets on the sheet perforation will be discussed in Chapter 8. The conventional spray experiments highlight that larger oil droplets are more efficient to reduce the proportion of small drops in the spray. These findings were restricted to a small range of oil droplet diameters as we have seen that emulsion oil droplets are broken into the nozzle if their diameter is larger than a threshold diameter that may depend on the nozzle used and the operating parameters. This information may be crucial in some case. We have seen that emulsion with smaller oil droplets are much less efficient to entail the perforation of the liquid sheet and so to reduce the proportion of small drops in the spray. Therefore if the nozzle used to pulverize the emulsion breaks the oil droplets into very small droplets it could completely annihilate the anti-drift properties of the emulsion whereas the same emulsion with bigger oil droplets would have been a really efficient anti-drift adjuvant. In conclusion, the oil droplet size distribution of the emulsion is a crucial parameter for anti-drift application. Unfortunately it is a parameter difficult to control in practice.

From an application point of view it is interesting to know for a given emulsion concentration what is the optimal number of oil droplets per liter and the optimal size of the oil droplets to formulate an anti-drift adjuvant. We have seen that bigger oil droplets are more efficient to onset the perforation and that the higher is the number of oil droplets per liter the higher is the total number of perforation events per liquid sheet. However, at a given emulsion concentration, these two parameters are not independent and so the optimal anti-drift adjuvant results from a balance between these two parameters. To illustrate this point, the evolutions of the total number of perforation events occurring in a liquid sheet, N_{tot}, as a function of the mean oil droplet size of the model emulsion, d_{oil}, for different concentrations of the model emulsion are plotted in Figure 5.19. We observe that N_{tot} follows a non monotonic evolution with d_{oil}, as a result of the balance between the size of the oil droplets and the number of oil droplets per liter. At a concentration up to 0.15 % v/v, the optimal oil droplet size is around 12 μm whereas at higher concentration (C=0.6 % v/v), our data suggest an optimal oil droplet size around 40 μm. For the flat-fan nozzle used for the spray experiments only oil droplets with a diameter lower than 5 μm are accessible. In this case, for all the emulsion concentrations, higher number of perforation events and so better anti-drift properties are obtained for oil droplets with the larger accessible diameter.

5.5 Conclusion

We have used the single-tear experimental set-up developed in the previous chapter to study the destabilization mechanism of model emulsion-based liquid sheet. We have shown that model emulsion liquid sheets are destabilized by the nucleation of holes within the sheet, following a perforation mechanism. We have characterized the perforation mechanism by quantifying the total number of holes nucleating within the sheet during

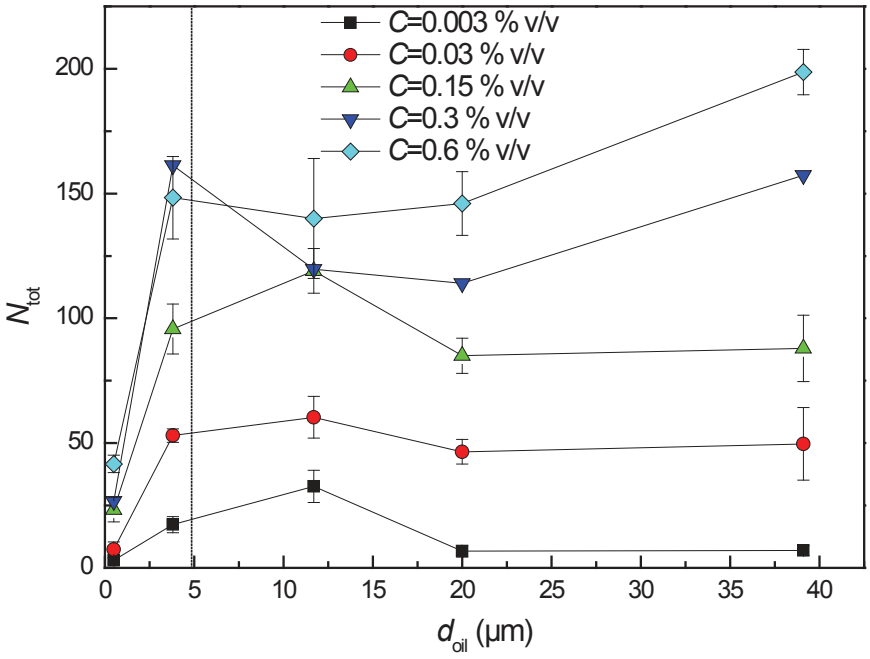

Figure 5.19: Evolution of the total number of perforation events occuring in a liquid sheet, N_{tot}, as a function of the mean oil droplet size of the model emulsion, d_{oil}, for different concentrations of the model emulsion, as indicated in the legend. A dashed line indicates the oil droplet threshold diameter such as bigger oil droplets are broken into the nozzle.

the whole process. We have compared the results obtained with the single-tear experiment to those collected with a conventional spray experiment. The spray experiment enables one to quantify the proportion of small drops in the spray and so to evaluate the anti-drift properties of a solution.

The influence of oil-in-water emulsion concentration and oil droplet size distribution on the perforation mechanism and on the proportion of small drops in the spray were investigated, for concentration spanning more than three orders of magnitude and for droplet sizes ranging from 0.5 to 40 μm. We have highlighted that these two parameters are crucial to control the anti-drift properties of dilute model emulsions.

A very good correlation between the total number of perforation events in a liquid sheet resulting from the impact of a single liquid tear on a small target and the proportion of small drops in the spray was obtained. Our experimental results show that the perforation mechanism of the emulsion liquid sheet is at the origin of the reduction of the proportion of small drops in the spray and so at the origin of the anti-drift properties of such dilute emulsions.

Our study demonstrates that the single-tear experiment is an appropriate model experiment to investigate and gain an understanding of the physical mechanisms governing the spray drop size distribution of anti-drift formulations, and especially of dilute emul-

sions. Quantifying the total number of perforation events that occur in a liquid sheet formed with the single-tear experiment gives an indication of the anti-drift properties of the emulsions investigated. Clearly, the effect of other physical and chemical parameters of the anti-drift formulations can be now simply and systematically investigated with our model experiment. Because a single tear of fluid is needed to perform these experiments, the impact of the nature of the fluid on the destabilization process can be extensively investigated. In fact, the obvious advantages of the single-tear experiments include the simplicity of the experimental set-up and the much smaller quantity of material needed, 30 μL as compared to 3 L for the spray experiment.

We have identified the destabilization mechanism that is at the origin of the anti-drift properties of the model emulsion: the nucleation of holes within the sheet. Our next objective is to understand the mechanism at the origin of the formation of holes within the liquid film.

Chapter 6

Perforation of a dilute emulsion-based liquid sheet driven by a Marangoni effect

Contents

By comparing the results obtained with the single-tear experiment set-up to those collected using a conventional spray technique, we have shown in the previous chapter that the anti-drift properties of the dilute model emulsions result from the perforation of holes within the sheet. The objective of this chapter is to understand the physical mechanisms at the origin of the nucleation of holes in the liquid film. We investigate the perforation mechanism of a model emulsion-based liquid sheet issued from the single-tear experiment. We use the experimental technique developed in the Chapter 4 to visualize the thickness modulations of the emulsion-based liquid sheet during the perforation process. In the first section of this chapter, we highlight the existence of a localized thinning of the sheet leading to the hole formation. In the second section, we study the overall kinematic fields (velocity and thickness) of the perforated liquid sheet. The last sections of this chapter are dedicated to the study of the growth dynamics of the holes and the thinning regions in the sheet and to the description of the mechanism at the origin of the perforation of the sheet. A part of the results presented in this chapter has been published in *Bursting of Dilute Emulsion-Based Liquid Sheets Driven by a Marangoni Effect*, C. Vernay, L. Ramos and C. Ligoure, Physical Review Letters, 115(198302), November 2015 [Vernay 2015b].

6.1 Localized thinning of the liquid sheet leading to hole formation

6.1.1 Experimental set-up and samples

6.1.1.1 Experimental set-up

Controlled liquid sheets are formed with the single-tear experimental set-up presented in Chapter 4. The impact velocity of the tear, u_0, is set at 4 m/s and the tear diameter, d_0, at 3.7 mm, i.e. the volume of the tear is $V_0 = 26.5$ μL.

The impact, the formation and the destabilization of the liquid sheet are visualized from the top with a weak angle using a fast camera (Phantom V7.3) operating at 9,708 pictures per second and with a resolution of 576 pixels $\times$ 552 pixels. The software ImageJ is used for image analysis.

6.1.1.2 Samples

The samples studied in this chapter are model emulsions. For details about the emulsion composition see section 2.1.1.2. The viscosity of the aqueous phase of the emulsion is modified thanks to glycerol/milliQ water mixtures. The different mixtures used as emulsion aqueous phase are: milliQ water (shear viscosity 1.0 mPa.s), glycerol/water 62/38 % w/w (shear viscosity=12.5 mPa.s, tabulated value at 20°C [Sheely 1932]) and

glycerol/water 75/25 % w/w (shear viscosity=36.5 mPa.s, tabulated value at 20°C [Sheely 1932]). In the following, if it is not specified, the aqueous phase is milliQ water. For all experiments, the emulsion concentration, C, is set at 0.3 % v/v. Emulsions are prepared by mechanical stirring. As described in section 2.1.3.3 the viscosity of the aqueous phase does not modify the oil droplet size distribution (see Figure 2.11). For the three different viscosities the volume median diameter of the oil droplets is (20 ± 4) μm.

For some experiments, a water soluble dye, erioglaucine disodium salt, is added to the aqueous phase at a concentration of 2.5 g/L (same dye and concentration as in section 2.1.1.2). The dye solution is filtered before to prepare the emulsion with a filter with pore size 5.0 μm. We have checked that the dye does not influence the viscosity and the surface tension of the aqueous phase. For erioglaucine solution prepared in pure water, we measure a viscosity of 1.0 mPa.s and a surface tension of 71.0 mN/m at 20°C, i.e. values comparable to the ones obtained for pure water. We also check that the addition of dye does not modify the emulsion oil droplet size distribution. In Figure 6.1 is shown microscopic images of a model emulsion prepared in pure water (a) and in water dyed solution (b). We observe similar oil droplet size distributions.

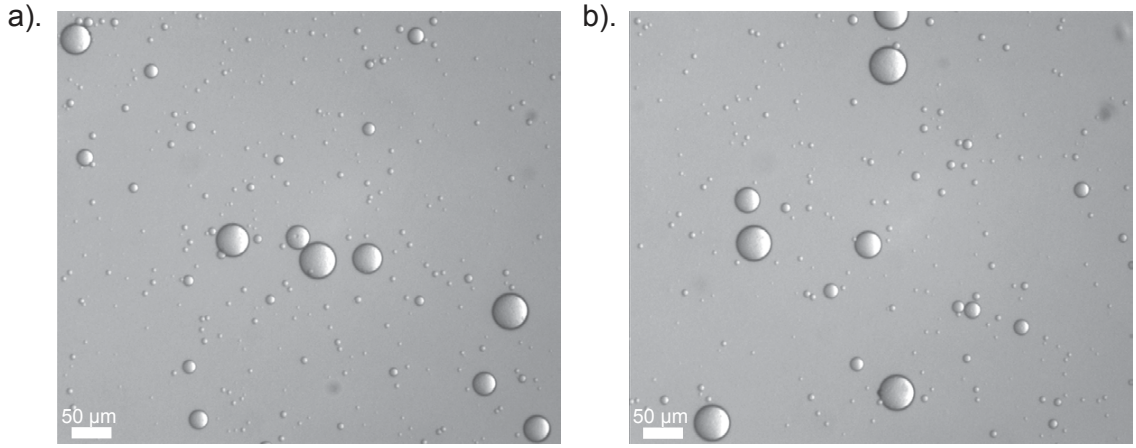

Figure 6.1: Microscopy images of the model emulsion at C=0.3 % v/v prepared in pure water (a) and in water dyed with erioglaucine (2.5 g/L) (b).

6.1.2 Evidence of the existence of pre-hole within the sheet

To investigate the mechanism at the origin of the nucleation of holes within the liquid sheet, we add dye to the model emulsion (as explained in section 6.1.1.2) in order to quantify the thickness field of the liquid sheet during the perforation process. Figure 6.2 displays the destabilization process of a dyed emulsion-based liquid sheet. During its expansion, holes perforate the sheet, and grow until they merge forming a web of ligaments. Thanks to the presence of dye in the emulsion, the modulations of the sheet thickness

are visualized. In Figure 6.2(a), 1.5 ms after the drop impact, the liquid sheet is not perforated, the modulations of the grey level (i.e. the thickness) are similar to the ones of a pure water liquid sheet (section 4.3.2.1 Figure 4.14(c)). In Figure 6.2(b), 4.8 ms after the drop impact, several holes have nucleated and grown in the liquid sheet. We also observe the presence of brighter zones in the sheet corresponding to a localized thinning of the liquid film (some are indicated with black arrows). In Figure 6.2(c), 5.9 ms after the drop impact, almost the whole sheet is perforated; we still observe the presence of brighter zones, which are larger and brighter than at t=4.8 ms. We find that the formation of a hole is systematically preceded by a localized thinning of the sheet (as depicted by brighter zones in the sheet). In the following, the brighter zone that precedes a hole is referred to as pre-hole. Below, we use the term "patch" to refer to both pre-hole and hole.

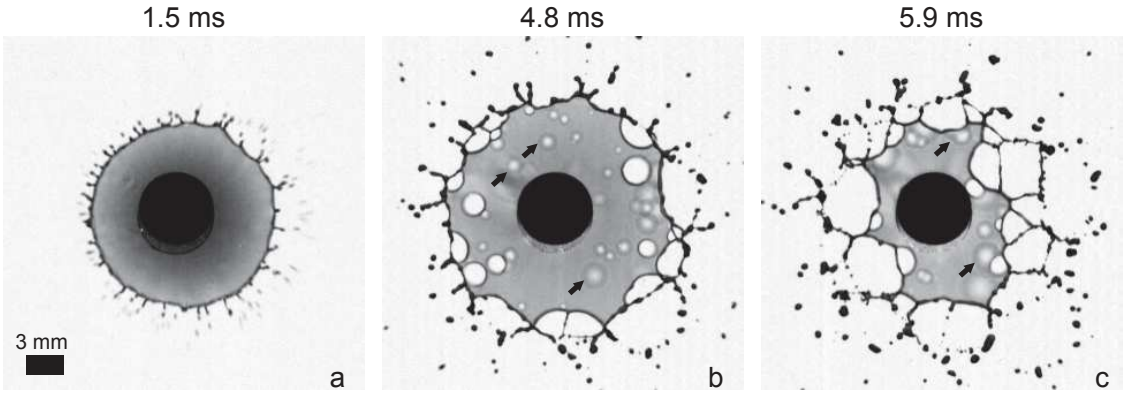

Figure 6.2: Formation and destabilization of a dyed emulsion-based liquid sheet. The origin of time, t, is taken at the drop impact. In (b,c), black arrows indicate some pre-holes.

Figure 6.3 illustrates the dynamics of a patch. The origin of t is taken as the drop impacts the target. At $t = 3.30$ ms we observe the formation of a pre-hole distinguishable by a bright zone surrounded by a darker rim. Until $t = 3.91$ ms, the pre-hole diameter significantly increases and in the same time the pre-hole becomes brighter and brighter highlighting a thinning of the pre-hole. At $t = 4.12$ ms, we observe the formation of a darker, i.e. thicker rim, highlighting the rupture of the liquid film and so the formation of a hole in the sheet. From $t = 4.12$ to 4.32 ms, we observe the growth of the hole that expands in the liquid sheet. The same observations are made for every hole that nucleates in the liquid: a pre-hole, which widens and thins out the sheet with time, systematically precedes the hole nucleation.

In the following, we will study the dynamics of the patches in the sheet. In the next section, we first describe the image analysis performed to characterize the thickness profile of patches.

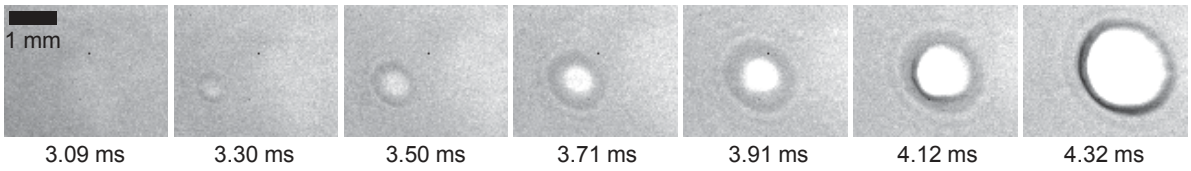

Figure 6.3: Sequence of events of the patch dynamics. The origin of time, t, is taken at the drop impact.

6.1.3 Image analysis

We use the method developed in the Chapter 4 to measure the thickness field of a liquid sheet. The objective is to determine the thickness profile of patches. The thickness measurement method relies on the correlation between the grey level of each pixel of the image of a dyed liquid sheet to the local thickness of the liquid sheet.

We want to determine the thickness profile of the patch as a function of the radial distance from the center of the patch, R, at different times, t. Two radial distances are defined here: r is the radial distance measured from the center of the target and R is the radial distance measured from the center of the patch., i.e. in the referential of the patch. We perform the image analysis in the referential of the patch. Hence, at each time, the origin of the referential is different (in the referential of the laboratory) as the patch is moving in the liquid sheet.

We measure for each pixel of polar coordinates (R,θ) the normalized intensity $I_{\text{norm}}(R,\theta)$ as the ratio between the measured intensity for a given image of the liquid sheet $I(R,\theta)$ and the measured intensity for an image taken just before the drop impact. The liquid sheet thickness $h(R,\theta)$ is then evaluated thanks to the calibration curve (section 4.2.2 Figure 4.11(a)). Then, the thickness profiles are averaged over all azimuthal angles, θ, to obtain a mean thickness that only depends on the radial distance from the center of the patch, R, and on time, t: $h(R,t) =< h(R,\theta,t) >_\theta$.

6.1.4 Thickness profiles of patches

The thickness profiles of the patch shown in Figure 6.3 are given in Figure 6.4. Here the thickness h of the film is plotted as a function of the radial distance R (the origin is taken at the center of the patch) for different times, t (where the origin of t is taken as the drop impacts the target). Below, the numerical values for t and h correspond to the patch considered in Figure 6.3 but the described scenario is robust, and holds for every patch. At short time, $t = 3.09$ ms, the pre-hole is not yet formed and the thickness profile, $h(R)$, is flat with a mean value equal to 71 μm. At $t = 3.30$ ms, the profile reveals a thinning in the center of the patch, $h(0) = 53$ μm, followed by a smooth bump with a maximal thickness of 81 μm corresponding to the rim of the pre-hole. Outside the bump, the thickness profile reaches a plateau, h_{out}, corresponding to the undisturbed

sheet. With time, the pre-hole thins down to $h(0) = 12\,\mu$m at $t = 3.91$ ms and widens up to a radius $R_{\rm ph} = 0.75$ mm. At $t = 4.12$ ms, the film ruptures in the center of the patch. The pre-hole to hole transition is clearly noticeable through a sharp peak in the thickness profile corresponding to the thicker, i.e. darker, rim surrounding the hole and a vanishing thickness of the inner zone of the patch.

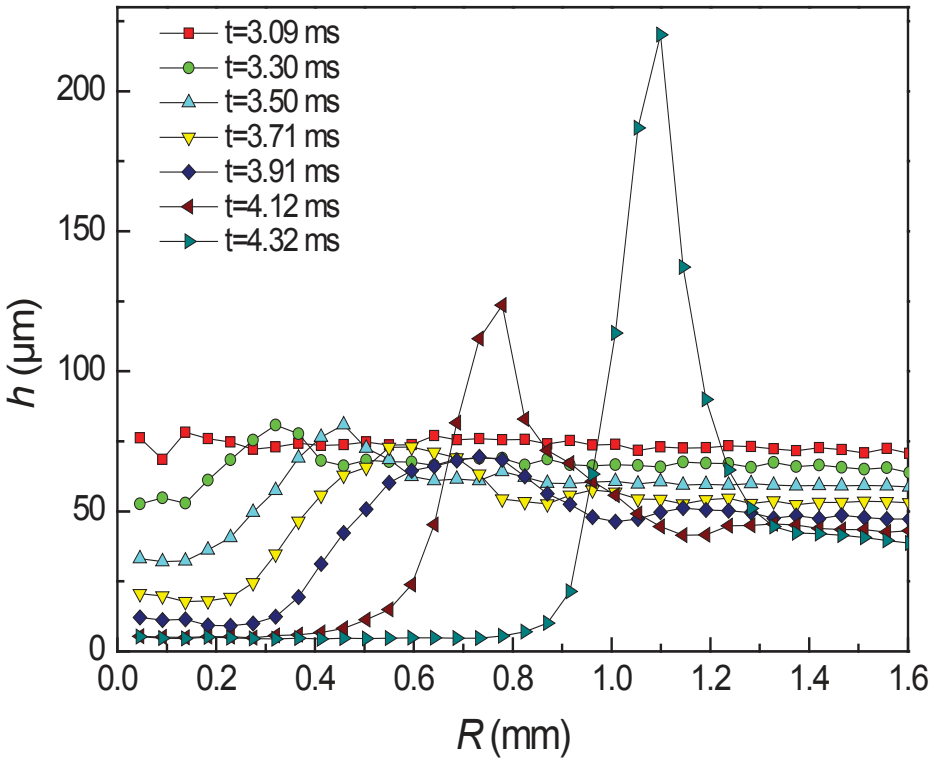

Figure 6.4: Thickness profiles of the patch (pre-hole, then hole) as a function of the radial distance from the patch center for different times as indicated in the legend.

6.2 Overall kinematic fields of the perforated liquid sheet

We here discuss the overall dynamics of the liquid sheet. In the first part of this section, we present the image analysis performed to characterize the kinematic fields of the perforated sheet. In the second and third parts, the results concerning the velocity and thickness fields of the emulsion-based liquid sheet are described.

6.2.1 Image analysis

We locate the patches in the sheet by binary thresholding the images using ImageJ. This allows one to determine the pre-hole and hole contours and to determine their position in the sheet, i.e. their radial distance from the origin taken at the center of the target. Thanks to these measurements, we are able to determine the trajectories of the patches within the sheet.

The thickness of the liquid film in the outside vicinity of the patch, h_{out}, is inferred from the thickness profiles of the patches (see Figure 6.4). These profiles reveal a thinning zone in the center surrounded by a thicker zone, the rim. Outside the bump corresponding to the rim, the thickness profile reaches a plateau value corresponding to the thickness in the outside vicinity of the patch, h_{out}. Knowing the trajectories of the patch within the liquid sheet, one is able to determine the evolution of h_{out} along the patch trajectory.

6.2.2 Velocity field of the perforated liquid sheet

Figure 6.5 displays the time evolution of the positions of the centers of the patches. We compile on the same graph data for holes observed without dye (open square symbols), pre-holes observed with dye (filled circle symbols) that perforate the sheet leading to the formation of holes (open circle symbols). For each patch, we observe that the radial position, r, (the origin of r is the center of the target) varies linearly with time, indicating a constant radial speed within the sheet, V_{patch}. No discontinuity at the perforation transition is depicted, as data corresponding to pre-holes (filled circles) and data corresponding to holes (open circles) follow a unique straight trajectory.

Once plotted as a function of r/t, we find that for all patches, V_{patch} is proportional to r/t, (Figure 6.6). This scaling is the one expected for a plain unperturbed expanding liquid sheet [Villermaux 2011, Rozhkov 2004]. We experimentally find a proportionality factor of 0.86, comparable to the theoretical one (1.0).

6.2.3 Thickness field of the undisturbed liquid sheet

The quantitative correspondence with unperturbed plain liquid sheets is further confirmed by measurement of the thickness field. Figure 6.7 shows the evolution of the thickness of the film in the outside vicinity of the patch, h_{out}, as a function of $1/rt$ for a pre-hole (filled symbols) and the corresponding hole (open symbols). The plot shows that there is no discontinuity of h_{out} at the pre-hole to hole transition, and that all over the process the thickness is proportional to $1/rt$, with a proportionality constant $\alpha = (1.19 \pm 0.23)$ mm^{2}ms. This thickness field corresponds quantitatively to that of an expanding plain water sheet (without holes) as experimentally observed in section 4.3.4 and theoretically predicted [Villermaux 2011]. The proportional constant α is theoretically predicted to read $\alpha = \frac{{d_0}^3}{12u_0}$ [Villermaux 2011]. With an impact velocity $u_0 = 4.0$ m/s

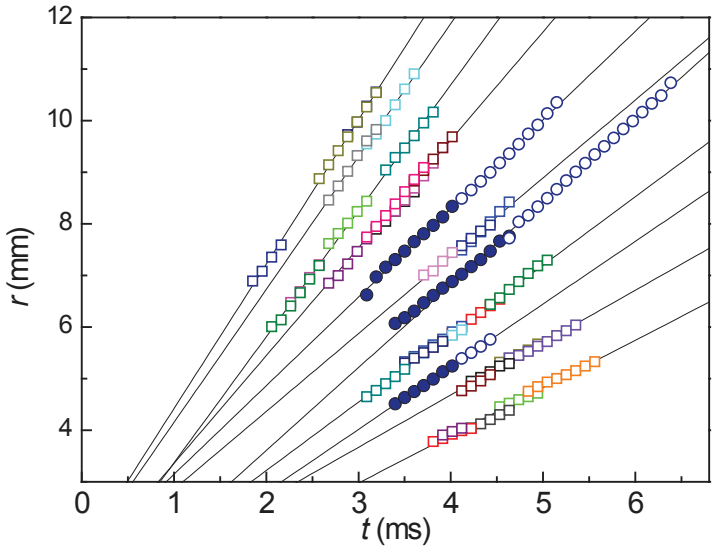

Figure 6.5: Trajectories of various patches (symbols), with the best linear fits (lines). Open squares: holes (without dye) ; filled circles: pre-holes (with dye) open circles : holes (with dye).

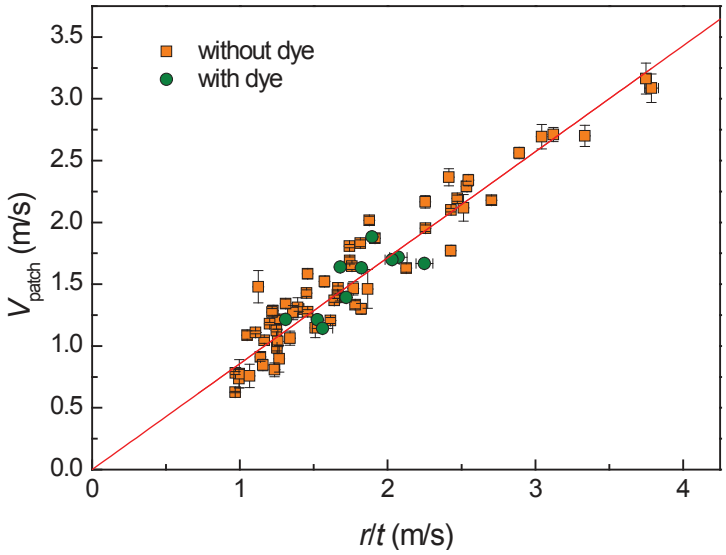

Figure 6.6: Evolution of the radial patch velocity as a function of r/t. The red lines is the best linear fit.

and an emulsion drop diameter $d_0 = 3.7$ mm, one finds $\alpha = 1.05$ mm^{2}ms, a value in very good agreement with the experimental one. This result indicates that the perforation of the sheet does not perturb the thickness field of the sheet outside the patches. Therefore each pre-hole can be viewed as a closed system, such that all the liquid evacuated from the pre-hole thinning zone is transferred in its rim.

Overall, the results of Figure 6.7 and Figure 6.6 conclusively demonstrate that the kinematic fields of the liquid sheet (velocity and thickness) are not perturbed neither by the presence of oil droplet in the sheet, or by the perforation events.

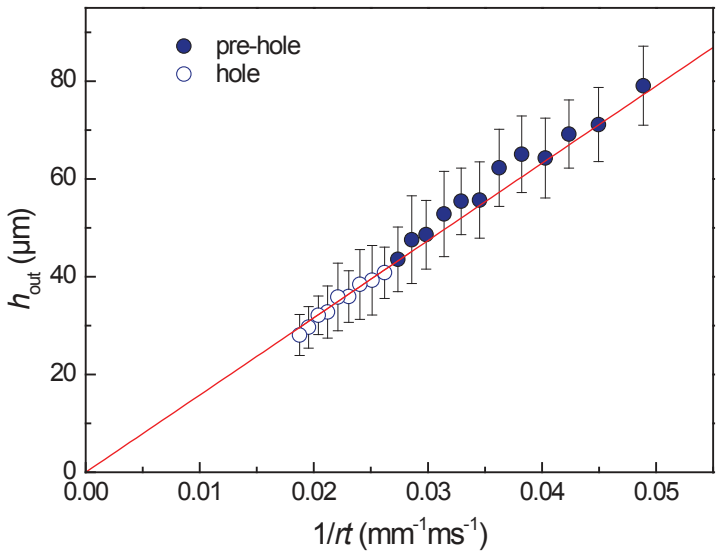

Figure 6.7: Evolution of the sheet thickness h_{out} in the vicinity of a patch with $1/rt$, where r is the radial distance from the center of the target. The red lines is the best linear fit.

6.3 Pre-hole to hole transition

In Figure 6.8 is plotted the evolution of the thickness in the center of the patch (R=0) with the time elapsed since the pre-hole formation, $T = t - t_{\text{ph}}$ (here t_{ph} corresponds to the time at which the pre-hole forms). At short time, the thickness in the center of the patch decreases rapidly with time, from 76 μm down to 5 μm in 1 ms. A thickness of 5 μm corresponds to the limit of the resolution of the thickness measurement method, this is why once the hole is formed (open symbols) we still measured a thickness of 5 μm. Therefore, given the uncertainty of our measurement at small thickness, the thickness in the center of the patch cannot be used as an unambiguous indicator of the pre-hole to hole transition. By contrast, this transition is clearly identified looking at the growth dynamics of the patch or at the thickness of the rim.

The evolution of the patch radius, R_{patch}, as measured at the maximum of the thickness profile, with the time elapsed since the pre-hole formation, T, is shown in Figure 6.9(a). The pre-hole to hole transition event, i.e. the rupture of the film, is clearly evidenced by a discontinuity in the dynamics of R_{patch}. This discontinuity separates two distinct regimes, corresponding to the pre-hole and hole growths. Those two regimes are described in details is sections 6.4 and 6.5.1. The pre-hole to hole transition event can also be inferred

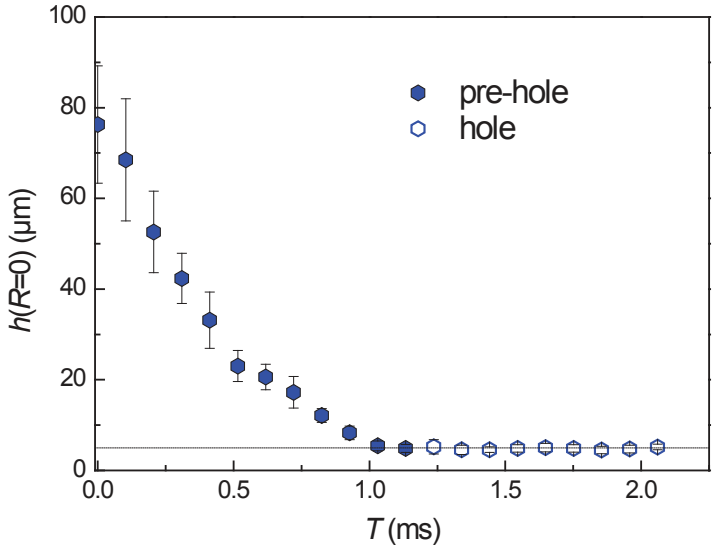

Figure 6.8: Evolution of the thickness in the center of the patch with the time elapsed since the formation of the pre-hole, T, for the patch shown in Figure 6.3.

from the time evolution of the thickness of the rim bounding the patch (Figure 6.9(b)). For the pre-hole, the thickness of the rim slightly decreases with time from a thickness of 78 μm at the pre-hole formation down to a thickness of 67 μm at T=0.9 ms. The rupture of the liquid film entails a sharp increase of the rim thickness up to 220 μm.

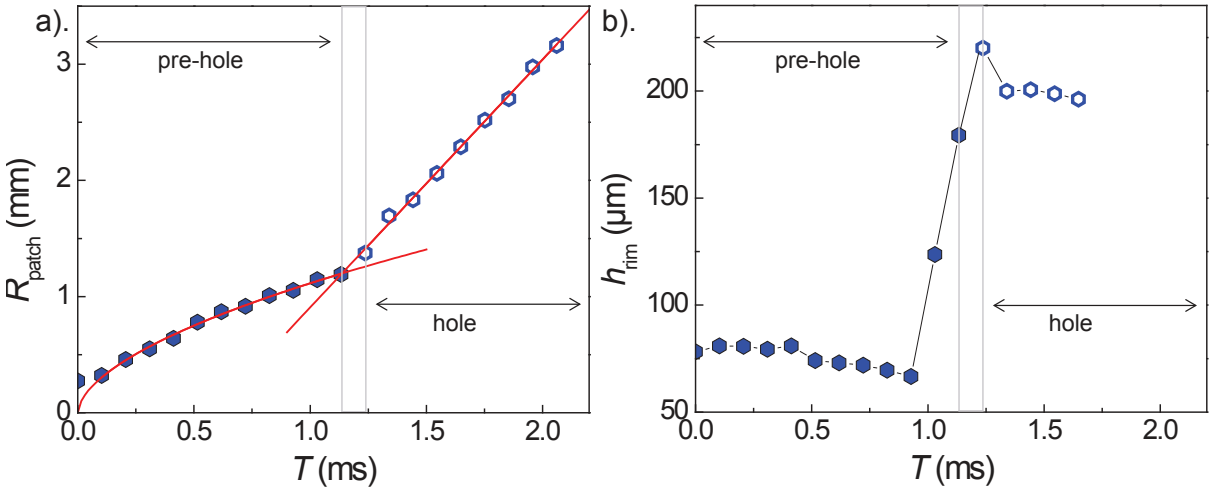

Figure 6.9: Evolution of a). the radius of the patch and b). the thickness of the rim of the patch (filled symbols: pre-hole, open symbols: hole) with the time elapsed since the formation of the pre-hole, T, for the patch shown in Figure 6.3. In (a) the solid lines are the best power law fit, resp. linear fit, for the dynamics of the pre-hole, resp. hole.

In conclusion, the rupture of the liquid film that leads to the nucleation of a hole in the

liquid sheet is clearly marked by discontinuities of the time evolution of the rim thickness and patch radius. These discontinuities separate two distinct regimes, corresponding to the pre-hole and hole growths. In the following sections, we will investigate separately these two regimes.

6.4 Hole growth dynamics

We first focus on the second regime of the time evolution of the patch radius. Figure 6.10 displays the evolution of the hole radii, R_h, for more than twenty holes as a function of the time elapsed since the nucleation of the hole, at time t_h. We find that R_h increases linearly with time with a constant opening velocity $V_\mathrm{c} = (1.64 \pm 0.16)$ m/s. The constant velocity results from a balance between the rim inertia and surface tension in the film as predicted by Taylor [Taylor 1959] and Culick [Culick 1960] for the rupture of a soap film:

$$V_\mathrm{c} = \sqrt{\frac{2\gamma}{\rho h_\mathrm{out}}} \tag{6.1}$$

with ρ the density of the liquid, γ its surface tension, and h_out the thickness of the film in the hole periphery. Taylor-Culick's law is very robust and is generally used to measure film thicknesses. Here, by contrast, our data allow one to quantitatively check this law. We take $\rho = 998$ kg/m^3 the density of the emulsion. We take the value of the surface tension of emulsion measured at short times ($\leq$ 50 ms) $\gamma = 70.1$ mN/m, which is determined with a bubble pressure tensiometer (see section A.1 for details about the bubble pressure tensiometer) and which is found comparable to that of pure water ($\gamma = 72.2$ mN/m). For the thickness of the film, one considers the thickness experimentally measured in the outside periphery of the hole at the hole formation, $h_\mathrm{out} = \alpha/rt$ with $\alpha = (1.19 \pm 0.23)$ mm^{2}ms (Figure 6.7) taking for r and $t = t_\mathrm{h}$ the values at the hole formation. An average over the twenty holes considered yields: $h_\mathrm{out} = (49.6 \pm 7.2)$ μm. One thus predicts $V_\mathrm{c} = (1.68 \pm 0.12)$ m/s, a numerical value in excellent agreement with the experimental value. The standard deviation of the theoretical value of V_c arises from the standard deviation of the thickness in the outside periphery of the hole at the hole formation. The range of the thickness of the sheet when a hole nucleates is very limited, $h_\mathrm{out} = (49.6 \pm 7.2)$ μm. This explains the low standard deviation of V_c and the superimposition of the experimental curves obtained for each hole in Figure 6.10. If the thicknesses at the hole formation were varying over a larger range for the different holes, we would expect the curves to not be superimposed and to have different slopes as the opening velocity, V_c, depends on the thickness at the hole formation.

Up to now, we have considered the thickness in periphery of the hole at the moment of the hole formation. However, the thickness in periphery of the hole decreases as the hole travels in the liquid sheet. We could expect a deviation of the Taylor-Culick law (Equation 6.1), which assumes a constant thickness in periphery of the hole, and so a non

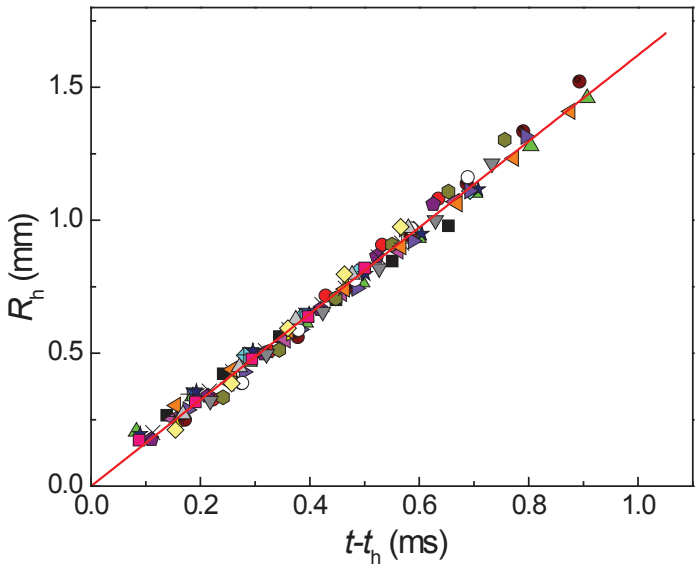

Figure 6.10: Evolution of the radius of the holes as a function of the time elapsed since the hole formation. Data for more than 20 holes are plotted, each color corresponding to a given hole. The red line is the best linear fit.

constant opening velocity of the holes. In the review paper of Altieri et al. [Altieri 2014] hole growth rate for a non constant thickness field is reported. The analysis leads to the following differential equation relating the hole opening velocity (V_c), the hole radius (R_h), the sheet thickness in periphery of the hole (h_{out}) and the time:

$$h_{out} V_c \frac{dR_h^2}{dt} + h_{out} {R_h}^2 \frac{dV_c}{dt} + R_h^2 V_c \frac{dh_{out}}{dt} = \frac{4R_h\gamma}{\rho} \tag{6.2}$$

For typical numerical experimental values ($h_{out} \approx 40$ μm; $\Delta h_{out} \approx 20$ μm; $\Delta t \approx 1$ ms; $V_c \approx 1.6$ m/s; $\Delta V_c \approx 0.4$ m/s; $R_h \approx 1$ mm), one can check that the last two terms of the left hand-side of Equation 6.2 are negligible compared to the first one, leading to the same expression as from the analysis of Taylor [Taylor 1959] and Culick [Culick 1960]:

$$V_c = \sqrt{\frac{2\gamma}{\rho h_{out}(t)}} \tag{6.3}$$

However in Equation 6.3 the time dependence of h_{out} has to be taken into account. Knowing the sheet thickness field (section 6.2.3, $h_{out} = \alpha/rt$ with $\alpha = (1.19 \pm 0.23)$ mm^{2}ms), one can express the opening velocity as a function of the hole coordinates in the liquid sheet (r, t):

$$V_c(t) = \sqrt{\frac{2\gamma r t}{\alpha\rho}} \tag{6.4}$$

In the section 6.2.2, we have seen that the holes travel in the liquid sheet with a constant radial velocity: $V_{patch} = \frac{r}{t}$. Hence, the radial position of a hole at time t is defined:

$$r = \frac{r_0}{t_h} t \tag{6.5}$$

with r_0 the radial position of the hole at its formation at time t_h. From Equation 6.4 and Equation 6.5, one can deduce the expression of the opening velocity, V_c, as a function of the time:

$$V_c(t) = \sqrt{\frac{2\gamma r_0}{\alpha \rho t_h}} t \tag{6.6}$$

By integrating this expression and considering that the hole nucleates at time t_h hence $R_h(t_h) = 0$, one obtains:

$$R_h(t) = \sqrt{\frac{\gamma r_0}{2\alpha \rho t_h}} (t^2 - {t_h}^2) \tag{6.7}$$

In Figure 6.11 is plotted for one given hole the experimental measurement of the evolution of the hole radius, R_h, as a function of the time elapsed since the hole formation, $t - t_h$, (blue square symbols). On the same graph is plotted the evolution of R_h as a function of the time elapsed since the hole formation given by Equation 6.7. We observe that in the time scale where the hole growth is measured, data can be very well accounted by the expression of R_h considering a constant thickness equal to that at the nucleation time ($t = t_h$) (dotted line). Over the time scale considered, the analytical expression of R_h given by Equation 6.7 does not strongly differ from the linear evolution predicted by the Culick-Taylor expression by considering a constant thickness in periphery of the hole equal to the thickness at the hole formation (dotted line). At larger time and larger hole radii, one nevertheless expect a stronger deviation from a linear evolution (as shown in the inset of Figure 6.11). This regime is not accessible in our experiments. This regime has been observed in a recent paper by Lastakowski et al. [Lastakowski 2014], the authors studied the opening velocity of holes produced in liquid sheets by a defect. Due to the fact that they observed a single hole, they were able to follow its dynamics during a time longer than the time of measurement in our experiments. Indeed, in our experiments, we are limited by the fact that a high number of holes nucleate in the liquid sheet. Lastakowski et al. measured the evolution of the hole radius with time and observed a parabolic evolution due to the variation of sheet thickness in periphery of the holes as explained above (Equation 6.7). With their experimental data, it is clearly visible that at longer time the evolution of the hole radius strongly deviates from a linear evolution.

6.5 Pre-hole formation due to Marangoni spreading of oil droplet at the air/water interface

6.5.1 Pre-hole growth dynamics

The evolution of the pre-hole radius, R_{ph}, as a function of the time elapsed since its formation, $T = t - t_{ph}$, is plotted in Figure 6.12 for different aqueous phases, whose zero-shear viscosity varies between 1 and 36.5 mPa.s. We find that, for the three aqueous phases investigated, R_{ph} increases with the time elapsed since the pre-hole formation

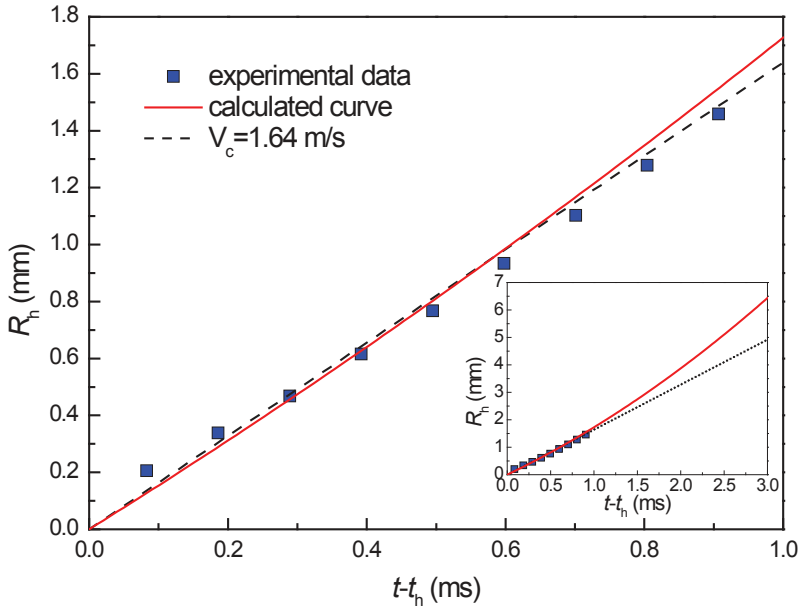

Figure 6.11: Evolution of the hole radius, R_{h}, as a function the time elapsed since the hole formation. On the plot are superimposed our experimental data points (blue square symbols), the parabolic expression of the hole radius which accounts for the variation with time of the sheet thickness in periphery of the hole (Equation 6.7, red solid line), and the curve obtained by considering a constant opening velocity calculated from Taylor-Culick expression (Equation 6.1) with h_{out} equal to the thickness in periphery of the hole at the hole formation (black dotted line). (Inset) Same data plotted over a larger range of time to highlight the deviation of the parabolic expression from the linear evolution for large radii.

as a power law with an exponent 3/4: $R_{\mathrm{ph}} = kT^{\frac{3}{4}}$. The sublinear power law of the time evolution of R_{ph} can also be visualized in the lin/lin plot in Figure 6.9(a) (filled symbols). In Figure 6.12, we note that the prefactor k is a decreasing function of the viscosity. This scaling suggests a widening dynamics in agreement with the dynamics of Marangoni spreading, i.e. the spontaneous spreading of a thin film (of, say, the oil phase) along the surface of a deep fluid layer (of, say, the aqueous phase) of higher surface tension [Fay 1969, Joos 1977, Foda 1980] (see section 6.5.2.1). We will argue that such mechanism can be at the origin of the pre-hole formation and growth.

6.5.2 Marangoni spreading

We here perform classical Marangoni spreading experiments. In the first part of this section, we describe the theoretical predictions concerning the spreading of an oil droplet at the air/water interface. Then, in a second part we present the experimental set-up used. The last part of this section is dedicated to the description of our experimental

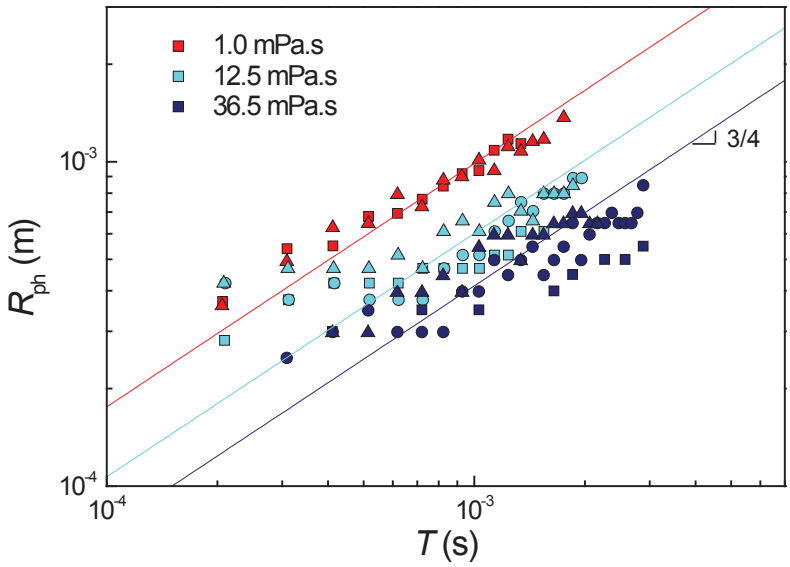

Figure 6.12: Evolution of the radius of the pre-hole, R_{ph}, as a function of T, the time elapsed since the pre-hole formation for the different viscosities of the emulsion aqueous phase. Different symbol types correspond to different experiments. The lines are the best fits of the experimental data of the form $R_{\mathrm{ph}} = kT^{3/4}$.

results.

6.5.2.1 Theoretical predictions

The spontaneous spreading of an oil droplet deposited at the air/water interface is a classical example of the Marangoni effect. The driving stress of the spreading is the surface tension gradient associated with the presence of an oil drop at the interface between the air and the liquid film. This driving stress leads to a viscous shear stress which causes the liquid in the film to flow from regions of low surface tension to regions of high surface tension resulting in the deformation of the interface with a localized thinning of the film and in the spreading of the oil drop at the interface.

The time evolution of the radius of a Marangoni driven thin film spreading on a deep liquid was first proposed by Fay [Fay 1969] and determined by a simple force balance. We consider a radially expanding oil layer at the air/water interface. The r coordinate denotes the radial direction of spreading and z the vertical direction. z=0 corresponds to the position of the air/water interface. We define $R_{\mathrm{spreading}}$ as the radius of the spreading drop (see Figure 6.13).

The force per unit of length driving the spreading process is the spreading coefficient, S, which results from the surface tension gradient stress along the spreading film.

$$\frac{d\gamma}{dr} = \frac{S}{R_{\mathrm{spreading}}} \tag{6.8}$$

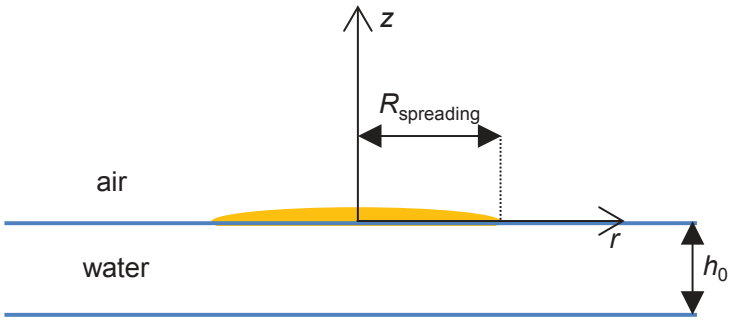

Figure 6.13: Sketch of the spreading of an oil droplet at the air/water interface with the definition of $R_{\text{spreading}}$ and the r- and z-axis.

S is defined as $S = \gamma_{\text{air/aq}} - \gamma_{\text{air/oil}} - \gamma_{\text{aq/oil}}$, where $\gamma_{\text{a/b}}$ stands for the interfacial tension between phases "a" and "b", and "aq" stands for the aqueous phase. A positive value of S indicates that it is thermodynamically favorable for the oil drop to spread at the interface, whereas a negative value implies that the oil drop remains as a lens at the interface. We here consider the simplest case that assumes a constant surface tension along the spreading film, i.e. a constant driving force. This driving force is retarded by the viscous drag force due to the viscous stress in the underlying liquid boundary layer. Indeed, during spreading a shearing stress, τ_{S}, is induced by the spreading film on the underlying liquid.

$$\frac{d\gamma}{dr} = \tau_{\text{S}} \tag{6.9}$$

The shear stress, τ_{S}, can be expressed as

$$\tau_{\text{S}} = \eta \left(\frac{\partial v_{\text{r}}}{\partial z} \right)_{z=0} \tag{6.10}$$

with η the viscosity of the bulk aqueous liquid and v_{r} the radial velocity. An exponential decreasing velocity profile into the underlying liquid is assumed: $v_{\text{r}} = v_{\text{r}}(r, z = 0, t)e^{mz}$ with m^{-1} the hydrodynamical penetration depth given by

$$m^{-1} = \sqrt{\frac{\eta t}{\rho}} \tag{6.11}$$

with η and ρ the viscosity and density of the bulk aqueous liquid. The spreading rate at the surface is

$$v_{\text{r}}(r, z = 0, t) = \frac{dR_{\text{spreading}}}{dt} \tag{6.12}$$

Consequently, the shearing stress, τ_{S} is

$$\tau_{\text{S}} = \left(\frac{\eta\rho}{t} \right)^{1/2} \frac{dR_{\text{spreading}}}{dt} \tag{6.13}$$

Integrating Equation 6.9 using Equation 6.13 gives the expression of the spreading radius $R_{\text{spreading}}$

$$R_{\text{spreading}} = \sqrt{\frac{4}{3}} \frac{S^{1/2}}{(\eta\rho)^{1/4}} t^{3/4} \tag{6.14}$$

Theoretical [Dipietro 2006] and experimental studies [Foda 1980, Camp 1987, Bergeron 1996] have confirmed the power-law behavior with an exponent 3/4. Some controversies remain about the value of the numerical prefactor, K. Here we take $K = \sqrt{4/3}$ but its exact value is subject to discussion and numerical values between 0.665 and 1.52 have been mentioned [Dussaud 1998]. This theoretical description holds for oil drops spreading on a deep fluid pool, i.e. when the thickness of the underlying liquid is larger than the hydrodynamical penetration depth, m^{-1} (Equation 6.11). In the other case, for the spreading of an oil droplet over a thin aqueous film of thickness h_0, the relevant length scale in the vertical direction is not anymore the penetration length, m^{-1}, but the thickness of the thin film, h_0, as $h_0 << m^{-1}$. Ahmad et al. [Ahmad 1972] predicted the evolution of $R_{\text{spreading}}$ for an oil droplet spreading over a thin film

$$R_{\text{spreading}} = \sqrt{\frac{2h_0 S}{\eta}} t^{1/2} \tag{6.15}$$

This expression is obtained by the same argument as for the deep pool configuration but considering h_0 instead of m^{-1} for the vertical characteristic length. Different experimental and theoretical studies [Dussaud 2005, Gaver 2006] have confirmed the power-law behavior but an exponent of 1/4 is measured, which differs from the one predicted by [Ahmad 1972] (Equation 6.15).

6.5.2.2 Experimental set-up and image analysis for macroscopic experiments

The radial spreading of an oil droplet at the air/water interface is measured by tracking hydrophobic particles on the surface. A glass Petri dish of 9 cm diameter is filled with the aqueous phase of the emulsion to a height of 1 cm. Talcum particles are sprinkled on the surface very carefully to not disturb the aqueous pool. A droplet of the oil phase of the emulsion (i.e. the mixture of oil and surfactants referred in the following as "oil phase") of 4 μL is carefully deposed at the air/water interface with a micropipette. The experimental procedure is depicted in Figure 6.14(a) and (b). The deposition of the oil droplet yields a radial spreading of the oil, visualized thanks to the particle motion (as shown in Figure 6.14(c)). The spreading process is recorded with a fast camera (Phantom V7.3) operating at 5,000 pictures per second.

The image analysis is performed using the software ImageJ. We locate the tracking particles by binary thresholding the images. This allows one to determine the contours of the spreading oil droplet and measure the spreading area (A). An apparent radius of the spreading oil droplet is simply deduced from the spreading area according to $R_{\text{spreading}} = \sqrt{\frac{A}{\pi}}$.

6.5.2.3 Spreading of oil droplets at the air/aqueous phase interface

The evolution of the radius of the oil spreading area, $R_{\text{spreading}}$, is plotted in Figure 6.15(a) as a function of time T (the origin is taken at the moment of the deposition of

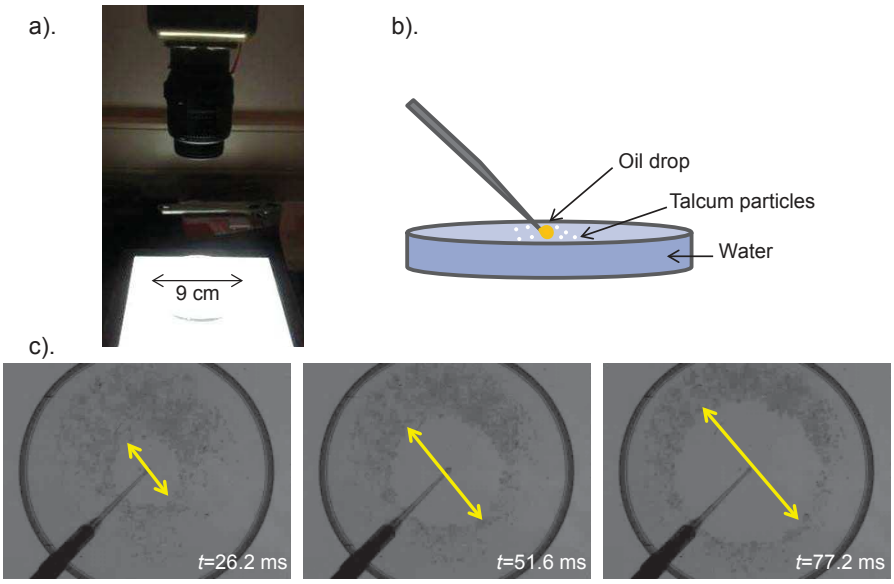

Figure 6.14: a). Picture of the experimental set-up with the Petri dish (diameter 9 cm) filled with the aqueous phase of the emulsion and the fast camera used to record the spreading process. b). Sketch of the deposition of the oil droplet with a micropipette at the air/water interface with talcum particles. c). Pictures of the spreading process at different time after the droplet deposition as indicated on the legend. The yellow arrows indicate the spreading diameter of the oil droplet.

the oil drop at the interface) for the different viscosities of the bulk liquid. As expected from the theoretical predictions of Marangoni spreading in deep pool regime (Equation 6.14), the data for $R_{\text{spreading}}$ follow a power law with an exponent 3/4: $R_{\text{spreading}} = kT^{3/4}$. Our results show moreover that the prefactor k decreases with the viscosity as theoretically predicted.

In the next section, we will compare the results obtained for the pre-hole growth dynamics (single-tear experiment, section 6.5.1) and the results obtained for the spreading of an oil drop at the air/water interface (classical Marangoni experiments) to determine if a same physical mechanism is at play in these two processes.

6.5.3 Comparison between single-tear experiments and classical Marangoni spreading experiments

In Figure 6.16(a) is superimposed the time evolution of the radius of the spreading area, $R_{\text{spreading}}$, for the classical Marangoni experiment (open symbols) and the time evolution of the pre-hole radius, R_{ph}, for the single-tear experiment (filled symbols), for the different viscosities of the aqueous phase. For the single-tear experiment, the origin of T is taken at the moment of the formation of the pre-hole and for the classical Marangoni experiment, the origin of T is taken at the moment of the deposition of the oil drop at

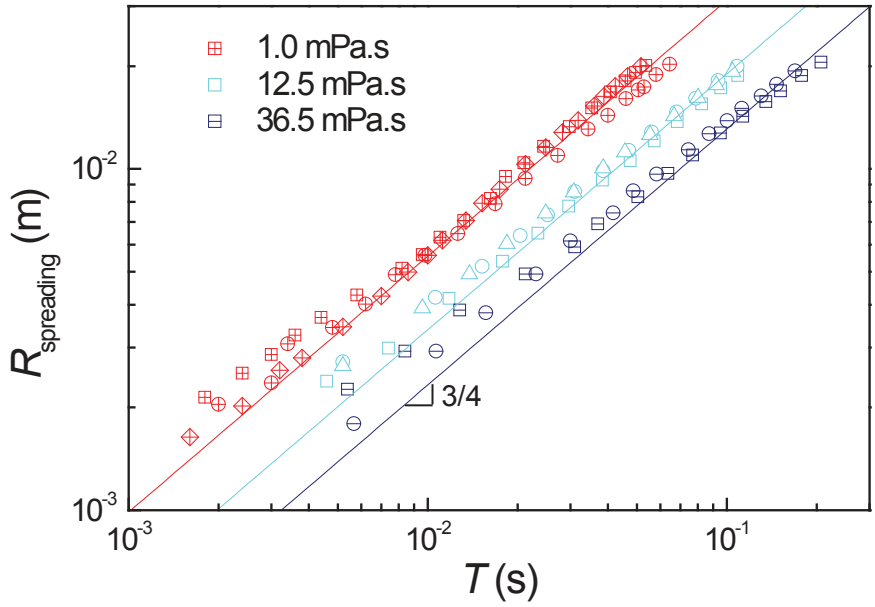

Figure 6.15: Evolution of the spreading radius, $R_{\text{spreading}}$, as a function of T, the time elapsed since the since the deposition of an oil drop. Different symbol types correspond to different experiments. The lines are the best fits of the experimental data of the form $R_{\text{spreading}} = kT^{3/4}$.

the interface. Hence, for both types of experiments, $T = 0$ corresponds to the beginning of the spreading.

We observe that, although the time scales involved in the two types of experiments are significantly different, the data points for R_{ph} and $R_{\text{spreading}}$ lie on a unique curve for each viscosity, suggesting the same prefactor, k, and showing that the same mechanism drives the two processes. For both experiments, the prefactor k manifestly decreases with viscosity. For surface tension gradient-driven spreading , the prefactor k is expected to vary as $k = KS^{1/2}/(\rho\eta)^{1/4}$, where $K = \sqrt{4/3}$. ρ and η are the density and the viscosity of the bulk aqueous liquid and S is the spreading coefficient (Equation 6.14).

To quantitatively check the scaling of the prefactor k, R_{ph} and $R_{\text{spreading}}$ are re-plotted as a function of the rescaled parameter $\chi = T^{3/4}/(\rho\eta)^{1/4}$ in Figure 6.16(b). Remarkably, all the data acquired in the two experiments and for different viscosities of the aqueous phases fall on a unique master curve, with a slope of 1, as expected. Hence R_{ph} and $R_{\text{spreading}}$ are proportional to χ with a proportionality constant $KS^{1/2}$ (Equation 6.14). A spreading parameter S can thus be directly extracted from the slope of the linear evolution of the spreading radius with χ (Figure 6.16(b)). One finds $S = (28.2 \pm 4.8)$ mN/m. This value can be directly compared to macroscopic measurements of the spreading parameter. The value of $\gamma_{\text{air/oil}}$ is measured with a Wilhelmy plate tensiometer and is equal to 29.5 mN/m. The surface tension of the aqueous phases of different viscosities, $\gamma_{\text{air/aq}}$, is also measured with a Wilhelmy plate tensiometer: $\gamma_{\text{air/aq}} = 72.2$ mN/m for η=1.0 mPa.s,

$\gamma_{air/aq}$ = 65.5 mN/m for η=12.5 mPa.s and $\gamma_{air/aq}$ = 64.9 mN/m for η=36.5 mPa.s. Averaged over the different viscosities, $\gamma_{air/aq} = (67.5 \pm 4.1)$ mN/m. The interfacial tension between the oil and aqueous phases is measured thanks to a spinning drop tensiometer (see Appendix A.2). Due to the lack of availability of the set-up, only the interfacial tension for the aqueous phase of viscosity equal to 1.0 mPa.s was measured: $\gamma_{aq/oil} = 1.1$ mN/m. From these surface tension measurements, one estimates $S = (36.9 \pm 4.1)$ mN/m. Hence, $S > 0$, a prerequisite for Marangoni spreading. Moreover, the values derived from direct measurements and the one derived from the master curve are in reasonable agreement considering, specifically, the fact that the numerical value of K. Here we take $K = \sqrt{4/3} \simeq 1.15$ but its exact value is subject to discussion as already mentioned (section 6.5.2.1 [Dussaud 1998]).

The deep pool assumption, for which the power law exponent of the spreading is 3/4, holds when the penetration length $m^{-1} = \sqrt{\frac{\eta T}{\rho}}$ is smaller than the thickness of the sub-phase, h. The time evolution of the penetration length for the different viscosities of the sub-phase is shown in Figure 6.17. For the classical Marangoni spreading experiments (time scale=$(3 \times 10^{-3} - 10^{-1})$ s), the thickness of the underlying liquid (set at 1 cm) is always larger than the penetration length. For the single-tear experiments (time scale=$(2 \times 10^{-4} - 3 \times 10^{-3})$ s), the penetration length, m^{-1}, varies between 14 to 78 μm at $T = 2 \times 10^{-4}$ s for the different viscosities and between 53 to 302 μm at $T = 3 \times 10^{-3}$ s. During the sheet expansion, its thickness ranges roughly from 25 to 225 μm. In Figure 6.17, the grey dashed area represents the time scale involved in the formation of pre-holes and the thickness of the liquid sheet, h. The assumption $m^{-1} < h$ is verified for pure water ($\eta = 1.0$ mPa.s) and marginally true for the two more viscous solutions. However, we do not measure significative deviation from the spreading law predicted in the deep pool regime, as one would expect once entering the thin-film regime ($m^{-1} \sim h$) [Ahmad 1972] (Equation 6.15). Hence, the rupture of the film seems to occur in the spreading regime predicted by the deep pool assumption. One possible reason is that the liquid sheet expands freely in the air (free boundary conditions) contrary to the assumptions in thin film models. We experimentally determine the time to rupture as the time elapsed from the pre-hole formation to the film rupture, t_c. For the water-based emulsion, an average over 10 pre-holes yields : $t_c = (1.15 \pm 0.44)$ ms. We find that this time is comparable to $\frac{\rho h_0^2}{\eta} = (2.8 \pm 0.07)$ ms the time at which $m^{-1} \sim h_0$, with $h_0 = (52.6 \pm 12.8)\mu$m, the thickness of the sheet when the pre-hole forms (averaged over the 10 pre-holes). In conclusion, we experimentally find that the film ruptures in the deep pool spreading regime.

The comparison of the pre-hole growth dynamics and of the spreading of an oil drop at the air/water interface clearly indicates that the same physical mechanism is involved in the two processes. Hence, the pre-hole formation and growth result from the spreading of an oil drop at the air/water interface. For the classical Marangoni experiment, the oil droplet is deposited at the air/water interface and for the pre-hole formation the oil droplet enters the air/water interface from the bulk aqueous phase. These two configurations are comparable once the oil droplet is at the air/water interface because the

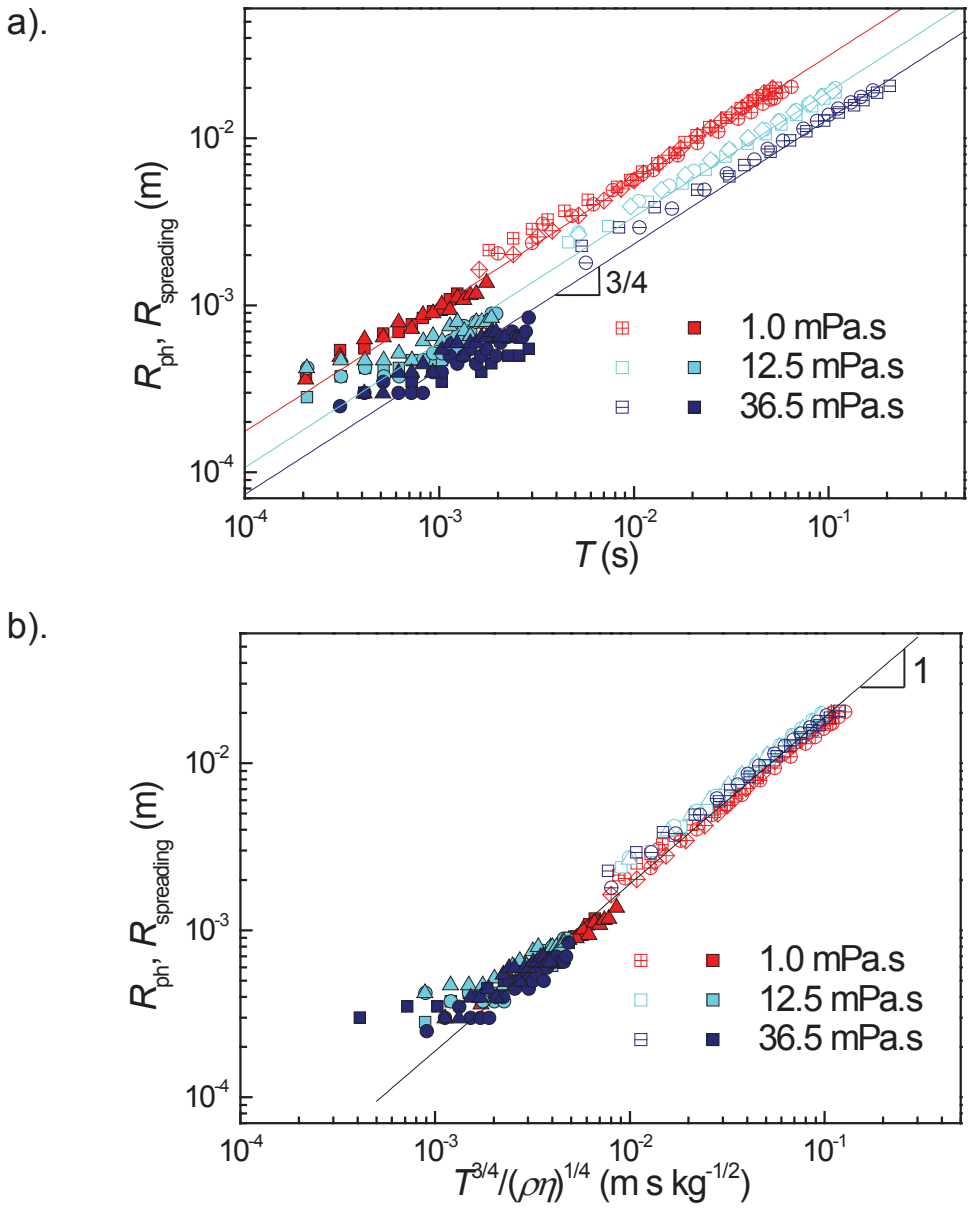

Figure 6.16: a). Evolution of the radius of the pre-hole, R_{ph}, in the single-tear experiment (filled symbols), resp. of the spreading radius, $R_{\mathrm{spreading}}$, in the standard Marangoni experiments (open symbols), as a function of T, the time elapsed since the pre-hole formation, resp. since the deposition of an oil drop. Different symbol types correspond to different experiments. The lines are the best fits of the experimental data of the form $R_{\mathrm{ph}} = kT^{3/4}$. b). Same data as in (a) plotted as a function of $T^{3/4}/(\rho\eta)^{1/4}$.

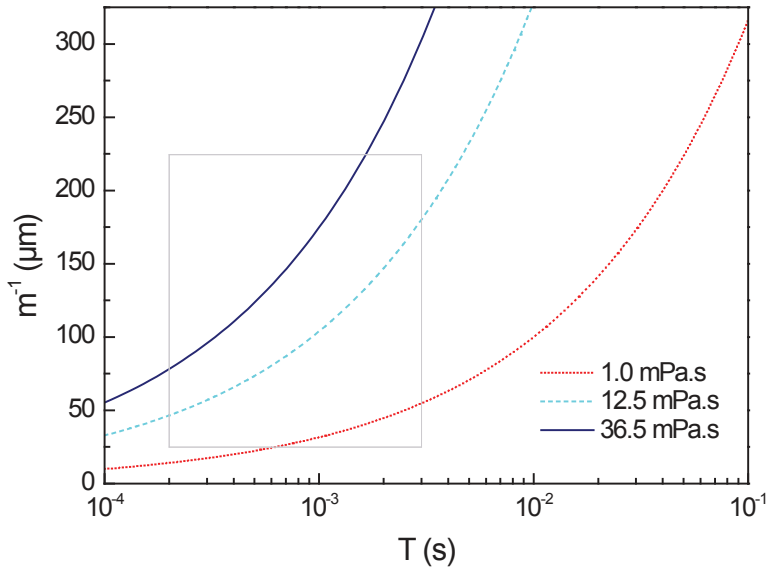

Figure 6.17: Time evolution of the penetration length m^{-1} for the different viscosities.

surfactants are not soluble in the aqueous phase. Hence the surfactants are only located in the oil phase and at the oil/water interface and not at the air/water interface (see sketch Figure 6.18).

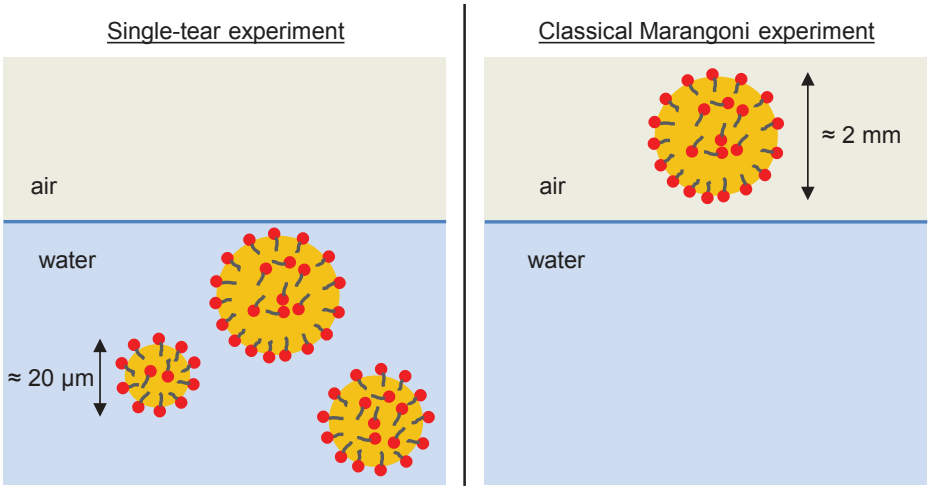

Figure 6.18: Sketch of the two experimental configurations. At the left, in the single-tear experiment, surfactant-stabilized oil droplets reach the air/water interface. At the right, in the classical Marangoni experiment, droplet of the mixture of oil and surfactants are deposited at the air/water interface.

In the next sections, we will detail the exact mechanism at the origin of the pre-hole formation and so at the origin of the nucleation of holes within the sheet. But first, we will compare our experimental results with some mechanisms proposed in the literature.

6.6 Mechanism at the origin of the perforation of the liquid sheet

6.6.1 Do the holes appear when the sheet thickness is comparable to the oil droplets?

As reviewed in the first chapter of the thesis (section 1.4), different mechanisms have been proposed in the literature to explain the formation of holes in liquid sheets made of suspension (solid suspension or oil-in-water emulsion). In particular, Dombrowski et al. suggested that the necessary conditions for perforation are a dewetting of the inclusions by the fluid and an inclusion diameter equal to or larger than the thickness of the liquid sheet in order that inclusions cause perforation by puncturing both interfaces of the sheet [Dombrowski 1954]. In their study, inclusions were solid particles or oil droplets. The authors argued that bigger inclusions would cause the perforation of the sheet at larger thicknesses of the liquid film.

To test this assumption, we measure the thickness of the liquid sheet in the hole periphery at the hole formation, h_{out}, for two model emulsions with different oil droplet size distributions (d_{oil}=20.0 μm and d_{oil}=0.5 μm).

In practice, we locate the holes at the moment of their nucleation in the sheet by binary thresholding the images using ImageJ. This allows one to determine the hole contours and to determine their position in the sheet, i.e. their radial distance from the origin taken at the center of the target. Knowing the moment of the hole nucleation, t_{h}, and the radial distance at the nucleation, r_0, one can calculate the thickness of the liquid sheet at the formation of the hole, h_{out}:

$$h_{\text{out}} = \frac{\alpha}{t_{\text{h}} r_0} \tag{6.16}$$

with $\alpha = (1.19 \pm 0.23)$ mm^{2}ms (see section 6.2.3).

Statistics over more than 100 holes for each emulsion yields $h_{\text{out}} = (56.5 \pm 27.4)$ μm for the emulsion with d_{oil}=20.0 μm and $h_{\text{out}} = (61.7 \pm 59.3)$ μm for the emulsion with d_{oil}=0.5 μm. First, we remark that for each emulsion the standard deviation of the thickness at the hole formation is very large (comparable to the mean value) indicating that the perforation does not occur at a given thickness of the liquid sheet. For example, for the emulsion with d_{oil}=0.5 μm, the maximum thickness at the hole nucleation is equal to 293.4 μm and the minimum thickness to 14.8 μm. Therefore, for both emulsion, holes are found to nucleate in the liquid sheet over a large range of thickness. Second, for each emulsion, many hole perforations occur when the thickness of the sheet is significantly larger than the size of the oil droplets. What is more, there is clearly no evolution of the thickness at the hole formation with the diameter of the emulsion oil droplets, which definitely rules out a puncture mechanism.

6.6.2 Entering and spreading of oil droplet at the air/water interface

The comparison between the growth dynamics of pre-holes and the spreading of oil drops at the air/water interface indicates that the formation of the pre-hole is due to the Marangoni-driven spreading of oil droplet at the air/water interface. We detail here the complete proposed mechanism leading to the nucleation of hole within the sheet.

The first step of the proposed mechanism is the entry of an oil droplet from the solvent sub-phase to the air/water interface (Figure 6.19(a,b)). This first step is facilitated by the thinning of the liquid sheet with time. In Appendix B, we calculate the time necessary for an oil drop to reach the air/water interface depending on its initial position within the sheet and the oil droplet diameter. Note that we estimate the time for the oil droplet to reach the interface and not to enter the interface. Hence, this simple model only takes into account the thinning of the liquid sheet with time and possibly the creaming of the oil droplet in the liquid film and does not take into account any entry barrier. We show that the creaming velocity is negligible compared to the thinning velocity of the sheet. For an oil droplet of diameter equal to 20 μm we calculate that (in average over the different initial positions within the liquid sheet), the droplet will reach the interface in 4 ms, i.e. a time scale comparable to the sheet life. Therefore, during the expansion of the liquid sheet oil droplets are susceptible to reach the air/water interface.

Once at the air/water interface, the oil droplet subsequently spreads over the underlying liquid due to the positive spreading coefficient, S (Figure 6.19(c)). The spreading of the oil droplet leads to a localized thinning of the sheet (i.e. the formation of a pre-hole), because of a Marangoni surface tension gradient (Figure 6.19(c)), and ultimately to the rupture of the film and so to the nucleation of hole within the sheet. This mechanism has been proposed as a possible mode of action of oil-based antifoams [Bergeron 1997, Denkov 2004], but has never been experimentally evidenced to the best of our knowledge.

6.7 Conclusion

We have investigated the perforation mechanisms of an emulsion-based liquid sheet produced with the single-tear experiment. During the sheet expansion, holes that perforate the sheet nucleate and grow. Thanks to the method that we have developed to measure the thickness field of liquid sheets, we have shown that each perforation event is preceded by the formation of a pre-hole that thins out the sheet and widens with time. We have shown that the growth kinetics of pre-holes and holes differ. The opening dynamics of holes obey the Taylor-Culick law [Taylor 1959, Culick 1960], whereas the pre-hole dynamics follows the power law evolution theoretically predicted for a Marangoni-driven spreading mechanism. We have performed classical Marangoni spreading experiments where the spreading of a drop of the oil phase of the emulsion deposited on a deep pool

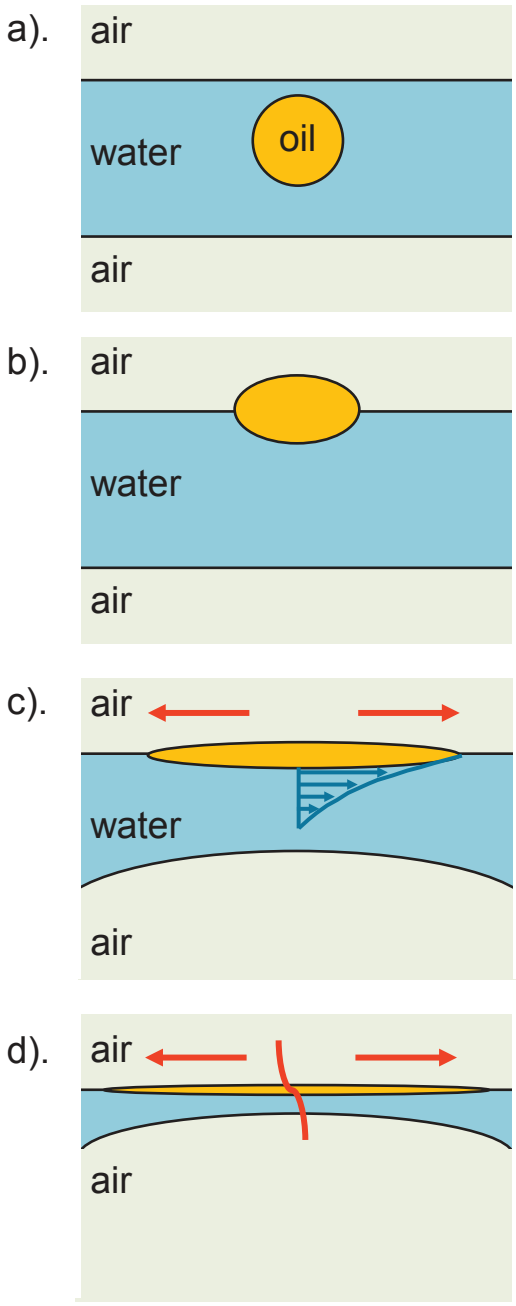

Figure 6.19: Schematic presentation of the proposed mechanism to explain the nucleation of hole within the liquid sheet. An oil droplet enters the liquid film surface (a,b). The oil droplet spreads at the air/water interface (c) causing a Marangoni-driven flow of water which leads to the localized thinning of the liquid film and its eventual rupture (d).

of the aqueous continuous phase of the emulsion is investigated to confirm our physical picture. We have shown that the pre-hole growth follows the same dynamics as the Marangoni-driven spreading of an oil drop at the air/water interface. These findings en-

ables us to formulate the mechanism at the origin of the pre-hole formation and growth. The entry of emulsion oil droplets at the air/water interface leads to a spreading of the oil because of a surface tension gradient stress. This stress is counterbalanced by a viscous stress that drags the subsurface fluid, whose flow causes a local film thinning which will ultimately lead to the rupture the film.

We have quantitatively shown that hole nucleation is governed by Marangoni spreading of the oil droplets at the air/water interface. This mechanism explains the nucleation of holes in the liquid and so the anti-drift properties of emulsions.

The nucleation mechanism can be divided in two successive steps. First, an oil droplet enters the air/water interface. Then, the oil droplet spreads at the interface leading to a localized thinning down to the film rupture.

The objective of the next Chapter will be to modify the physical-chemical parameters of the emulsion to play on both steps of the perforation mechanism.

Chapter 7

Playing with emulsion formulation to tune the perforation of liquid sheet

Contents

In the previous chapter, we have proposed a mechanism for the role of dilute oil-in-water emulsions as anti-drift adjuvants: the oil droplets enter the air/water interface and spread at the interface leading to a localized thinning of the liquid film due to a Marangoni stress. This thinning leads to the rupture of the film and so the nucleation of a hole. Hence, the proposed mechanism implies a succession of two necessary steps: (i) the entering of oil droplets at the air/water interface and (ii) the spreading of the oil droplets at the interface. This mechanism has been established thanks to the observation of the thickness modulations of liquid sheets made of model emulsions. In this chapter, we modify the physico-chemical parameters of emulsions to play on the perforation

mechanism. Up to now, the studied emulsions were stabilized by non-ionic surfactants that are soluble in the oil, the dispersed phase of the emulsion. In this chapter, we study emulsions stabilized by ionic surfactants that are soluble in the aqueous continuous phase. In the first part, we will present the thermodynamical requirements for an oil droplet to enter and spread at the air/water interface. Then, we will investigate the influence of the addition of salt in the emulsion aqueous phase on the destabilization mechanism of sheets made of emulsions stabilized by anionic surfactant (SDS). We will show the effect of salt concentration on sheet perforation and on spray formation, and investigate its influence on the perforation mechanism. In the third part, we will investigate the influence of the addition of salt and amphiphilic copolymers in the emulsion aqueous phase on the destabilization of sheets made of emulsions stabilized by cationic surfactants (CpCl). In the last section, we will discuss the influence of the emulsion formulation on the two steps of the perforation mechanism.

7.1 Entering and spreading of oil droplets at the air/water interface

In the previous chapter, we have proposed a perforation mechanism based on the entering and spreading of oil droplets at the air/water interface. In this section, we present the thermodynamical requirements for an oil droplet to enter and spread at the air/water interface. We also describe the entry barriers that can limit the entering process.

The entering of an oil droplet at the air/aqueous phase interface is thermodynamically described by the entering coefficient, E, defined as:

$$E = \gamma_{\text{air/aq}} + \gamma_{\text{aq/oil}} - \gamma_{\text{air/oil}} \tag{7.1}$$

, with $\gamma_{\text{a/b}}$ stands for the interfacial tension between phases "a" and "b", and "aq" stands for the aqueous phase. The value of E predicts whether a droplet will enter the interface or remain submerged [Harkins 1941]. A positive value of the entering coefficient E means that it is thermodynamically favorable for an oil droplet to enter the air/aqueous phase interface from the aqueous phase (see Figure 7.1).

Although a positive entering coefficient is a necessary condition for drop entry, it is not sufficient. The entering coefficient E only indicates if the entering of oil droplets is thermodynamically favorable but it does not take into account various surface forces that are susceptible to stabilize the thin aqueous film formed between the air/aqueous phase interface and the approaching oil droplet. In particular, the entering coefficient does not take into account thin-film forces such as electrostatic repulsions, van der Waals attractions and steric forces [Bergeron 1993]. These thin-film forces may stabilize the aqueous film and so hinder or suppress the drop entering. Hence, even though a positive entering coefficient ($E > 0$) predicts the entry of oil droplet at the interface, the entering may be kinetically limited by energy barriers arising from thin-film forces.

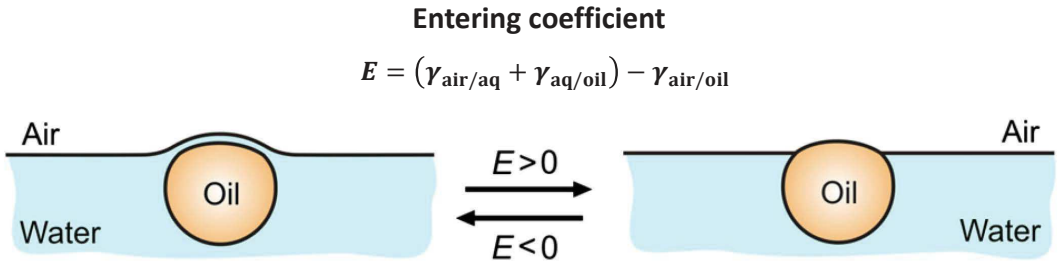

Figure 7.1: Schematic presentation of the physical meaning of the entering coefficient, E [Denkov 2013].

Once at the air/water interface, the oil droplet can remain as a lens or spread along the surface. The spreading of an oil droplet at the air/aqueous phase interface is thermodynamically described by the spreading coefficient S, defined as:

$$S = \gamma_{air/aq} - \gamma_{aq/oil} - \gamma_{air/oil} \tag{7.2}$$

A positive value of S indicates that it is thermodynamically favorable for the oil droplet to spread over the interface, whereas a negative value implies that the oil droplet remains as a lens at the interface [Harkins 1941].

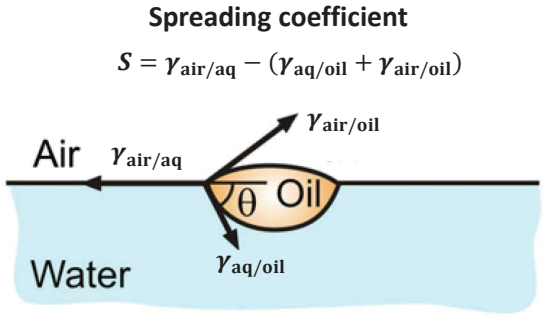

Figure 7.2: Schematic presentation of the physical meaning of the spreading coefficient, S [Denkov 2013].

The perforation mechanism proposed in the previous chapter necessary implies positive entering and spreading coefficients in order for the oil droplets to enter and spread at the air/water interface. Energy barriers arising from thin film forces are susceptible to hinder the entering of oil droplets. In this chapter, we will modify the formulation of the emulsions to play on the entering and spreading of emulsion oil droplets at the air/water interface.

7.2 Emulsions stabilized by anionic surfactants

This section is dedicated to the destabilization mechanism of liquid sheets made of emulsions stabilized by anionic surfactants. We first present the samples studied and then the influence of the addition of salt in the emulsion aqueous phase on sheet perforation and on spray formation. In the last part of this section, we investigate the influence of salt and surfactant concentrations on the two steps of the perforation mechanism.

7.2.1 Samples

The emulsions studied in this section are stabilized by anionic surfactants: sodium dodecyl sulfate (SDS). The oil phase of the emulsion is composed of methyllaurate (i.e. the same oil as for model emulsions) and the emulsion concentration, C, is set at 0.3 % v/v. The aqueous phase of the emulsion is a solution of SDS at different concentrations in milliQ water. The range of concentration investigated is (0.1-2.5) g/L, corresponding to molar concentrations in the range: (0.35-8.67) mM. The critical micelle concentration (CMC) of SDS in pure water is equal to 2.4 g/L [Umlong 2007]. Thus, the higher concentration investigated is slightly larger than the CMC whereas all the other concentrations are below the CMC. Sodium chloride is added to the aqueous phase at a weight concentration C_{NaCl} ranging from 5 to 40 g/L, i.e. molar concentration ranging from 0.09 to 0.68 mol/L. Note that the CMC of SDS significantly decreases with the addition of NaCl. For instance at C_{NaCl}=30 g/L, the CMC is equal to 0.12 g/L (see Figure 7.3 [Umlong 2007]). For more details about the emulsion composition see section 2.1.1.3.

All the emulsions are prepared by mechanical stirring. As described in section 2.1.3.4, the concentration of salt in the emulsion aqueous phase does not modify the oil droplet size distribution: the mean value of d_{oil} averaged over the different salt concentrations is equal to (9.4 ± 1.9) μm for C_{SDS}=2.5 g/L (see Figure 2.12(a)). The increase of the surfactant concentration in the emulsion aqueous phase decreases the oil droplet diameter: for a concentration of SDS equal to 0.1 g/L, d_{oil}=20.3 μm whereas d_{oil}=9.6 μm for a concentration of SDS equal to 2.5 g/L (without salt), see Figure 2.12(b) for more details.

7.2.2 Effect of the addition of salt on sheet perforation and on spray formation

We quantitatively investigate the effect of the salt and surfactant concentrations in the emulsion aqueous phase on the perforation of liquid sheets and on the spray drop size distribution. The results for the two experimental set-ups are presented separately in the first two sections. In the third section, we show the correlation between the perforation of the liquid sheet and the spray drop size distribution.

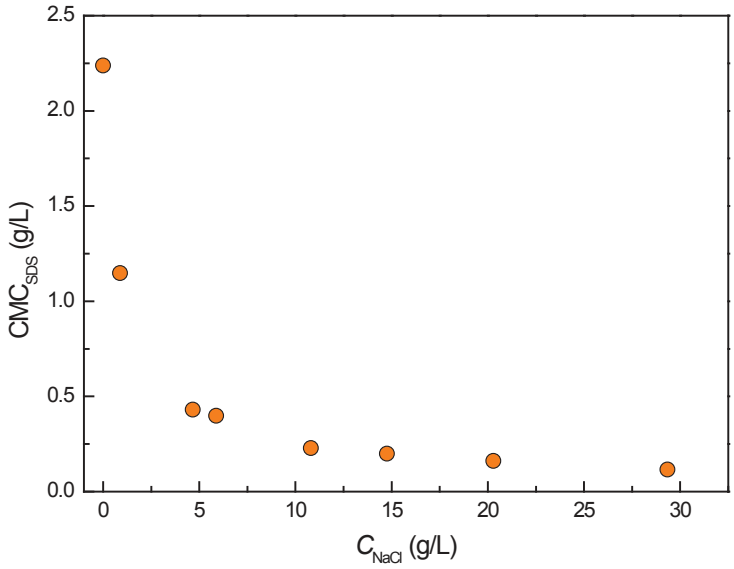

Figure 7.3: Evolution of the CMC of SDS with the NaCl concentration in the surfactant solution. These values are deduced from surface tension measurements performed at 20°C with a Wilhelmy plate tensiometer [Umlong 2007].

7.2.2.1 Single-tear model experiments

Liquid sheets made of emulsions are formed with the single-tear experimental set-up presented in the section 4.2.1. The tear impact parameters are the same as the ones used in Chapter 5 for the study of the destabilization of liquid sheets made of model emulsions: the tear diameter, d_0, is set at 3.7 mm and the impact velocity, u_0, at 4 m/s. The perforation of the emulsion-based liquid sheet is characterized by the quantification of the total number of perforation events, N_{tot}, as presented in section 5.1.3.2.

For a first set of experiments, the surfactant concentration in the aqueous phase of the emulsion is fixed at 2.5 g/L, i.e. a concentration slightly above the CMC. Figure 7.4 shows images of the sheets for different concentrations of NaCl in the emulsion aqueous phase taken at the same time after the tear impact. We observe that without salt (Figure 7.4(a)), the liquid sheet is not perforated and is destabilized by the same mechanism as a pure water liquid sheet, i.e. by the ejection of drops from the rim. The addition of salt at a concentration of 10 g/L triggers the perforation of the liquid film (Figure 7.4(b)). Then, the amount of perforation events increases with increasing the salt concentration as visible in Figure 7.4(c) for C_{NaCl}=20 g/L and in Figure 7.4(d) for C_{NaCl}=40 g/L.

The total number of perforation events, N_{tot}, is plotted as a function of the NaCl concentration in Figure 7.5. On the bottom x-axis, the NaCl concentrations are expressed in g/L and on the top x-axis in mol/L. We find that up to a salt concentration of 5 g/L, there is no perforation of the liquid film. At C_{NaCl}=10 g/L, a few perforation events (around 15) are observed. Then, we find that the increase of the salt concentration entails a continuous increase of N_{tot} up to 143 holes for C_{NaCl}=40 g/L. The oil droplet size

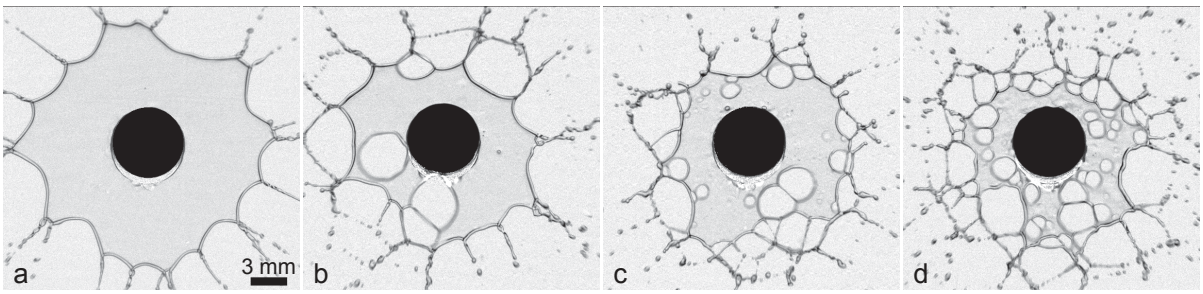

Figure 7.4: Images of liquid sheets made of emulsions stabilized by SDS for different concentrations of NaCl in the aqueous phase. The images are taken 3.6 ms after the impact of the tear. a). C_{NaCl}=0 g/L b). C_{NaCl}=10 g/L c). C_{NaCl}=20 g/L and d). C_{NaCl}=40 g/L. Here the SDS concentration is set at 2.5 g/L.

distribution of the emulsions are comparable for the different salt concentrations ($d_{\mathrm{oil}} = (9.4 \pm 1.9)$ μm averaged over the different salt concentrations). Therefore, our findings are not due to an effect of the oil droplet size, neither of the emulsion concentration (as it is equal to 0.3 % v/v for all the emulsions investigated).

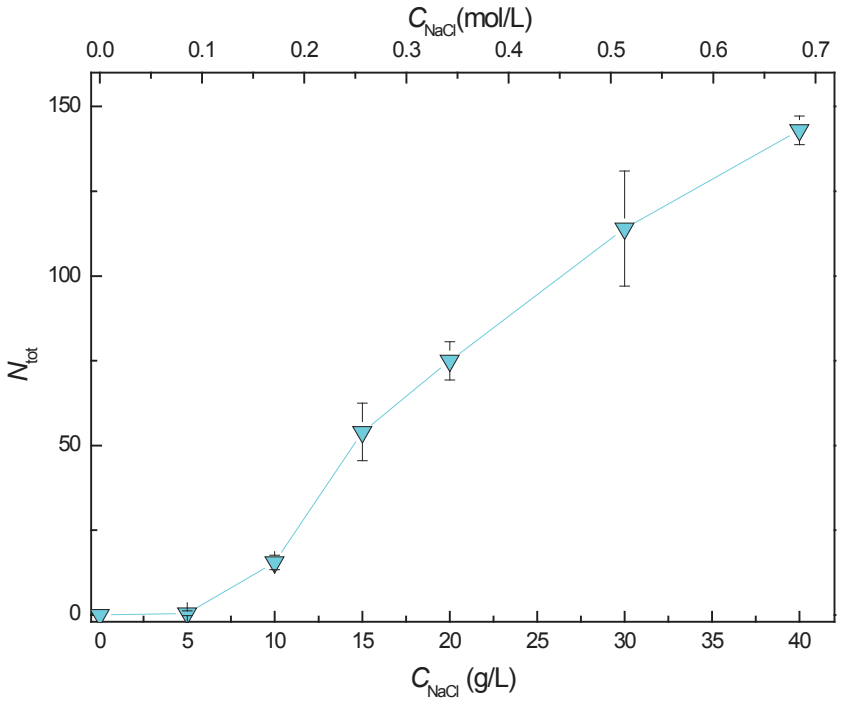

Figure 7.5: Evolution of the total number of perforation events, N_{tot}, as a function of the NaCl concentration in the aqueous phase of emulsions stabilized by SDS. Here the SDS concentration is set at 2.5 g/L.

We can draw interesting conclusions from this first set of experiments. First, it is clear

that it is not sufficient to have a dispersion of oil droplets in an aqueous phase to entail the perforation of liquid sheets. Up to now, all the emulsions investigated were triggering the perforation of liquid films. However, emulsions stabilized by SDS without salt and at low salt concentration (C_{NaCl}=5 g/L) do not entail the sheet perforation. Hence, other specificities for the emulsions are required to provoke the sheet perforation.

We have checked that simple solutions of surfactants corresponding to the aqueous phase of the emulsions do not entail the perforation of liquid sheets. Figure 7.6 shows images of sheets made of surfactant solution (C_{SDS}=2.5 g/L) with salt (Figure 7.6(b), C_{NaCl}=20 g/L) and without salt (Figure 7.6(a)). For both sheets, we observe no perforation. Hence, the perforation observed for emulsions stabilized by SDS with high salt concentrations is directly related to the presence of oil droplets in the liquid film.

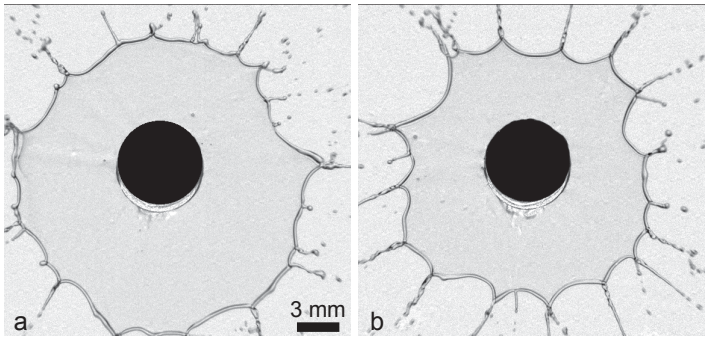

Figure 7.6: Images of liquid sheets made of surfactant solutions (C_{SDS}=2.5 g/L) for different concentrations of NaCl taken 3.6 ms after the impact of the tear. a). C_{NaCl}=0 g/L b). C_{NaCl}=20 g/L. Here the SDS concentration is set at 2.5 g/L.

In a second set of experiments, the surfactant concentration in the emulsions aqueous phase is modified. Three other concentrations of SDS are investigated: 0.1 g/L, 0.25 g/L and 0.5 g/L. These three concentrations are below the CMC without NaCl but might be above at higher NaCl concentrations, as indicated in Figure 7.7. For these concentrations, we study, as previously for C_{SDS}=2.5 g/L, the influence of the addition of NaCl at different concentrations in the emulsion aqueous phase. The experimental results are summarized in Figure 7.7 with the evolution of the total number of perforation events as a function of the salt concentration.

First, for all SDS concentrations, a behavior similar to the one described previously for C_{SDS}=2.5 g/L is measured. We observe that for each surfactant concentration, the total number of perforation events, N_{tot}, increases with the salt concentration and eventually reaches a plateau at higher salt concentration. For the low surfactant concentrations, C_{SDS}=0.1 and 0.25 g/L, N_{tot} increases very rapidly with the salt concentration and reaches a plateau for C_{NaCl}=5 g/L. For C_{SDS}=0.5 g/L, the plateau is obtained for C_{NaCl}=20 g/L. For the highest surfactant concentration investigated, C_{SDS}=2.5 g/L, the total number of perforation events keeps increasing with the salt concentration and no saturation are

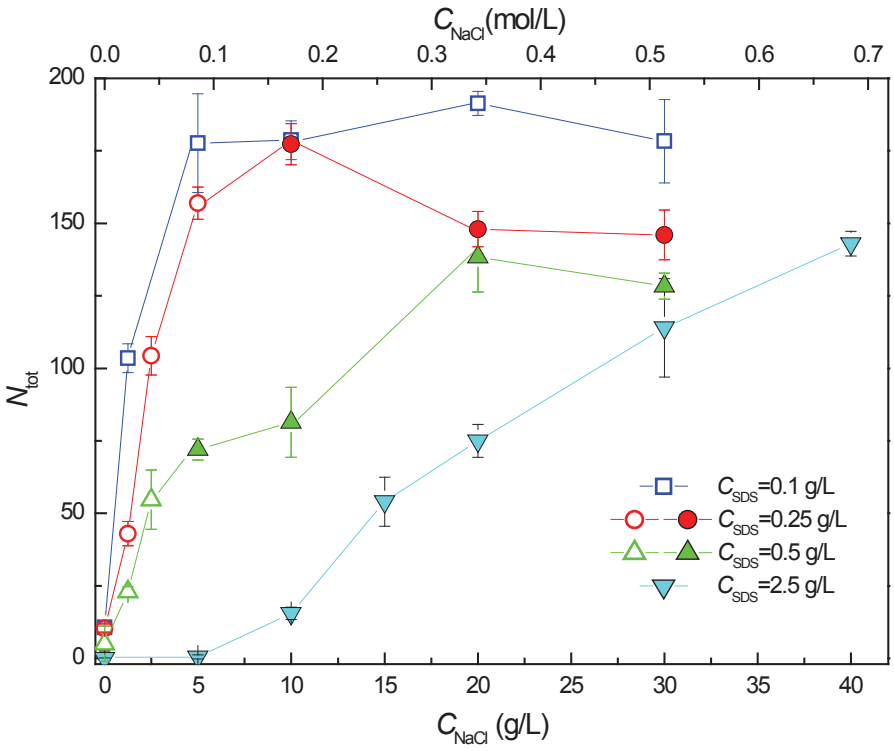

Figure 7.7: Evolution of the total number of perforation events, N_{tot}, as a function of the NaCl concentration in the aqueous phase of emulsions stabilized by SDS, for different concentrations of SDS as indicated in the legend. The filled symbols correspond to SDS concentrations above the CMC and the open symbols to SDS concentration below the CMC.

observed up to C_{NaCl}=40 g/L. We note also that the maximum total number of perforation events tends to decrease as C_{SDS} increases (from 191 for C_{SDS}=0.1 g/L down to 143 C_{SDS}=2.5 g/L).

The emulsion oil droplet size distribution varies with the SDS concentration as described in details in section 2.1.3.4 (Figure 2.12(b)). For a concentration of SDS equal to 0.1 g/L, d_{oil}=20.3 μm whereas d_{oil}=9.6 μm for a concentration of SDS equal to 2.5 g/L (without salt). In the section 5.3, we have shown that for the model emulsions, at a given number of oil droplets per liter, bigger oil droplets are more efficient to onset the perforation of liquid sheets. Hence, we can wonder if the influence of the SDS concentration on the perforation is due to the difference in the emulsion oil droplet size distributions. Here, the different emulsions are prepared at the same volumetric concentration of oil, C, which is set at 0.3 % v/v. Hence, the number of oil droplets per liter is not the same for the emulsions prepared at different SDS concentrations: more oil droplets are produced at C_{SDS}=2.5 g/L than at C_{SDS}=0.1 g/L. For C_{SDS}=0.1g/L, there are fewer oil droplets but there are more efficient to onset the perforation compared to emulsion with C_{SDS}=2.5 g/L. Based on the results obtained for the model emulsions, at a given emulsion

concentration (C=0.3 % v/v), the number of perforation events obtained for emulsions with d_{oil} ≈10 μm and d_{oil} ≈20 μm are comparable (respectively around 114 and 120), see Figure 5.19. Therefore, we believe that the effect of the SDS concentration of the emulsion aqueous phase on the perforation process is not an effect of the oil droplet size but really arises from the different surfactant concentrations.

In Figure 7.8 is plotted the evolution of N_{tot} with the Debye length, κ^{-1}, of the emulsion aqueous phase for the different SDS concentrations. The Debye lengths are calculated from the ionic strength of the solutions following:

$$\kappa^{-1}(\text{nm}) = \frac{0.304}{\sqrt{I(\text{mol/L})}} \tag{7.3}$$

The ionic strength I is defined as following:

$$I = \frac{1}{2}\sum_i C_i {z_i}^2 \tag{7.4}$$

with C_i the molar concentration of ion i and z_i the charge number of this ion. The sum is taken over the surfactant counterion (Na^+) and the added salt (Na^+, Cl^-). The Debye length characterizes the electrostatic effect of charge carrier in solution, and express the length scale over which electrostatic effects play a role. For all the SDS concentrations investigated, N_{tot} decreases with the Debye length, κ^{-1}. Hence, the perforation process seems limited and even completely inhibited when the range of electrostatic repulsion forces increases sufficiently. We observe that for a given Debye length, the total number of perforation events spans over one order of magnitude, depending on the surfactant concentration. For example, for a Debye length around 0.7 nm, 15 perforation events are obtained for C_{SDS}=2.5 g/L and 180 for C_{SDS}=0.1 g/L. Hence, the influence of the SDS concentration on the perforation of liquid films cannot be explained by only electrostatic considerations, otherwise the curves would have been superimposed once plotted as a function of the Debye length.

The physical origin of the effect of the salt and surfactant concentrations on the perforation mechanism will be discussed in the last section of this chapter. We will first investigate the effect of the salt concentration on the spray drop size distribution with the conventional spray experiment.

7.2.2.2 Spray drop size distribution

We present in this section, the spray drop size distribution measured with the Spraytec Malvern device for emulsions stabilized by SDS at a concentration of 2.5 g/L in the aqueous phase. The experiment set-up used is the same as the one presented in section 5.1.1. The evolution of the parameter $DV50$, the threshold diameter for which drops represent 50 % of the total volume of the spray drops, is represented in Figure 7.9(a) as a

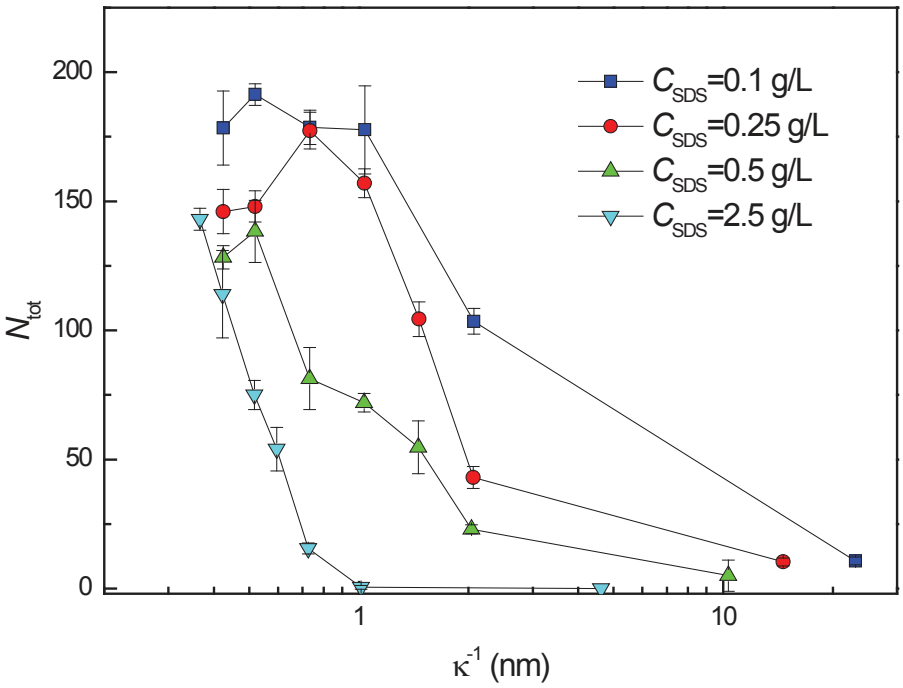

Figure 7.8: Evolution of the total number of perforation events, N_{tot}, as a function of the Debye length of the aqueous phase of emulsions stabilized by SDS, for different concentrations of SDS as indicated in the legend. The Debye length is varied by the addition of various concentrations of NaCl in the emulsion aqueous phase.

function of x, the location with respect to the spray. Data for pure water and emulsions with different salt concentrations are plotted.

First, we observe that the increase of the salt concentration in the emulsion aqueous phase influences the spray angle. As shown in Figure 7.9(b), the spray angle continuously increases from 105° without NaCl to 113° as the salt concentration increases up to C_{NaCl}=40 g/L. Note that without salt, the spray angle is smaller than the one obtained for pure water sprays (108°). To obtain a spray angle comparable to the one obtained for pure water a concentration of sodium chloride of 10 g/L is required.

Second, we find a clear effect of the emulsions stabilized by SDS and the addition of salt on the drop size distribution at the center of the spray, whereas there is no effect at the edges of the sprays (Figure 7.9(a)). Without salt and at low salt concentration (C_{NaCl}=5 g/L), the emulsions decrease the volume median diameter of the spray compared to pure water. Then, a further increase of the salt concentration increases the spray drop size compared to water.

We have quantified this effect by computing the volume median diameter $DV50$ averaged over the whole spray, over the center of the spray and over the edges of the spray, see Chapter 5 section 5.2.2 for the exact definitions of the different portions of the spray. The evolution with salt concentration of $DV50$ averaged over the different portions of

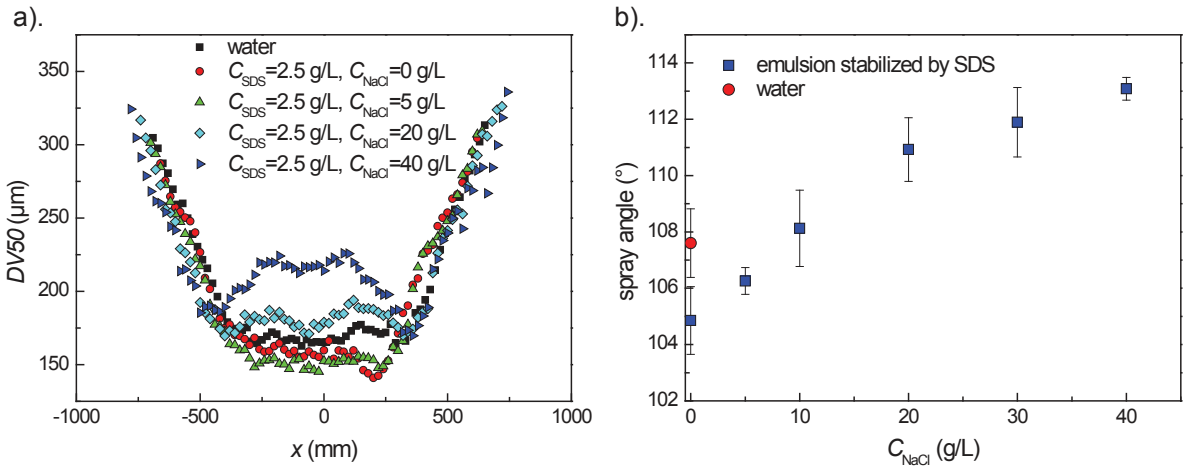

Figure 7.9: a). Evolution of the parameter $DV50$ of the spray drop size distribution as a function of the location along the spray axis for pure water and emulsions stabilized by SDS (2.5 g/L) at different salt concentrations, as indicated in the legend. b). Evolution of the spray angle as a function of the salt concentration. Here the oil concentration is set at 0.3 % v/v.

the spray is plotted in Figure 7.10(a). The values for water are indicated with dotted lines. As observed for water and model emulsions (Chapter 5), the spray drops are larger at the edges of the spray than in the center.

For the data averaged over the edges of the spray (green triangle data points), the value of $DV50$ for pure water is comparable to the one obtained for an emulsions with solution of SDS 2.5 g/L (without salt) as aqueous phase. The increase of the salt concentration has no influence on the value of $DV50$: averaged over the different salt concentrations $DV50$=(237 $\pm$ 5) μm. By contrary, the salt concentration has a strong influence on the spray drop size distribution averaged over the spray center (red circle data points). For C_{NaCl}=0 g/L, we find $DV50$=148 μm and $DV50$=203 μm for C_{NaCl}=40 g/L, i.e. a relative increase by 37 %. The same behavior is observed if the volume median diameter is averaged over the whole spray (blue square data points), $DV50$ is equal to 176 μm without salt and is measured to continuously increase with the salt concentration up to a value of 211 μm for C_{NaCl}=40 g/L. The relative increase on the whole spray is smaller than on the spray center, as the emulsion impacts principally the size distribution in the center of the spray.

In Figure 7.10(b) is computed the evolution of the volume fraction of small drops in the spray, $V150$, as a function of the salt concentration in the aqueous phase of the emulsions. Similar conclusions to the ones obtained with the evolution of $DV50$ are derived. The addition of salt has no effect on the proportion of small drops at the edges of the spray. On the contrary, the addition of salt in the emulsion aqueous phase has a strong influence for the whole spray and at the center of the spray. $V150$ decreases with the addition of salt, from 50.8 % for C_{NaCl}=5 g/L to 29.3 % for C_{NaCl}=40 g/L (at the

spray center), i.e. a relative decrease by 42.3 %.

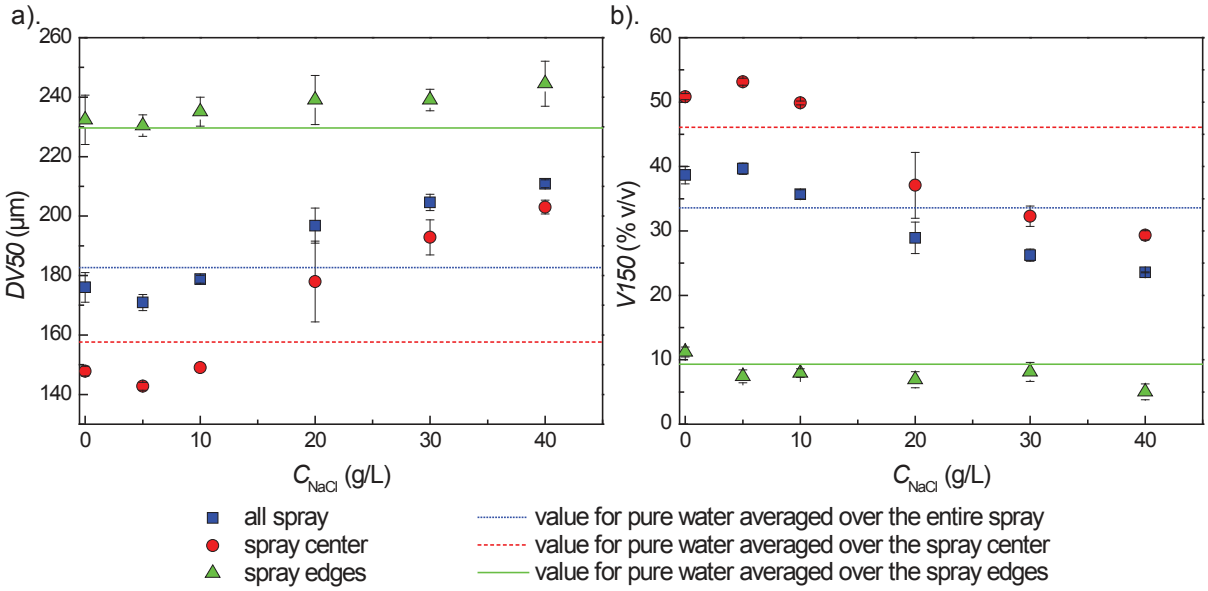

Figure 7.10: a). Evolution of the volume median diameter ($DV50$) of the spray drop size distribution as a function of the salt concentration in the aqueous phase of emulsions stabilized by SDS (C_{SDS}=2.5 g/L) averaged over the entire spray fan, averaged over the center of the spray and averaged over the edges of the spray. b). Evolution of the volume fraction of small drops (diameter $\leq$ 150 μm) in the spray averaged over the entire spray fan, averaged over the center of the spray and averaged over the edges of the spray. Symbols are averaged value and error bars correspond to standard deviation. The values for pure water are indicated with dotted lines.

In conclusion, emulsions stabilized by SDS without salt entail a decrease of the spray drop size compared to pure water spray and an increase of the proportion of small drops in the spray. An increase of the salt concentration in the aqueous phase of the emulsions entails a continuously increase of the volume median diameter of the spray drops and a decrease of the proportion of driftable drops in the spray.

7.2.2.3 Correlation between model and standard spray experiments

Both model-single tear experiments and spray drop size distribution measurements show clearly an impact of the salt concentration of the emulsions aqueous phase. Both experiments demonstrate an effect that is triggered by a salt concentration of C_{NaCl}=10 g/L and then increases with the salt concentration. The effect of the salt concentration on the sheet perforation is quantified by the total number of perforation events, N_{tot}, and the effect on the spray drop size distribution is quantified by the parameters $DV50$ and $V150$.

Here, similarly to what has been done for model emulsions (Chapter 5), we directly correlate those two sets of parameters. In Figure 7.11 is plotted the evolution of $DV50$ and $V150$ averaged over the center of the spray as a function of N_{tot} for the different salt concentrations in the emulsion aqueous phase. We find a continuous increase (resp. decrease) of $DV50$ (resp. $V150$) as N_{tot} increases, illustrating a clear correlation between those parameters. More quantitatively we find that functional forms such as $DV50 = DV50_{[\text{NaCl}]=0\text{g/L}} + kN_{\text{tot}}$ and $V150 = V150_{[\text{NaCl}]=0\text{g/L}} - k'N_{\text{tot}}$ account well for the experimental data, with $DV50_{[\text{NaCl}]=0\text{g/L}}$ and $V150_{[\text{NaCl}]=0\text{g/L}}$ the values obtained for an emulsion stabilized by SDS without salt. The best fits are shown in Figure 7.11 and the values of the various fitting parameters are listed in the caption of Figure 7.11.

This results confirm the ones previously obtained for the model emulsion (section 5.2.3). As explained in section 5.4 for the model emulsion, an increase of the total number of perforation events, N_{tot}, entails the liquid sheet to be destabilized closer to the nozzle where the sheet is thicker. Therefore, an increase of the number of perforation events entails the formation of bigger drops and so a reduction of the proportion of driftable drops in the spray. The results obtained with the emulsions stabilized by SDS surfactants confirm the ones obtained for the model emulsion and so validate our analysis.

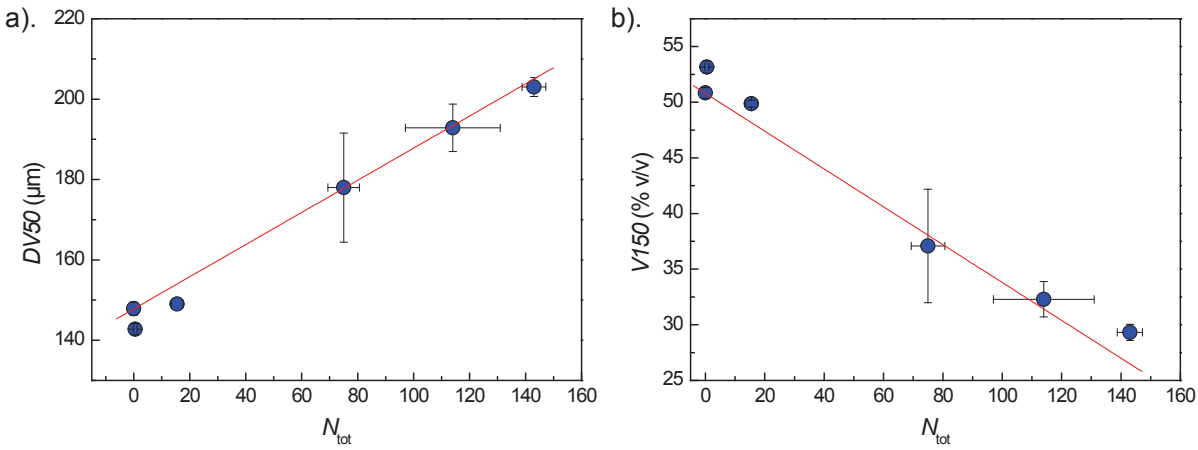

Figure 7.11: Correlation between the total number of perforation events, N_{tot}, and a). the volume median diameter of the spray drop size distribution, $DV50$, b). the volume fraction of small drops in the spray, $V150$, averaged over the spray center for emulsions stabilized by SDS (C_{SDS}=2.5 g/L) with variable NaCl concentrations in the emulsion aqueous phase. Symbols are experimental data and the continuous lines are fits of the form: $DV50 = DV50_{[\text{NaCl}]=0\text{g/L}} + kN_{\text{tot}}$ and $V150 = V150_{[\text{NaCl}]=0\text{g/L}} - k'N_{\text{tot}}$ with k (k') fitting parameters. The best fits yield a) $k = 0.40$, $R^2 = 0.99$, b) $k' = 0.17$, $R^2 = 0.99$.

7.2.3 Effect of the addition of salt on the perforation mechanism

We have shown that emulsions stabilized by SDS do not entail the perforation of liquid films. The addition of NaCl in the aqueous phase of the emulsion triggers the perforation process. Once a critical salt concentration is exceeded, a further increase of the salt concentration entails a continuous increase of the total number of perforation events. The critical salt concentration to provoke the perforation process depends on the SDS concentration, more exactly it decreases with the SDS concentration. At a given salt concentration, low SDS concentrations in the emulsion aqueous phase are more efficient to trigger the perforation of liquid films.

To understand the effect of the NaCl and SDS concentrations on the sheet perforation, we investigate their influence on the perforation mechanism. In Chapter 6, we have proposed a mechanism to explain the nucleation of holes in the liquid film. First, the oil droplets enter the air/aqueous phase interface, then due to a positive spreading coefficient ($S > 0$) the oil droplets spread at the interface leading to a localized thinning of the liquid film and to the rupture of the film. We investigate the influence of the salt and surfactant concentrations of the emulsion aqueous phase on the two steps of the perforation mechanism. We first present the result concerning the spreading of the oil droplet and then those concerning the entering of emulsion oil droplets at the air/aqueous phase interface.

7.2.3.1 Pre-hole widening dynamics

In this section, we investigate the localized thinning of the liquid film (pre-hole) due to the spreading of oil droplets at the air/aqueous phase interface. We use the method detailed in Chapter 6 to measure the widening of the pre-hole. A dye is added to the emulsion aqueous phase (erioglaucine at a concentration of 2.5 g/L). As already explained, the addition of dye permits to visualize the pre-hole formation and to measure its evolution with time. We perform these experiments for three different compositions of the emulsion aqueous phase:

1. C_{SDS}=2.5 g/L and C_{NaCl}=10 g/L,
2. C_{SDS}=2.5 g/L and C_{NaCl}=20 g/L,
3. C_{SDS}=0.1 g/L and C_{NaCl}=10 g/L.

For the first one (C_{SDS}=2.5 g/L and C_{NaCl}=10 g/L), very few perforation events were observed (around 15), on the contrary for the two others (C_{SDS}=2.5 g/L and C_{NaCl}=20 g/L; C_{SDS}=0.1 g/L and C_{NaCl}=10 g/L) a large number of perforation events were observed (respectively 76 and 179). The objective is to investigate if those discrepancies are due to differences in the spreading dynamics of the oil droplets at the interface and so to differences in the pre-hole widening dynamics.

In Figure 7.12 is plotted the evolution of the pre-hole radius, R_{ph}, as a function of the time elapsed since its formation, $T = t - t_{\mathrm{ph}}$, for the different compositions of the emulsion aqueous phase. We find that, for the three aqueous phases investigated, R_{ph} increases with T as a power-law with an exponent 3/4: $R_{\mathrm{ph}} = kT^{3/4}$. These results are in agreement with the ones obtained for model emulsions in Chapter 6 and so confirm a widening dynamics of pre-hole in agreement with the dynamics of Marangoni spreading.

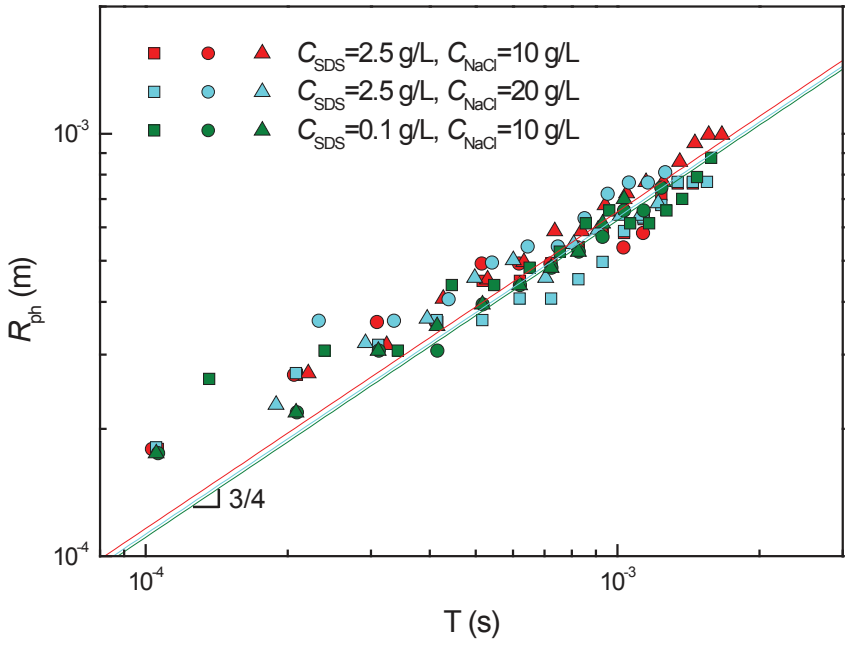

Figure 7.12: Evolution of the radius of the pre-hole, R_{ph}, as a function of T, the time elapsed since the pre-hole formation for emulsions stabilized by SDS with different concentrations of NaCl and SDS in the emulsion aqueous phase. The exact compositions of the emulsion aqueous phase are indicated in the legend. Different symbols correspond to different experiments. The lines are the best fits of the experimental data of the form: $R_{\mathrm{ph}} = kT^{3/4}$.

In Figure 7.12, we observe that the data points corresponding to the different compositions of the emulsion aqueous phase are superimposed. Hence, the widening dynamics of the pre-hole and so the spreading dynamics of oil droplets at the air/aqueous phase interface is the same for the different compositions of the emulsion aqueous phase. From the fit of the experimental data points, we deduce the experimental values of the parameter k. Following the dynamics of Marangoni spreading described in Chapter 6: $k = \sqrt{\frac{4}{3}}\frac{S^{1/2}}{(\rho\eta)^{1/4}}$. Therefore, from the experimental values of k and knowing the emulsion aqueous phase density (ρ) and zero-shear viscosity (η), one is able to deduce a spreading parameter S, denoted as S_{fit} as it is deduced from the fit of our experimental data. These values are summarized in Table 7.1. We remark that the values obtained for S_{fit} are really similar for the three compositions of the emulsion aqueous phase ($S_{\mathrm{fit}} = (9.6 \pm 0.5)$ mN/m av-

eraged over the three compositions), as expected from the superimposition of the R_{ph} vs T curves (Figure 7.12). These values can be directly compared to macroscopic measurements of the spreading parameter as $S = \gamma_{air/aq} - \gamma_{aq/oil} - \gamma_{air/oil}$. The value of $\gamma_{air/oil}$ is measured with a Wilhelmy plate tensiometer and is equal to 29.6 mN/m. The surface tension of the aqueous phases of different compositions, $\gamma_{air/aq}$, are also measured with a Wilhelmy plate tensiometer and are reported in Table 7.1. As expected the surface tension decreases with the increases of the SDS concentration. The addition of salt entails a slight decrease of the surface tension of the aqueous phase $\gamma_{air/aq}$ at C_{SDS}=2.5 g/L. The interfacial tension between the oil and aqueous phases, $\gamma_{aq/oil}$, is measured thanks to a spinning drop tensiometer (see Appendix A.2). The values are reported in the second column of Table 7.1. From these surface tension measurements, one can estimate the values of the spreading parameter, denoted $S_{measured}$ and reported in the third column of Table 7.1.

emulsion aqueous phase composition	$\gamma_{air/aq}$ (mN/m)	$\gamma_{aq/oil}$ (mN/m)	$S_{measured}$ (mN/m)	S_{fit} (mN/m)	S^* (mN/m)
C_{SDS}=0.1 g/L and C_{NaCl}=10 g/L	40.6	3.2	7.8	9.2	39.4
C_{SDS}=2.5 g/L and C_{NaCl}=10 g/L	32.6	0.2	2.8	10.1	42.4
C_{SDS}=2.5 g/L and C_{NaCl}=20 g/L	31.4	0.2	1.6	9.5	42.4

Table 7.1: Values of $\gamma_{air/aq}$ and $\gamma_{aq/oil}$ for the three different compositions of the emulsion aqueous phase and values of $S_{measured}$ calculated from these values with $\gamma_{air/oil}$=29.6 mN/m. The values of S_{fit} extracted from the fits of the evolutions of R_{ph} vs T are also reported. The values of S^* correspond to the spreading coefficient if $\gamma_{air/aq}$ is equal to $\gamma_{air/water}$, i.e. in the case surfactant molecules do not have time to diffuse at the air/water interface.

We observe that for the three aqueous phase compositions $S_{measured}>0$, a prerequisite for Marangoni spreading. Moreover, the values measured for $S_{measured}$ are in the same range for the different emulsion aqueous phases ($S_{measured} = (4.1 \pm 3.3)$ mN/m averaged over the three compositions), confirming that oil droplets have a similar tendency to spread over the different aqueous phases. The values of the spreading parameter derived from direct measurements, $S_{measured}$, and the one derived from the fit of the curves R_{ph} vs T, S_{fit}, are of the same order of magnitude even if S_{fit} is systematically larger than $S_{measured}$.

Note that to calculate $S_{measured}$ we have considered equilibrium values of the different surface tensions. However, the tear impact and the formation of pre-holes are really fast processes (few milliseconds) and it is not obvious that all the surfactant molecules will have the time to diffuse at the interface at this short time scale. Therefore, the $\gamma_{air/aq}$

surface tension involved for the spreading of oil droplets may be higher than the equilibrium values, which would explain the higher values of the spreading coefficient deduced from the pre-hole widening, S_{fit}, compared to the one calculated using equilibrium surface tensions, S_{measured}.

It would have been interesting to measure the dynamic surface tension of SDS and NaCl solutions at short time (i.e. 5-10 ms) to determine a spreading coefficient at short time and compare this value to S_{fit} and S_{measured}. Frese at al. [Frese 2003] have measured the dynamic surface tension of solution of SDS at short time scale with a maximum bubble pressure tensiometer. They measured that for a pure SDS concentration at a concentration of 2.6 g/L, $\gamma_{air/aq}$ is equal to 45 mN/m at a surface age of 10 ms, for an equilibrium surface tension of 40 mN/m. Hence, at the time scale of few milliseconds, some of the surfactant molecules have time to diffuse at the air/aqueous phase interface to lower the surface tension. We can estimate the time needed for a SDS molecule to diffuse at the interface by a diffusion limited process. The time evolution of the surfactant surface concentration, Γ, is given by:

$$\Gamma = 2\sqrt{\frac{Dt}{\pi}}C_{\text{B}} \tag{7.5}$$

, with D the bulk diffusion coefficient of the surfactant and C_{B} the bulk surfactant concentration [Bonfillon 1994]. We can deduce from Equation 7.5, the diffusion time, t_{D}, necessary to reach the equilibrium surfactant surface concentration, Γ_{eq}:

$$t_{\text{D}} = \frac{\pi}{4}\frac{1}{D}\left(\frac{\Gamma_{\text{eq}}}{C_{\text{B}}}\right)^2 \tag{7.6}$$

Weinheimer et al. [Weinheimer 1981] measured the bulk diffusion coefficient of SDS, D, at different concentrations. They measured $D = 1.76 \times 10^{-6}$ cm^2/s for $C_{\text{B}} = 10^{-2}$ mol/L (i.e. C_{B}=2.9 g/L). From the adsorption isotherms of SDS solutions measured by Mattura et al. [Matuura 1958]: $\Gamma_{\text{eq}} \approx 3 \times 10^{-10}$ mol/cm^2 for $C_{\text{B}} = 10^{-2}$ mol/L. From Equation 7.5, we calculate t_{D}=0.4 ms. Hence, the SDS molecules diffuse at the air/aqueous phase interface in relatively short time (<1 ms).

We can reasonably think that from the formation of the liquid sheet to the pre-hole widening, some of the surfactant molecules will have diffused to the air/aqueous phase interface and lowered the surface tension. Hence, the air/aqueous phase surface tension relevant for the pre-hole widening is closer to the equilibrium surface tension than to the air/water surface tension. Accordingly, the values of S deduced from the spreading dynamics ($S_{\text{fit}} = (9.6 \pm 0.5)$ mN/m averaged over the three compositions) are closer (although slightly larger) to the measured values assuming an equilibrium surface tension ($S_{\text{measured}} = (4.1 \pm 3.3)$ mN/m averaged over the three compositions) than to the ones measured assuming an air/water surface tension ($S^* = (41.4 \pm 1.7)$ mN/m averaged over the three compositions).

In conclusion, we have seen that the salt and surfactant concentrations of the emulsion aqueous phase do not modify the widening dynamics of pre-holes and so the spreading of oil droplets at the air/aqueous phase interface. As the spreading behavior is the same for the different compositions of the emulsion aqueous phase, we will now investigate the first step of the perforation mechanism, which is the entering of oil droplets at the air/aqueous phase interface.

7.2.3.2 Entering of emulsion oil droplets at the air/aqueous phase interface

To investigate the influence of salt concentration on the entering of oil droplets at the air/aqueous phase interface, we perform experiments to monitor the coalescence of oil droplets with the interface. The experimental set-up that we used was originally designed by Hotrum et al. [Hotrum 2002]. The idea is to measure the time evolution of the surface tension of the emulsion aqueous phase with a Wilhelmy plate tensiometer upon injection of a minute volume of emulsion below the interface. The entering and spreading of oil droplets at the air/aqueous phase interface are detected by a sharp decrease of the surface tension due to the presence of an oil film at the surface. This experimental set-up permits to estimate the time needed for surfactant-stabilized oil droplets to enter the interface. The sharp decrease of the surface tension is due to the spreading of oil droplets at the interface. However, we have seen in the previous section that for the systems investigated the oil droplets always spread at the interface as $S > 0$. Therefore, a decrease of the surface tension gives information on the capacity and rapidity for the oil droplets to enter the interface.

In Figure 7.13 are shown some pictures of the experimental set-up. A 5 cm diameter Petri dish is filled with 20 mL of the emulsion aqueous phase. A tube connected to a syringe is fixed at the bottom of the Petri dish (Figure 7.13(b,c)). Thanks to a syringe pump a minute volume of emulsion (0.15 mL) is injected below the interface (at approximatively 1 cm) at a flow rate of 0.12 mL/min. The dead volume of the tube is equal to 0.08 mL, therefore only 0.04 mL are effectively injected in the Petri dish. During the whole process, the surface tension of the solution is measured with a Wilhelmy plate. We first measure the surface tension of the aqueous phase at rest, after 300 seconds the injection is launched and 50 seconds later the emulsion is effectively injected in the Petri dish. The results obtained are the time evolutions of the surface tension.

In Figure 7.14 are represented the evolutions of the surface tension measured at the air/aqueous phase interface during the entering of emulsion oil droplets. Three emulsion aqueous phase compositions were investigated. For the three emulsions the surfactant concentration is set at 2.5 g/L, the salt concentration is varied and equal to 0, 10 and 20 g/L. For each curve, at short time we observe a plateau value corresponding to the equilibrium surface tension of the emulsion aqueous phase. The black arrows indicate the injection of emulsion oil droplets in the Petri dish. After the injection, we observe for each curve a sharp decrease of the surface tension corresponding to the entering and spreading of oil droplets at the interface. We note that the time elapsed from the injection

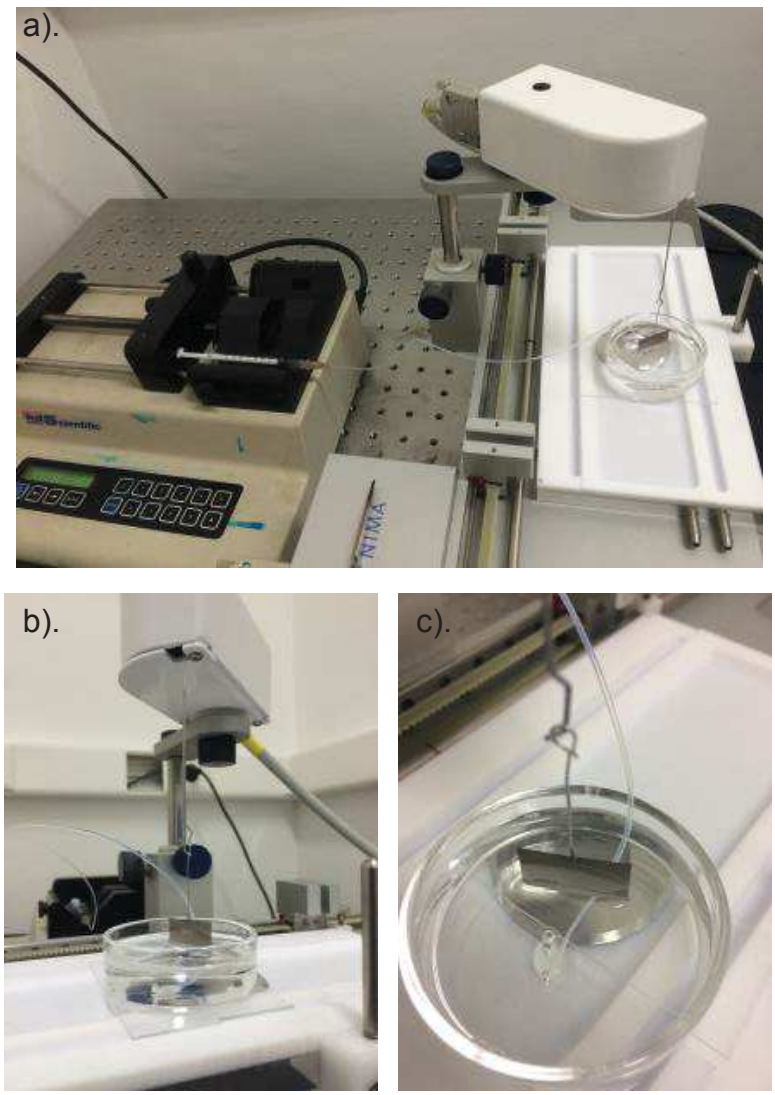

Figure 7.13: Pictures of the experimental set-up used to monitor the entering of oil droplets at the air/aqueous phase interface.

to the sharp decrease of the surface tension (defined as the entering time) depends on the salt concentration in the aqueous phase. The evolution of the entering time, t_{entering}, with the salt concentration in the emulsion aqueous phase is shown in Figure 7.15. The errors bars correspond to standard deviations calculated over four repetitions of the same experiments. Without NaCl, the entering time is equal to (81 ± 18) s then an increase of the salt concentration entails a decrease of the entering time, which is equal to (36 ± 7) s for C_{NaCl}=10 g/L and to (27 ± 7) s for C_{NaCl}=20 g/L. We note that the entering time range is lower than the time expected from the simple creaming of oil droplets at the

interface. The creaming velocity reads

$$v_{\text{creaming}} = \frac{2}{9}\frac{\Delta\rho g {r_{\text{oil}}}^2}{\eta} \tag{7.7}$$

with $\Delta\rho$ the density difference between the aqueous and oil phases of the emulsion, η the viscosity of the aqueous phase and r_{oil} the oil droplet radius. For a droplet of diameter 20 μm, setting at 1 cm from the interface (distance from the tip of the tube to the air-water interface) the time to reach the interface is around 330 s. This time is much larger than the delay between the issuing of the droplet and the decrease of the surface tension. This is presumably due to the fact that the oil droplets have an initial velocity when their are injected in the solution, and thus reach much faster the interface.

In conclusion, these experimental results highlight that the addition of salt in the aqueous phase of emulsions stabilized by SDS promotes the entering of emulsion oil droplets at the air/aqueous phase interface.

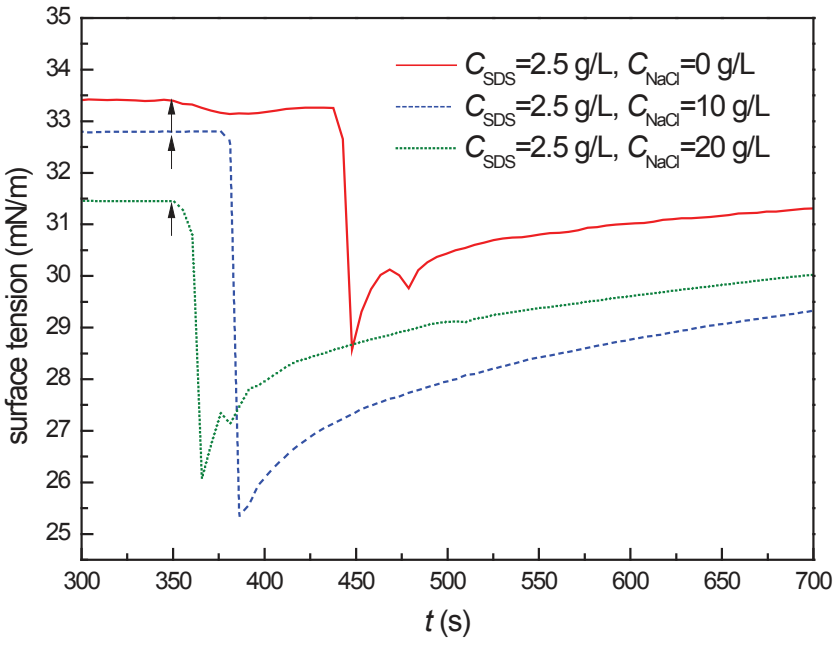

Figure 7.14: Time evolution of the surface tension of the aqueous phase solutions to monitor the entering of emulsion oil droplets at the air/aqueous phase interface for emulsions stabilized by SDS (C_{SDS}=2.5 g/L) with different concentrations of NaCl in the aqueous phase. The exact compositions of the emulsion aqueous phase are indicated in the legend. Black arrows indicate the injection time of the emulsion.

Note that this experimental set-up does not exactly mimic the entering of oil droplet at the air/aqueous phase interface during the sheet expansion. Indeed, in the single-tear experiment, the oil droplets enter an interface that is in expansion and so not at equilibrium. By contrary, in the entering experimental set-up, the aqueous solution is at equilibrium at the beginning of the experiment and so we measure equilibrium surface

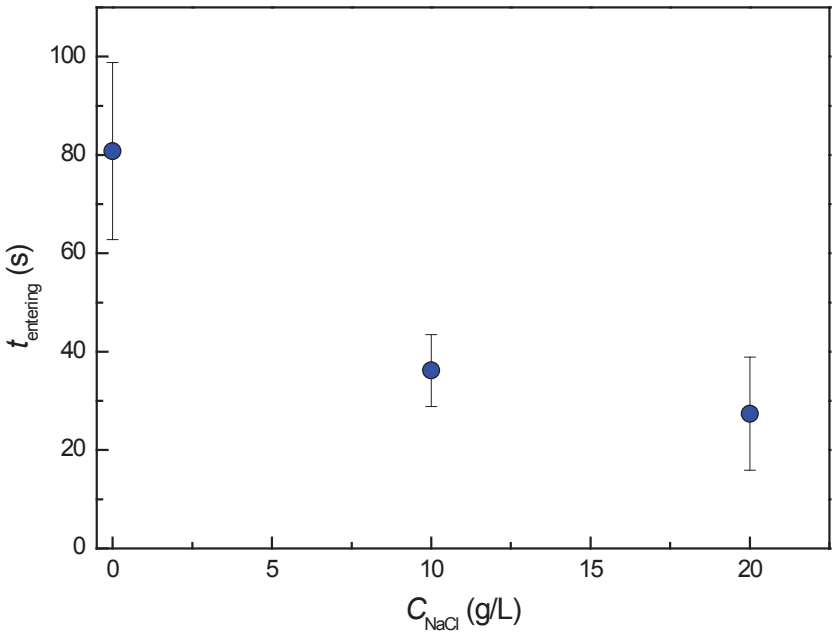

Figure 7.15: Evolution of the entering time, t_{entering}, with the salt concentration in the aqueous phase of emulsion stabilized by SDS (C_{SDS}=2.5 g/L).

tensions. However, even if we are not in the exact same conditions than for the single-tear experiment, the entering experimental set-up gives an idea of the tendency of oil droplets to enter the air/aqueous phase interface depending on the emulsion aqueous phase composition. We can reasonably think that the entering of oil droplets would be facilitated by the expansion of the interface (as it will entail a decrease of surfactant concentration at the interface) and so the entering times would be shorter than the ones measured with the entering experimental set-up.

The physical mechanism at the origin of the decrease of the entering time with the salt concentration will be discussed in the last part of this chapter. We first present the results concerning emulsions stabilized by cationic surfactants.

7.3 Emulsions stabilized by cationic surfactants

This section is dedicated to the destabilization mechanisms of liquid sheet made of emulsions stabilized by cationic surfactants. We study the influence of salt and amphiphilic copolymer concentrations of the emulsion aqueous phase on the perforation process. The objective is to investigate if an increase of the salt concentration has the same effect on the perforation of liquid sheet made of emulsions stabilized by cationic surfactants as observed for emulsions stabilized by anionic surfactants (SDS). From an application point of view, the utilization of cationic surfactants is not recommended due to their higher toxicity compared to anionic surfactants. The main reason of the utilization

of cationic surfactants for this study is that they do not interact with neutral copolymers on contrary to anionic surfactants such as SDS [Hayakawa 1991]. Hence, with cationic surfactant-stabilized emulsions, we can study the influence of the addition of amphiphilic copolymers in the emulsion aqueous phase on the perforation process. We first present the samples studied and then the influence of the addition of monovalent and divalent salts on sheet perforation. Then, we investigate the effect of the addition of amphiphilic copolymers in the emulsion aqueous phase on sheet perforation. In the last part of this section, we study the influence of salt and copolymer concentrations on the two steps of the perforation mechanism.

7.3.1 Samples

The emulsions studied in this section are stabilized by cationic surfactants: cetylpyridinium chloride (CpCl). The oil phase of the emulsion is composed of methyllaurate (i.e. the same oil as for model emulsions) and the emulsion concentration, C, is set at 0.3 % v/v. The aqueous phase of the emulsion is a solution of CpCl at a concentration of 0.9 mM in milliQ water. This concentration corresponds to the critical micelle concentration of CPCl.

For some experiments, a monovalent (sodium chloride) or a divalent (sodium sulfate) salt is added to the aqueous phase. Sodium chloride salt is added to the aqueous phase at a weight concentration ranging from 1 to 20 g/L, i.e. molar concentration ranging from 0.02 to 0.34 mol/L. Sodium sulfate salt is added to the aqueous phase at a weight concentration ranging from 0.07 to 2.8 g/L, i.e. molar concentration ranging from 0.5 to 20 mM.

In another set of experiments, a water-soluble polymer, Pluronic F108, is added to the aqueous phase of the emulsion. The objective is to decorate the emulsion oil droplets with polymer chains that adsorb at the interfaces. The Pluronic F108 is a commercial PEO.PPO.PEO triblock copolymer composed of a central chain of polypropylene oxide (PPO) with two lateral chains of polyethylene oxide (PEO). On average, the PPO block is made of 56 monomers and each PEO block of 132 monomers. At room temperature, the PPO central block of the polymer is hydrophobic and the two PEO lateral blocks hydrophilic. The hydrophobic PPO block can adsorb at the oil/aqueous phase interface whereas the hydrophobic tails (PEO blocks) remains in the aqueous phase. The radius of gyration of PEO blocks of the copolymer is equal to 2.6 nm [Cabane 1982]. The polymer is dissolved in the emulsion aqueous phase at a concentration ranging from 0.1 to 1 % w/w. These concentrations are below the critical micelle concentration (CMC), which is equal to 3 % w/w at 20°C [Molino 1998]. Therefore we expect the polymer molecules to be dispersed in a unimolecular way in solutions, and to not form micelles. For more details about the emulsion composition see section 2.1.1.4.

All the emulsions are prepared by mechanical stirring. As described in section 2.1.3.5, the addition of monovalent or divalent salts and the addition of Pluronic F108 copolymer

do not drastically modify the drop size distribution of the emulsion (see Figure 2.13). For all the compositions of the emulsion aqueous phase, the drop size distributions are comparable with $d_{\text{oil}} = (13.3 \pm 2.0)$ μm (averaged over the different compositions).

7.3.2 Effect of the addition of salt on sheet perforation

As for the emulsions stabilized by anionic surfactants (section 7.2.2.1), we investigate the influence of the addition of salt on the perforation of liquid sheets produced with the single-tear experimental set-up. Here, the emulsion aqueous phase is a solution of CpCl at 0.9 mM with increasing concentration of salt. The experimental impact parameters are the same as the ones reported in section 7.2.2.1. The perforation process is quantified by the value of the total number of perforation events N_{tot}.

7.3.2.1 Monovalent salt

In Figure 7.16 are shown images of the sheets obtained for different concentrations of NaCl in the emulsion aqueous phase. As for the emulsions stabilized by SDS (Figure 7.4), we observe that without salt there is almost no perforation of the sheet (Figure 7.16(a)). The addition of salt at 1 g/L triggers the perforation (Figure 7.16(b)), a further increase of the NaCl concentration entails an increase of the number of perforation events (Figure 7.16(c,d)).

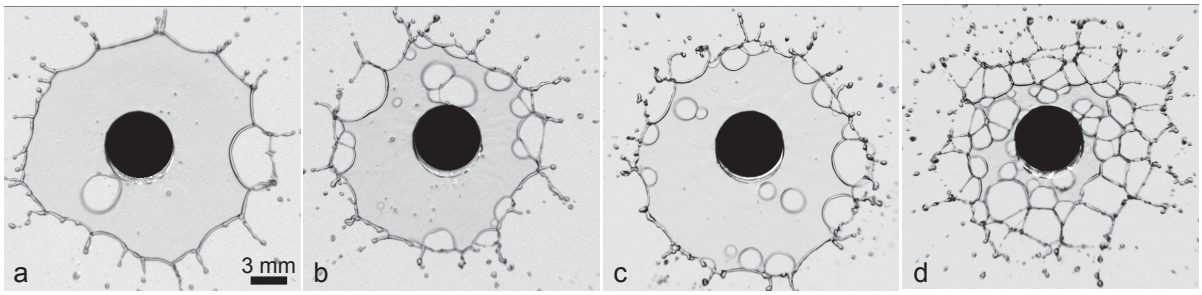

Figure 7.16: Images of liquid sheets made of emulsions stabilized by CpCl for different concentrations of NaCl in the aqueous phase. The images are taken 3.6 ms after the impact of the tear. a). C_{NaCl}=0 g/L b). C_{NaCl}=1 g/L c). C_{NaCl}=2.5 g/L and d). C_{NaCl}=10 g/L.

The evolution of the total number of perforation events, N_{tot}, as a function of the NaCl concentration is plotted in Figure 7.17. On the bottom x-axis, the NaCl concentrations are expressed in g/L and on the top x-axis in mol/L. We find that an increase of the salt concentration from 0 g/L to 20 g/L entails an increase of the total number of perforation events from 15 to 137.

For the emulsions stabilized by anionic surfactants, we have shown that the total number of perforation events, N_{tot}, decreases with the Debye length, κ^{-1}, i.e. with the

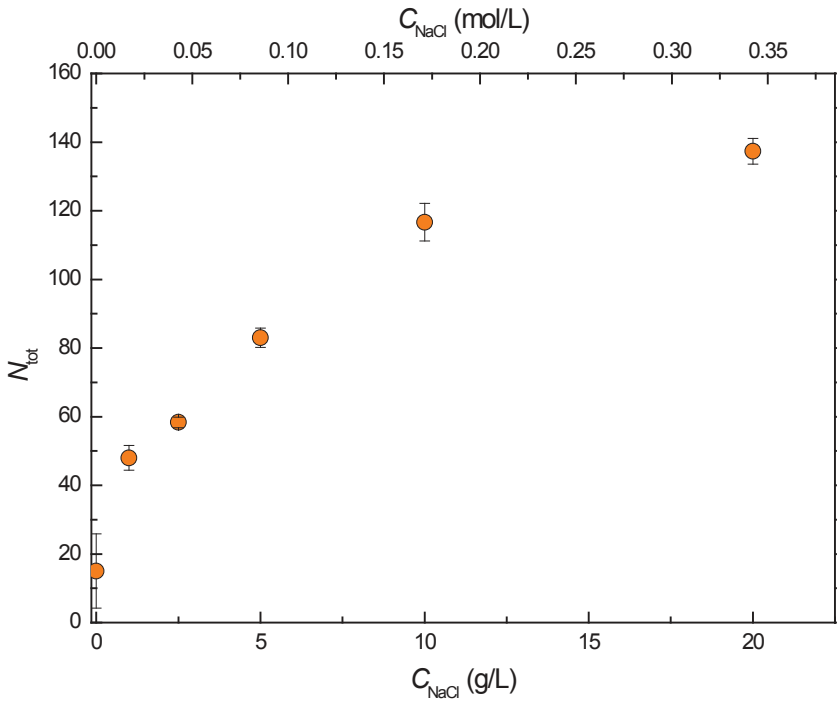

Figure 7.17: Evolution of the total number of perforation events, N_{tot}, as a function of the NaCl concentration in the aqueous phase of emulsions stabilized by CpCl.

range of the electrostatic repulsive forces. The Debye length is an inverse function of the ionic strength (I) (Equation 7.3) that strongly depends on the charge number of ions (Equation 7.4). For a same molar concentration, the ionic strength, I, of a divalent salt in solution will be larger than for a monovalent salt and so the Debye length shorter. To further investigate the influence of the Debye length on the sheet perforation, we add divalent salt in the emulsion aqueous phase and compare the results to those obtained with monovalent salt.

7.3.2.2 Divalent salt

We use sodium sulfate, Na_2SO_4, as divalent salt. In Figure 7.18 is shown the evolution of the total number of perforation events as a function the Na_2SO_4 concentration in the emulsion aqueous phase. As expected, we observe that without salt the sheet is not perforated. An increase of the divalent salt concentration entails a continuous increase of the total number of perforation events, from 23 for $C_{Na_2SO_4}$=0.07 g/L to 126 for $C_{Na_2SO_4}$=2.8 g/L. Hence, the same influence is observed for the divalent salt (Na_2SO_4) as for the monovalent salt (NaCl). We will now compare the influence of these two salts on the sheet perforation.

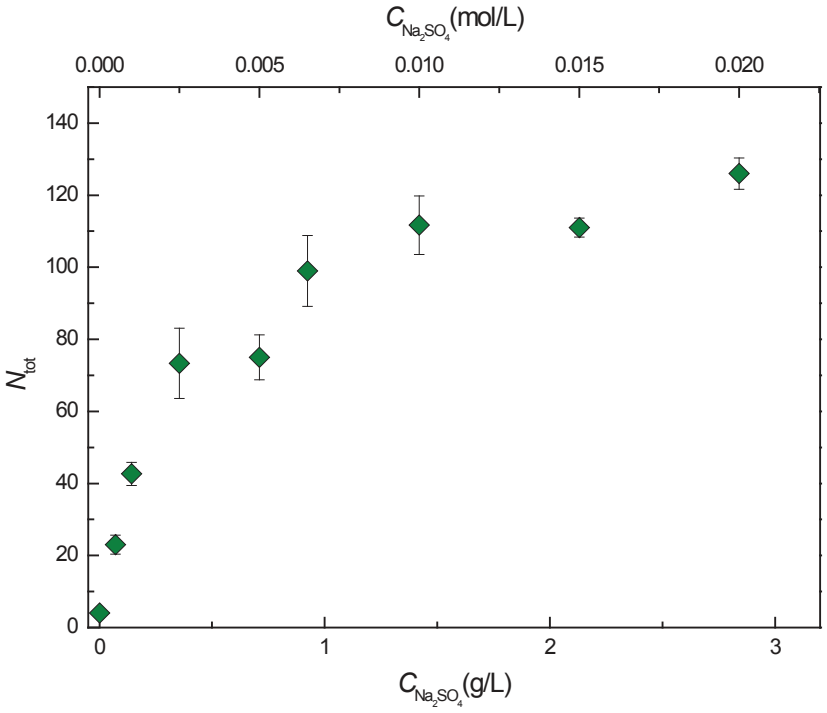

Figure 7.18: Evolution of the total number of perforation events, N_{tot}, as a function of the Na_2SO_4 concentration in the aqueous phase of emulsions stabilized by CpCl.

7.3.2.3 Comparison of the influence of monovalent and divalent salts

In Figure 7.19(a) is plotted the evolution of the total number of perforation events as a function of the salt molar concentration in the emulsion aqueous phase for monovalent salt (NaCl, orange circle symbols) and for divalent salt (Na_2SO_4, green diamond symbols). As previously observed, for both salts, N_{tot} increases with salt concentration. However, the curve is shifted to larger salt concentrations for the monovalent salt compared to the divalent one. Hence, at the same molar concentration, the divalent salt is more efficient to promote the sheet perforation. In Figure 7.19(b) is plotted the evolution of the total number of perforation events as a function of the Debye length of the emulsion aqueous phase for the two salts. N_{tot} decreases with the Debye length for both salts. An increase of the range of the electrostatic repulsion forces (the Debye length) prevents the perforation of liquid sheets. Compared to Figure 7.19(a), we observe a better collapse of the data points for the two salts once plotted as a function of the Debye length. This collapse highlights that the perforation of liquid sheets is controlled by the range of the electrostatic repulsion forces. The collapse is however not perfect and for a given Debye length, κ^{-1}, the divalent salt is slightly more efficient to promote the sheet perforation.

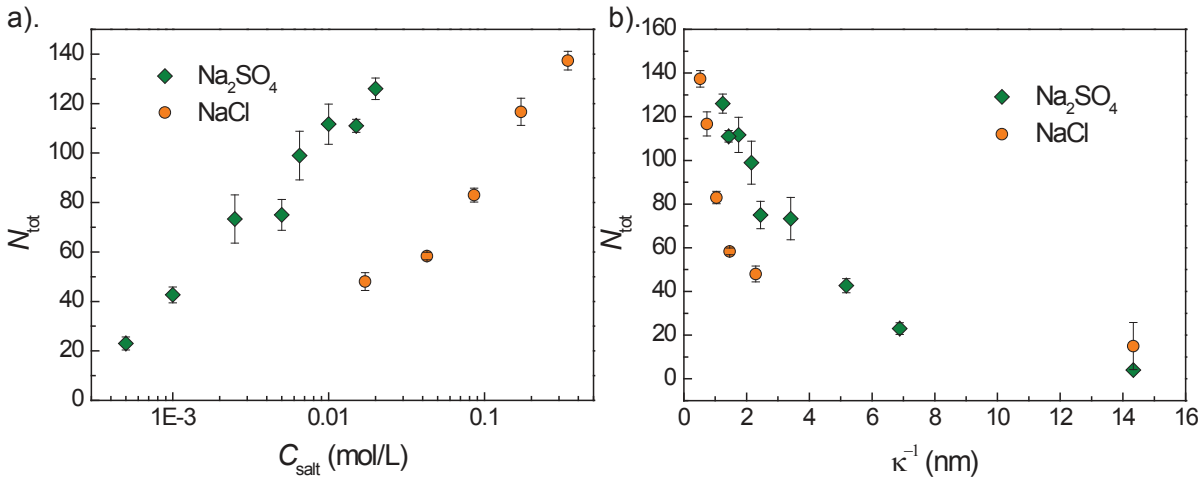

Figure 7.19: a). Evolution of the total number of perforation events, N_{tot}, as a function of the salt concentration in the aqueous phase of emulsions stabilized by CpCl, for monovalent salt (NaCl) and divalent salt (Na_2SO_4). b). Evolution of the total number of perforation events, N_{tot}, as a function of the Debye length, κ^{-1}, of the aqueous phase of emulsions stabilized by CpCl, for monovalent salt (NaCl) and divalent salt (Na_2SO_4).

7.3.3 Effect of the addition of amphiphilic copolymer on sheet perforation

Amphiphilic triblocks copolymer (Pluronic F108) is added to the aqueous phase of the emulsion. We investigate the influence of the Pluronic F108 concentration on the sheet perforation for different sodium chloride concentrations. Figure 7.20 shows images of the sheets for different concentrations of Pluronic F108 in the aqueous phase of the emulsion taken at the same time after the tear impact. Here the NaCl concentration in the emulsion aqueous phase is set at 20 g/L. As observed previously, without Pluronic F108 and at high salt concentration (20 g/L), a high number of perforation events are observed in the liquid sheet (Figure 7.20(a)). Then, the addition of Pluronic F108 entails a continuous decrease of the number of perforation events observed in the liquid sheets (Figure 7.20(b,c)). For a concentration in Pluronic F108 equal to 7.5 g/L, we do not observe any perforation of the liquid film (Figure 7.20(d)). The pictures presented in Figure 7.20 correspond to a salt concentration of 20 g/L but the same phenomenon is observed for the different NaCl concentrations investigated.

In Figure 7.21(a) is plotted the evolution of the total number of perforation events, N_{tot}, with the Pluronic F108 concentration in the emulsion aqueous phase for different NaCl concentrations. For a given salt concentration, we observe that an increase of the copolymer concentration entails a large decrease of N_{tot}. For C_{NaCl}=20 g/L, N_{tot} is equal to 146 for C_{F108}=1 g/L and to 3 for C_{F108}=7.5 g/L. The addition of Pluronic F108 permits to completely inhibit the perforation process. The same phenomenon is observed for the different salt concentrations, but a decrease of the salt concentration entails a

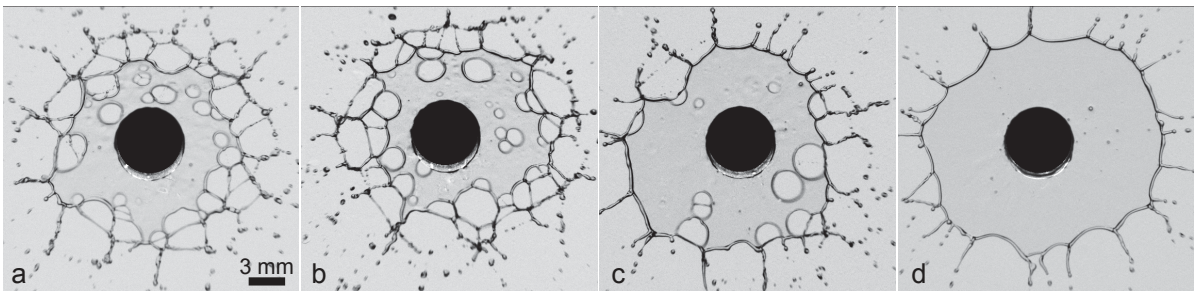

Figure 7.20: Images of liquid sheets made of emulsions stabilized by CpCl for different concentrations of Pluronic F108 in the aqueous phase. Images are taken 3.6 ms after the impact of the tear. a). C_{F108}=0 g/L b). C_{F108}=2.5 g/L c). C_{F108}=4 g/L and d). C_{F108}=7.5 g/L. Here the NaCl concentration in the emulsion aqueous phase is set at 20 g/L.

shift of the curve towards smaller values of N_{tot}. For example, at C_{F108}=2.5 g/L, 113 perforation events are counted for a salt concentration of 20 g/L and only 22 without salt. The influence of the concentration of sodium chloride on the sheet perforation is highlighted in Figure 7.21(b), where the same data as in Figure 7.21(a) are plotted as a function of the salt concentration for the different Pluronic F108 concentrations. This representation emphasizes that an increase of the salt concentration entails an increase of the total number of perforation events and that this effect is stronger as the Pluronic F108 concentration is lower.

7.3.4 Effect of the addition of salt and amphiphilic copolymer on the perforation mechanism

We have seen that for monovalent and divalent salts, the addition of salt in the emulsion aqueous phase triggers the perforation process. Then, a further increase of the salt concentration entails a continuous increase of the total number of perforation events. We have shown that the addition of amphiphilic copolymer (Pluronic F108) entails a decrease of the total number of perforation events. The addition of an adequate copolymer amount permits to completely inhibit the sheet perforation process. To understand the origin of these phenomena, we investigate the influence of the different parameters (salt and copolymer concentrations) on the two steps of the perforation mechanism: (i) the entering of oil droplet at air/aqueous phase interface and (ii) the spreading of oil droplet at the interface.

7.3.4.1 Pre-hole widening dynamics

In this section we investigate the localized thinning of the liquid film (pre-hole) due to the spreading of oil droplets at the air/aqueous phase interface. We perform these

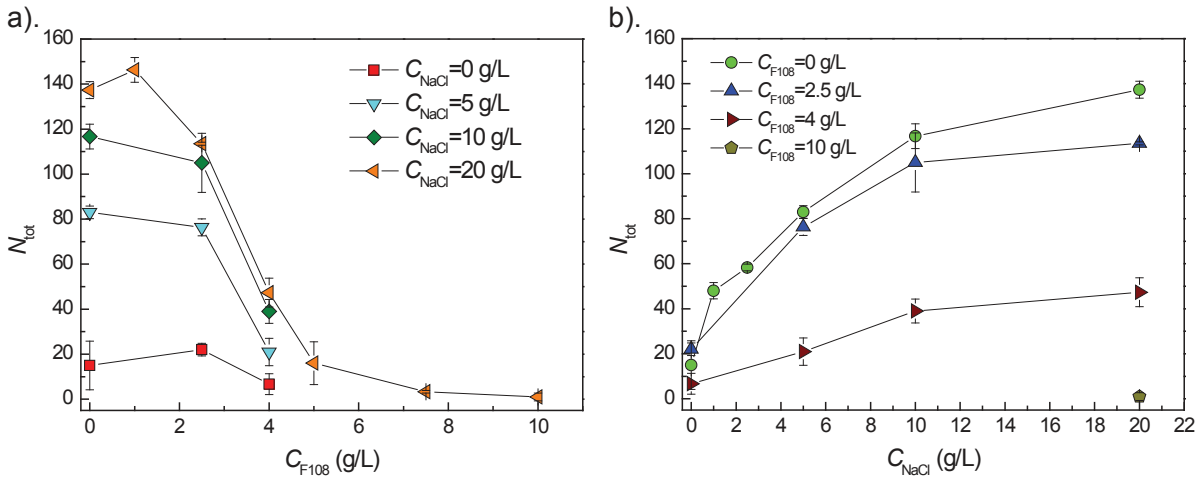

Figure 7.21: a). Evolution of the total number of perforation events, N_{tot}, as a function of the Pluronic F108 concentration in the aqueous phase of emulsions stabilized by CpCl for different NaCl concentrations as indicated in the legend. b). Evolution of the total number of perforation events, N_{tot}, as a function of the NaCl concentration in the aqueous phase of emulsions stabilized by CpCl for different concentrations of Pluronic F108 as indicated in the legend.

experiments for three different compositions of the emulsion aqueous phase :

1. C_{CpCl}=0.9 mM,
2. C_{CpCl}=0.9 mM and C_{NaCl}=20 g/L,
3. C_{CpCl}=0.9 mM, C_{NaCl}=20 g/L and C_{F108}=5 g/L.

For the first emulsion aqueous phase composition (C_{CpCl}=0.9 mM), very few perforation events were observed (around 15), on the contrary for the second composition (C_{CpCl}=0.9 mM and C_{NaCl}=20 g/L) a large number of perforation events were observed (around 137). For the third composition (C_{CpCl}=0.9 mM, C_{NaCl}=20 g/L and C_{F108}=5 g/L), very few perforation events were again observed (around 16). The objective is to investigate if those discrepancies are due to a difference of spreading behavior of oil droplets at the interface and so to a difference in the pre-hole widening dynamics.

In Figure 7.22 is plotted the evolution of the pre-hole radius, R_{ph}, as a function of the time elapsed since its formation, $T = t - t_{\text{ph}}$, for the different compositions of the emulsion aqueous phase. We find that, for the three aqueous phases investigated, R_{ph} increases with T as a power-law with an exponent 3/4: $R_{\text{ph}} = kT^{3/4}$. Once again, these results are in agreement with the ones obtained for model emulsions in Chapter 6 and so confirm a widening dynamics of pre-hole in agreement with the dynamics of Marangoni spreading.

In Figure 7.22, we observe a very good collapse of the curves obtained for the three different compositions of the emulsion aqueous phase. Hence, the widening dynamics

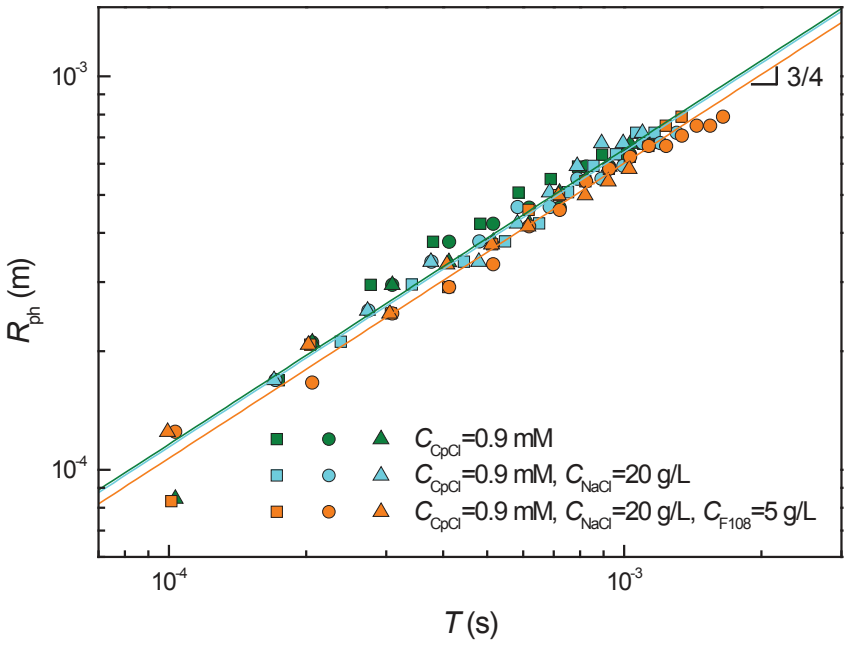

Figure 7.22: Evolution of the radius of the pre-hole, R_{ph}, as a function of T, the time elapsed since the pre-hole formation for emulsions stabilized by CpCl with different concentrations of NaCl and Pluronic F108 in the emulsion aqueous phase. The exact compositions of the emulsions aqueous phase are indicated in the legend. Different symbols correspond to different experiments. The lines are the best fits of the experimental data of the form: $R_{\mathrm{ph}} = kT^{3/4}$.

of the pre-hole and so the spreading dynamics of oil droplet at the air/aqueous phase interface are the same for the different compositions. Therefore, the differences observed in the perforation of liquid sheets for the different emulsion compositions do not arise from a different spreading behavior of the oil droplets at the air/aqueous phase interface.

As explained in section 7.2.3.1, we can extract from the fit of the experimental curves R_{ph} vs T, a value of the spreading parameter S_{fit}. These values are summarized in Table 7.2. We remark that the values obtained for S_{fit} are really close for the three compositions of the emulsion aqueous phase ($S_{\mathrm{fit}} = (9.5 \pm 0.8)$ mN/m averaged over the three compositions), as expected from the superimposition of the R_{ph} vs T curves (Figure 7.22). The values of S_{fit} can be directly compared to macroscopic measurement of the spreading parameter. The relevant surface tensions are presented in Table 7.2. The value of $\gamma_{\mathrm{air/oil}}$ is measured with a Wilhelmy plate tensiometer and is equal to 29.6 mN/m. The surface tension of the aqueous phases of different compositions, $\gamma_{\mathrm{air/aq}}$, are also measured with a Wilhelmy plate tensiometer and are reported in Table 7.2. The interfacial tension between the oil and aqueous phases, $\gamma_{\mathrm{aq/oil}}$, is measured thanks to a spinning drop tensiometer (see Appendix A.2). The values are reported in the second column of Table 7.2. From these surface tension measurements, one can estimate the

values of the spreading coefficient denoted S_{measured} and reported in the third column of Table 7.2.

For the three aqueous phase compositions $S_{\text{measured}} > 0$, which is a prerequisite for Marangoni spreading. The values measured for S_{measured} for the three compositions of the emulsion aqueous phase are comparable ($S_{\text{measured}} = (6.2 \pm 2.9)$ mN averaged over the three compositions) highlighting a similar tendency of oil droplets to spread over the aqueous phase of different compositions. The values of S_{measured} are in quantitative agreement with the values of the spreading coefficient deduced from the fits, S_{fit}. We remark that the values of S_{fit} are systematically larger than the values of S_{measured}, which suggest that the relevant air/aqueous phase surface tension for the pre-hole widening dynamics is not the equilibrium one, as explained in details for emulsions stabilized by SDS (section 7.2.3.1).

emulsion aqueous phase composition	$\gamma_{\text{air/aq}}$ (mN/m)	$\gamma_{\text{aq/oil}}$ (mN/m)	S_{measured} (mN/m)	S_{fit} (mN/m)
C_{CpCl}=0.9 mM	42.7	3.8	9.3	10.1
C_{CpCl}=0.9 mM and C_{NaCl}=20 g/L	35.4	0.7	5.1	9.8
C_{CpCl}=0.9 mM, C_{NaCl}=20 g/L and C_{F108}=5 g/L	34.3	0.6	4.1	8.6

Table 7.2: Values of $\gamma_{\text{air/aq}}$ and $\gamma_{\text{aq/oil}}$ for the three different compositions of the emulsion aqueous phase and values of S_{measured} calculated from these values with $\gamma_{\text{air/oil}}$=29.6 mN/m. The values of S_{fit} extracted from the fit of the evolution of R_{ph} vs T are also reported.

In conclusion, we have seen that the addition of salt and amphiphilic copolymer in the emulsion aqueous phase do not modify the widening dynamics of pre-holes and so the spreading of oil droplets at the air/aqueous phase interface. As the spreading behavior is the same for the different compositions of the emulsion aqueous phase, we will now investigate the influence of the compositions on the first step of the perforation mechanism, i.e. the entering of oil droplets at the air/aqueous phaser interface.

7.3.4.2 Entering of emulsion oil droplets at the air/aqueous phase interface

We investigate the entering properties of emulsion oil droplets at the air/aqueous phase interface thanks to the entering experimental set-up described in section 7.2.3.2. In Figure 7.23 is plotted the evolution of the surface tension measured at the air/aqueous phase interface during the entering of emulsion oil droplets. Three emulsion aqueous phase compositions are investigated (the same as for the study of the pre-hole widening dynamics):

1. C_{CpCl}=0.9 mM,

2. C_{CpCl}=0.9 mM and C_{NaCl}=20 g/L,

3. C_{CpCl}=0.9 mM, C_{NaCl}=20 g/L and C_{F108}=5 g/L.

For each curve, we observe at short time a plateau value corresponding to the equilibrium surface tension of the emulsion aqueous phase. The black arrows indicate the time of injection of emulsion oil droplets in the Petri dish. For the emulsions with aqueous phase composed of C_{CpCl}=0.9 mM and C_{CpCl}=0.9 mM, C_{NaCl}=20 g/L and C_{F108}=5 g/L, we observe a plateau value of the surface tension during the whole experiment (1000 s, i.e. 650 s after the injection of emulsion below the interface). For the emulsion with the aqueous phase composed of C_{CpCl}=0.9 mM and C_{NaCl}=20 g/L, we observe a sharp decrease of the surface tension around 100 s after the injection. The decrease of the surface tension corresponds to the entering and spreading of oil droplets at the interface.

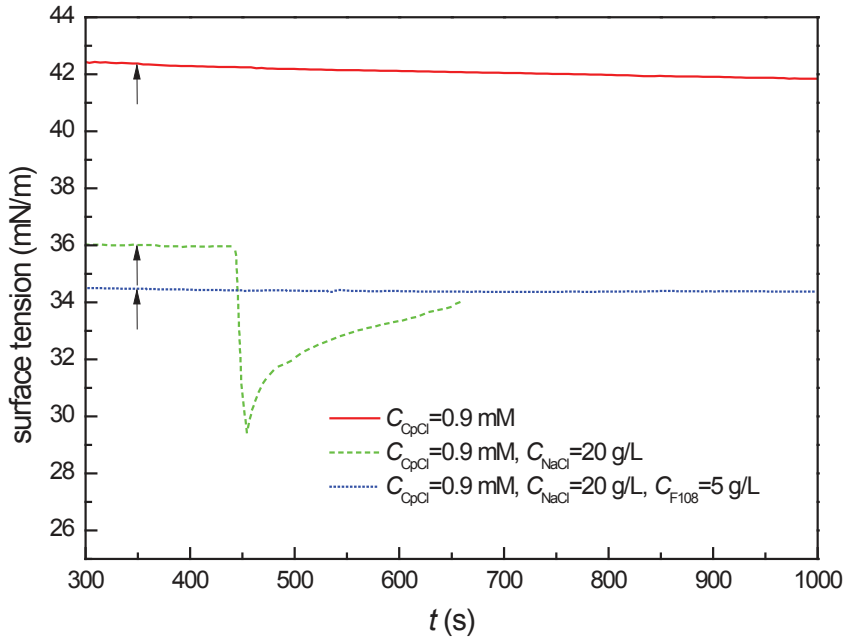

Figure 7.23: Time evolution of the surface tension of the aqueous phase solutions to monitor the entering of emulsion oil droplets at the air/aqueous phase interface for emulsions stabilized by CpCl with different concentrations of NaCl and Plutonic F108 in the aqueous phase. The exact compositions of the emulsion aqueous phase are indicated in the legend. Black arrows indicate the injection time of the emulsion.

In conclusion, for the emulsion stabilized by CpCl with a high concentration of NaCl (20 g/L) in the aqueous phase, the emulsion oil droplets enter the air/aqueous phase interface relatively rapidly ($t_{\mathrm{entering}} = (94 \pm 14)$ s) after the injection of the emulsion whereas for the emulsions stabilized by CpCl and by CpCl with high concentrations of NaCl (20 g/L) and Pluronic F108 (5 g/L), emulsion oil droplets never enter the air/aqueous phase interface during the experiment time (i.e. $t_{\mathrm{entering}} > 650$ s). Hence, the addition of NaCl

in the aqueous phase of emulsion stabilized by CpCl promotes the entering of oil droplets at the air/aqueous phase interface. On the contrary, the addition of an amphiphilic copolymer (Pluronic F108) in the aqueous phase of emulsion stabilized by CpCl and NaCl hinders the entering. The physical origin of the influence of the salt and copolymer concentrations on the entering of oil droplets at the air/aqueous phase interface will be discussed in the next section.

7.4 Discussion

We have seen that the addition of salts or amphiphilic copolymers on emulsions stabilized by ionic surfactants can trigger or inhibit the perforation process. We have shown that these two parameters do not modify the spreading properties of emulsion oil droplets at the air/aqueous phase interface but strongly alter the entering of oil droplets at the interface. In this section, we rationalize the influence of the salt and amphiphilic copolymer concentrations on the entering of oil droplets at the air/aqueous phase interface.

The entering and spreading of oil droplets at the air/aqueous phase interface are thermodynamically described by the entering, E, and spreading, S, coefficients. Those parameters have been previously defined (Equation 7.1 and 7.2). Positive values of these coefficients indicate that it is thermodynamically favorable for an oil droplet to enter and spread at the interface. In Table 7.3 are summarized the values of the entering and spreading coefficients for the different compositions of the aqueous phase of the emulsions that we have investigated. The values reported are the ones calculated from the macroscopic measurement of the various surface tensions. In Table 7.3 are gathered data for emulsions stabilized by anionic surfactants (SDS) and by cationic surfactants (CpCl).

As already highlighted, all the values of E and S are positive indicating that for all the investigated systems, it is thermodynamically favorable for an oil droplet to enter and spread at the air/aqueous phase interface. Hence, the two necessary conditions for the perforation mechanism are fulfilled. However, these two conditions are necessary but not sufficient. As highlighted by our experimental data, for some compositions of the emulsion aqueous phase (C_{SDS}=2.5 g/L, C_{NaCl}=10 g/L; C_{CpCl}=0.9 mM; C_{CpCl}=0.9 mM, C_{NaCl}=20 g/L, C_{F108}=5 g/L), very few perforation events are observed, whereas for other compositions (C_{SDS}=0.1 g/L, C_{NaCl}=10 g/L; C_{SDS}=2.5 g/L, C_{NaCl}=20 g/; C_{CpCl}=0.9 mM, C_{NaCl}=20 g/L), a large number of perforation events are observed (see Table 7.3), although E and S are positive for all emulsion compositions. An important feature to keep in mind is that positive values of E and S only indicate that it is thermodynamically favorable for oil droplets to enter and spread at the air/aqueous phase interfaces. However such thermodynamic approach does not consider the energy barriers that can kinetically limit these processes.

emulsion aqueous phase composition	E (mN/m)	S (mN/m)	N_{tot} (mN/m)
C_{SDS}=0.1 g/L, C_{NaCl}=10 g/L	14.2	7.8	179
C_{SDS}=2.5 g/L, C_{NaCl}=10 g/L	3.2	2.8	15
C_{SDS}=2.5 g/L, C_{NaCl}=20 g/L	2.0	1.6	76
C_{CpCl}=0.9 mM	16.9	9.3	15
C_{CpCl}=0.9 mM, C_{NaCl}=20 g/L	6.5	5.1	137
C_{CpCl}=0.9 mM, C_{NaCl}=20 g/L, C_{F108}=5 g/L	5.3	4.1	16

Table 7.3: Values of the entering, E, and spreading, S, coefficients for emulsions stabilized by SDS and CpCl. The exact compositions of the emulsion aqueous phase are indicated in the first column. The values of E and S are calculated from the surface tension measurements. In the last column are reported the total number of perforation events, N_{tot}, observed with the single-tear experiment for liquid sheets made of corresponding emulsions.

7.4.1 Influence of the salt concentration

We first discuss the influence of the addition of salt on emulsions stabilized by ionic surfactants. For the emulsions stabilized by SDS, we compare the results obtained for the following compositions of the aqueous phase of the emulsion:

- C_{SDS}=2.5 g/L and C_{NaCl}=10 g/L,
- C_{SDS}=2.5 g/L and C_{NaCl}=20 g/L

and for the emulsions stabilized by CpCl:

- C_{CpCl}=0.9 mM,
- C_{CpCl}=0.9 mM and C_{NaCl}=20 g/L.

For both surfactants, we observe that without salt or at low salt concentrations, very few perforation events are observed whereas at high salt concentrations the liquid sheets are largely perforated (high values of N_{tot}). With the entering model experiments, we have seen that the addition of salt promotes the entering of oil droplets at the air/aqueous phase interface. For the different compositions, the values of E are of the same order of magnitude and we observe no correlation of N_{tot} with E. Hence, the discrepancies observed for the different salt concentrations cannot be explained by a thermodynamical favored entering of oil droplets at the interface. We suggest that the influence of salt concentration arises from the existence of energy barriers that prevent the entering of oil droplets at the air/aqueous phase interface.

To understand the influence of the addition of salt on emulsions stabilized by ionic surfactants, we have to consider the electrostatic repulsion forces. SDS and CpCl surfactants are amphiphilic molecules with a hydrophobic tail and a charged headgroup.

The surfactant molecules are present at the air/aqueous phase and oil/aqueous phases interfaces, as schematically represented in Figure 7.24 (for SDS surfactants). When an oil droplet approaches the air/aqueous phase interface, there is an electrostatic repulsion between surfactant charged headgroups (Figure 7.24). These repulsive forces stabilize the thin aqueous film formed between the oil droplets and the interface and so prevent the entering of the oil droplets at the interface. Hence, no perforation of the liquid sheet occurs, as experimentally observed for ionic surfactant stabilized-emulsions without salt. The addition of salt decreases the range of the electrostatic repulsion forces and so promote the entering of oil droplets at the interface. Hence, a decrease of the range of the electrostatic repulsion forces promotes the perforation process. This point is confirmed experimentally. In Figure 7.25 are plotted the evolutions of N_{tot} with the Debye length, κ^{-1}, for the different systems investigated. The Debye length (Equation 7.3) characterizes the range of the electrostatic repulsion forces. For all the investigated compositions, N_{tot} increases with decreasing Debye length, indicating that a decrease of the electrostatic repulsion range promotes the perforation process.

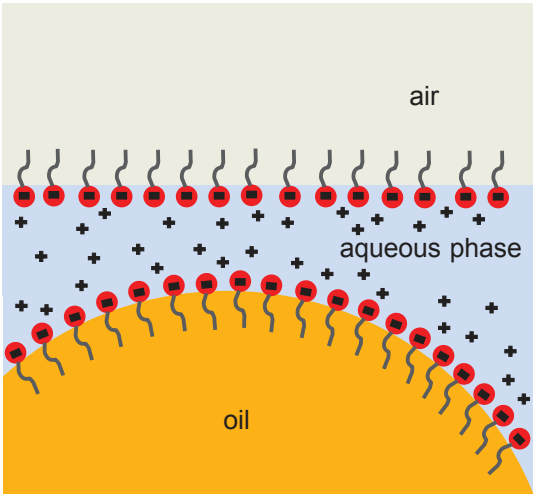

Figure 7.24: Sketch of an oil droplet stabilized by anionic surfactants approaching the air/aqueous phase interface covered by surfactants. The counterions in solution are represented.

We have seen that at a given molar concentration, divalent salt (Na_2SO_4) promotes the perforation process compared to monovalent salt (NaCl) (see Figure 7.19). Divalent salts are more efficient than monovalent salt to screen the electrostatic repulsion forces between the surfactant charged headgroups. Hence, at a given molar concentration, divalent salts decrease to a greater extent the range of the electrostatic repulsion forces compared to monovalent salt. Consequently, at a given molar concentration, divalent salt facilitates the entering of oil droplets at the interface, and promotes the perforation process compared to a monovalent salt. As visible in Figure 7.19 and Figure 7.25, once

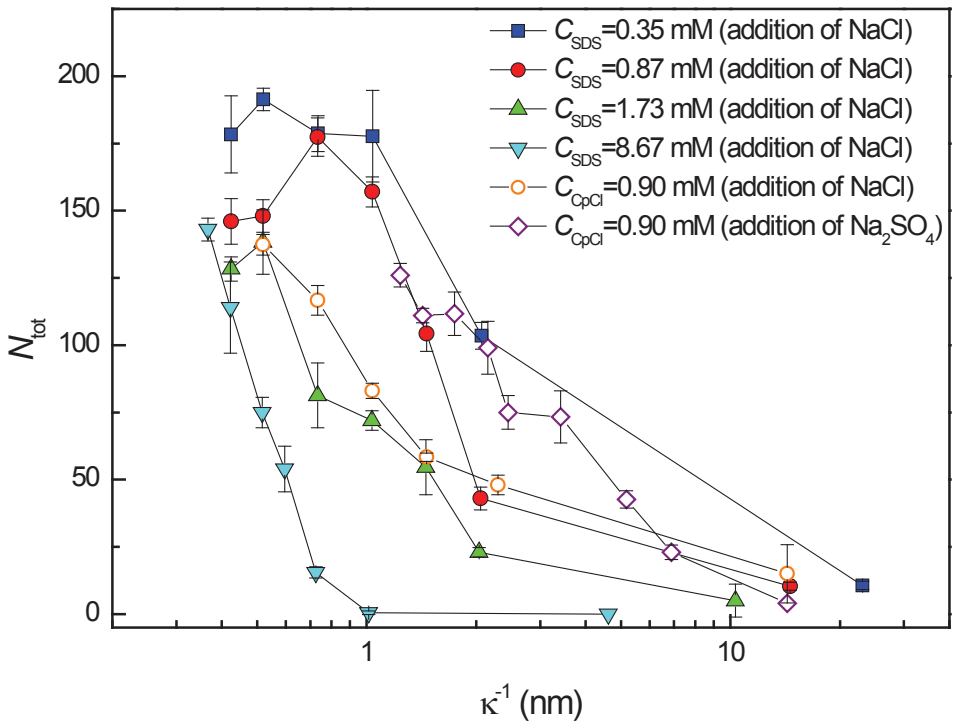

Figure 7.25: Evolution of the total number of perforation events, N_{tot}, as a function of the Debye length of the aqueous phase of emulsions stabilized by anionic (SDS) and cationic (CpCl) surfactants. The exact compositions of the emulsion aqueous phase are indicated in the legend. The salts added at different concentrations to modify the Debye length are indicated in parentheses.

plotted as a function of the Debye length, the evolutions of N_{tot} for the two salts (Na_2SO_4 and NaCl, for emulsions stabilized by CpCl) are not perfectly superimposed: at a given Debye length, Na_2SO_4 is more efficient to promote the perforation. Manifestly, the two anions, Cl^- and SO_4^{2-}, do not shield surfactant headgroup repulsions with the same efficiency.

7.4.2 Influence of the surfactant concentration

We then discuss the influence of the surfactant concentration on the perforation process. This parameter has been studied only for emulsions stabilized by anionic surfactants (SDS). We have seen that at a given salt concentration, a decrease of the surfactant concentration promotes the perforation of liquid sheets. We have shown that the surfactant concentration does not modify the spreading properties of oil droplets at the air/aqueous phase. Hence, we suggest that the surfactant concentration modifies the entering properties of oil droplets at the interface. As already highlighted, once plotted as a function of the Debye length (Figure 7.25), the evolution of N_{tot} for the different surfactant con-

centrations are not superimposed. Hence, the influence of the surfactant concentration on the perforation of liquid films cannot be explained by electrostatic considerations.

To elucidate the influence of the surfactant concentration, we compare the values of the entering coefficient, E, for the following compositions of the emulsion aqueous phase where the surfactant concentration is varied whereas the salt concentration is kept constant (see Table 7.3):

- C_{SDS}=0.1 g/L and C_{NaCl}=10 g/L, E=14.2 mN/m
- C_{SDS}=2.5 g/L and C_{NaCl}=10 g/L, E=3.2 mN/m

We observe that the entering parameter, E, is significantly larger for the emulsion with C_{SDS}=0.1 g/L than for the emulsion with C_{SDS}=2.5 g/L (Table 7.3). This effect is due to the higher surface tension, $\gamma_{air/aq}$, of the aqueous phase with low SDS concentration (C_{SDS}=0.1 g/L) compared to the solution with high SDS concentration (C_{SDS}=2.5 g/L). A higher surface tension implies that it is easier for an oil droplet to enter the air/aqueous phase interface. Hence, more perforation events occurred at low surfactant concentration, as experimentally measured.

In conclusion, a decrease of the surfactant concentration in the emulsion aqueous phase thermodynamically favors the entering of oil droplets at the air/aqueous phase interface and so promote the perforation of liquid films. A similar effect of the surfactant concentration on the entering of oil droplets at the air/aqueous phase interface has been reported for antifoams [Hadjiiski 2001].

7.4.3 Influence of the amphiphilic copolymer concentration

Finally, we discuss the influence of amphiphilic copolymer concentration on the perforation of liquid films. We have seen that the addition of copolymers in the aqueous phase of emulsions stabilized by CpCl and various concentrations of NaCl permits to limit the perforation process. The addition of an adequate copolymer concentration permits to completely inhibit the perforation. We have shown that the addition of copolymer does not modify the spreading properties of oil droplets at the air/aqueous phase interface. On the contrary, a strong influence of the copolymer concentration was highlighted on the entering properties of oil droplets at the air/aqueous phase interface with the entering model experiment. The addition of copolymer inhibits the entering of oil droplets.

From the entering coefficients, E, reported in Table 7.3 for emulsions with and without copolymer, it is clear that the addition of copolymer does not thermodynamically favor or prevent the oil droplet entering, as the values of E are comparable (E=6.5 mN/m without Pluronic F108 and E=5.3 mN/m for C_{F108}=5 g/L). Hence, we suggest that the influence of amphiphilic copolymer arises from thin-film forces that stabilize the liquid film and prevent the entering of oil droplets at the air/aqueous phase interface.

Due to their amphiphilic nature, the copolymer chains are present at the oil/aqueous phase and air/aqueous phase interfaces. Without copolymer, the perforation of the liquid

sheet is favored by the high salt concentration. The addition of copolymer entails a steric repulsion due to the presence of polymer chains at the oil/aqueous phase interface (see sketch Figure 7.26). The steric repulsions stabilize the thin aqueous film formed between the interface and the approaching oil droplet and so limit the entering of the droplet at the interface. The increase of the copolymer concentration increases the range of the steric repulsion up to a range for which the entering of oil droplet is completely inhibited and so no perforation is observed in the liquid film.

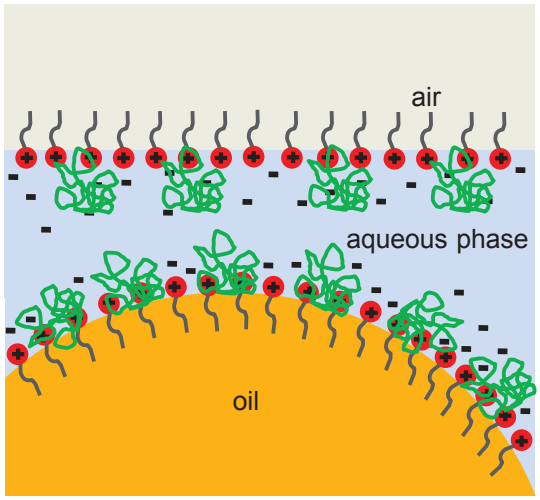

Figure 7.26: Sketch of an oil droplet stabilized by cationic surfactants and amphiphilic copolymers approaching the air/aqueous phase interface covered by surfactants. The counterions in solutions are represented. The copolymer gyration radius is estimated R_G=4.1 nm [Cabane 1982], i.e. around four times larger than CpCl molecules. Hence, we assume that the copolymer molecules have the time to diffuse at the air/aqueous phase interface at the time scale of the experiment.

There is a competition between the effect of salt and the effect of amphiphilic copolymers. The addition of salt promotes the entering of oil droplets at the air/aqueous phase interface by screening the electrostatic repulsion forces, whereas the addition of amphiphilic copolymer prevents the droplets entering due to steric repulsion forces. Hence, the entering of oil droplets and so the perforation process, is governed by the ranges of the electrostatic and steric repulsion forces. If the electrostatic repulsion range exceeds the steric repulsion range, the electrostatic effects are dominant and the perforation process is limited due to the electrostatic repulsion between surfactant charged headgroups. On the contrary, if the steric repulsion range exceeds the electrostatic repulsion range, the steric effects are dominant and the perforation process is limited due to the steric repulsion induced by the polymer chains at the oil/aqueous phases interface.

In Figure 7.21(a) are compared the influences of NaCl and Pluronic F108 concentrations on the sheet perforation. At high salt concentration (C_{NaCl}=20 g/L), the range of

the electrostatic repulsion forces is very short (κ^{-1}=0.5 nm) so a large number of perforation events are observed without copolymer. The addition of amphiphilic copolymer increases the range of the steric repulsion forces. The steric repulsion forces are dominant at low copolymer concentration (C_{F108}=2.5 g/L) due to the short Debye length and so the number of perforation events decreases rapidly with the copolymer concentration. Here, the inhibition of the perforation process is due to the steric repulsion forces. At intermediate salt concentrations (C_{NaCl}=5 and 10 g/L), the electrostatic repulsion forces range, κ^{-1}, is equal to (0.7-1.0) nm. These electrostatic repulsion forces are not sufficient to hinder oil droplets entering at the air/aqueous phase interface as large numbers of perforation events are observed. The addition of amphiphilic copolymer entails a decrease of the number of perforation events as soon as the range of the steric repulsion is long enough, i.e. for C_{F108}=4 g/L. Without salt, the electrostatic repulsion forces range is equal to 14 nm and the perforation process is very limited. The addition of amphiphilic copolymer has no influence on the number of perforation events and so on the perforation process as the electrostatic repulsions between the surfactant headgroups are sufficient to inhibit the perforation of liquid films. Here, the inhibition of the perforation is due to the electrostatic repulsion forces.

To quantitatively analyze these results, we need to estimate the range of the steric repulsion. The length scale of the steric repulsion depends on the conformation of the copolymer chains adsorbed at the oil/aqueous phase interface and so on the grafting density of copolymer at the interface, which is directly related to the copolymer concentration. The different conformations of the polymer chains at the interface, depending on the copolymer concentration, and the corresponding effective thickness, h_{eff}, are schematically represented in Figure 7.27. We estimate the range of the steric repulsion to be equal to the effective thickness of the copolymer layer adsorbed at the interface. Without amphiphilic copolymer, the range of the steric repulsion is equal to 0 nm. At low polymer concentration, Figure 7.27(a), the polymer chains are in a mushroom conformation at the interface, the steric range is inferior to the radius of gyration of the PEO block, R_G=2.6 nm. At higher polymer concentration, the grafting density of the polymer chains increases and so entails a change of conformation of the polymer chains at the interface, from a mushroom regime to a brush regime. At this transition, Figure 7.27(b), the range of the steric repulsion is equal to the radius of gyration of the PEO block (2.6 nm). Then, at higher concentration, Figure 7.27(c), the polymer chains are in a brush conformation, hence the steric repulsion range keep increasing and is superior to R_G. Finally, the longer steric range reachable is expected when the polymer chains are fully extended, which corresponds to a length scale of the steric repulsion of 52.8 nm [Barnes 2000], Figure 7.27(d).

To estimate the range of the steric repulsion in our system we calculate the copolymer grafting density following:

$$\sigma = \frac{2C_{F108}N_a}{MA_{interface}} \tag{7.8}$$

with C_{F108} the mass concentration in copolymer, N_a the Avogadro number, M the copoly-

mer molar mass and $A_{\text{interface}}$ the total surface of the oil/aqueous phase interface. The prefactor 2 accounts for the two PEO blocks. For an emulsion concentration set at 0.3 % v/v, we evaluate the total surface of the oil/aqueous phase interface to 1.29 m^2 for 1 liter of emulsion with d_{oil}=13 μm. If we consider that all the copolymer added is at the oil/aqueous phase interface, the grafting density is equal to 67 chains/nm^2 for $C_{\text{F108}} = 1$ g/L and to 667 chains/nm^2 for $C_{\text{F108}} = 10$ g/L. These high grafting densities correspond to a distance between grafting points of 0.12 nm for $C_{\text{F108}} = 1$ g/L and 0.04 nm for $C_{\text{F108}} = 10$ g/L. These values are below the size of a monomer, a=0.4 nm. This is physically not possible. Hence, a not negligible amount of the added polymer chains is not adsorbed at the oil/aqueous phases interface. To quantify the proportion of polymer adsorbed at the interface, we need to know the adsorption enthalpy of the polymer at the oil/aqueous phase interface. Without knowing this parameter, we cannot quantify the grafting density of copolymer at the interface and so the range of the steric repulsion. We could not find in the literature numerical values for the enthalpy for formulations comparable to ours.

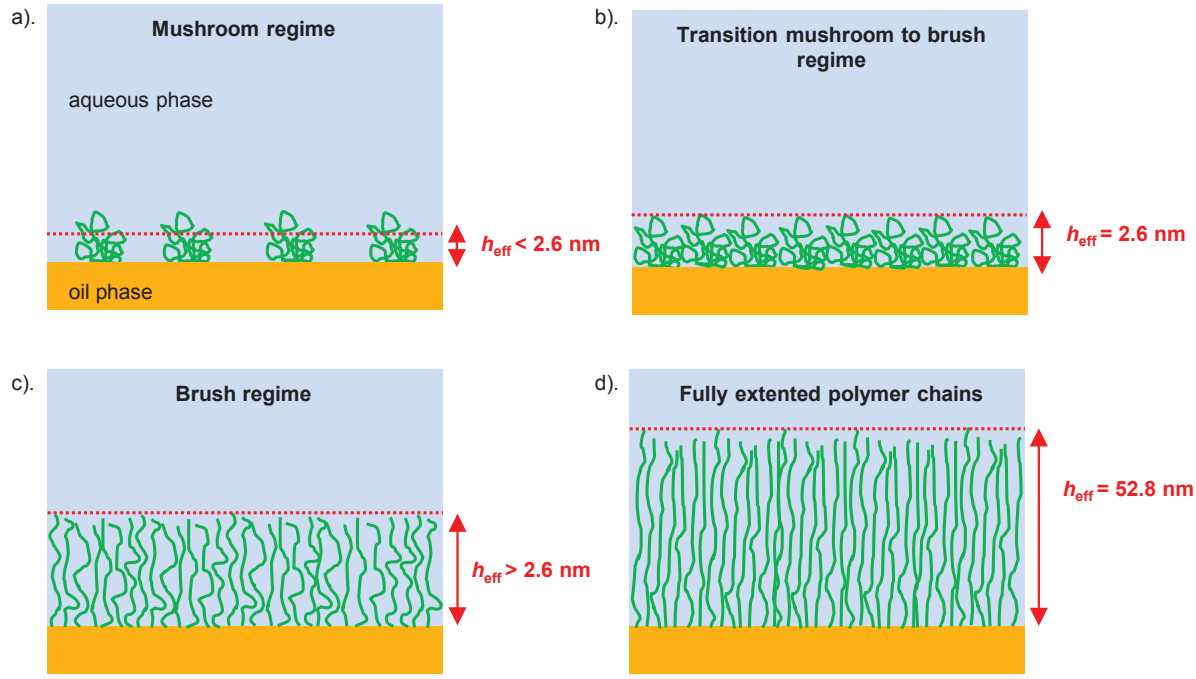

Figure 7.27: Schematic representation of copolymer chains at the oil/aqueous phase interface for the different conformations of the chains.

In conclusion, the influence of the addition of amphiphilic copolymer on the entering of oil droplets at the air/aqueous phase interface is due to steric repulsion forces that stabilize the liquid film. The perforation of the sheet is governed by the range of the electrostatic and steric repulsion forces. We only qualitatively interpret our experimental results concerning the relative influence of the salt and amphiphilic copolymer concentration due to the fact that we were not able to quantitatively determine the range of the

steric repulsion.

7.4.4 Conclusion

We have seen that the addition of salt on emulsions stabilized by ionic surfactants (negatively (SDS) or positively (CpCl) charged) promotes the entering of oil droplets at the air/aqueous phase interface and so promotes the perforation process. Without salt in the emulsion aqueous phase, electrostatic repulsion forces between the charged headgroups of surfactants at the air/aqueous phase and at the oil/aqueous phases interfaces stabilize the aqueous film formed between the interface and the approaching oil droplet and thus prevent the entering of oil droplets at the interface. The addition of salt screens the electrostatic repulsive forces and so promotes the entering of oil droplets at the interface and thus the perforation process. The addition of amphiphilic copolymer also stabilizes the aqueous film by the means of steric repulsion forces due to the presence of copolymer chains at the oil/aqueous phase interface. These steric repulsive forces prevent the entering of oil droplets at the interface and so inhibit the perforation process. Finally, a decrease of the surfactant concentration of the emulsion aqueous phase thermodynamically favors the entering of oil droplets at the air/aqueous phase interface and thus promote the perforation of liquid sheets.

7.5 Conclusion

Thanks to the single-tear experimental set-up we have investigated the influence of emulsions stabilized by ionic surfactants on the destabilization mechanism of liquid sheets. We have seen that liquid sheets made of emulsions only stabilized by ionic surfactants (SDS or CpCl) are destabilized through the same mechanism as water liquid sheets, without perforation of the liquid film. We have shown that the compositions of the emulsions aqueous phase strongly modifies the destabilization mechanism of liquid sheets. The addition of salt or amphiphilic copolymers can trigger or completely inhibit the perforation mechanism. Hence, the emulsions stabilized by ionic surfactants are a really interesting system for our study as we can switch on / switch off the perforation process by tuning simple parameters such as the salt or amphiphilic copolymer concentrations.

We have rationalized the influence of the composition of the emulsion aqueous phase on the perforation mechanism. We have shown that the aqueous phase composition does not modify the spreading of oil droplet at the air/aqueous phase interface whereas the entering of oil droplets at the interface is strongly altered. The entering of oil droplets at the air/water interface is always thermodynamically favored for the different systems investigated ($E > 0$). The different entering behaviors arise from thin-film forces that stabilize the thin aqueous film formed between the air/aqueous phase interface and the approaching oil droplets and thus creates a energy barrier that has to be overcome. Electrostatic

and/or steric repulsions between the oil droplet and the air/aqueous phase interface hinder the entering of oil droplets at the air/aqueous phase interface, and thus inhibit the perforation process. Hence, this study highlights that the principal limiting step of the perforation mechanism is the entering of oil droplets at the air/aqueous interface.

Finally, thanks to the conventional spray experiments and in full consistency with the single-tear experiments, we have shown that emulsions stabilized by sodium dodecyl sulfate and sodium chloride are an interesting new formulation for anti-drift adjuvants as they reduce to a large extent the proportion of driftable drops in the spray. The anti-drift properties of the emulsions stabilized by sodium dodecyl sulfate and sodium chloride are comparable to the ones of the model emulsions (Chapter 5).

Chapter 8

Mechanism of perforation: a critical summary

Contents

The objective of this short chapter is to summarize the influence of the physico-chemical parameters of emulsions on the perforation mechanism that we have proposed. In the previous chapter, we have shown the influence of salts and amphiphilic copolymer for emulsions stabilized by water-soluble ionic surfactants. In Chapter 5, we have studied the influence of oil concentration and oil droplet size distribution for dilute model emulsions (emulsion stabilized by oil-soluble non-ionic surfactants). The objective is now to rationalize the influences of these parameters in the light of the proposed perforation mechanism. In a first section, we rapidly remind the proposed perforation mechanism. Then, we summarize the influence of the emulsion composition on the perforation mechanism. In a third section, we rationalize the influences of the emulsion oil droplets concentration and size on the perforation mechanism. Finally, we critically compare the perforation mechanism proposed to the ones suggested in the literature.

8.1 Proposed mechanism

The proposed mechanism to explain the nucleation of holes in liquid sheets of emulsions is based on the entering and spreading of emulsion oil droplets at the air/aqueous phase interface. First, the emulsion oil droplets enter the air/aqueous phase interface, then the droplets spread at the interface leading to a local thinning of the liquid film due to a Marangoni stress. This thinning leads to the rupture of the film and so the nucleation of a hole (see Figure 8.1 for a schematic representation of the perforation mechanism). Hence, in this mechanism the oil droplets should first enter the solution

surface. As described in details in the previous chapter, a positive value of the entering coefficient, E, indicates that it is thermodynamically favorable for an oil droplet to enter the air/aqueous phase interface. Similarly, the spreading of an oil droplet at the air/aqueous phase interface is thermodynamically described by the spreading coefficient, S. A positive value of S indicates that it is thermodynamically favorable for an oil droplet to spread over the interface. Hence, the proposed perforation mechanism implies positive values of the entering and spreading coefficients ($E > 0$ and $S > 0$).

As highlighted in the previous chapter, a positive value of E does not guarantee the entering of oil droplets at the air/water interface due to entry barrier originating from thin-film forces that stabilize the thin aqueous film formed between the air/aqueous phase interface and the approaching oil droplet. Colloidal forces, such as electrostatic and steric forces, repel the oil droplets from the interface. The nature of these forces depends on the type of molecules adsorbed at the air/aqueous phase and oil/aqueous phase interfaces.

We have observed a strong analogy with the oil-based antifoams. Indeed, the mechanism that we have proposed was originally developed to explain the antifoam action of dilute oil-in-water emulsions. The two configurations are highly comparable: both imply the rupture of a liquid film due to the presence of oil droplets dispersed in an aqueous phase. One difference between the two configurations is the range of the film thickness around 10 μm for foam films and around 100 μm for liquid sheets.

8.2 Influence of the emulsion composition

The perforation mechanism depends strongly on the emulsion composition and more exactly on the nature of the molecules adsorbed at the different interfaces.

In the case of emulsions stabilized by ionic surfactants soluble in the aqueous phase (Chapter 7), charged surfactants are present at the air/aqueous phase and aqueous phase/oil interfaces, see scheme Figure 8.2(a) for emulsion stabilized by anionic surfactants. For the investigated emulsions, the entering and spreading coefficients are largerly positive (see Chapter 7), indicating that it is thermodynamically favorable for an oil droplet to enter and spread at the air/aqueous phase interface. We have measured that the spreading dynamics is the same for the different compositions of the aqueous phase indicating that the limiting step of the mechanism is the entering of oil droplets at the air/aqueous phase interface. The electrostatic repulsive forces generated by the charged surfactant molecules present at the air/aqueous phase and oil/aqueous phase interfaces prevent the oil droplets from entering at the air/aqueous phase interface and so inhibit the perforation process. The addition of salt reduces the electrostatic repulsion between the oil droplets and the air/aqueous phase interface, allowing the oil droplets to approach closer to the interface and so promote the entering of oil droplets and the perforation process. The addition of long polymer chains of amphiphilic copolymer that adsorb preferentially at the oil/aqueous phase interface (see scheme Figure 8.2(b)) also prevents the oil droplets from approaching the air/aqueous phase interface due to steric repulsive

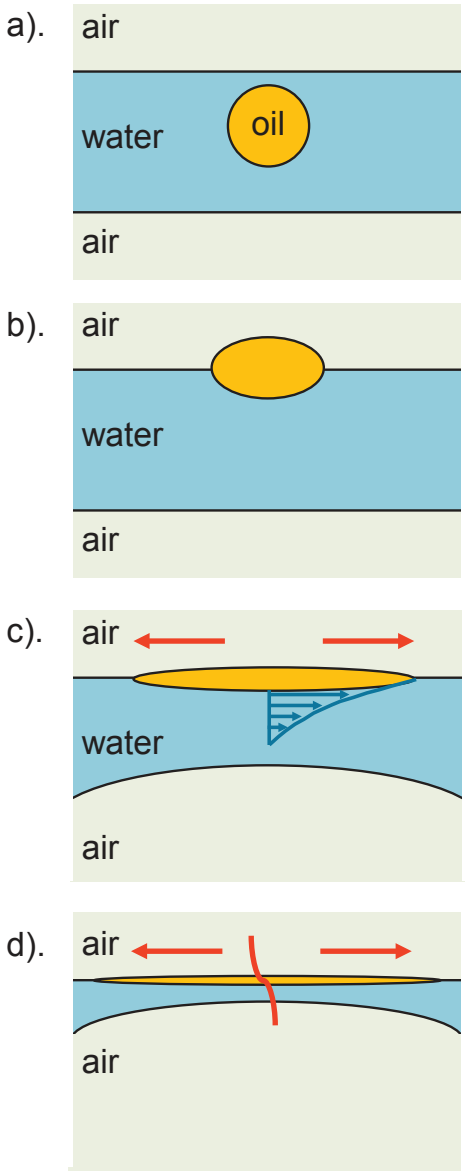

Figure 8.1: Schematic presentation of the proposed mechanism to explain the nucleation of hole within the liquid sheet. An oil droplet enters the liquid film surface (a,b). The oil droplet spreads at the air/water interface (c) causing a Marangoni-driven flow of water, which leads to the localized thinning of the liquid film and its eventual rupture (d).

forces and so inhibits the perforation process.

In the case of the model emulsions studied in details in Chapter 5 and 6, the oil droplets are stabilized by non-ionic surfactants soluble in the oil phase of the emulsion. Hence, the surfactant are principally present at the oil/aqueous phase interface and possibly in the interior of the oil droplets but not at the air/aqueous phase interface due to their low solubility in water, see Figure 8.2(c). For the model emulsion, the entering and spreading

coefficients are largerly positive: $E = 43.8$ mN/m and $S = 41.6$ mN/m, indicating that it is thermodynamically favorable for an oil droplet to enter and spread at the air/aqueous phase interface. On contrary to emulsions stabilized by water-soluble ionic surfactants, no thin-film force barrier prevents the entering of oil droplet at the interface. Hence model emulsion-based liquid sheets are highly perforated (see Chapter 4, Figure 4.30).

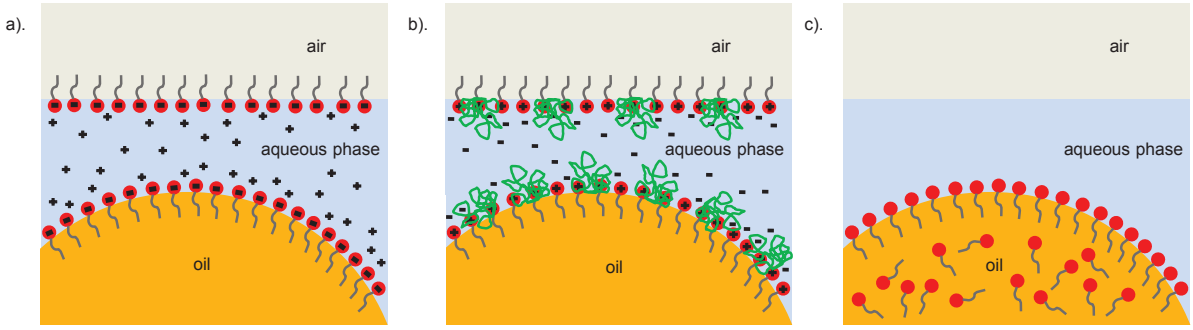

Figure 8.2: Sketch of an oil droplet stabilized by surfactants approaching the air/water interface a). oil droplet stabilized by water-soluble anionic surfactants present at the air/water and oil/water interfaces, b). oil droplet stabilized by water-soluble cationic surfactants and amphiphilic copolymer present at the air/water and oil/water interfaces, c). oil droplet stabilized by oil-soluble non-ionic surfactants present at the oil/water interfaces.

In Chapter 6, we have modified the viscosity of the model emulsion aqueous phase to investigate its influence on the spreading dynamics. We have shown that an increase of the aqueous phase viscosity entails a slowing down of the spreading dynamics but it does not notably affect the perforation process. Indeed, for the three viscosities investigated a large perforation of the liquid sheets was observed (see in Figure 8.3 images of the highly perforated liquid sheets obtained for the three viscosities). Hence, a slower spreading dynamics does not inhibit the perforation process.

8.3 Influence of oil droplets concentration and size

In Chapter 5, we have investigated the influence of the model emulsion concentration on the perforation process. We have shown that an increase of the emulsion concentration entails a continuous increase of the number of perforation events up to a saturation. At the light of the proposed perforation mechanism, this effect seems clear. Each perforation event results from the entering and spreading of an oil droplet at the air/aqueous phase interface. An increase of the emulsion concentration entails an increase of the number of oil droplets in solution and so an increase of the number of perforation events (as observed experimentally, see Figure 8.4) as there are more oil droplets in solution likely to enter and spread at the interface. At low emulsion concentration ($C \leq 0.006$ % v/v)

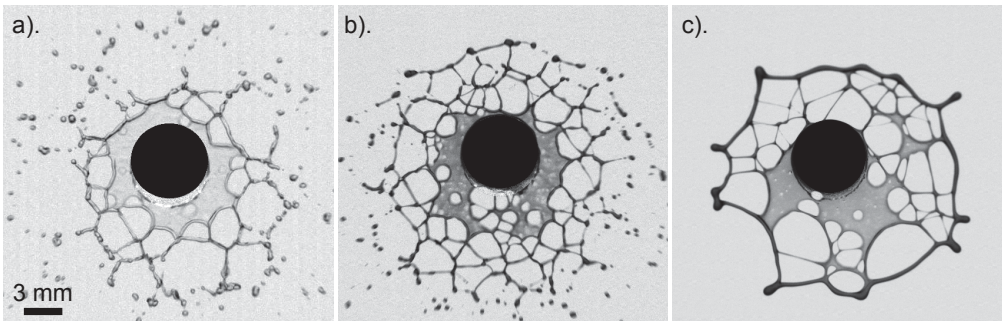

Figure 8.3: Images of liquid sheets made of model emulsions with different zero shear viscosities of the aqueous phase a). $\eta = 1$ mPa.s (image taken 4.1 ms after the tear impact), b). $\eta = 12.5$ mPa.s (image taken 3.1 ms after the tear impact) and c). $\eta = 3.65$ mPa.s (image taken 5.1 ms after the tear impact).

for $d_{\text{oil}} = 40$ μm, about 40 % of the oil droplets enter and spread at the interface leading to the nucleation of a hole, hence the process is quite efficient. At higher emulsion concentration, the efficiency of the process decreases significantly and at $C \geq 0.3$ % v/v we observe a saturation of the perforation process with no evolution of the total number of perforation events with the number of oil droplets in solution as C increases up to 2.4 % v/v. We suggest that, at these high concentrations, the liquid sheets are already highly perforated and that there is no more free-hole liquid surface available for the entering and spreading of oil droplets to entail new nucleation events even if the number of oil droplets in solution increases.

In Chapter 5, we have also investigated the influence of the model emulsion droplet size distribution on the perforation process of liquid sheets. We have shown that, for equal number of oil droplets in solution, bigger droplets are more efficient to onset the perforation, see Figure 8.5. A similar effect of the oil droplet diameter has been reported for oil-based antifoams in several studies [Bergeron 1997, Basheva 2000, Basheva 2001]. Basheva et al. measure that the entry barrier of antifoam oil droplets at the foam surface decreases with the oil droplet radius, hence it is easier for bigger oil droplets to enter the air/aqueous phase interface. Bergeron et al. highlight a strong correlation between antifoam performance and oil droplet size with bigger droplets more efficient as antifoam. The authors argue that droplet size affects the entering kinetics. Smaller oil droplets need to approach the interface much more closely (considering the center of mass of the droplets) before they can rupture the thin aqueous film and enter the interface. This phenomenon is highlighted in the Appendix B, where we estimate the time necessary for an oil droplet to reach the air/aqueous phase interface depending on its initial position in the liquid film and on its diameter. We show a clear dependence of the time to reach the interface with the oil droplet diameter. Averaged over the different initial positions within the liquid film, an oil droplet of diameter 0.5 μm would reach the interface in 24 ms whereas an oil droplet of diameter 20 μm would reach the interface in 3 ms. Hence,

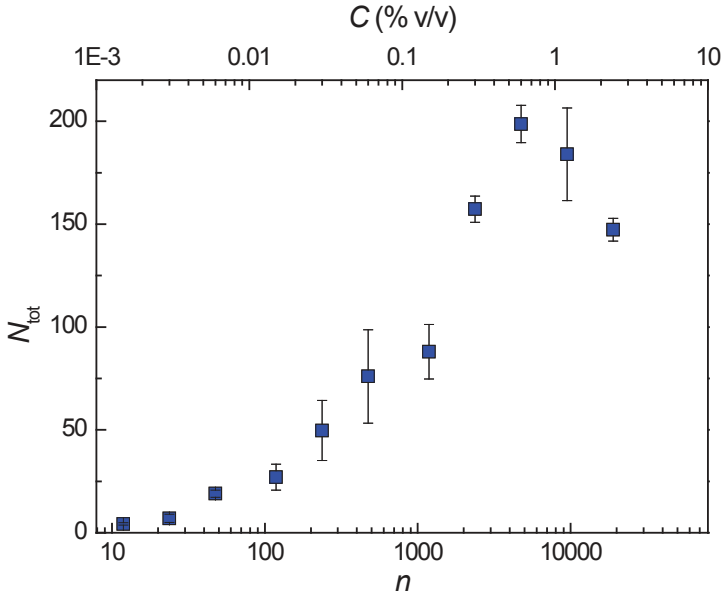

Figure 8.4: Evolution of the total number of perforation events, N_{tot}, as a function of the model emulsion concentration, C, (top x axis) and of the number of oil droplets per impacting tear, n, (bottom x axis).

a decrease of the oil droplet radius entails a decrease of the frequency of drop entering at the air/aqueous phase interface and so limits the perforation process, as observed experimentally in Figure 8.5.

8.4 Comparison with the perforation mechanisms proposed in the literature

We finally compare the proposed perforation mechanism to the ones established in the literature.

First, in 1954 Dombrowski et al. [Dombrowski 1954] suggested a "bridging-dewetting" mechanism to explain the perforation of liquid sheets by oil droplets. This mechanism has been then described more in details for antifoam application [Denkov 2004], see Figure 8.6. As explained in section 1.4.1, the "bridging-dewetting" mechanism implies that oil droplets enter both interfaces of the liquid film and that the droplets are dewetted by the aqueous film to lead to the film rupture. Hence, the mechanisms implies that the hole nucleation occured when the liquid film is of thickness comparable to the oil droplet diameter. In this manuscript, we have shown several experimental proofs that are in contradiction with this mechanism. First, in section 6.6.1, we have shown that there is no correlation between the thickness of the liquid film at the perforation and the

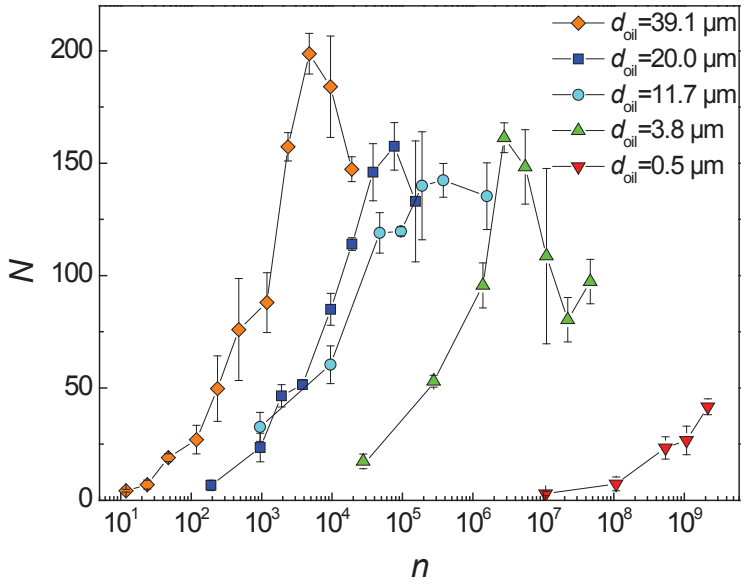

Figure 8.5: Evolution of the total number of perforation vents, N_{tot}, as a function of the number of oil droplets per impacting tear, n, for model emulsions with different oil droplet size distributions as indicated in the legend.

diameter of the oil droplets. Second, in section 6.1.2, we have shown that the nucleation of a hole in a liquid sheet is systematically precedes by a local thinning of the liquid film, which is not predicted by the "bridging-dewetting" mechanism. Theses two experimental studies rule out the "bridging-dewetting" mechanism to explain the nucleation of holes in emulsion-based liquid sheets.

Hilz et al. [Hilz 2013a] suggested a mechanism similar to the one we proposed to explain the nucleation of holes within emulsion-based liquid sheets. They argued that the perforation of liquid sheets are due to the entering and spreading of emulsion oil droplets at the air/aqueous phase interface. However, as described earlier (section 1.4.4), their findings were only based on measurements of spray drop size distributions and they did not observe directly the perforation mechanism. The authors also argued that the addition of water-soluble surfactants in the emulsion aqueous phase entails a decrease of the spreading coefficient, S, and so slows down the spreading process and prevents the perforation. This explanation is in desagreement with our experimental findings. We have shown, by direct observation of the pre-hole widening, that the water-soluble surfactant concentration does not modify the spreading dynamics of oil droplets at the air/aqueous phase interface (see section 7.2.3.1, Figure 7.12) and that the increase of the surfactant concentration in the emulsion aqueous phase thermodynamically prevents the entering of oil droplets at the air/aqueous phase interface. Hence, we argue that the effect of the water-soluble surfactant concentration in emulsion aqueous phase arises from the first step of the perforation mechanism, i.e. the entering of oil droplets at the air/aqueous phase interface. This is in sharp contrast to Hilz et al. who claims that it

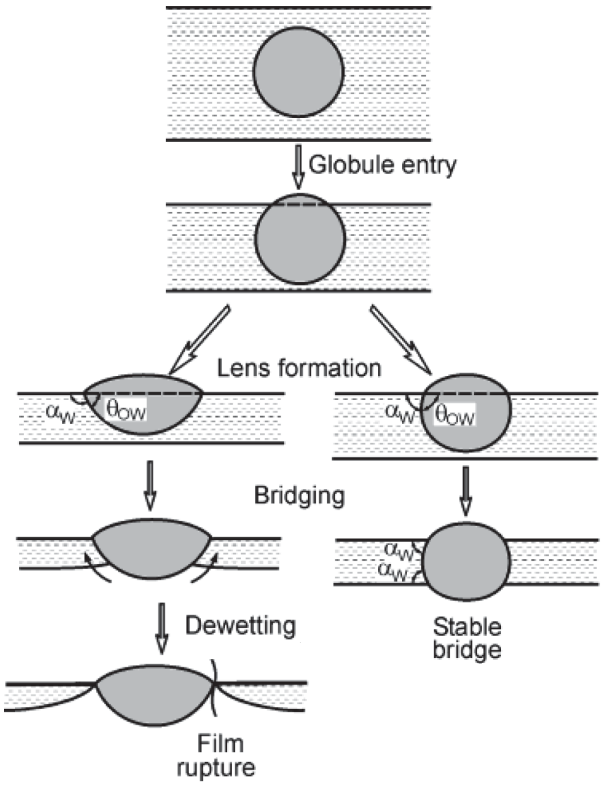

Figure 8.6: Schematic representation of the "bridging" mechanism. An oil droplet enters both interfaces of the liquid film when its diameter is equal to the thickness of the liquid film. If the particle is hydrophobic (left part), the formation of an oil bridge between the two film surfaces leads to a dewetting of the hydrophobic oil droplet and so the rupture of the liquid film. If the particle is hydrophilic (right part), a stable oil bridge is formed [Denkov 2004].

modifies the last step of the perforation mechanism, i.e. the spreading of oil droplets at the air/aqueous phase interface. What is more, for the model emulsions, we have shown that a slowing down of the spreading of the oil droplets over the interface (due to an increase of the emulsion aqueous phase viscosity) does not have a strong influence on the perforation process.

8.5 Conclusion

In conclusion, we argue that the nucleation of holes in emulsion-based liquid sheet is due to the entering and spreading of emulsion oil droplets at the air/aqueous phase interface. The two steps of the perforation mechanism are thermodynamcally favorable as the entering and spreading coefficients are both positives for all the investigated systems. We have shown that the entering of emulsion oil droplets at the air/aqueous phase interface

is the limiting step of the perforation mechanism. A high entering energy barrier can prevent the droplet entry process. Thin-film forces, in particular electrostatic and steric repulsive forces, stabilize the thin aqueous film formed between the air/aqueous phase interface and the approaching oil droplet, thus preventing the entering of droplets. In this case, even if the entering is thermodynamically favorable, the entering process is strongly limited and even suppressed by the enhanced stability of the thin film. We have shown that a slowing down of the spreading dynamics of oil droplets over the air/aqueous phase interface does not inhibit the perforation mechanism. However, even if the spreading of oil droplets at the interface is not the limiting step of the perforation, it is nevertheless crucial as several studies have emphasized that solid particles that enter the air/aqueous phase interface but do not spread at the interface do not entail the perforation of liquid sheets [Dexter 2001, Qin 2010].

General conclusions and perspectives

During my PhD project, I have studied the destabilization mechanisms of liquid sheets of dilute emulsions in order to characterize the influences of oil droplets on spray drop size distribution and so elucidate the origin of their anti-drift properties. Dilute oil-in-water emulsions have been used since the last decade as a new class of anti-drift adjuvants. In the whole thesis, I have compared the behavior of dilute oil-in-water emulsions to two reference systems: pure water and dilute solution of high-molecular-weight polymer, which constitutes the second category of anti-drift adjuvants. Flat fan nozzles used to spray pesticide solutions on cultivated crops produce a free sheet of fluid, which is subsequently destabilized into drops. By contrast with most of the studies aiming to understand the role of emulsions as anti-drift adjuvants, we have decided not to use a spray set-up to produce liquid sheets and to study their destabilization mechanisms. Our original strategy relies on the utilization of model experiments to investigate the destabilization mechanisms of liquid sheets comparable to the ones formed at the exit of agricultural hydraulic nozzles.

During the first part of my work, I have focused on the last step of the atomization process, which is the destabilization of liquid ligaments into drops. With two model experiments based on the detachment of a pendant drop from a reservoir and the destabilization of stretched ligaments fed by a reservoir, we have mimicked the destabilization taking place during the spray formation. We have checked that dilute solutions of high-molecular-weight polymer drastically modify the destabilization of liquid ligaments with the apparition of a characteristic "beads-on-string" structure. This specific destabilization mechanism, extensively studied in the literature, is at the origin of their anti-drift properties. The novelty of this study was to show that dilute emulsions do not modify the destabilization mechanism of liquid ligaments compared to pure water. Hence, we can affirm that the anti-drift properties of dilute-oil-in-water emulsions do not arise from the destabilization of liquid ligaments into drops. As dilute oil-in-water emulsions do not alter the last step of the atomization process, we have then focused on the first step of the process, i.e. the destabilization of liquid sheets. Once again, we have decided to use a model experiment to produce and study the destabilization of controlled liquid sheets. The model experiment is based on the impact of a single tear of liquid on a small target, which produces a free liquid sheet expanding in the air comparable to the ones produced by agricultural hydraulic nozzles. An important part of my work has been dedicated to the development of an original method to measure the thickness field of this class of liquid sheets. This method was then applied to the measurement of the thickness field of a pure water sheet, the results are reported in the publication *Free radially expanding liquid sheet in air: time- and space-resolved measurement of the thickness field*, C. Vernay, L. Ramos and C. Ligoure, Journal of Fluid Mechanics, 764(428-444), January 2015 [Vernay 2015c].

Thanks to the single-tear model experiment, we have shown that liquid sheets made of dilute oil-in-water emulsions are destabilized by a perforation mechanism, with the nucleation of holes in the liquid film. By comparing the perforation process of emulsion-based liquid sheets and the drop size distribution of spray of dilute emulsions produced with agricultural hydraulic nozzles, we have shown that the anti-drift properties of dilute emulsions arise from the perforation mechanism of liquid sheets. We have highlighted a strong dependence of the perforation process and so of the anti-drift properties with the physical-chemical parameters of the dilute emulsions such as the emulsion concentration and the emulsion droplet size distribution. We have shown that an increase of the emulsion concentration entails an increase of the number of perforation up to a saturation and that bigger oil droplets are more efficient to onset the perforation. These results are reported in the publication *Drop impact experiment as a model experiment to investigate the role of oil-in-water emulsions in controlling the drop size distribution of an agricultural spray*, C. Vernay, L. Ramos, J. P. Douzals, R. Goyal, J. C. Castaing, and C. Ligoure that has been accepted for publication in Atomization and Sprays [Vernay 2015a].

With the method developed to measure the thickness field of the sheets, we have shown that the nucleation of holes in dilute emulsion-based liquid sheets is systematically preceded by a local thinning (pre-hole). The study of the pre-hole dynamics enables us to elucidate the mechanism at the origin of the hole nucleation in emulsion-based liquid sheets: the entering and spreading of oil droplets at the air/aqueous phase interface lead to a localized thinning of the liquid film due to a Marangoni stress and finally to the film rupture. This study has been reported in the article *Bursting of Dilute Emulsion-Based Liquid Sheets Driven by a Marangoni Effect*, C. Vernay, L. Ramos and C. Ligoure, Physical Review Letters, 115(198302), November 2015 [Vernay 2015b].

Finally, by modifying the physical chemical parameters of the emulsions, we have shown that the formulation of the emulsion is a critical parameter to control the perforation. The addition of salt or amphiphilic copolymer in the aqueous phase of emulsions stabilized by water-soluble ionic surfactants can kinetically trigger or completely inhibit the perforation mechanism. We have shown that the entering of oil droplets at the air/aqueous phase interface is the limiting step of the mechanism. Thin-film forces such as electrostatic or steric repulsion forces stabilize the thin film formed between the interface and the approaching oil droplets delaying the entering of oil droplets at the interface and so inhibit the perforation process.

The originality of my PhD project was to compare the results obtained with the model experiments to the results of conventional spray experiments used to evaluate the influence of emulsion formulation on the spray drop size distribution. These measurement have highlighted the anti-drift properties of the model dilute oil-in-water emulsions. By modifying the composition of the emulsions, we have established a new formulation with high anti-drift properties, based on emulsions stabilized by sodium dodecyl sulfate and

sodium chloride. This new formulation of anti-drift emulsion adjuvant has been the subject of a patent application in 2015.

In conclusion, my PhD project has permitted to establish the mechanism at the origin of the anti-drift properties of dilute oil-in-water emulsions thanks to the study of the destabilization mechanisms of liquid sheets. Up to know, the development of new formulations of emulsion anti-drift adjuvant was based on a "trial and error" method. Now that the mode of action and so the requirements for the emulsion compositions are better understood, we can imagine to develop new and more efficient formulations for anti-drift emulsion adjuvants.

Another perspective for the development of new additives is to combine the two class of anti-drift adjuvants, dilute oil-in-water emulsion and dilute solution of high-molecular-weight polymer, to create a synergy between the two specific modes of action. We have performed some experiments to test this hypothesis. In Figure 8.7 is presented the formation and destabilization of a liquid sheet of a mixture of dilute solution of polymer of high-molecular weight (PEO) and dilute oil-in-water emulsion (model emulsion). The mixture is such as the final emulsion concentration is equal to 0.3 % v/v and the final polymer concentration is equal to 0.015 % v/v. Upon impact the liquid sheet spreads out radially surrounded by a thicker rim (Figure 8.7(a)). As for an emulsion-based liquid sheet, we rapidly observe the nucleation of holes within the sheet (Figure 8.7(b)). The holes grow until they coalesce and form a web of ligaments (Figure 8.7(d)). The ligaments are then destabilized following the specific mechanism of ligaments of dilute solution of high-molecular-weight polymer, with the formation of a "beads-on-string" structure as observed for the destabilization of a PEO solution-based liquid sheet. In conclusion, the first step of the atomization of a liquid sheet made of a mixture of dilute emulsion and high-molecular-weight polymer solution is dominated by the perforation mechanism with the nucleation of holes within the liquid film. Once the liquid sheet is destabilized into a web of ligaments, the specific destabilization of high-molecular-weight polymer solution becomes predominant. Hence, the destabilization liquid sheets of a mixture of the two class of anti-drift adjuvants, dilute oil-in-water emulsion and dilute solution of high-molecular-weight polymer, highlights a clear synergetic effects of the mode of action of the two adjuvants. The two steps of the sheet destabilization process is successively affected by the addition of high-molecular-weight polymer and dilute oil-in-water emulsion in water. First the destabilization of the sheet in ligaments is modified with the nucleation of holes due to the presence of emulsion droplets, then the destabilization of the ligaments into drops is modified due to the long polymeric chains in solution. Such formulations should deserve further investigations.

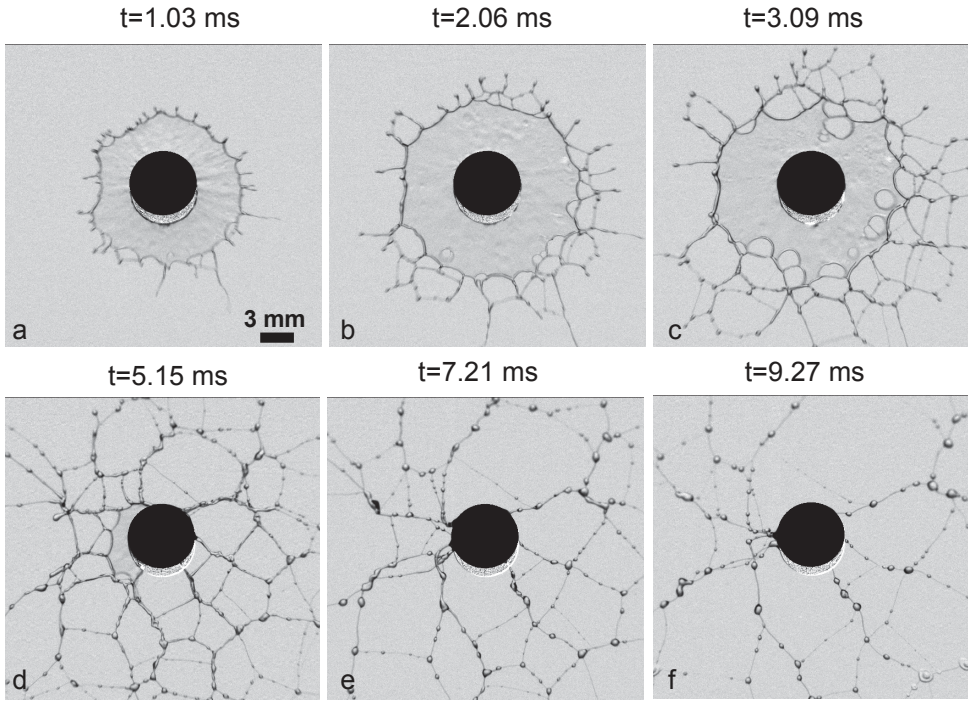

Figure 8.7: Sequence of events of the formation and destabilization of a liquid sheet of a mixture of dilute PEO solution (1,000,000 g/mol at 0.05 % w/w) and dilute model emulsion (C=0.3 % v/v). The drop diameter is d_0 = 3.7 mm, the impact velocity is u_0 = 4.0 m/s, and the target diameter is 6 mm. The origin of time is taken at the moment of the drop impact.

Appendix A

Dynamic surface tension and equilibrium interfacial tension

The equilibrium surface tension of the liquids investigated is an interesting properties. However, as the formation of a spray is a really fast process, typically few milliseconds, we are also interested in the dynamic surface tension of our systems. What is more, as we studied dispersions of oil droplets into an aqueous phase, the interfacial tension between these two phases is a crucial parameter. In this appendix, we present the methods used to measure the dynamic surface tension of liquid with air and the equilibrium interfacial tension between the aqueous and oil phases of the emulsions.

A.1 Dynamic surface tension

The dynamic surface tension measurements are performed with a maximum bubble pressure tensiometer from KRUSS in the laboratory IRSTEA in Montpellier. In this method, air bubbles are blown away by a capillary immersed in the investigated solution. The internal pressure of the bubble is measured. The pressure of a spherical bubble is directly related to the radius of curvature of the bubble and the surface tension of the solution, according to the Young-Laplace equation. When a bubble is produced in a liquid at the extremity of a capillary, the bubble pressure is maximum when the curvature radius of the bubble is equal the capillary radius. Knowing the capillary radius, the surface tension can be calculated from the maximum internal pressure of the bubble. This surface tension value corresponds to a precise surface age equal to the time elapsed from the beginning of the bubble formation to the occurrence of the maximum pressure. The dynamic surface tension can be measured by varying the bubbling frequencies i.e. varying the age of the bubble surface. The KRUSS maximum bubble pressure tensiometer can measure surface tension on the range $(10 - 100)$ mN/m with a resolution of 0.01 mN/m. The accessible surface age range is 5 to 200,000 ms. This dynamic surface tension method is used to measure the surface tension of emulsions at short time scale corresponding to the time scale of the spray formation.

A.2 Equilibrium interfacial tension

In this section we present the method used to measure the interfacial tension between the aqueous and oil phases of the emulsion. These measurements are challenging as, for most of the emulsions investigated, the interfacial tensions are really low.

Different techniques have been developed to measure the surface tension between two liquids. Most of these techniques rely on the analysis of a drop under the influence of a force field. Some use the balance between interfacial force and gravitational force, such as the pendant drop, the Wilhelmy plate, the Du Nouy ring and the sessile drop techniques. Those techniques are not adapted to measure low interfacial tensions (< 1 mN/m), particularly those relying on gravitational forces. In other techniques the drop shape is distorted by centrifugal force such as the spinning drop technique. For low interfacial tension systems, the spinning drop is the most appropriate technique. The principle of spinning drop tensiometer is to use a capillary containing two phases. The capillary is filled with the denser fluid (aqueous phase in our case) and a drop of the less dense fluid (oil phase) is added, then the capillary rotates with a sufficiently high rate along the horizontal axis, see Figure A.1. Under the centrifugal force, the less dense fluid will migrate to the rotation axis and find an equilibrium position i.e. a cylindrical shape with hemispherical ends. The shape at equilibrium can be explained by the balance of the centrifugal force, which act to elongate the less dense phase, and the surface tension force, which tends to reduce the interfacial area and maintain a spherical shape. The interfacial tension is deduced from the characteristic shape of the drop depending on the density difference between the two phases and the capillary rotation speed.

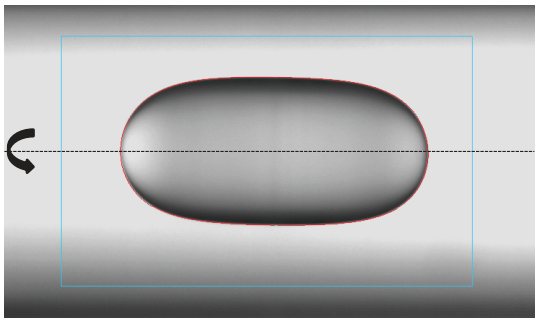

Figure A.1: Image of spinning drop tensiometer measurement: a drop of the oil phase in a capillary filled with the aqueous phase of the emulsion is rotated along the horizontal axis.

We perform the interfacial tension measurement with a DataPhysics Spinning Drop Video Tensiometer 20N in the laboratory SIMM (ESPCI). The two phases of the emulsion are pre-equilibrated for 24h prior the measurement to ensure that both phases are mutually saturated. The capillary is filled with the pre-equilibrated aqueous phase, this operation is really delicate as the capillary must be filled absolutely bubble-free. Then,

the capillary is inserted into the measuring cell and rotated at 300 rpm. A drop of the oil phase is injected into the filled capillary with a syringe and a long needle. The rotation rate is then increased up to 3,000 rpm and the oil drop is stabilized at the middle of the capillary by modifying the tilt. The interfacial tension is then automatically calculated from the fit of the drop shape. A slowly decreasing of interfacial tension values with time is observed due to the rearrangement of surface active components. Therefore, the sample is maintained under rotation (about twenty minutes) until the interfacial tension values remain constant and we consider the interfacial tension as the average value calculated over this steady period.

Appendix B

Time scale for an oil droplet to reach the air/water interface

This Appendix is dedicated to the description of a simple model to estimate the time needed for an oil droplet to reach the air/water interface. Note that we estimate the time to reach the interface and not to enter the interface. Hence, this simple model does not take into account any entry barrier. An oil droplet will reach the air/water interface due to the creaming process in the liquid film and the thinning of the liquid sheet with time. In this Appendix, we evaluate the creaming and thinning velocities to estimate the time needed for an oil droplet to reach the air/water interface depending on its radius and initial position in the liquid film.

B.1 Definitions of the parameters and the initial conditions

We consider a liquid sheet formed by the impact of a tear on a small target. The origin of time t is taken at the moment of impact of the tear. The radial distance, r, is measured from the center of the target. The z-axis is defined perpendicular to the liquid film, i.e. a vertical axis. The altitude z=0 corresponds to the middle of the liquid sheet. The thickness field of the liquid sheet is designed by $h(r,t)$. We consider an oil droplet in the liquid film. The position of the oil droplet is described by the coordinates of its center on the r- and z- axes: the radial distance from the center of the target, $r_{\mathrm{p}}(t)$, and the distance along the z-axis, $z_{\mathrm{p}}(t)$ (see Figure B.1 for the definitions of the different parameters).

The initial conditions are defined in $t = \tau_{\mathrm{coll}} = \frac{d_0}{u_0}$, with d_0 the diameter of the impacting tear and u_0 the impacting velocity. r_{p_0} and z_{p_0} are respectively the radial and vertical positions of the oil droplet in the liquid film at $t = \tau_{\mathrm{coll}}$.

B.2 Motion of oil droplets in the liquid film

Oil droplets are moving in the liquid sheet along the z-axis due to the balance between buoyancy and gravity. We define $\boldsymbol{v}_{\mathbf{creaming}}$, the creaming velocity of the oil droplet. The

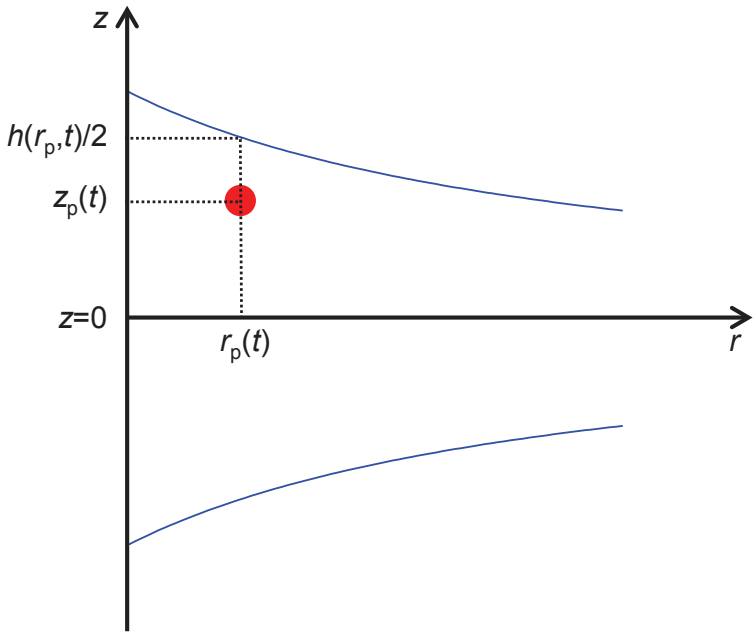

Figure B.1: Schematic representation of an oil droplet in the liquid sheet with the definition of the different parameters.

oil droplets are moving in the liquid sheet with a velocity $\boldsymbol{u(r, z, t)}$. In Chapter 6, we have seen that the radial component of the velocity of the oil droplets is equal to:

$$u_{\mathrm{r}}(r,t) = \frac{r}{t} \tag{B.1}$$

Considering the fluid as incompressible, $\mathrm{div}\,\vec{u} = 0$, we obtain the z-component of the velocity field:

$$u_{\mathrm{z}}(z,t) = \frac{-2z}{t} \tag{B.2}$$

Hence,

$$\frac{\mathrm{dr}}{\mathrm{dt}} = \frac{r}{t} \tag{B.3}$$

$$\frac{\mathrm{dz}}{\mathrm{dt}} = \frac{-2z}{t} \tag{B.4}$$

From Equation B.3, B.4, the initial conditions $(r_{\mathrm{p0}}, z_{\mathrm{p0}})$ defined in $t = \tau_{\mathrm{coll}}$ and considering the creaming velocity of the oil droplets, we determine the coordinates of the oil droplet in the liquid film at time t :

$$r_{\mathrm{p}}(t) = \frac{r_{\mathrm{p0}}\, t}{\tau_{\mathrm{coll}}} \tag{B.5}$$

$$z_{\mathrm{p}}(t) = \frac{z_{\mathrm{p0}}\, {\tau_{\mathrm{coll}}}^2}{t^2} + v_{\mathrm{creaming}}(t - \tau_{\mathrm{coll}}) \tag{B.6}$$

We have defined the coordinates of the oil droplet at time t after the moment of the tear impact. An important feature to keep in mind is the thinning of the sheet with time. In order to evaluate the time for the oil droplet to reach the air/water interface, we have to take into account the creaming velocity of the oil droplet but also the thinning velocity of the sheet that causes the interface to come closer to the oil droplet.

B.3 Estimation of the creaming and thinning velocities

In this section, we estimate the creaming and the sheet thinning velocities separately in order to eventually compare it. The creaming velocity is defined as

$$v_{\text{creaming}} = \frac{2}{9}\frac{\Delta\rho g {r_{\text{oil}}}^2}{\eta} \tag{B.7}$$

with $\Delta\rho$ the density difference between the aqueous and oil phases of the emulsion, η the viscosity of the aqueous phase and r_{oil} the oil droplet radius. For the model emulsion with pure water as aqueous phase, $\Delta\rho$=128.2 kg/m^3 and $\eta = 1.0$ mPa.s. For an oil droplet of radius 10 μm, the creaming velocity is about 0.03 μm/ms.

To evaluate the thinning velocity of the liquid sheet, we use our experimental measurements of the thickness field of a pure water liquid sheet (section 4.3.3 Figure 4.21). From these data, it is obvious that the thinning velocity is several order of magnitude larger than the creaming velocity. For example, in one millisecond (from t=2 ms to t=3 ms), the sheet thickness decreases from 140 μm to 91 μm at r=3.54 mm, and from 49 μm to 40 μm at r=7.95 mm. These give a mean thinning velocity of 49 μm/ms in r=3.54 mm and of 9 μm/ms in r=7.95 mm. In both cases, the thinning velocity is to a great extent superior to the creaming velocity.

In conclusion, the creaming velocity of the oil droplet is negligible compared to the thinning velocity of the liquid sheet. Hence, in the following, we consider: $z_{\text{p}}(t) = \frac{{z_{\text{p}_0}\tau_{\text{coll}}}^2}{t^2}$.

B.4 Time for an oil droplet to reach the air/water interface

In the following, we only consider the case $z_{\text{p}_\text{i}} > 0$, the situation is symmetrical as the creaming velocity is negligible. The condition for the oil droplet to be at the interface at time t_i, radial position r_{p_i} and vertical position z_{p_i} is:

$$\frac{h(r_{\text{p}_\text{i}}, t_\text{i})}{2} = z_{\text{p}_\text{i}} + r_{\text{oil}} \tag{B.8}$$

In the section 4.3.4, we have determined the thickness field of liquid sheet:

$$h(r,t) = \alpha {d_0}^3 u_0 \frac{t}{r^3} \quad \text{for} \quad \text{r} > \text{r}_\text{l}(\text{t}) \tag{B.9}$$

$$h(r,t) = \beta \frac{\pi}{6}\frac{{d_0}^3}{u_0}\frac{1}{rt} \quad \text{for} \quad \text{r} < \text{r}_\text{l}(\text{t}) \tag{B.10}$$

with $r_l(t) = \sqrt{\frac{\alpha 6}{\beta \pi}} u_0 t$, $\beta = 0.142$ and $\alpha = 0.061$.

In Figure B.2 is represented in a diagram (r_p,t), different initial positions of oil droplets within the liquid sheet and their trajectories (circle symbols and the corresponding dashed color lines). The red solid line indicates the limit between the two regimes of thickness $r_p = r_l(t)$ (Equations B.9 and B.10). Below this curve, the thickness of the liquid sheet is described by Equation B.10 and above this curve by Equation B.9. With this diagram, it is clear that during the whole travel of an oil droplet within the liquid film, the thickness of the sheet at the position of the oil droplet is described by the same model depending on the initial radial position of the oil droplet, r_{p_0}, compared to $r_l(\tau_{coll})$. If $r_{p_0} > r_l(\tau_{coll})$, during the whole travel of the oil droplet: $h(r_p, t) = \alpha {d_0}^3 u_0 \frac{t}{r_p^3}$ (Equation B.9). Whereas, if $r_{p_0} < r_l(\tau_{coll})$, during the whole travel of the oil droplet: $h(r_p, t) = \beta \frac{\pi}{6} \frac{{d_0}^3}{u_0} \frac{1}{r_p t}$ (Equation B.10).

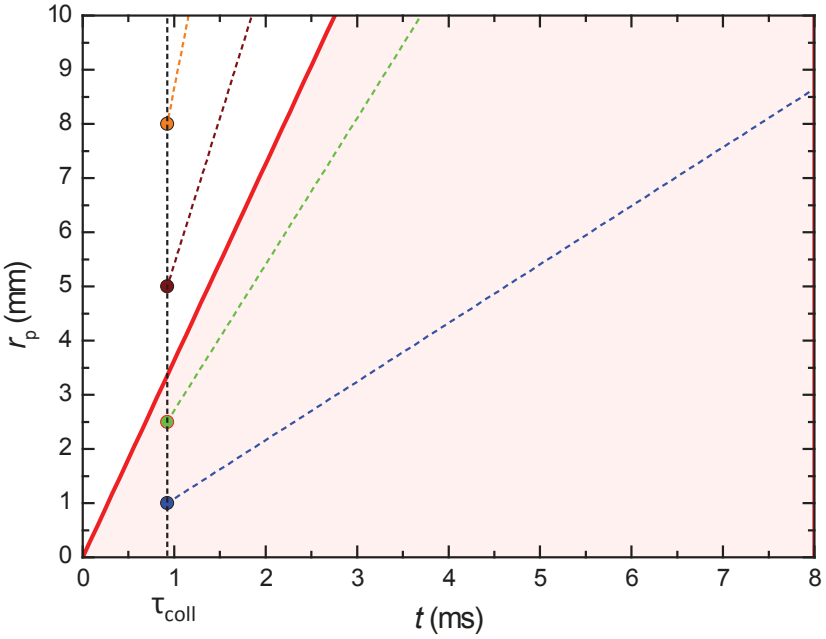

Figure B.2: Diagram (r_p,t) of the position of oil droplets within the liquid sheet. The red curve corresponds to $r_p = r_l(t)$, the red area corresponds to the droplet positions where the thickness of the sheet is described by Equation B.9, whereas the white area corresponds to the droplet positions where the thickness of the sheet is described by Equation B.10. Circle symbols corresponds to possible initial positions of oil droplets (defined in $t = \tau_{coll}$), the corresponding color lines represent the trajectories of the oil droplet within the liquid sheet.

B.4.1 First case: $r_{\mathrm{p}_0} > r_{\mathrm{l}}(\tau_{\mathrm{coll}})$

Equation B.8 with the thickness field given in Equation B.9 yields

$$\frac{\alpha}{2} {d_0}^3 u_0 \frac{t_{\mathrm{i}}}{{r_{\mathrm{p_i}}}^3} = z_{\mathrm{p_i}} + r_{\mathrm{oil}}. \tag{B.11}$$

Considering $r_{\mathrm{p_i}} = \frac{r_{\mathrm{p}_0}}{\tau_{\mathrm{coll}}} t_{\mathrm{i}}$, $z_{\mathrm{p_i}} = \frac{z_{\mathrm{p}_0} {\tau_{\mathrm{coll}}}^2}{{t_{\mathrm{i}}}^2}$ and $\tau_{\mathrm{coll}} = \frac{d_0}{u_0}$, we obtain directly the time for an oil droplet to reach the interface:

$$t_{\mathrm{i}}(r_{\mathrm{p}_0}, z_{\mathrm{p}_0}) = \frac{d_0}{u_0} \sqrt{\frac{\frac{\alpha}{2} {d_0}^4 \frac{1}{{r_{\mathrm{p}_0}}^3} - z_{\mathrm{p}_0}}{r_{\mathrm{oil}}}} \tag{B.12}$$

B.4.2 Second case: $r_{\mathrm{p}_0} < r_{\mathrm{l}}(\tau_{\mathrm{coll}})$

Equation B.8 with the thickness field given in Equation B.10 yields

$$\frac{\beta}{2} \frac{\pi}{6} \frac{{d_0}^3}{u_0} \frac{1}{r_{\mathrm{p_i}} t_{\mathrm{i}}} = z_{\mathrm{p_i}} + r_{\mathrm{oil}}. \tag{B.13}$$

Considering $r_{\mathrm{p_i}} = \frac{r_{\mathrm{p}_0}}{\tau_{\mathrm{coll}}} t_{\mathrm{i}}$, $z_{\mathrm{p_i}} = \frac{z_{\mathrm{p}_0} {\tau_{\mathrm{coll}}}^2}{{t_{\mathrm{i}}}^2}$ and $\tau_{\mathrm{coll}} = \frac{d_0}{u_0}$, the time for an oil droplet to reach the interface is equal to:

$$t_{\mathrm{i}}(r_{\mathrm{p}_0}, z_{\mathrm{p}_0}) = \frac{d_0}{u_0} \sqrt{\frac{\beta \frac{\pi}{12} {d_0}^2 \frac{1}{r_{\mathrm{p}_0}} - z_{\mathrm{p}_0}}{r_{\mathrm{oil}}}} \tag{B.14}$$

In conclusion, the time for an oil droplet to reach the air/water interface depends on the impact parameters of the tear (diameter of the tear, d_0, and impact velocity, u_0), on the initial position of the oil droplet within the liquid sheet (r_{p_0} and z_{p_0}) and on the oil droplet radius, r_{oil}.

B.5 Averaged time for oil droplets to reach the air/water interface

We calculate an averaged value of t_{i} by integrating over the different initial positions of the oil droplets $(r_{\mathrm{p}_0}, z_{\mathrm{p}_0})$.

$$< t_{\mathrm{i}} >= \frac{\int_{r_{\mathrm{p}_0}} \int_{z_{\mathrm{p}_0}} 2\pi r_{\mathrm{p}_0} n_0 t_{\mathrm{i}}(r_{\mathrm{p}_0}, z_{\mathrm{p}_0}) \, \mathrm{d}r_{\mathrm{p}_0} \mathrm{d}z_{\mathrm{p}_0}}{\int_{r_{\mathrm{p}_0}} \int_{z_{\mathrm{p}_0}} 2\pi r_{\mathrm{p}_0} n_0 \, \mathrm{d}r_{\mathrm{p}_0} \mathrm{d}z_{\mathrm{p}_0}} \tag{B.15}$$

with n_0 the number of oil droplets per unit of volume.

The integration limits are defined as following:

- $r_{p_0} \in [0 - r_{sheet}]$, with r_{sheet} the radius of the sheet at $t = \tau_{coll}$.
- $z_{p_0} \in \left[0 - \left(\frac{h(r_{p_0},\tau_{coll})}{2} - r_{oil}\right)\right]$

For $r_{p_0} > r_l(\tau_{coll})$

$$t_i(r_{p_0}, z_{p_0}) = \frac{d_0}{u_0}\sqrt{\frac{\frac{\alpha}{2}{d_0}^4\frac{1}{{r_{p_0}}^3} - z_{p_0}}{r_{oil}}} \tag{B.16}$$

$$h(r_{p_0}, \tau_{coll}) = \alpha {d_0}^3 u_0 \frac{\tau_{coll}}{r_{p_0}^3} = \alpha \frac{{d_0}^4}{r_{p_0}^3} \tag{B.17}$$

For $r_{p_0} < r_l(\tau_{coll})$

$$t_i(r_{p_0}, z_{p_0}) = \frac{d_0}{u_0}\sqrt{\frac{\beta\frac{\pi}{12}{d_0}^2\frac{1}{r_{p_0}} - z_{p_0}}{r_{oil}}} \tag{B.18}$$

$$h(r_{p_0}, \tau_{coll}) = \beta\frac{\pi}{6}\frac{{d_0}^3}{u_0}\frac{1}{r_{p_0}\tau_{coll}} = \beta\frac{\pi}{6}\frac{{d_0}^2}{r_{p_0}} \tag{B.19}$$

By integrating Equation B.15 with Equations B.16, B.18, B.17 and B.19, one obtains:

$$< t_i >= 2\frac{d_0}{u_0}\frac{1}{\sqrt{r_{oil}}}\frac{\frac{4}{3}(\beta\frac{\pi}{12})^{3/2}{d_0}^3\sqrt{r_l(\tau_{coll})} - \frac{1}{3}{r_{oil}}^{3/2}{r_{sheet}}^2 + \frac{4}{15}(\frac{\alpha}{2})^{3/2}{d_0}^6(r_l(\tau_{coll})^{-5/2} - {r_{sheet}}^{-5/2})}{\beta\frac{\pi}{6}{d_0}^2 r_l(\tau_{coll}) + \alpha{d_0}^4\left(\frac{1}{r_l(\tau_{coll})} - \frac{1}{r_{sheet}}\right) - r_{oil}{r_{sheet}}^2} \tag{B.20}$$

To estime $< t_i >$, we consider for the different parameters their experimental values as detailed below:

- d_0=3.7 mm
- u_0=4.0 m/s
- α=0.061
- β=0.142
- $r_l(\tau_{coll})$=3.35 mm (calculated from the values of α, β and u_0)
- r_{sheet}=6.6 mm (deduced from the experimental measurements of the evolution of the sheet diameter with time, see section 4.3.2.1).

In Figure B.3 is shown the evolution of the averaged time to reach the interface $< t_i >$ as a function of the oil droplet radius. As expected the time to reach the interface decreases with the oil droplet radius. For small values of r_{oil}, r_{oil}<3 μm, $< t_i >$ is directly proportional to $1/\sqrt{r_{oil}}$ as highlighted by the constant slope equal to $-1/2$ (blue dashed line), hence the other terms in r_{oil} in Equation B.20 are negligible. For r_{oil}>3 μm, the curve of $< t_i >$ differs from the blue dashed curve corresponding to an evolution of $< t_i >$ proportional to $1/\sqrt{r_{oil}}$, hence the other terms in r_{oil} in Equation B.20 are not anymore negligible. $< t_i >$ is equal to 23.7 ms for oil droplets of radius 0.25 μm and is equal to 3.07 ms for oil droplets of radius 20 μm. It is interesting to compare these values of $< t_i >$ to the time for the sheet to reach its maximal extension (t=4.6 ms). We remark that bigger oil droplets (r_{oil}>7.5 μm) will reach the air/water interface during the expansion phase of the liquid sheet, whereas smaller oil droplets will not reach the interface at so short time scales. In conclusion, there is a clear influence of the oil droplet radius on the time needed for the droplets to reach the air/water interface.

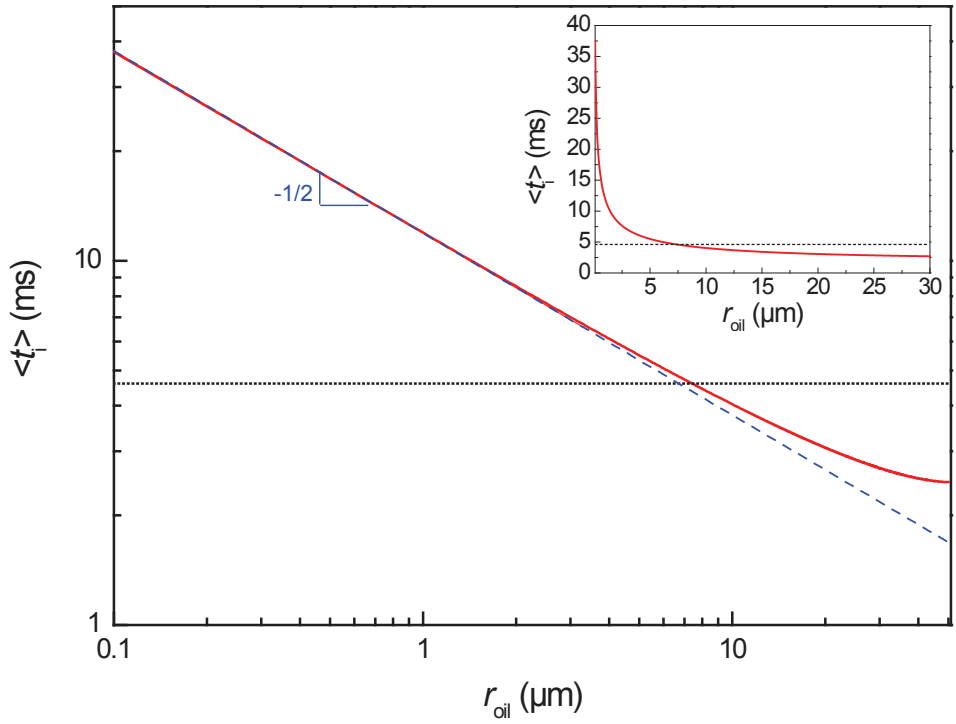

Figure B.3: Evolution of the averaged time to reach the interface $< t_i >$ as a function of the oil droplet radius, r_{oil}, in a lin/log graph and in a lin/lin graph in the inset. The black dotted line corresponds to the sheet maximal expansion. The blue dashed line corresponds to an evolution of $< t_i >$ proportional to $1/\sqrt{r_{oil}}$.

Appendix C

Size distribution of drops issued from liquid sheet destabilization

This Appendix is dedicated to the evaluation of the size distribution of drops issued from the destabilization of liquid sheets produced with the single-tear experiment. In this appendix, we consider liquid sheets made of the model emulsion at different concentrations (0.003 % v/v, 0.3 % v/v and 2.4 % v/v). With the conventional spray experiment, we have shown that an increase of the emulsion concentration entails a continuous increase of the size of the spray drops up to a saturation. The objective of this appendix is to measure the size distribution of drop issued from the destabilization of liquid sheets formed with the single-tear experiment to determine whether the same effect is measurable. In the first section, we present the analysis method used to measure the drop size distribution. In a second section, we compare the drop size distribution of liquid sheet made of emulsions at different concentrations.

C.1 Image analysis

In Figure C.1 is detailed the image analysis used to determine the size distribution of the drops issued from the sheet destabilization. The software ImageJ is used for the image analysis. For each experiment, the image analysis is performed on one image . The average values are calculated over four experiments for each concentration. We select for each experiment the first image where the sheet is completely destabilized into drops, i.e. where the web of ligaments is not visible anymore (Figure C.1(a)). First, the selected image is divided by an image of the background (i.e. an image taken just before the tear impact). Then, we apply a binary threshold on the image, Figure C.1(b), allowing one to count and measure the drop area, A_{drop}, Figure C.1(c). An apparent diameter of the drop, d_{drop}, is simply deduced from the area of the drops according to $d_{\text{drop}} = \sqrt{\frac{4A_{\text{drop}}}{\pi}}$. The resolution of the experimental set-up is such that drops smaller than 71 μm could not be measured. From the measurement of the drop diameter, we determine the drop size distribution by plotting the relative and cumulative frequencies as a function of the drop diameter.

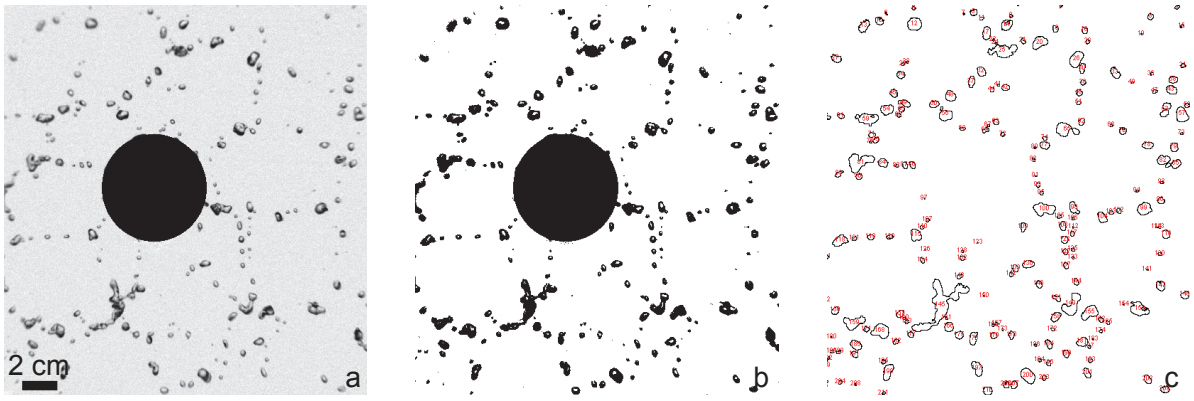

Figure C.1: Image analysis to determine the size distribution of drops issued from sheet destabilization. a). Image of the drops issued from the sheet destabilization. b). Binary thresholded image. c). Determination of the number and area of the drops.

C.2 Drop size distribution for different emulsion concentrations

In Figure C.2 is represented the drop size distribution in number for the three model emulsion concentrations investigated. For the three concentrations, we observe a very large distribution of sizes ranging from approximately 70 μm (the resolution limit) to 1200 μm with a main peak around 200 μm. In Table C.1 are summarized the number of drops counted, N, the mean diameter of the drop size distribution, d_{mean}, the standard deviation, STD, and the percentage in number of drops with a diameter lower than 150 μm, $V150$. We observe that an increase of the emulsion concentration entails an increase of the mean drop diameter, from 383 μm for C=0.003 % v/v to 410 μm for C=2.4 % v/v, i.e. a relative increase by 7 %. An increase of the emulsion concentration, from C=0.003 % v/v to C=2.4 % v/v entails a reduction of $V150$ by 33 %. Hence, an increase of the emulsion concentration entails a decrease of the proportion of small drops produced by the destabilization of liquid sheets formed with the single-tear experiment. The same effect of the emulsion concentration was observed on the size distribution of spray drops measured with a conventional spray experiment (section 5.2.2).

Note that due to the resolution limit of our experimental set-up (71 μm), we clearly underestimate the proportion of small drops in the spray. To characterize more accurately the size distribution of drops issued from sheet destabilization, we should have increased the spatial resolution of our experimental set-up and increased the number of drops counted. However, since we were able to determine directly the size distribution produced by a spray, we have decided to not focus our work on optimizing the measurement of size distribution of drops issued from sheet destabilization.

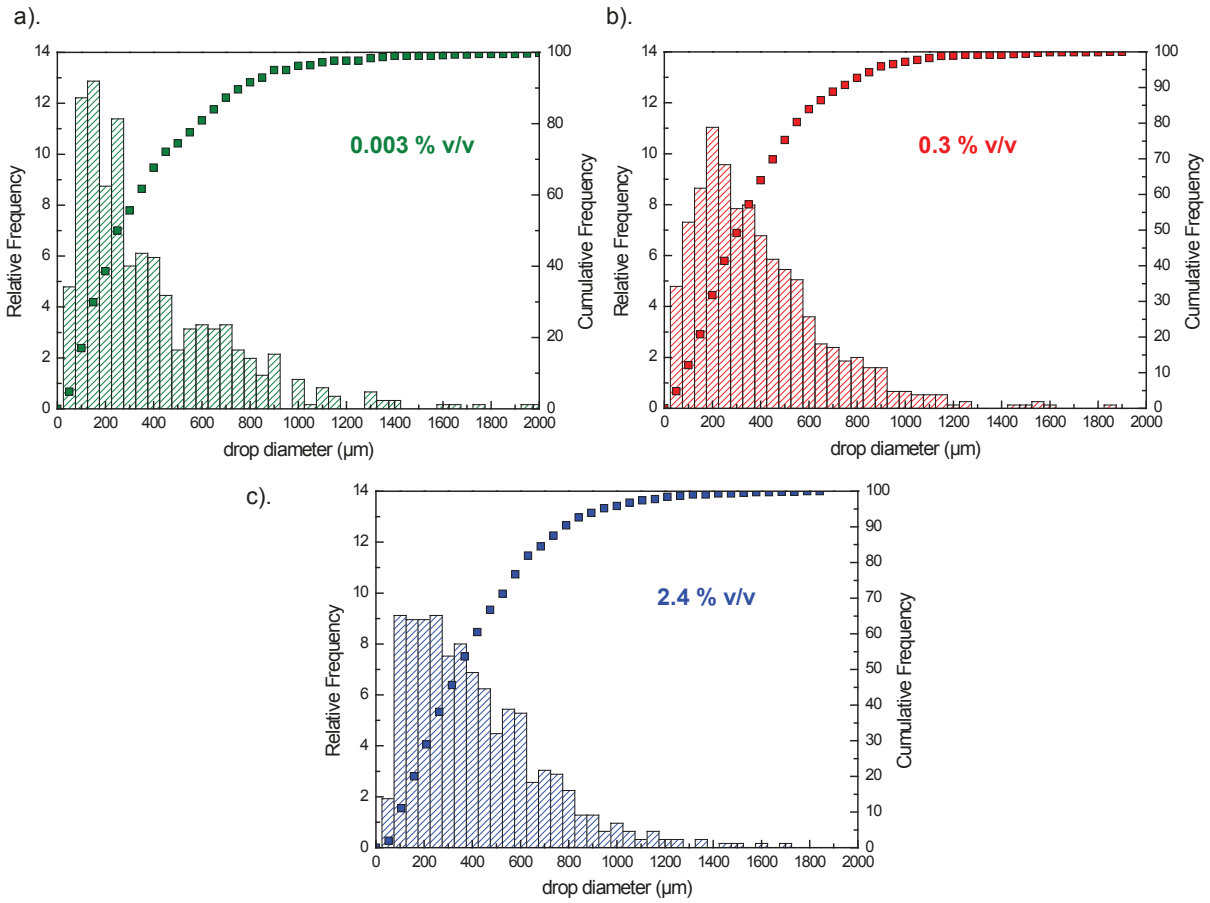

Figure C.2: Size distribution of the drops issued from the destabilization of liquid sheets of model emulsion at different concentrations a). C=0.003 % v/v, b). C=0.3 % v/v and c). C=2.4 % v/v.

	N	d_{mean} (μm)	STD (μm)	$V150$ (%)
C=**0.003 % v/v**	606	383	313	29.9
C=**0.3 % v/v**	752	391	265	20.7
C=**2.4 % v/v**	625	410	270	20.0

Table C.1: Characteristic parameters of the size distribution of the drop issued from the destabilization of liquid sheets of model emulsion at different concentrations. The number of drops counted, N, the mean diameter of the drop size distribution, d_{mean}, the standard deviation, STD, and the percentage in number of drops with a diameter lower than 150 μm, $V150$, are reported.

Bibliography

[Addo-Yobo 2011] F. O. Addo-Yobo, M. J. Pitt and H. A. Obiri. *The effects of particle size on the mechanisms of atomization of suspensions using hydraulic spray nozzles*. AIChE Journal, vol. 57, no. 8, pages 2007–2024, 2011. (Cited on pages 18 and 98.)

[Ahmad 1972] J. Ahmad and R. S. Hansen. *A simple quantitative treatment of the spreading of monolayers on thin liquid films*. Journal of Colloid and Interface Science, vol. 38, no. 3, pages 601–604, 1972. (Cited on pages 145 and 148.)

[Al Heidary 2014] M. Al Heidary, J. P. Douzals, C. Sinfort and A. Vallet. *Influence of spray characteristics on potential spray drift of field crop sprayers: A literature review*. Crop Protection, vol. 63, pages 120–130, September 2014. (Cited on pages 8 and 9.)

[Altieri 2014] A. Altieri, S. A. Cryer and L. Acharya. *Mechanisms, Experiment and Theory of Liquid Sheet Breakup and Drop Size from Agricultural Nozzles*. Atomization and Sprays, vol. 24, no. 8, pages 695–721, 2014. (Cited on pages 1, 18, 98 and 140.)

[Amarouchene 2001] Y. Amarouchene, D. Bonn, J. Meunier and H. Kellay. *Inhibition of the finite-time singularity during droplet fission of a polymeric fluid*. Physical Review Letters, vol. 86, no. 16, pages 2–5, 2001. (Cited on pages 46, 53, 54 and 57.)

[Arvidsson 2011] T. Arvidsson, L. Bergström and J. Kreuger. *Spray drift as influenced by meteorological and technical factors*. Pest Management Science, vol. 67, no. 5, pages 586–598, 2011. (Cited on pages 7, 8 and 9.)

[Bakshi 2007] S. Bakshi, I. V. Roisman and C. Tropea. *Investigations on the impact of a drop onto a small spherical target*. Physics of Fluids, vol. 19, no. 3, page 032102, 2007. (Cited on page 71.)

[Barnes 2000] T. J. Barnes and C. A. Prestidge. *PEO - PPO - PEO Block Copolymers at the Emulsion Droplet - Water Interface*. Langmuir, vol. 16, no. 9, pages 4116–4121, 2000. (Cited on page 192.)

[Basaran 2004] O. A. Basaran. *Small scale free surface flows with breakup, drop formation and emergining applications*. AIChE Journal, vol. 48, no. 9, pages 1842–1848, 2004. (Cited on pages 46 and 47.)

[Basheva 2000] E. S. Basheva, D. Ganchev, N. D. Denkov, K. Kasuga, N. Satoh and K. Tsujii. *Role of betaine as foam booster in the presence of silicone oil drops*. Langmuir, vol. 16, no. 6, pages 1000–1013, 2000. (Cited on page 201.)

[Basheva 2001] E. S. Basheva, S. Stoyanov, N. D. Denkov, K. Kasuga, N. Satoh and K. Tsujii. *Foam boosting by amphiphilic molecules in the presence of silicone oil*. Langmuir, vol. 17, no. 7, pages 969–979, 2001. (Cited on page 201.)

[Bennett 1993] T. Bennett and D. Poulikakos. *Splat-quench solidification: estimating the maximum spreading of a droplet impacting a solid surface*. Journal of Materials Science, vol. 28, no. 4, pages 963–970, 1993. (Cited on page 83.)

[Bergeron 1993] V. Bergeron, M. E. Fagan and C. J. Radke. *Generalized entering coefficients: a criterion for foam stability against oil in porous media*. Langmuir, vol. 9, no. 7, pages 1704–1713, July 1993. (Cited on page 156.)

[Bergeron 1996] V. Bergeron and D. Langevin. *Monolayer Spreading of Polydimethylsiloxane Oil on Surfactant Solutions*. Physical Review Letters, vol. 76, no. 17, pages 3152–3155, April 1996. (Cited on page 145.)

[Bergeron 1997] V. Bergeron, P. Cooper, C. Fischer, J. Giermanska-Kahn, D. Langevin and A. Pouchelon. *Polydimethylsiloxane (PDMS)-based antifoams*. Colloids and Surfaces A: Physicochemical and Engineering Aspects, vol. 122, pages 103–120, 1997. (Cited on pages 23, 24, 152 and 201.)

[Bergeron 2003] V. Bergeron. *Designing intelligent fluids for controlling spray applications*. Comptes Rendus Physique, vol. 4, no. 2, pages 211–219, March 2003. (Cited on pages 1, 8, 14, 20 and 25.)

[Berhanu 2013] M. Berhanu and E. Falcon. *Space-time-resolved capillary wave turbulence*. Physical Review E, vol. 87, no. 3, page 033003, March 2013. (Cited on page 74.)

[BFS] *Billericay Farm Services*. http://www.bfs.uk.com/farm-services/how-air-bubble-jets-work/. (2015-06-16). (Cited on page 13.)

[Bonfillon 1994] A. Bonfillon, F. Sicoli and D. Langevin. *Dynamic surface tension of ionic surfactant solutions*. Journal of Colloid and Interface Science, vol. 168, pages 497–504, 1994. (Cited on page 171.)

[Bremond 2006] N. Bremond and E. Villermaux. *Atomization by jet impact*. Journal of Fluid Mechanics, vol. 549, pages 273–306, February 2006. (Cited on pages 66 and 67.)

[Bremond 2007] N. Bremond, C. Clanet and E. Villermaux. *Atomization of undulating liquid sheets*. Journal of Fluid Mechanics, vol. 585, pages 421–456, August 2007. (Cited on pages 18 and 19.)

[Brown 2004] R. B. Brown, M. H. Carter and G. R. Stephenson. *Buffer zone and windbreak effects on spray drift deposition in a simulated wetland*. Pest Management Science, vol. 60, no. 11, pages 1085–1090, 2004. (Cited on page 11.)

[Bush 2004] J. W. M. Bush and A. E. Hasha. *On the collision of laminar jets: fluid chains and fishbones*. Journal of Fluid Mechanics, vol. 511, pages 285–310, July 2004. (Cited on page 66.)

[Butler Ellis 1997] M. C. Butler Ellis, C. R. Tuck and P. C. H. Miller. *The effect of some adjuvants on sprays produced by agricultural flat fan nozzles*. Crop Protection, vol. 16, no. 1, pages 41–50, 1997. (Cited on pages 1 and 21.)

[Butler Ellis 1999a] M. C. Butler Ellis and C. R. Tuck. *How adjuvants influence spray formation with different hydraulic nozzles*. Crop Protection, vol. 18, no. 2, pages 101–109, March 1999. (Cited on pages 1 and 21.)

[Butler Ellis 1999b] M. C. Butler Ellis, C. R. Tuck and P. C. H. Miller. *Dilute emulsions and their effect on the breakup of the liquid sheet produced by flat-fan spray nozzles*. Atomization and Sprays, vol. 9, pages 385–397, 1999. (Cited on pages 1, 18, 21, 66 and 98.)

[Butler Ellis 2010] M. C. Butler Ellis, A. G. Lane, C. M. O'Sullivan, P. C. H. Miller and C. R. Glass. *Bystander exposure to pesticide spray drift: New data for model development and validation*. Biosystems Engineering, vol. 107, no. 3, pages 162–168, 2010. (Cited on page 7.)

[Cabane 1982] B. Cabane and R. Duplessix. *Organization of surfactant micelles adsorbed on a polymer molecule in water : a neutron scattering study*. Journal Phys. France, vol. 43, pages 1529–1542, 1982. (Cited on pages 30, 39, 176 and 191.)

[Camp 1987] D. W. Camp and J. C. Berg. *The spreading of oil on water in the surface-tension regime*. Journal of Fluid Mechanics, vol. 184, pages 445–462, 1987. (Cited on page 145.)

[Christanti 2001] Y. Christanti and L. M. Walker. *Surface tension driven jet break up of strain-hardening polymer solutions*. Journal of Non-Newtonian Fluid Mechanics, vol. 100, no. 1-3, pages 9–26, September 2001. (Cited on pages 44, 46, 47, 48, 49, 53 and 57.)

[Christanti 2002] Y. Christanti and L. M. Walker. *Effect of fluid relaxation time of dilute polymer solutions on jet breakup due to a forced disturbance*. Journal of Rheology, vol. 46, no. 3, page 733, 2002. (Cited on pages 47 and 54.)

[Clanet 1999] C. Clanet and J. C. Lasheras. *Transition from dripping to jetting*. Journal of Fluid Mechanics, vol. 383, pages 307–326, 1999. (Cited on page 45.)

[Clanet 2002] C. Clanet and E. Villermaux. *Life of a smooth liquid sheet*. Journal of Fluid Mechanics, vol. 462, pages 307–340, August 2002. (Cited on pages 67, 68 and 70.)

[Clark 1971] C. J. Clark and N. Dombrowski. *The dynamics of the rim of a fan spray sheet.* Chemical Engineering Science, vol. 26, no. 11, pages 1949–1952, November 1971. (Cited on page 16.)

[Clark 1972] C. J. Clark and N. Dombrowski. *On the formation of drops from the rims of fan spray sheets.* Journal of Aerosol Science, vol. 3, pages 173–183, 1972. (Cited on pages 16, 18 and 124.)

[Combellack 1996] J. H. Combellack, N. M. Westen and R. G. Richardson. *A comparison of the drift potential of a novel twin fluid nozzle with conventional low volume flat fan nozzles when using a range of adjuvants.* Crop Protection, vol. 15, no. 2, pages 147–152, 1996. (Cited on page 8.)

[Culick 1960] F. E. C. Culick. *Comments on a Ruptured Soap Film.* Journal of Applied Physics, vol. 31, no. 6, page 1128, 1960. (Cited on pages 139, 140 and 152.)

[Denkov 2004] N. D. Denkov. *Mechanisms of foam destruction by oil-based antifoams.* Langmuir, vol. 20, no. 22, pages 9463–505, October 2004. (Cited on pages 21, 22, 23, 24, 152, 202 and 204.)

[Denkov 2013] N. D. Denkov, K. G. Marinova and S. S. Tcholakova. *Mechanistic understanding of the modes of action of foam control agents.* Advances in Colloid and Interface Science, vol. 206, pages 57–67, 2013. (Cited on page 157.)

[Dexter 1996] R. W. Dexter. *Measurement of extensional viscosity of polymer solutions and its effects on atomization from a spray nozzle.* Atomization and Sprays, vol. 6, pages 167–191, 1996. (Cited on pages 20 and 25.)

[Dexter 2001] R. W. Dexter. *The effect of fluid properties on spray quality from a flat fan nozzle.* In Pesticide formulations and application systems: twentieth volume, ASTM STP 1400. 2001. (Cited on pages 1, 14, 18, 22, 23, 66, 98, 113 and 205.)

[Dhiman 2010] R. Dhiman and S. Chandra. *Rupture of thin films formed during droplet impact.* Proceedings of the Royal Society A: Mathematical, Physical and Engineering Sciences, vol. 466, pages 1229–1245, December 2010. (Cited on page 73.)

[Dipietro 2006] N. D. Dipietro, C. Huh and R. G. Cox. *The hydrodynamics of the spreading of one liquid on the surface of another.* Journal of Fluid Mechanics, vol. 84, no. 03, page 529, April 2006. (Cited on page 145.)

[Dombrowski 1954] N. Dombrowski and R. P. Fraser. *A photographic investigation into the disintegration of liquid sheets.* Philosophical transactions of the Royal Society of London. Series A, Mathematical, Physical and Engineering sciences, vol. 247, pages 101–130, 1954. (Cited on pages 16, 17, 18, 19, 20, 21, 23, 25, 66, 67, 98, 151 and 202.)

[Dombrowski 1960] N. Dombrowski, D. Hasson and D. E. Ward. *Some aspects of liquid flow through fan spray nozzles*. Chemical Engineering Science, vol. 12, pages 35–50, 1960. (Cited on pages 16, 123 and 124.)

[Dorr 2013] G. J. Dorr, A. J. Hewitt, S. W. Adkins, J. Hanan, H. Zhang and B. Noller. *A comparison of initial spray characteristics produced by agricultural nozzles*. Crop Protection, vol. 53, pages 109–117, November 2013. (Cited on pages 1 and 13.)

[Dussaud 1998] A. D. Dussaud and S. M. Troian. *Dynamics of spontaneous spreading with evaporation on a deep fluid layer*. Physics of Fluids, vol. 10, no. 1, pages 23–38, 1998. (Cited on pages 145 and 148.)

[Dussaud 2005] A. D. Dussaud, O. K. Matar and S. M. Troian. *Spreading characteristics of an insoluble surfactant film on a thin liquid layer: comparison between theory and experiment*. Journal of Fluid Mechanics, vol. 544, no. -1, page 23, November 2005. (Cited on page 145.)

[Eggers 1993] J. Eggers. *Universal pinching of 3D axisymmetric free-surface flow*. Physical Review Letters, vol. 71, no. 21, pages 3458–3460, 1993. (Cited on page 46.)

[Eggers 2008] J. Eggers and E. Villermaux. *Physics of liquid jets*. Reports on Progress in Physics, vol. 71, no. 3, page 036601, March 2008. (Cited on pages 44 and 45.)

[Eggers 2010] J. Eggers, M. Fontelos, C. Josserand and S. Zaleski. *Drop dynamics after impact on a solid wall: Theory and simulations*. Physics of Fluids, vol. 22, no. 6, page 062101, 2010. (Cited on pages 83, 93, 94 and 95.)

[Fay 1969] J. A. Fay. The spread of oil slicks on a calm sea. Plenum Press, New York, 1969. (Cited on pages 142 and 143.)

[FOCUS 2007a] FOCUS. *"Landscape and mitigation factors in aquatic risk assessment. Volume 1. Extended summary and recommendations". Report of the FOCUS working group on landscape and mitigation factors in ecological risk assessment, EC document reference SANCO/10422/2005 v2.0*. Rapport technique September, 2007. (Cited on pages 7, 11 and 24.)

[FOCUS 2007b] FOCUS. *"Landscape and mitigation factors in aquatic risk assessment. Volume 2. Detailed technical reviews". Report of the FOCUS working group on landscape and mitigation factors in ecological risk assessment, EC document reference SANCO/10422/2005 v2.0*. Rapport technique September, 2007. (Cited on pages 7, 11 and 24.)

[Foda 1980] M. Foda and R. G. Cox. *The spreading of thin liquid films on a water-air interface*. Journal of Fluid Mechanics, vol. 101, no. 1, page 33, April 1980. (Cited on pages 142 and 145.)

[Frese 2003] C. Frese, S. Ruppert, M. Sugár, H. Schmidt-Lewerkühne, K. P. Wittern, V. B. Fainerman, R. Eggers and R. Miller. *Adsorption kinetics of surfactant mixtures from micellar solutions as studied by maximum bubble pressure technique.* Journal of Colloid and Interface Science, vol. 267, no. 2, pages 475–482, 2003. (Cited on page 171.)

[Gart 2013] S. Gart, B. Chang, B. Slama, R. Goodnight, S. H. Um and S. Jung. *Dynamics of squeezing fluids: Clapping wet hands.* Physical Review E, vol. 88, no. 2, page 023007, August 2013. (Cited on pages 67 and 68.)

[Gaver 2006] D. P. Gaver and J. B. Grotberg. *The dynamics of a localized surfactant on a thin film.* Journal of Fluid Mechanics, vol. 213, no. -1, page 127, April 2006. (Cited on page 145.)

[Green 2007] J. M. Green and G. B. Beestman. *Recently patented and commercialized formulation and adjuvant technology.* Crop Protection, vol. 26, no. 3, pages 320–327, 2007. (Cited on page 14.)

[Grisso 2013] R. Grisso, P. Hipkins, S. D. Askew, L. Hipkins and D. Mccall. *Nozzles : Selection and Sizing.* Rapport technique, Virginia State University, 2013. (Cited on page 10.)

[Hadjiiski 2001] A. Hadjiiski, S. Tcholakova, N. D. Denkov, P. Durbut, G. Broze and A. Mehreteab. *Effect of oily additives on foamability and foam stability - 2. Entry barriers.* Langmuir, vol. 17, no. 9, pages 6999–7010, 2001. (Cited on page 190.)

[Harkins 1941] W. D. A. Harkins. *A general thermodynamic theory of the spreading of liquids to form duplex films and of liquids or solids to form monolayers.* The Journal of Chemical Physics, vol. 9, pages 552–568, 1941. (Cited on pages 156 and 157.)

[Hayakawa 1991] K. Hayakawa and J. T. C. Kwak. *Cationic surfactants.* In D. N. Rubingh and P. M. Holland, editeurs, Cationic surfactants physical chemistry, page 189. Marcel Dekker Inc., New York, 1991. (Cited on pages 30 and 176.)

[Hilz 2013a] E. Hilz, A. V. P. Vermeer, M. A. Cohen Stuart and F. A. M. Leermakers. *Mechanism of perforation based on spreading properties of emulsified oil.* Atomization and Sprays, vol. 22, no. 12, pages 1053–1075, 2013. (Cited on pages 1, 15, 18, 23, 24, 25, 49, 66, 98, 113 and 203.)

[Hilz 2013b] E. Hilz and A. W. P. Vermeer. *Spray drift review: The extent to which a formulation can contribute to spray drift reduction.* Crop Protection, vol. 44, pages 75–83, February 2013. (Cited on page 1.)

[Holterman 2003] H. J. Holterman. *Kinetics and evaporation of water drops in air*. Rapport technique July, Institute of Agricultural and Environmental Engendering, Wageningen, 2003. (Cited on page 8.)

[Hotrum 2002] N. E. Hotrum, T. van Vliet, M. A. Cohen Stuart and G. A. van Aken. *Monitoring entering and spreading of emulsion droplets at an expanding air/water interface: a novel technique.* Journal of Colloid and Interface Science, vol. 247, no. 1, pages 125–31, March 2002. (Cited on page 172.)

[Joos 1977] P. Joos and J. Pintens. *Spreading kinetics of liquids on liquids.* Journal of Colloid and Interface Science, vol. 60, no. 3, pages 507–513, July 1977. (Cited on page 142.)

[Keller 1983] J. B. Keller and M. J. Miksis. *Surface tension driven flows.* SIAM Journal on Applied Mathematics, vol. 43, no. 2, pages 268–277, 1983. (Cited on page 46.)

[Kim 2005] J. Kim and M. H. Kim. *A photochromic dye activation method for measuring the thickness of liquid films.* Bulletin-Korean Chemical Society, vol. 26, no. 6, pages 966–970, 2005. (Cited on page 74.)

[Lastakowski 2014] H. Lastakowski, F. Boyer, A. L. Biance, C. Pirat and C. Ybert. *Bridging local to global dynamics of drop impact onto solid substrates.* Journal of Fluid Mechanics, vol. 747, pages 103–118, 2014. (Cited on pages 75, 93 and 141.)

[Leal-Calderon 2007] F. Leal-Calderon, V. Schmitt and J. Bibette. Emulsion science basic principles, volume 40. Springer, second édition, March 2007. (Cited on page 120.)

[Lefebvre 1989] A. H. Lefebvre. Atomization and Sprays. Hemisphere Publishing Corporation, New York, 1989. (Cited on page 103.)

[Lhuissier 2013] H. Lhuissier and E. Villermaux. *Effervescent atomization in two dimensions.* Journal of Fluid Mechanics, vol. 714, pages 361–392, January 2013. (Cited on pages 19, 98 and 104.)

[Lilleleht 1961] L. U. Lilleleht and T. J. Hanratty. *Measurement of interfacial structure for co-current air-water flow.* Journal of Fluid Mechanics, vol. 11, no. 1, pages 65–81, 1961. (Cited on page 74.)

[Makarytchev 2001] S. V. Makarytchev, T. A. G. Langrish and R. G. H. Prince. *Thickness and velocity of wavy liquid films on rotating conical surfaces.* Chemical Engineering Science, vol. 56, pages 77–87, 2001. (Cited on page 74.)

[Marengo 2011] M. Marengo, C. Antonini, I. V. Roisman and C. Tropea. *Drop collisions with simple and complex surfaces.* Current Opinion in Colloid & Interface Science, vol. 16, no. 4, pages 292–302, August 2011. (Cited on pages 73 and 83.)

[Matuura 1958] R. Matuura, H. Kimizuka, S. Miyamoto and R. Shimozawa. *The Study of the Adsorption of Detergents at a Solution-Air Interface by Radiotracer Method. I. Adsorption Isotherm for the Solution of Sodium Alkyl Sulfates.* Bulletin of the Chemical Society of Japan, vol. 31, no. 5, pages 532–538, 1958. (Cited on page 171.)

[Miller 2000] P. C. H. Miller and M. C. Butler Ellis. *Effects of formulation on spray nozzle performance for applications from ground-based boom sprayers.* Crop Protection, vol. 19, no. 8-10, pages 609–615, 2000. (Cited on pages 1, 15 and 21.)

[Miller 2003] P. C. H. Miller. *Spray Drift.* Pesticide Outlook, no. June, pages 205–209, 2003. (Cited on page 7.)

[Miller 2005] E. Miller, B. Gibson, E. McWilliams and J. P. Rothstein. *Collision of viscoelastic jets and the formation of fluid webs.* Applied Physics Letters, vol. 87, no. 1, page 014101, 2005. (Cited on page 66.)

[Miller 2011] P. C. H. Miller, M. C. Butler Ellis., A. G. Lane., C. M. O Sullivan. and C. R. Tuck. *Methods for minimising drift and off-target exposure from boom sprayer applications.* Aspects of Applied Biology, vol. 106, pages 281–288, 2011. (Cited on page 8.)

[Molino 1998] F. R. Molino, J.-F. Berret, G. Porte, O. Diat and P. Lindner. *Identification of flow mechanisms for a soft crystal.* The European Physical Journal B, vol. 3, no. 1, pages 59–72, 1998. (Cited on pages 30 and 176.)

[Mouza 2000] A. A. Mouza, N. A. Vlachos, S. V. Paras and A. J. Karabelas. *Measurement of liquid film thickness using a laser light absorption method.* Experiments in Fluids, vol. 28, pages 355–359, 2000. (Cited on page 74.)

[Mun 1998] R. P. Mun, J. A. Byars and D. V. Boger. *The effects of polymer concentration and molecular weight on the breakup of laminar capillary jets.* Journal of Non-Newtonian Fluid Mechanics, vol. 74, no. 1-3, pages 285–297, January 1998. (Cited on page 46.)

[Mun 1999] R. P. Mun, B. W. Young and D. V. Boger. *Atomisation of dilute polymer solutions in agricultural spray nozzles.* Journal of Non-Newtonian Fluid Mechanics, vol. 83, no. 1-2, pages 163–178, June 1999. (Cited on pages 1, 14, 20, 25 and 48.)

[Murphy 2000] S. D. Murphy, P. C. H. Miller and C. S. Parkin. *The Effect of Boom Section and Nozzle Configuration on the Risk of Spray Drift.* Journal of Agricultural Engineering Research, vol. 75, no. 2, pages 127–137, 2000. (Cited on page 7.)

[Nuyttens 2007] D. Nuyttens, K. Baetens, M. De Schampheleire and B. Sonck. *Effect of nozzle type, size and pressure on spray droplet characteristics.* Biosystems

Engineering, vol. 97, no. 3, pages 333–345, July 2007. (Cited on pages 10, 13 and 16.)

[Oerke 2004] E. C. Oerke and H. W. Dehne. *Safeguarding production - Losses in major crops and the role of crop protection*. Crop Protection, vol. 23, no. 4, pages 275–285, 2004. (Cited on page 5.)

[Ohyama 1988] T. Ohyama, K. Endoh, A. Mikami and Y. H. Mori. *Optical interferometry for measuring instantaneous thickness of transparent solid and liquid films*. Review of Scientific Instruments, vol. 59, pages 2018–2022, 1988. (Cited on page 74.)

[Papageorgiou 1995] D. T. Papageorgiou. *On the breakup of viscous liquid threads*. Physics of Fluids, vol. 7, no. 7, page 1529, 1995. (Cited on page 46.)

[Permin 1992] O. Permin, L. N. Jø rgensen and K. Persson. *Deposition characteristics and biological effectiveness of fungicides applied to winter wheat and the hazards of drift when using different types of hydraulic nozzles*. Crop Protection, vol. 11, no. 6, pages 541–546, 1992. (Cited on page 7.)

[Qin 2010] K. Qin, H. Tank, S. Wilson, B. Downer and L. Liu. *Controlling Droplet-Size Distribution Using Oil Emulsions in Agricultural Sprays*. Atomization and Sprays, vol. 20, no. 3, pages 227–239, 2010. (Cited on pages 1, 15, 22, 23, 49, 66, 122 and 205.)

[Rozhkov 2002] A. Rozhkov, B. Prunet-Foch and M. Vignes-Adler. *Impact of water drops on small targets*. Physics of Fluids, vol. 14, no. 10, pages 3485–3501, 2002. (Cited on pages 68, 69, 72, 79, 80 and 100.)

[Rozhkov 2004] A. Rozhkov, B. Prunet-Foch and M. Vignes-Adler. *Dynamics of a liquid lamella resulting from the impact of a water drop on a small target*. Proceedings of the Royal Society A: Mathematical, Physical and Engineering Sciences, vol. 460, pages 2681–2704, 2004. (Cited on pages 69, 70, 71, 80, 83, 84, 88, 94, 95, 96, 97 and 135.)

[Rozhkov 2006] A. Rozhkov, B. Prunet-Foch and M. Vignes-Adler. *Dynamics and disintegration of drops of polymeric liquids*. Journal of Non-Newtonian Fluid Mechanics, vol. 134, pages 44–55, March 2006. (Cited on page 98.)

[Rozhkov 2010] A. Rozhkov, B. Prunet-Foch and M. Vignes-Adler. *Impact of drops of surfactant solutions on small targets*. Proceedings of the Royal Society A: Mathematical, Physical and Engineering Sciences, vol. 466, no. 2122, pages 2897–2916, April 2010. (Cited on page 94.)

[Savart 1833] F. Savart. *Mémoire sur le choc d'une veine liquide lancée contre un plan circulaire*. Ann. de Chim., vol. 54, 1833. (Cited on pages 66 and 68.)

[Sheely 1932] M. L. Sheely. *Glycerol viscosity tables.* Industrial and Engineering Chemisty, vol. 24, no. 9, pages 1060–1064, 1932. (Cited on pages 28, 130 and 131.)

[Spielbauer 1994] T. M. Spielbauer and C. K. Aidun. *The cause and effects of perforations in a liquid sheet from a splash-plate spray nozzle.* Atomization and Sprays, no. 514, 1994. (Cited on page 19.)

[Stainier 2006] C. Stainier, M. F. Destain, B. Schiffers and F. Lebeau. *Droplet size spectra and drift effect of two phenmedipham formulations and four adjuvants mixtures.* Crop Protection, vol. 25, no. 12, pages 1238–1243, 2006. (Cited on page 8.)

[Stephenson 2006] G. R. Stephenson, I. G. Ferris, P. T. Holland and M. Nordberg. *Glossary of terms relating to pesticides (IUPAC Recommendations 2006).* Pure and Applied Chemistry, vol. 78, no. 11, pages 2075–2154, 2006. (Cited on page 6.)

[Taylor 1959] G. I. Taylor. *The dynamics of thin sheets of fluid iii. disintegration of fluid sheets.* Proceedings of the Royal Society of London. Series A: Mathematical, Physical and Engineering Sciences, vol. 253, pages 313–321, 1959. (Cited on pages 139, 140 and 152.)

[Taylor 2004] W. A. Taylor, A. R. Womac, P. C. H. Miller and B. P. Taylor. *An Attempt to Relate Drop Size to Drift Risk.* International conference on pesticide Application for drift management Octobre 27-29, pages 210–223, 2004. (Cited on page 8.)

[Thoroddsen 2012] S. T. Thoroddsen, K. Takehara and T. G. Etoh. *Micro-splashing by drop impacts.* Journal of Fluid Mechanics, vol. 706, pages 560–570, July 2012. (Cited on page 80.)

[Tibiriçá 2010] C. B. Tibiriçá, F. J. Do Nascimento and G. Ribatski. *Film thickness measurement techniques applied to micro-scale two-phase flow systems.* Experimental Thermal and Fluid Science, vol. 34, no. 4, pages 463–473, May 2010. (Cited on page 74.)

[Tirtaatmadja 2006] V. Tirtaatmadja, G. H. McKinley and J. J. Cooper-White. *Drop formation and breakup of low viscosity elastic fluids: Effects of molecular weight and concentration.* Physics of Fluids, vol. 18, no. 4, page 043101, 2006. (Cited on pages 46, 47 and 54.)

[TOPPS] TOPPS. *Train operators to promote best management practices and sustainability - Water protection.* http://www.topps-life.org/. (2015-06-22). (Cited on pages 6 and 12.)

[Umlong 2007] I. M. Umlong and K. Ismail. *Micellization behaviour of sodium dodecyl sulfate in different electrolyte media.* Colloids and Surfaces A: Physicochemical and Engineering Aspects, vol. 299, no. 1-3, pages 8–14, 2007. (Cited on pages 158 and 159.)

[Vallet 2011] A. Vallet and C. Tinet. *Surfactant Influence on Droplet Size and Velocity Spectra from Hollow Cone and Air Induced Sprays.* Journal of Agricultural Science and Technology B, vol. 1, pages 718–727, 2011. (Cited on page 104.)

[Vallet 2013] A. Vallet and C. Tinet. *Characteristics of droplets from single and twin jet air induction nozzles: A preliminary investigation.* Crop Protection, vol. 48, pages 63–68, 2013. (Cited on page 104.)

[van de Zande 2004] J. C. van de Zande, H. J. Holterman and H. A. J. Porskamp. *Influence of reference nozzle choice on spray drift classification.* In International conference on pesticide application for drift management, volume 03, 2004. (Cited on page 103.)

[Vassallo 1991] P. Vassallo and N. Ashgriz. *Satellite formation and merging in liquid jet breakup.* Proceedings of the Royal Society of London. Series A: Mathematical, Physical and Engineering Sciences, vol. 433, pages 269–286, 1991. (Cited on page 44.)

[Vernay 2015a] C. Vernay, L. Ramos, J.P. Douzals, R. Goyal, J. C. Castaing and C. Ligoure. *Drop impact experiment as a model experiment to investigate the role of oil-in-water emulsions in controlling the drop size distribution of an agricultural spray.* in press, Atomization and Sprays, 2015. (Cited on pages 102 and 208.)

[Vernay 2015b] C. Vernay, L. Ramos and C. Ligoure. *Bursting of Dilute Emulsion-Based Liquid Sheets Driven by a Marangoni Effect.* Physical Review Letters, vol. 115, no. 19, page 198302, November 2015. (Cited on pages 130 and 208.)

[Vernay 2015c] C. Vernay, L. Ramos and C. Ligoure. *Free radially expanding liquid sheet in air: time- and space-resolved measurement of the thickness field.* Journal of Fluid Mechanics, vol. 764, pages 428–444, January 2015. (Cited on pages 66, 123 and 207.)

[Villermaux 2002] E. Villermaux and C. Clanet. *Life of a flapping liquid sheet.* Journal of Fluid Mechanics, vol. 462, pages 341–363, August 2002. (Cited on page 16.)

[Villermaux 2011] E. Villermaux and B. Bossa. *Drop fragmentation on impact.* Journal of Fluid Mechanics, vol. 668, pages 412–435, January 2011. (Cited on pages 69, 70, 71, 72, 73, 79, 80, 83, 84, 86, 88, 94, 95, 97, 104 and 135.)

[Wagner 2005] C. Wagner, Y. Amarouchene, D. Bonn and J. Eggers. *Droplet Detachment and Satellite Bead Formation in Viscoelastic Fluids.* Physical Review Letters, vol. 95, no. 16, page 164504, October 2005. (Cited on pages 46, 53 and 57.)

[Weinheimer 1981] R. M. Weinheimer, D. F. Evans and E. L. Cussler. *Diffusion in surfactant solutions.* Journal of Colloid and Interface Science, vol. 80, no. 2, pages 357–368, 1981. (Cited on page 171.)

[Wentworfh 1966] W. E. Wentworfh. *Dependence of the Beer-Lambert absorption law on monochromatic radiation.* Journal of Chemical Education, vol. 43, pages 262–264, 1966. (Cited on page 76.)

[Young 2004] B. Young. *Illinois crop protection technology conference.* In Basics and benefits of drift control agents, pages 45–47, 2004. (Cited on page 14.)

Déstabilisation de nappes liquides d'émulsions diluées

Abstract: Le phénomène de dérive constitue un enjeu environnemental et sanitaire majeur lors de la pulvérisation de solutions phytosanitaires sur les surfaces agricoles. Sous l'action du vent, des gouttelettes peuvent dériver loin des champs ciblés et être source de pollution. Une stratégie pour limiter la dérive est de contrôler la distribution de taille des gouttes de spray, en réduisant la proportion de petites gouttes. Dans ce but, des additifs anti-dérives, tels que des émulsions diluées d'huile dans l'eau, ont été développés. Bien que largement étudiés, les effets de ces émulsions ne sont pas encore bien compris. L'objectif de cette thèse est d'élucider les mécanismes à l'origine de l'augmentation de la taille des gouttes de spray à base d'émulsions.

La pulvérisation implique la fragmentation d'un flux de liquide par une buse hydraulique. A la sortie de la buse, une nappe libre de liquide est formée, puis déstabilisée en gouttes. Afin d'élucider les mécanismes à l'origine des effets anti-dérives des émulsions, nous étudions l'influence de ces émulsions sur les mécanismes de déstabilisation des nappes liquides. Une expérience modèle basée sur la collision d'une goutte de solution sur une cible solide est utilisée pour produire et visualiser des nappes liquides. Lors de l'impact, la goutte s'aplatit en une nappe qui s'étend radialement dans l'air, bordée par un bourrelet plus épais. Différents mécanismes de déstabilisation sont observés en fonction des propriétés des fluides. Une nappe d'eau pure s'étale radialement puis se rétracte par effet de la tension de surface ; simultanément, le bourrelet est déstabilisé en gouttelettes. Pour une émulsion diluée d'huile dans l'eau, le mécanisme de déstabilisation dominant est considérablement modifié: les nappes sont déstabilisées par la nucléation de trous qui perforent le film liquide lors de son expansion; les trous grandissent jusqu'à la formation d'un réseau de ligaments, qui est ensuite déstabilisé en gouttes.

Une étude systématique de l'influence des paramètres physico-chimiques de l'émulsion, tels que la concentration en huile et la distribution de taille de gouttelettes d'huile, sur le mécanisme de perforation est conduite. Nous établissons une corrélation entre le nombre d'évènements de perforations observés dans les nappes modèles et la distribution de taille de gouttes de sprays formés avec des buses de pulvérisation agricoles. Ce résultat démontre la pertinence expérimentale de notre expérience modèle pour comprendre les mécanismes d'actions des formulations anti-dérives. Nous montrons ainsi que le mécanisme à l'origine de l'augmentation de la taille des gouttes de spray à base d'émulsion est un mécanisme de perforation.

Pour comprendre les mécanismes à l'origine de la perforation, nous développons une technique optique permettant de mesurer le champ d'épaisseur de nappes liquides. Nous constatons que la formation d'un trou dans la nappe est systématiquement précédée par un amincissement local du film liquide. Nous montrons que cet amincissement est le résultat de l'entrée puis de l'étalement par effet Marangoni de gouttelettes d'huile à l'interface air/eau. L'amincissement du film liquide conduit in fine à sa rupture.

Nous proposons un mécanisme de perforation en deux étapes: les gouttelettes d'huile (i) entrent à l'interface air/eau, et (ii) s'étalent à l'interface. La formulation de l'émulsion est un paramètre critique pour contrôler le processus de perforation. L'addition de sels ou de copolymères amphiphiles à des émulsions stabilisées par des tensio-actifs ioniques peut soit déclencher, soit inhiber le mécanisme de perforation. Nous montrons que l'entrée de gouttelettes d'huile à l'interface air/eau est l'étape limitante de ce mécanisme. Les interactions répulsives de nature stérique et/ou électrostatique entre les gouttelettes d'huile et l'interface stabilisent le film liquide, empêchant les gouttelettes d'entrer à l'interface, et ainsi inhibent le processus de perforation.

Keywords: émulsion huile dans eau, nappe liquide, spray, impact de goutte, effet Marangoni, adjuvant anti-dérive

Destabilization of liquid sheets of dilute emulsions

Abstract: One of the major environmental issues related to spraying of pesticides on cultivated crops is the drift phenomenon. Because of the wind, small droplets may drift away from the targeted crop and cause contamination. One way to reduce the drift is to control the spray drop size distribution and reduce the proportion of small drops. In this context, anti-drift additives have been developed, including dilute oil-in-water emulsions. Although being documented, the effects of oil-in-water emulsions on spray drop size distribution are not yet understood. The objective of this thesis is to determine the mechanisms at the origin of the changes of the spray drop size distribution for emulsion-based sprays.

Agricultural spraying involves atomizing a liquid stream through a hydraulic nozzle. At the exit of the nozzle, a free liquid sheet is formed, which is subsequently destabilized into droplets. In order to elucidate the mechanisms causing the changes of the spray drop size distribution, we investigate the influence of emulsions on the destabilization mechanisms of liquid sheets. Model single-tear experiments based on the collision of one tear of liquid on a small solid target are used to produce and visualize liquid sheets with a fast camera. Upon impact, the tear flattens into a sheet radially expanding in the air bounded by a thicker rim. Different destabilization mechanisms of the sheet are observed depending on the fluid properties. A pure water sheet spreads out radially and then retracts due to the effect of surface tension. Simultaneously, the rim corrugates forming radial ligaments, which are subsequently destabilized into droplets. The destabilization mechanism is drastically modified when a dilute oil-in-water emulsion is used. Emulsion-based liquid sheets are destabilized through the nucleation of holes within the sheet that perforate the sheet during its expansion. The holes grow until they merge together and form a web of ligaments, which are then destabilized into drops.

The physical-chemical parameters of the emulsion, such as emulsion concentration and emulsion droplet size distribution, are modified to rationalize their influence on the perforation mechanism. We correlate the size distribution of drops issued from conventional agricultural spray with the amount of perforation events in single-tear experiments, demonstrating that the single-tear experiment is an appropriate model experiment to investigate the physical mechanisms governing the spray drop size distribution of anti-drift formulations. We show that the relevant mechanism causing the increase of drops size in the emulsion-based spray is a perforation mechanism.

To gain an understanding of the physical mechanisms at the origin of the perforation events, we develop an optical technique that allows the determination of the time and space-resolved thickness of the sheet. We find that the formation of a hole in the sheet is systematically preceded by a localized thinning of the liquid film. We show that the thinning results from the entering and Marangoni-driven spreading of emulsion oil droplet at the air/water interface. The localized thinning of the liquid film ultimately leads to the rupture of the film. We propose the perforation mechanism as a sequence of two necessary steps: the emulsion oil droplets (i) enter the air/water interface, and (ii) spread at the interface. We show that the formulation of the emulsion is a critical parameter to control the perforation. The addition of salt or amphiphilic copolymers can trigger or completely inhibit the perforation mechanism. We show that the entering of oil droplets at the air/water interface is the limiting step of the mechanism. Thin-film forces such as electrostatic or steric repulsion forces stabilize the thin film formed between the interface and the approaching oil droplets preventing the entering of oil droplets at the interface and so inhibit the perforation process.

Keywords: oil-in-water emulsion, liquid sheet, spray, drop impact, Marangoni effect, anti-drift adjuvant